MOLECULAR IMAGING WITH MASS SPECTROMETRY: INSTRUMENTAL AND METHODOLOGICAL ADVANCES FOR BIOLOGICAL APPLICATIONS

BY
ERIC JOSEPH LANNI

DISSERTATION

Submitted in partial fulfillment of the requirements
for the degree of Doctor of Philosophy in Chemistry
in the Graduate College of the
University of Illinois at Urbana-Champaign, 2014

Urbana, Illinois

Doctoral Committee:

Professor Jonathan V. Sweedler, Chair
Emeritus Professor Alexander Scheeline
Professor Mary L. Kraft
Professor Lori T. Raetzman

ABSTRACT

Mass spectrometry imaging (MSI) is an analytical technique providing a unique combination of capabilities: label-free, non-targeted, and highly multiplex detection and imaging of chemical species ranging in mass from single protons to large proteins exceeding 100 kDa, identifiable by mass and confirmed (when possible) by structural information obtained through tandem MS experiments. These capabilities make MSI a powerful tool for biological investigations especially in cases where analytes of interest are not known *a priori*, and where one wishes to comprehensively survey the spatiochemical composition of a specimen in order to generate more refined hypotheses that will guide subsequent targeted work. In the past several decades MSI has been extensively developed for and applied to macroscopic or “tissue-level” biomolecular imaging studies, and parallel effort has focused on improving MSI capability in the microscopic or “cell-scale” regime in a number of ways. The latter work faces many additional challenges, however, such as designing instrumentation with suitable spatial resolution as well as achieving sufficient sampling efficiency (through instrumentation and experimental protocols) to detect the minute amounts of a compound which are present in micro-scale volumes.

This thesis presents a body of work with two main goals: 1) improving cell-scale MSI capabilities through development of new instrumentation and compatible methodologies, and 2) developing methods for combining MSI with other imaging techniques in order to enhance the information gleaned from an experiment. A main step towards the first goal here is development of a hybrid mass spectrometer of novel design which combines two complementary MSI probes – a laser and a polyatomic ion beam – on a system with other advantageous features such as high mass resolution and tandem MS capability. The system is characterized, applied to visualize chemical distributions on single cultured neurons, and combined with electron microscopy to correlate chemical localizations with physical features of the cells. Towards the second goal, MSI is combined with confocal Raman microscopy (CRM) – a label-free photospectroscopic chemical imaging technique – to obtain complementary information about the molecular composition of bacterial biofilms. A new method is similarly developed for combining multiple MSI approaches in order to precisely correlate chemical images on multiple size scales, and this is also applied to bacterial biofilm imaging.

Finally, the two main efforts of the work are integrated to demonstrate "heterocorrelated imaging" where CRM is combined with MSI performed on the new hybrid instrument in order to visualize secondary metabolite distributions in the biofilms. A novel microspot array approach is developed for precise correlation of images generated by the two different techniques, and the hybrid instrument's tandem MS capability is employed with the SIMS microprobe to confirm tentative mass assignments by *in situ* analysis. Correlation of these two techniques here also importantly demonstrates how cross-validation between mass- and vibration-based chemical imaging modalities can address ambiguity in each individual data set.

To my family,

for their love, support, and encouragement.

ACKNOWLEDGMENTS

This work could not have been accomplished without a great number of contributions from many others. Professor Jonathan Sweedler is truly an incredible advisor to all of us in the group, providing support in the form of high quality scientific proposals, abundant resources, and a positive work environment where our own ideas are welcomed and respected and where science is challenging yet fun. I've learned an incredible amount about science, research, and professional skills from Jonathan in the past five years, and I consider myself very fortunate to have had such a positive graduate school experience thanks in large part to the environment he creates for us and the extraordinary effort he makes to mentor us.

I also wish to thank the rest of my thesis committee members, Profs. Mary Kraft, Lori Raetzman, and Alex Scheeline, for their support throughout the PhD program. They have all offered thoughtful feedback and useful input on my work, and I recognize the time they took from their busy schedules to do so. Prof. Scheeline is an exceptional teacher, I learned a great deal about science and research from his graduate level courses, and his mentoring contributions to the UIUC analytical chemistry graduate program were invaluable in and of themselves.

The Sweedler research group as a whole has been a wonderfully supportive community to work with. Research scientists Drs. Stanislav Rubakhin and Elena Romanova are very generous with their time, always willing to demonstrate a lab technique, explain a procedure, or discuss results when asked, and I have learned a great deal from them. I'm also especially grateful to numerous colleagues and ex-colleagues who contributed to my work directly or indirectly, lent assistance when it was desperately needed, or provided stimulating scientific discussion along the way, especially: Sage Dunham, Jordan Aerts, Ta-Hsuan Ong, Itamar Livnat, Sarah Dowd, and Drs. Callie Croushore, Peter Nemes, Erik Jansson, and Ann Knolhoff. Some of these contributions are noted in the chapters that follow here while others were more diffuse, but all of them helped to form the positive, collaborative group environment that was great to work in. I am grateful for the assistance of Stephanie Baker in manuscript preparation, and to Xiying Wang for her expert cell culturing skills which many of us benefit from.

The UIUC School of Chemical Sciences likewise provides a highly supportive environment to work in, and my work benefitted from the contributions of other several others in this larger community. Julie Sides is an invaluable member of the analytical chemistry division,

and I am very grateful for all of her guidance and administrative assistance – always cheerfully provided - since my very first visit to the school. Fellow graduate student Mike Porambo (McCall research group) went above and beyond in helping with technical instrumentation issues on multiple occasions, and did so happily despite having plenty of his own work to accomplish, and I'm very grateful to him for that. I'm also grateful to the SCS machinists, especially Michael Harland and Roger Smith, who are not only very skilled at their work but also offered valuable design and fabrication advice. Kyle Webb likewise offered helpful advice for troubleshooting vacuum systems, and Scott Robinson does a wonderful job managing the Beckman Institute Microscopy Suite at a high performance level, happily lending a hand in experiments whenever needed, which was often for me.

Outside of UIUC, I'd like to acknowledge our colleagues at University of Notre Dame for a productive and fun collaboration which yielded much of the data presented here: Rachel Masyuko, Callan Driscoll, Prof. Paul Bohn, and Prof. Joshua Shrout. I'm very grateful to the support provided by Dr. Randall Pedder at Ardara Tech., Dr. Sasha Loboda at AB SCIEX, and Prof. Nick Winograd (along with several of his group members) at Pennsylvania State University, all of whom provided valuable input on instrumental design and troubleshooting. I'd also like to thank Profs. Michael Golde and George Bandik at University of Pittsburgh for kindling my interest in chemistry many years ago, Prof. Alan Waggoner at Carnegie Mellon University for giving me room to grow (up) as a young researcher, and to Prof. Mark Bier at Carnegie Mellon University for sharing his passion and skills with mass spectrometric instrumentation, which in large part led to what I've accomplished here.

Last but certainly not least, I'd like to thank my family for their amazing support, encouragement, and love, without which I would certainly not be where I am right now. My wife Ana has done a wonderful job of managing our family on very limited resources these past five years while simultaneously supporting and encouraging me through the challenges of my research, and I am extremely grateful for her hard work. The unconditional love and joy of my children, Patrick and Evangelina, was likewise something I could not have completed this work without. I'm also eternally grateful to the Coleman Family for their immense support and encouragement, and to my parents, Catherine and Frederick Lanni, for raising me with a strong work ethic and for imparting much of the knowledge and skills that I drew upon to complete this work.

TABLE OF CONTENTS

CHAPTER 1

INTRODUCTION AND THESIS OVERVIEW

Analytical chemistry is the science of chemical measurement – qualitative and quantitative determination of the chemical composition of matter in the world around us. In a sense, for visual creatures such as ourselves, an ultimate analytical chemistry tool might be one which allows us to glance at a specimen and visualize its full chemical composition without any physical modification. Such a tool has not yet been created, but there do exist several *chemical imaging* techniques in development which begin to approach it by providing the combined capabilities of label-free, non-targeted, and multiplex visualization of chemical distributions. These capabilities give such techniques unique advantages in the chemical imaging repertoire, such as the ability to serve as “hypothesis-generating tools” by surveying a large number of analyte distributions and identifying unanticipated spatio-chemical features for further study.

This thesis presents a body of work done to advance one such technique, *mass spectrometry imaging (MSI),* specifically for application in microscopic biological studies. Mass spectrometry (MS), sometimes referred to as “the world’s smallest scale,” allows direct, label-free detection of the atomic elements and chemical compounds in a complex mixture by ionizing them, separating them by mass, and then detecting them to generate a *mass spectrum*. The mass spectrum generally yields both qualitative and quantitative information about the mixture - *what* is there, and *how much* is present – and MS is capable of detecting biomolecules of virtually every class, including proteins, nucleic acids, lipids, carbohydrates, and metabolites. More sophisticated MS-based experiments can also provide additional information about molecular structure, molecular conformation,[1] and noncovalent interactions.[2] While there are certainly many challenges involved in acquiring this information and for obtaining a comprehensive chemical profile from a complex biological sample with MS, it is nevertheless among the most capable analytical techniques for doing so.

With suitable instrumentation and sample preparation methods, MS can be used to *profile* a sample spatially; that is, to acquire separate mass spectra representing the chemical composition at different spatial locations.[3] Taken a step further, MSI is performed by profiling a sample in a rectangular array of points defined over a surface area of interest.[4] A full mass spectrum is acquired at each point, and chemical images (technically *ion images*) can be generated from this data by treating each point as a pixel in the image where pixel brightness (in false color) represents the relative abundance of some ion of interest, as shown in **Figure 1.1**. A typical mass spectrum includes tens to hundreds of unique detected ions, so one MSI experiment can likewise yield correlated images for hundreds of unique compounds, and can do so *ex post facto* due to the non-targeted nature of MS. MSI has been extensively and successfully applied to imaging of tissue sections in biological and clinical research,[5-6] and has been particularly useful in the visualization of lipid distributions[7] as well as in classification of diseased tissue states.[8]

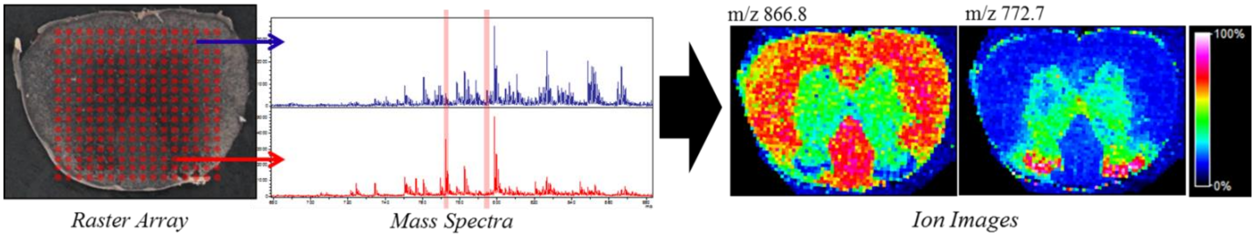

Figure 1.1: Overview of mass spectrometry imaging (MSI). MS spectra are acquired in a rectangular array of points across a sample (here, a spinal cord tissue section), then ion images are generated in false color to represent the relative abundance of particular ions across the surface.

Current MSI development efforts at instrumental and methodological levels include improvement of spatial resolution, detection limits, multivariate data analysis, quantitation, further characterization of detected compounds, and meaningful correlation with other imaging techniques. The work presented here touches on all of these topics to some extent, with a focus on advancing 1) cell-scale chemical characterization and visualization and 2) correlation of MSI with other microscopic imaging techniques.

Recent progress and current state of cell-scale MS imaging and profiling are discussed in several recent reviews including one focused on single cell metabolomics[9] and another which emphasizes secondary ion mass spectrometry (SIMS) and matrix-assisted laser desorption/ionization (MALDI) MS, presented in **Chapter 2** of this thesis.[10] **Chapter 3** presents original work involving the development of a unique hybrid mass spectrometer which combines SIMS and MALDI capabilities in a single setting to leverage their complementarity for advanced biological imaging and profiling experiments.[11] Instrumental design and characterization are described in detail, and initial application to MSI of nervous system tissue and individual cultured neurons is also demonstrated. **Chapter 4** further applies and extends this work by combining the new instrument with electron microscopy; by acquiring scanning electron microscope (SEM) images of individual cultured cells subsequent to SIMS imaging, chemical features can be correlated with physical features observable in the higher-resolution electron micrograph. Furthermore, this combination allows the physical effect of the ion beam on biological material to be directly studied, and serves as a proof-of-principle experiment preceding the addition of an integrated electron microscope system on the hybrid mass spectrometer.

The second main effort of this thesis involves demonstrating how multiple chemical imaging techniques may be combined beneficially, with a focus on combining MSI with confocal Raman microscopy (CRM), another label-free chemical imaging technique. MSI and CRM are complementary techniques in that they provide unique, "orthogonal" information about chemical composition; while MSI identifies constituents by mass, CRM utilizes inelastically-scattered light to characterize the chemical bonds and functional groups present in a sample. The challenges, advantages, and potential applications of correlated imaging (with emphasis on MSI and CRM) are reviewed and discussed in detail in **Chapter 5**, providing background for the body of work that follows.[12] In **Chapter 6**, MALDI MSI and CRM are combined to chemically characterize *Pseudomonas aeruginosa*,[13] a bacterial opportunistic pathogen known for forming recalcitrant biofilms in the rhizosphere as well as in human infections.[14-15] The complementarity of the two imaging techniques is demonstrated here; CRM detects multiple biomolecular classes and visualizes their microscopic distributions, while MALDI detects multiple congeners of a single metabolic class – rhamnolipid surfactants – and visualizes differences in their macroscopic spatial distribution across the biofilm surface. These results (and the previous work of others[16]) indicated that meaningful spatio-chemical heterogeneity exists in biofilms across multiple size scales. Building on this work, **Chapter 7** presents methods developed for correlating MALDI MS and SIMS imaging on a single biofilm specimen in order to visualize both macroscopic and microscopic chemical features. A mutually-compatible sample preparation workflow is described, and the combination of MSI techniques enables detection and visualization of numerous metabolites including rhamnolipids and 4-quinolones, an extensive and largely-uncharacterized class of multifunctional secondary metabolites.[17] Finally, true correlated MSI/CRM imaging of *P. aeruginosa* biofilms is presented in **Chapter 8**, utilizing the hybrid mass spectrometer previously described. A novel sample navigation approach utilizing a chemical microspot array is developed and used to precisely re-locate a CRM-imaged region for subsequent SIMS imaging. Microscopic quinolone distributions are observed by both techniques in good agreement, electron microscopy is applied to associate quinolone localization with single bacterial cells present on the biofilm surface, and the tandem MS capability of the hybrid mass spectrometer is also applied to confirm previously-tentative mass assignments directly from the biofilm surface. This body of work demonstrates how complementary chemical imaging techniques such as SIMS, MALDI MS, and CRM may be effectively combined to glean additional information from a biological specimen, and makes several interesting new observations about an important biological model which may be developed into biologically-significant conclusions with some additional work.

In addition to the two main efforts described above, a number of MSI-related side projects are included in **Chapter 9** including development of improved chemical inkjet printing apparatus, method development for detection of a small molecule (pharmacological agent) in nervous tissue, and imaging of lipids and signaling peptides in the mammalian nervous system in the context of studying nociception. These projects did not reach publishable conclusions but may do so with additional experiments, or at least offer useful information about how (or how not) to perform MSI experiments in similar work. Finally, **Chapter 10** summarizes the work described here and suggests future opportunities which build on it, **Appendix A** provides a supplemental user’s manual for the custom-built hybrid mass spectrometer, and **Appendix B** describes a robust procedure developed and used in this thesis work for MALDI and SIMS MSI sample pretreatment.

References

1. Yan, X.; Maier, C., Hydrogen/Deuterium Exchange Mass Spectrometry. In *Mass Spectrometry of Proteins and Peptides*, Lipton, M.; Paša-Tolic, L., Eds. Humana Press: 2009; Vol. 492, pp 255-271.
2. Yin, S.; Loo, J., Mass Spectrometry Detection and Characterization of Noncovalent Protein Complexes. In *Mass Spectrometry of Proteins and Peptides*, Lipton, M.; Paša-Tolic, L., Eds. Humana Press: 2009; Vol. 492, pp 273-282.
3. Monroe, E. B.; Jurchen, J. C.; Koszczuk, B. A.; Losh, J. L.; Rubakhin, S. S.; Sweedler, J. V., Massively Parallel Sample Preparation for the MALDI MS Analyses of Tissues. *Analytical Chemistry* **2006,** *78* (19), 6826-6832.
4. Rubakhin, S.; Sweedler, J., A Mass Spectrometry Primer for Mass Spectrometry Imaging. In *Mass Spectrometry Imaging*, Rubakhin, S. S.; Sweedler, J. V., Eds. Humana Press: 2010; Vol. 656, pp 21-49.
5. Chughtai, K.; Heeren, R. M. A., Mass Spectrometric Imaging for Biomedical Tissue Analysis. *Chem Rev* **2010,** *110*, 3237-3277.
6. Setou, M., *Imaging mass spectrometry : protocols for mass microscopy*. Springer: Tokyo, 2010; p x, 262 p.
7. Gode, D.; Volmer, D. A., Lipid imaging by mass spectrometry - a review. *Analyst* **2013,** *138* (5), 1289-1315.
8. Calligaris, D.; Norton, I.; Feldman, D. R.; Ide, J. L.; Dunn, I. F.; Eberlin, L. S.; Graham Cooks, R.; Jolesz, F. A.; Golby, A. J.; Santagata, S.; Agar, N. Y., Mass spectrometry imaging as a tool for surgical decision-making. *Journal of Mass Spectrometry* **2013,** *48* (11), 1178-1187.
9. Rubakhin, S. S.; Lanni, E. J.; Sweedler, J. V., Progress toward single cell metabolomics. *Current Opinion in Biotechnology* **2013,** *24* (1), 95-104.
10. Lanni, E. J.; Rubakhin, S. S.; Sweedler, J. V., Mass spectrometry imaging and profiling of single cells. *Journal of Proteomics* **2012,** *75* (16), 5036-5051.
11. Lanni, E. J.; Dunham, S. J. B.; Nemes, P.; Sweedler, J. V., Biomolecular Imaging with C_{60}-SIMS: Instrumentation, Matrix Enhancement, and Single Cell Analysis. **2014,** *submitted for publication.*
12. Masyuko, R.; Lanni, E. J.; Sweedler, J. V.; Bohn, P. W., Correlated imaging - a grand challenge in chemical analysis. *Analyst* **2013,** *138* (7), 1924-1939.
13. Masyuko, R. N.; Lanni, E. J.; Driscoll, C. M.; Shrout, J. D.; Sweedler, J. V.; Bohn, P. W., Spatial organization of Pseudomonas aeruginosa biofilms probed by combined matrix-assisted laser desorption ionization mass spectrometry and confocal Raman microscopy. *Analyst* **2014**, *in press*.
14. Costerton, J. W.; Stewart, P. S.; Greenberg, E. P., Bacterial biofilms: A common cause of persistent infections. *Science* **1999,** *284* (5418), 1318-1322.
15. Shrout, J. D.; Chopp, D. L.; Just, C. L.; Hentzer, M.; Givskov, M.; Parsek, M. R., The impact of quorum sensing and swarming motility on Pseudomonas aeruginosa biofilm formation is nutritionally conditional. *Mol. Microbiol.* **2006,** *62* (5), 1264-1277.
16. Diggle, S. P.; Matthijs, S.; Wright, V. J.; Fletcher, M. P.; Chhabra, S. R.; Lamont, I. L.; Kong, X.; Hider, R. C.; Cornelis, P.; Cámara, M.; Williams, P., The Pseudomonas aeruginosa 4-Quinolone Signal Molecules HHQ and PQS Play Multifunctional Roles in Quorum Sensing and Iron Entrapment. *Chem. Biol.* **2007,** *14* (1), 87-96.
17. Huse, H.; Whiteley, M., 4-Quinolones: Smart Phones of the Microbial World. *Chem Rev* **2010,** *111* (1), 152-159.

CHAPTER 2

MASS SPECTROMETRY IMAGING AND PROFILING OF SINGLE CELLS

NOTES AND ACKNOWLEDGMENTS

This chapter was published as a literature review in *Journal of Proteomics* **2012**, 75 (16), 5036-5051 with coauthors S. S. Rubakhin J. V. Sweedler, adapted and reproduced here with permission from Elsevier. The work was supported by Award No. P30 DA018310 from the National Institute on Drug Abuse (NIDA) and the Department of Energy by Award No. DE-SC0006642. Stephanie Baker is gratefully acknowledged for assistance with manuscript preparation. Copyright 2012 Elsevier Publishing Company.

INTRODUCTION

Visualization is arguably the single most powerful capability we possess for analyzing the physical, chemical, and biological world around us. Though we as humans image the world primarily by observing interactions of matter with light in a narrow wavelength range, technology has increased our ability to use a greatly expanded portion of the electromagnetic spectrum, higher-order interactions of light with matter,[1] and even to image by other phenomena such as compression waves through matter and the propensity of electrons to tunnel through it. While most imaging techniques provide chemical information about a subject, nearly all leave some ambiguity about its exact chemical composition. This is especially true for biological structures that are made up of a myriad of distinct compounds comprised largely of the same handful of elements, and where biomolecules of differing function may be similar in easily-visualized characteristics such as visible light absorbance profiles. Labeling biomolecules with a distinct and easily-detected aid, such as a radionuclide or fluorescent tag, is an effective and widely-used solution for selective imaging; however, this requires targeting of known molecules and also limits the output to preselected compounds. If one goal of visualization techniques is to detect and subsequently identify a broad range of chemical species that are present in a sample, including those heretofore unknown, chemical labeling is not the answer.

As an alternative to labeling for chemical characterization, one of the most successful analytical methods of the 20th century has been mass spectrometry (MS) with MS/MS capabilities. A half century ago, MS was shown to be useful as an imaging method;[2] now known as mass spectrometry imaging (MSI), it can be performed with secondary ion mass spectrometry (SIMS), matrix-assisted laser desorption ionization (MALDI), and other ionization sources.[3-7] Typically, the technique involves acquiring separate mass spectra in a spatially defined grid, then applying mass filters to the resulting spectra to generate ion images that reveal the distribution of specific chemical species. Acquisition can be accomplished in microprobe mode[8] by scanning a focused laser, ion beam, or sampling inlet across the sample surface, or in microscope mode[9] where the entire field of view is sampled at once and ions are conducted to a position-sensitive detector via a mass analyzer, which preserves spatial information. MSI is a powerful microscopic chemical imaging tool for several reasons: It offers the chemical specificity and versatility inherent to MS, analytes of interest need not be preselected or even known prior to analysis, and the number of co-registered ion images producible from a single MSI experiment is limited (in theory) only by the number of distinct ions detected and resolved in the spectra, which can number from tens to thousands. MSI has been applied extensively in a variety of fields including biomedical research,[10] microbiology,[11] plant biology,[12] and in the pharmaceutical sciences.[13-14] For procedural details, the reader is directed to the following resources that describe multiple protocols for a diverse array of MSI applications and techniques.[15-16]

Despite recent progress in MSI instrumentation, sample preparation, and data analysis methods, further advances are needed, especially as interest grows in the ability to reliably visualize the distributions of intact molecules at micron and submicron resolutions. Beyond the challenge of designing suitable micro- or nanoprobes for this purpose, sensitivity becomes a major issue. Specifically, the sampled surface area diminishes rapidly with a decrease in probe radius; a 50 nm circular probe can interrogate only 0.01% the surface area of a 5 µm spot. Therefore, a 10,000-fold increase in some combination of instrument sensitivity and volume sampled (e.g., as a deeper voxel) is required in order to detect a given analyte at the same mass fraction. The sensitivity issue is compounded by the matrix suppression effect (discussed in detail later), a general scarcity of larger molecules (e.g., proteins) relative to metabolites and endogenous inorganic ions, and the low sampling efficiency of many microprobe ionization sources, especially for thick insulating specimens.[17-18] The combination of these issues effectively limits cell-scale MSI to a subset of abundant biomolecules, leaving much room for improvement.

In this review we focus on the reported cell and subcellular applications of MSI, innovative analytical instrumentation and methods that enable such studies, and current efforts to address the major challenges facing technological advances.

SECONDARY ION MASS SPECTROMETRY (SIMS)

Developed in the 1960s, SIMS was the first mass spectrometric technique applied to chemical imaging[2] and has been used to image a broad range of biological specimens, including single cells.[19] Generally offering the highest spatial resolution (<50 nm) among the MSI approaches, it can provide relative[20] and absolute[21] quantitative chemical information. The scope of this discussion is confined to SIMS imaging applied at cellular length scales; a recent review by Boxer et al.[22] covers SIMS fundamentals and thoroughly examines broader biological applications.

SIMS is a surface analysis method that involves bombarding the sample with a beam of energetic primary ions (e.g., Cs^+ or O^-) in order to induce desorption of intact molecules, fragments, and atoms from the first few nanometers of the sample surface. This desorption event—termed sputtering—produces predominantly neutral species but also cations and anions. Secondary ions of a single polarity are extracted and subsequently transferred into a mass analyzer, usually a magnetic and/or electrostatic sector or a time-of-flight (TOF) analyzer, although quadrupole ion traps[23] and hybrid quadrupole-TOF analyzers[24] have also been effective in enabling MS/MS functionality. SIMS is a relatively hard ionization method compared with other ion sources such as ESI or MALDI. Detectable ions are typically limited to a narrow mass range of only a few hundred Daltons; however, cluster ion sources (e.g, C_{60}^+ and Bi_3^+) have effectively extended this limit to ~2 kDa.[25] Matrix enhancement has also been shown to extend the mass range considerably.[26] Fragments can frequently be characteristic of a particular biomolecular species or class, such as the choline “head group” (*m/z* 86), corresponding to any lipid of the phosphatidylcholine or sphingomyelin classes, or the $C_5H_9^+$ fatty acid tail fragment, both observed in abundance from cell membranes.[27] CH^- and CN^- ions also generate ubiquitous biological background signals (and can in fact be produced by post-desorption recombination[28]), which is useful in pixel normalization procedures.[29]

Dynamic SIMS

Dynamic SIMS is a well-developed technique for cellular MSI, and a recent article by Chandra[30] in the *Encyclopedia of Mass Spectrometry* provides a good overview of its history, preparation protocols, and current capabilities. The approach implements a constant, high fluence ($>10^{13}$ primary ions/cm^2 delivered to sample) bombardment of the sample by primary ions followed by analysis of resulting secondary ions, oftentimes by electric and or magnetic sector instruments. Although capable of providing excellent lateral resolution and imaging sensitivity on the order of parts-per-million,[31] dynamic SIMS breaks many of the covalent bonds of larger biomolecule constituents. The result is a mass spectral output of mainly monatomic secondary ions along with some small organic fragments such as CN^- and CH^-.[32] Instrumentation usually allows collection of a small handful of selected ions simultaneously from a sample, e.g., the "new generation" nanoSIMS from CAMECA has up to seven detectors, each of which can be calibrated to a single *m/z* window.[31] Due to these limitations, dynamic SIMS ion images are frequently correlated with results from cell investigations using other high-resolution imaging techniques, including electron,[33-34] atomic force,[35] and fluorescence microscopy,[36-37] in order to draw more meaningful conclusions.

Nonetheless, a large amount of information can be obtained from dynamic SIMS data alone. Elemental sulfur and phosphorous ion maps can be used to demarcate the general localization of proteins (with sulfur-containing cysteine and methionine residues) and nucleic acids (by phosphorous in the backbone) within cells, thereby providing a coarse molecular map upon which additional ion images can be superimposed.[38] Certain endogenous inorganic ions (e.g., Na^+, K^+, Mg^{2+}, Ca^{2+}, and Cl^-) can reveal much about the physiological state of cells, such as membrane potential, membrane transport, and mitosis.[30] In SIMS, the K^+:Na^+ ratio within cells can also generally guide the selection of intact cultured specimens for imaging since this ratio will be approximately ten for healthy cells, whereas it will be lower for those that have been damaged or lysed.[34]

In more specific applications, interactions of Ca^{2+} and Mg^{2+} with chromatin have been studied by dynamic SIMS in correlation with immunofluorescence in order to label scaffold proteins, determine a binding ratio for each ion, and show that the calcium exclusively localizes with the scaffold protein and also causes structural deformation when depleted.[37] This is particularly interesting when considered alongside a separate SIMS imaging study of dividing human glioblastoma tumor cells in culture showing that calcium is notably absent, specifically from the mitotic spindle region during metaphase,[39] and also in comparison with normal dividing cells, which actually concentrate the calcium in the same region.[34] The depth-resolving capability of dynamic SIMS was crucial in these studies as it allowed separation of the spindle region from the outer cytoplasm, which if observed together, would not have shown the localization. Label-free dynamic SIMS has been informative in research on other disease states that involve characteristic endogenous elements. In Alzheimer's disease for example, the subcellular localization of iron was mapped to specific subcellular compartments in the hippocampus of human patients, and also shown to colocalize with calcium in mineralized amyloid deposits in a mouse model.[40-41] Soft tissue biomineralization (calcification) has been studied successfully with SIMS in correlation with transmission electron microscopy (TEM) and immunostaining to reveal organelle-level location of hydroxyapatite crystals (detected as a CaO^- fragment) in epithelial cells.[42]

Dynamic SIMS can be effective for high-resolution mapping of any unlabeled exogenous molecule that contains a unique element within the biological system under investigation. The element is used as a built-in tracer of the molecule, and in some cases, can elucidate related processes. This has become a powerful and well-established method for following the localization of drugs at size scales ranging from tissue sections[43] to single organelles.[44] Early work showed that halogens from steroids and pyrimidine analogs can be located within cells,[45] and extensive SIMS investigations of boron neutron capture therapy (BNCT) cancer treatment pharmaceuticals have been successfully performed, largely by Chandra and colleagues,[46-47] for over two decades. In BNCT, glioblastoma tumor cells are loaded with boron atoms and then irradiated with low-energy neutrons; the neutrons cause no significant damage to the surrounding tissue but result in alpha decay of the boron nuclei, which are destructive within a ~10 µm radius, i.e., primarily to the cells containing them.[44] BNCT agents are a broad class of drugs designed to deliver the boron atoms preferentially to glioblastoma cells with a partition ratio (relative to healthy tissue) adequate to selectively destroy the tumor. Effectiveness, therefore, hinges critically on where the drug localizes within a tumor cell population and in what partition ratio, as well as where exactly the boron accumulates within the tumor cells. Because the cell nucleus is more sensitive to boron decay, it is the ideal target for the therapy. Since dynamic SIMS can quantitatively map the boron directly at subcellular resolution, it has been used successfully to evaluate the efficacy of a variety of BNCT pharmaceuticals,[48-49] compare responses to the treatment by multiple cell types within a cell co-culture simultaneously and quantitatively,[50] and compare boron concentrations amongst subcellular regions.[44]

Absolute quantification usually is not possible with MSI due to a variety of factors that affect the intensities of ion signals recorded across cells or tissues. In some cases, however, it has been successfully performed using dynamic SIMS. Inductively-coupled plasma atomic emission spectroscopy is used to create a set of "relative sensitivity factors" needed for quantitative MSI measurements of the elemental species of interest (e.g., B, Ca, K, Mg, Na).[47] These factors permit absolute quantitation of the targeted species by comparing their signals (on each detector pixel) to that of carbon. The harsh nature of the high-current SIMS beam works advantageously because it ionizes the elements from various tissue or intracellular regions indiscriminately. This calibration approach has been used to determine the effect of a drug's infusion time on treatment outcome,[43] and for quantitative comparison of drug uptake by cells in different stages of the cell cycle.[21]

The SIMS approaches reported for BNCT research can be applied to the study of other drugs, provided the drug in question contains a unique element or can be labeled with one. In fact, SIMS imaging has been used in an assortment of other drug studies. Examples include investigating the anti-cancer drug Cisplatin's cytotoxicity as it relates to cell calcium stores,[51] evaluating the use of platinum-containing delivery agents for hadron therapy cancer treatment,[52] and visualization of the copper-chelating drug ATN-224, used in prostate cancer treatment and located within cells by its characteristic MoS^- and MoS_2^- fragments.[36] Dynamic SIMS imaging has proven useful for direct cancer detection, for example, by imaging the distribution of the melanoma marker iodobenzamide by iodine anion formation in mice, shown to be confined to submicron-sized melanosomes.[53] Another recent study by Wedlock et al.[38] focused on evaluating the distribution of a new potential gold-containing anti-cancer drug in order to elucidate its functional mechanism; dynamic SIMS was used in conjunction with energy-filtered electron microscopy in order to visualize the gold complex amongst cell contents. Remarkably clear, high-resolution SIMS images, such as those shown in **Figure 2.1**, revealed not only that the gold penetrates the treated cells and aggregates within the nucleus and cytoplasm, but also that the cell morphology changes significantly after treatment. More importantly, the perfectly-registered ion images acquired by SIMS revealed that the gold complex was colocalized with sulfur rather than phosphate within the cell, suggesting that it functions through interference with thiol-containing proteins rather than direct interaction with DNA.

In cases where endogenous or exogenous species of interest do not include characteristic elements by which they may be easily detected, stable isotope labeling can used in dynamic SIMS experiments. Most commercial instruments provide sufficient mass resolution to discern nearly-isobaric ions; for example, $^{12}C^{1}H^{-}$ and $^{13}C^{-}$, which differ by 4.4 mDa.[54] If naturally-occurring but rare isotopes such as ^{13}C and ^{15}N can be incorporated into a drug, nutrient, or other molecule of interest, then they can be used to trace and quantify analyte distribution at a subcellular level. Lechene and colleagues have designed an impressive assortment of experiments utilizing isotopic labels with nanoSIMS to examine free fatty acid uptake by cultured adipocytes,[29] molecular nitrogen fixation by bacteria in single cells of marine worms [20], protein synthesis in hair cells,[55] cellular metabolism and DNA strand segregation.[56] In these studies, relative quantitation was performed by ratiometric measurements of enriched and naturally-abundant labeled elements, e.g., ^{13}C:^{12}C. Isotopic labeling has also been notably used by Kraft et al.[32, 57] to study phase separation of lipid membranes in supported bilayer models. Because isotopic-labeling does not significantly alter the shape of the lipids forming the membrane as a fluorescent tag might, SIMS can be used to study the unperturbed system. This work has been highly informative in the elucidation of nanoscale lipid layer organization, and we expect future studies will aid in understanding the function (and dysfunction) of membrane-bound proteins. Most recently this work has been extended to examine the effect of cholesterol incorporation on membrane behavior with SIMS and correlated atomic force microscopy (AFM) measurements.[35]

Static SIMS (TOF-SIMS)

When SIMS is conducted with a primary ion fluence of $<10^{13}$ ions/cm^2 (the static limit), it is considered to be sampling an unperturbed surface, i.e., any particular sample area is probed by a primary ion only once. This is referred to as static SIMS or sometimes TOF-SIMS, since the pulsed primary ion beam is conveniently coupled directly to a TOF analyzer, which can acquire full mass spectra at each image pixel rather than monitoring a few preselected ions as with sector-based dynamic SIMS instruments.[31] Less material is ultimately ablated per unit surface area for ionization and detection (due to the static limit), which makes MSI of low-abundance analyte distributions more difficult and limited to a small dynamic range of concentrations as per-pixel ion counts are frequently in the single digits. However, static SIMS is well suited to the study of intact molecular ions and larger biomolecular fragments such as peptides,[25] since it almost exclusively interrogates undamaged sample surfaces and measures across a broad, continuous mass range. With microprobes focusable to a submicron diameter, but not quite the <50 nm achievable with dynamic SIMS due to the surface availability of the analyte, static SIMS provides relatively more chemical information at lower but still "subcellular" lateral resolutions.

Static SIMS instrumentation advances

Polyatomic "cluster" primary ion beam sources are major recent innovations in static SIMS imaging, enabling new studies from a range of biological samples. In contrast with traditional monatomic sources (Cs^+ and Ga^+), cluster ions (SF_5^+, C_{60}^+, Bi_3^+ and Au_3^+) generally produce softer ionization and much greater secondary ion yields, especially at higher masses,[58] thus extending the practical mass limit of static SIMS to approximately 2,000 Da [25] and permitting acquisition of more molecular information. While Bi_3^+ clusters have been shown to provide superior sensitivity and lateral resolution (>100 nm)[59-60] with biomolecules, the C_{60}^+ cluster source [61] uniquely produces far less damage to organic samples upon impact in comparison with other cluster sources.[62] As a result, the C_{60}^+ primary ion beam can be applied at a fluence far exceeding the static limit in order to strip or "etch" material from a sample surface in fairly uniform layers. This enabled TOF-SIMS instruments to investigate subsurface cell contents and even generate three-dimensional (3-D) images.[63]

Many state-of-the-art TOF-SIMS instruments are now equipped with such cluster sources, which enhance biological sample analysis.[64] Carado and colleagues[24, 65] added a C_{60}^+ source to a commercial MALDI quadrupole-TOF hybrid mass spectrometer (QSTAR XL, SCIEX), enabling molecular SIMS experiments to benefit from both the relatively high mass resolution (>12,000) and MS/MS (CID) capabilities of the spectrometer's native configuration. These are both highly useful features for investigating complex biological samples such as cells that produce dense, information-rich spectra in the wider mass range now accessible, as many detected molecular ions could potentially be further identified by MS/MS. Another impressive instrumental design, called the "J-105 3D chemical imager", has been introduced as a product of several groups in collaboration with Ionoptika, Ltd. (Manchester, UK);[66-68] it includes several features known to be useful for successful cell-level SIMS imaging. The instrument utilizes a time-focusing ion buncher[67] to maximize sensitivity, in conjunction with a coaxial TOF analyzer to enable accurate (5 ppm), sensitive, and high-mass resolution (7000) measurements at a simultaneously-high (stated 200 nm beam focus limit) spatial resolution using an Au_3^+ cluster primary beam. A C_{60}^+ beam serves a dual purpose: as an alternative primary ion source and as an in-source etching and sputter-cleaning tool. The sophisticated sample handling system on the J-105 includes an Ar-filled glove box for air-free preparation and a cryo-cooled stage with a "cryoshield" apparatus to inhibit surface contamination by ice, as well as a semi-automatic freeze-fracture system to expose cell contents under vacuum.[69] Initial results indicate that the design indeed permits exceptional cellular chemical imaging to be performed in two and three dimensions with cluster SIMS.[68] More recently a C_{60}^+ source has been coupled with an FT-ICR analyzer for high (100,000) mass resolution, sub-ppm mass accuracy and CID MS/MS capability; this combination promises great subcellular MSI potential once its sensitivity is improved to permit a suitably small microprobe.[70]

Static SIMS applications to cellular imaging

The application of static SIMS to cellular MSI has been mostly confined to a small assortment of detectable endogenous molecules comprised primarily of membrane phospholipids (reviewed in [71]), and a few other membrane-localized small molecules such as cholesterol[72-73] and vitamin E.[27] These molecules are abundant on the surface of cells and in tissues of interest (e.g., brain[74] and spinal cord[75]), easily ionized, and often produce characteristic fragments that can be used to improve image quality.[72] The capability of static SIMS to image the distribution of membrane constituents, lipids in particular, is highly valuable in bioanalytical studies since few other methods can do so at all, and if a label is used, it may significantly perturb native chemistry. Microbes made a convenient initial static SIMS imaging biological model owing to their appropriate (~1 µm) cell size and tolerance to various chemical treatments during sample preparation.[76-77] More recently, membrane composition analysis of cultured mammalian cells has also become possible. Ostrowski et al.[78] used static SIMS to visualize the distribution of membrane cholesterol in cultured macrophages and by correlation with fluorescence imaging, they relatively quantified the difference between control and cholesterol-enriched cellular populations in a single imaging experiment. Lipids have been relatively quantified between cell populations as well as between the membrane and cytoplasm of individual cultured cells.[79] Mammalian cardiac tissue and individual isolated cardiac cells have been imaged to visualize both tissue-level and subcellular localization of phosphocholine and other lipids such as cardiolipins, revealing complimentary distributions and correlating them with particular fatty acids.[73] Lanekoff et al.[80] used a stable-isotope labeling approach to determine membrane lipid exchange rates in PC12 cells by imaging the membrane to trace deuterated phospholipids that were incorporated into the cells from culture medium at various time points. Low rates of exchange were observed, leading the authors to conclude that small membrane compositional changes may result in large changes in cellular activity, e.g., exocytosis, as observed in their previous work with a comparable cell treatment.[81] Using a similar labeling approach, Kraft and coworkers[82] employed static SIMS to extensively study phase separation (a.k.a. “lipid rafts”) in supported model lipid membranes, applying principal component analysis (PCA) to enhance phospholipid distribution image contrast by utilizing subtle differences in species-specific fragmentation profiles.

Prior successes with the visualization of membrane components notwithstanding, cellular MSI of the other macromolecule classes—carbohydrates, nucleic acids, and proteins (including peptides)—continues to be a main focus of development efforts for biological static SIMS. Observations of small, nonspecific amino acid- and nucleic acid-related fragment ions may be used for broad subcellular-mapping purposes.[83] When single characteristic ions are not available to define subcellular regions, statistical analysis of MSI data has been employed to find analyte signatures specific for particular image regions using methods that include PCA,[69] k-means clustering,[84] and maximum autocorrelation factor,[85] among others. Sulfur and phosphor stable isotope labels can also be used to distinguish different co-cultured cells by static SIMS.[86] However, imaging of the localization of intact large molecules such as proteins has been limited due to their in-source fragmentation, relatively low abundance, and difficulties in sputtering large molecules from highly intertwined cellular matrix and ion suppression effects. Nevertheless, instrumental and method developments have led to some significant and promising results. Altelaar et al.[26] were able to detect the neuropeptide APGWamide from *Lymnaea stagnalis* nervous tissue and image its distribution at a 3 µm spatial resolution with SIMS, and Komatsu et al.[25] demonstrated that human serum albumin deposited in a thin film could be digested *in situ* with acidified trypsin microdroplets to produce peptides in the 500–2000 Da mass range. These peptides were detectable with a Bi_3^+ cluster source. Nygren and colleagues[87] have shown that subcellular protein mapping is possible with a similar approach, as shown by their results in **Figure 2.2**. Thyroglobulin, a 660 kDa protein produced in the thyroid gland, was digested on-tissue by trypsin and then over a dozen resulting tryptic peptides were detected simultaneously with <60 ppm mass accuracy. This allowed for protein identification by database search (MS-Digest, ProteinProspector) and also high-resolution (3 µm) mapping of the protein distribution, which was revealed to be localized heterogeneously around the epithelial border of pig thyroid follicle cells but not inside them. This serves as a valid proof-of-principle for the simultaneous analyte identification and visualization of the subcellular localization of large proteins by static SIMS. Piwowar and coworkers[88] have described a promising "top-down" approach to characterizing various subcellular regions by fractionating them via centrifugation and then profiling each fraction by static SIMS to obtain "reference spectra." In theory, a library of these spectra can be used to identify subcellular features in chemical images as well as changes in analyte profiles corresponding to cellular activity.

Ion signal suppression is a significant obstacle to detecting and quantifying analytes in chemically complex samples. This is clearly illustrated by the relatively small assortment of biomolecules that have been imaged by SIMS to date, compared with the large number of compounds known to be present within cells at concentrations that should be detectable using current SIMS instrumentation. Gunnarsson et al.[59] have shown that individual 300 nm artificial vesicles can be discerned by their characteristic lipid fragments using cluster static SIMS, suggesting that separate analysis of naturally-occurring intracellular organelles on the same size scale is entirely possible if signal suppression effects can be addressed. Fundamental studies on this subject have shown that the propensity for individual analytes to ionize over others in a desorbed mixture can be judged broadly by their relative gas-phase basicities;[89] consequently, the composition of the sputtered cloud of particles can greatly enhance or suppress individual ion yields. A single pulse of primary ions during the SIMS sputter event may generate only a few tens of unique gas-phase molecules; nevertheless, a staggeringly complex assortment of possible interactions and additional factors, such as local acidic proton availability and density in the region of desorption, add yet another layer of complexity.[90] Practical approaches to improving the coverage of cellular analytes, in part by addressing the signal suppression issue, have therefore been to increase ionization efficiency overall and/or bias ionization in favor of the analytes of interest. Metal-assisted SIMS and matrix-enhanced SIMS improve detection of a variety of bioanalytes by coating sample surfaces with either a thin layer of metal such as Ag or Au, or a typical MALDI matrix compound such as 2,5-dihydroxybenzoic acid.[26, 91-92] Water can also act as an effective matrix for analytes in SIMS investigations. Controlling the sublimation-condensation equilibrium of water on the sample surface during analysis has been shown to enhance ion yields by up to two-fold during depth profiling experiments.[93-94] Surprisingly, leaking water vapor directly over the sample has also produced significant enhancement of analyte detection.[95] Post-desorption photoionization is another way to generate more detectable ions from the neutral molecules that comprise the vast majority of desorption events.[96] None of these techniques has provided the cure-all to the signal suppression problem, but in combination with new instrumental configurations and sample preparation techniques, they may assist in the detection of additional species of interest.

Sample preparation for static SIMS imaging of cells

A successful SIMS imaging experiment hinges on a properly selected and executed sample preparation method, perhaps more than the data acquisition process itself. Much of the recent progress for static SIMS of biomolecules has been in the area of method development to improve the information yield of the technique. Unlike MALDI, laser ablation-inductively coupled plasma (LA-ICP) MS, or other ionization methods performed routinely at atmospheric pressure,[17, 97-98] SIMS is strictly a high-vacuum approach; therefore, cultured cell or tissue samples must be dry and/or frozen prior to analysis, leading to loss of cell viability. At the same time, several other general conditions must be met in order to produce high quality images: (i) the features of interest must be present at the sample surface; (ii) external contamination from culture medium, air, and other sources must be removed; (iii) chemical composition and cellular structure must be preserved, at least for the analyte of interest; (iv) cell morphology should be unperturbed; and (v) ion signal suppression should be minimized by removing suppressive constituents such as undesired salts and lipids, but without otherwise compromising the previously-stated conditions. This final condition is particularly difficult to meet given the inherent complexity of biological systems and the fact that wet chemical treatments, which are routine for non-imaging MS or tissue-level imaging, usually result in some delocalization of small molecules. This makes such approaches less suitable for high resolution imaging, especially when small and diffusible analytes are investigated.[99]

One popular solution is cryogenic freeze-fracture preparation of cultured cells, introduced as a sample preparation approach for electron microscopy investigations[100] in 1957 and adapted for dynamic SIMS imaging by Chandra et al. in 1986.[99, 101] This technique involves flash-freezing the cells while sandwiched between two substrates (e.g., Si wafers), then prying them apart in vacuum or inert gas in order to randomly expose various internal cell surfaces.[102] Freeze-fracture sample preparation has been frequently used in cell-level static SIMS imaging,[103] including MSI of red blood cells[104] and tumor cells, [48] and was also instrumental in the success of experiments investigating lysozyme lipid membrane permeability.[105] After flash-freezing, which reduces damage to cells by avoiding large ice crystal formation,[106] samples may either be freeze-dried to remove water content or maintained at low temperature in a frozen-hydrated state in which water content remains present throughout the SIMS analysis. The frozen-hydrated approach requires careful temperature control at subsequent stages, but recent instrumentation advances such as the "mouse trap" spring-loaded *in vacuo* fracturing apparatus[107] streamline the procedure.

Comparison with other preparation techniques such as freeze drying and formalin fixation indicates that frozen-hydrated preparation provides the best physical and chemical cell preservation[66] and increases ion yields due to the water matrix enhancement effect.[93, 108] However, it was also recently reported that frozen-hydrated sample preparation may result in localized chemical image artifacts and inconsistent sputter rates and that freeze-drying samples avoids these drawbacks while adequately preserving cell morphology, chemical and elemental composition.[109] Simple non-cryogenic "wash and dry" and chemical substitution approaches for sample preparation have also been investigated and found to be successful by some groups,[110-111] although it was noted by Berman et al.[110] that drying may lead to cell collapse and cell cytosol spreading, resulting in delocalization of diffusible species. Sjovall et al.[112] demonstrated subcellular "imprint-imaging" where cells are pressed onto an Ag surface, thereby transferring membrane components, which can then be imaged at sub-micron lateral resolution; nuclear and plasma membrane compositions of red blood cells were compared using this technique. Overall, these sample preparation approaches have varying procedural complexities and offer different levels of preservation for the physical and chemical integrity of specimens; therefore, the suitability of each must be evaluated on a per-case basis.

In-source milling, etching and three-dimensional imaging with SIMS

Aside from the traditional freeze-fracture technique, more recent work has demonstrated that clean internal cell planes can alternatively be exposed by in-SIMS milling or etching approaches, each of which have their own advantages. Grazing-incidence fast ion bombardment (FIB) milling has been used by Szakal et al.[84] to expose the contents of freeze-dried (but not fractured) HeLa cells, followed by imaging with static SIMS. Alternating mill and analysis cycles allowed depth-imaging of the cells in precise 20 nm increments. Weber et al.[33] took the same approach to expose and image a cross section of 1-µm diameter *Bacillus* bacterial spores by nanoSIMS, revealing elemental differences in the bacterial core, cortex, and coat layers. The latter work also demonstrated that the more involved "lift-out" FIB method often employed in TEM sample preparation allows consecutive removal of thin layers during 3-D sample analysis by MSI. In addition to these milling techniques, the low-damage impact of the C_{60}^+ ion primary beam on biomaterials has allowed its use as a high-angle rastered etching tool. Impressively, Kurczy and coworkers[113] used the approach to selectively remove a several nanometers-thick contamination overcoat to reveal nearly-unperturbed chemical features, such as patterned cholesterol film, without causing excessive signal loss. This surface-cleaning method was also shown to be highly effective with cultured and freeze-dried cells, removing culture medium-related surface contamination and improving cell:substrate contrast markedly.[64] The same study also compared various wash methods involved in cellular sample preparation and concluded that ammonium acetate provided the best overall results, in agreement with similar studies that used either this as a wash or ammonium formate.[110-111] The etching technique has more recently been used to improve the identification of cells in co-culture by multivariate analysis of surface chemistry,[114] and elsewhere to visualize the localization of antibiotics inside and outside of the bacteria *Streptomyces coelicolor*, demonstrating that one molecular species may be retained within the cell while another may not.[115]

Milling and etching techniques can be combined with static SIMS analysis to produce 3-D ion images. Depth-resolved elemental ion image stacks have been reported for quite some time using dynamic SIMS instrumentation,[39] but the ability of the C_{60}^+ beam to reliably and repeatedly etch an organic sample surface with a 12–30 nm depth resolution[116] now extends this approach to the detection of intact molecules and characteristic fragments. Fletcher and coworkers[117] reported early 3-D biomolecular imaging results using the C_{60}^+ beam in alternating etch/analysis modes, and the same group has now detected and visualized characteristic cytoplasmic and nucleus-abundant ions (phosphocholine at *m/z* 184 and adenine at *m/z* 136.1) in much smaller HeLa cells.[69] The C_{60}^+ beam can also be used to etch in conjunction with a second "analytical" beam, such as Au_3^+ or Bi_3^+, for higher imaging resolution and sensitivity, and has been applied for 3-D visualization of single thyroid carcinoma cells.[118] These initial proof-of-principle studies are encouraging, but reliable and informative 3-D MSI still faces a major challenge in the accurate 3-D localization of detected ions in some samples; for example, in cells that have significant topographical variations and heterogeneous ultrastructural consistency. Simple depth calibration has been performed by the detection of signal from a substrate (such as silicon) underlying a sample[83] or post-SIMS AFM measurements,[64] and the effects of variables such as sample temperature, primary beam energy, and primary beam angle have been assessed.[116, 119]

MALDI MS

Since its conception[120] and application to the analysis of large biomolecules,[121] MALDI has rapidly grown to become one of the two most widely used ionization methods in biological MS alongside electrospray. MALDI incorporates analyte molecules into a matrix of organic substance crystals or liquid crystals and then irradiates the sample with a focused, pulsed or continuous laser beam. Absorption of the incident energy by the matrix leads to desorption of the analyte molecules and their ionization, often by gas-phase protonation or deprotonation reactions. The ions from the desorbed particle plume are then extracted from the source, analyzed (typically by TOF), and detected. MALDI MS has been effectively applied for analysis of proteins, peptides, lipids, DNA, and RNA, and is often the bioanalytical method of choice owing to its sensitivity, high impurity tolerance during analysis of complex mixtures, and ease of sample preparation.

Single-cell and subcellular MALDI MS profiling

In an MS profiling experiment, a single point (pixel) of a specimen is examined (MSI can be thought of as a set of MS profiling measurements performed at ordered array of locations). Several groups demonstrated in the mid-1990s that MALDI MS could be used effectively in profiling mode to interrogate the contents of individual cells.[122-125] In one such early experiment by Van Veelen and colleagues,[122] large (<100 µm diameter soma) single neurons from *L. stagnalis* were either sampled *in situ* by micropipette or isolated and lysed into a small volume of matrix solution, dried on a conventional sample plate, and then investigated directly with MALDI MS. Both of these approaches produced remarkably high-quality spectra revealing both expected neuropeptides as well as unidentified species such as C-terminally elongated peptide variants. Jiménez and colleagues[126] took this work a step further by interrogating individual neurons in a simple neural circuit of *L. stagnalis* responsible for heartbeat modulation. They were able to show some variability in the peptidergic content of identified individual neurons, highlighting the value of MS profiling in revealing cell-to-cell heterogeneity. MS/MS analysis was used to sequence the peptides; the accuracy of this sequencing was supported by *in situ* hybridization, which showed that the transcripts responsible for the expression of the detected peptides were also present in the cells. This work established that beyond proof-of-principle, MS microanalysis techniques can yield important information regarding single-cell function. For example, single-cell measurements include the ability to relate peptides found in specific neurons to animal behaviors,[127-130] as well as characterize rare post-translational modifications such as a D-amino acid in a peptide.[131] Peptide profiling experiments can be accomplished with smaller mammalian cells,[132] and detailed protocols are now available to delineate the techniques.[133] MALDI MS profiling has also been used to profile metabolites in single HeLa cells and large microbes.[134-135] Furthermore, recent work has shown that relative and even absolute quantitation is possible at the level of a few cells or even a single cell by various methods including isotopic labeling, succinic anhydride labeling and standard addition, with a 19 fmol limit of detection and a 64 fmol limit of quantitation demonstrated for the peptide cerebrin from small cell clusters via the standard addition approach.[136]

The contents of micron-sized organelles can be profiled using similar bioanalytical techniques. Individual secretory dense core vesicles from the atrial gland of *Aplysia californica* with 1–2 µm diameters and internal volumes of only a few hundred attoliters—known for containing high (mM) concentrations of peptide signaling molecules—were isolated by micropipette, deposited onto glass slides, rinsed quickly in NaCl-containing solution to remove externally-adsorbed material, then mixed with a picoliter amount of matrix and dried for analysis by MALDI MS, as shown in **Figure 2.3**.[137] Results revealed that many peptides from several genes were contained within individual vesicles; these peptide identities were confirmed by post-source decay fragmentation analysis of tissue-scale blots of the same gland from *A. californica.* Comparing the tissue blots to the single-vesicle profiles also revealed an informative difference: fully-processed califin peptides were detected from within individual vesicles while the blots showed yet-unassembled peptide subunits elsewhere. Clearly, with the proper collection techniques, MS profiling becomes a powerful tool for biological inquiry at the subcellular level.

Cell-scale MALDI MSI

In a typical MALDI MSI experiment the laser probe is rastered across a sample, much like the primary ion beam during SIMS imaging. Caprioli et al.[3] were among the first to describe in detail the MALDI MSI approach and demonstrate its applicability to investigations of biological specimens. The low spatial resolution of subcellular MALDI MSI of larger cultured *A. californica* neurons was reported six years later.[138] The neurons were profiled at subcellular resolution with individually-deposited matrix microdroplets and also imaged at 50 µm lateral resolution to show that different relative peptide concentrations were observed in the cell soma as compared to its neurite outgrowths, which extended a few hundred microns from the soma. Recent MALDI instrumentation advances have resulted in a growing body of MSI studies performed at “cellular length scales” (usually defined as single micron-scale resolution or better), with true cell-per-pixel or subcellular resolutions achieved in a number of these cases. Instrumental features required to achieve subcellular MSI include the ability to focus the laser beam microprobe to submicron diameters and higher laser fluence in order to ionize adequate amounts of analytes from small sample areas.[139] One response to the probe focusing issue was presented by Altelaar and colleagues;[140] using a stigmatic SIMS instrument (TRIFT II, PHI Electronics) modified for MALDI MSI, a defocused laser was used to illuminate a large region of a sample for microscope-mode imaging. Shown to achieve 4 µm lateral resolution, the instrument was used to image contrasting localization patterns of several peptides in rat, mouse and human pituitary glands. An alternative to stigmatic imaging for high spatial resolution is to use sophisticated optics to focus the laser into a near-diffraction-limited microprobe directed at the sample. Several decades ago, Hillenkamp et al.[141] demonstrated this approach for elemental analysis with the laser microprobe mass analyzer (or LAMMA) in which the laser was introduced coaxially (with respect to the ion extraction path) from behind the sample via an immersion lens and a vacuum glass window, ablating material directly into a TOF analyzer. Spengler and Hubert[142] reported a similar system, delivering the laser coaxially from the other direction via a central aperture bored through the quartz optical lenses. In this configuration, the laser is focusable to a 260 nm diameter, enabling subcellular resolution with a scanning microprobe-type instrument. The effective lateral imaging resolution becomes limited by sampling efficiency and was found to fall between 0.6–1.5 µm, depending on sample consistency. The instrument has been used to image human renal carcinoma cells at a two micron resolution and detecting masses up to 5 kDa, as shown in **Figure 2.4**.[143] This work demonstrates that subcellular biological imaging with MALDI is possible and in fact, offers rich chemical information beyond the small molecules and fragments observed by SIMS and other methods.

Spengler's group[144] has also recently introduced another instrument employing a similar optical setup applied to an atmospheric pressure (AP) MALDI source combined with either an ion trap or an FT-ICR analyzer for high-sensitivity or high-mass resolution imaging, respectively. Initial demonstrations showed that patterned biomolecules can be detected at biologically-relevant sensitivities—tens of attomoles per pixel—using either mass analyzer. More recent results include detection and identification of ten neuropeptides in mouse pituitary gland, and 5 µm lateral resolution which reveals cell-scale heterogeneity.[145] Similarly, Setou and colleagues[146] have described results from their own high-resolution AP-MALDI instrument, or "mass microscope," which is actually a microprobe-mode imaging instrument capable of 4 µm resolution. They have used their mass microscope to visualize varying relative concentrations of membrane phosphatidylcholines in the retinal layers of the *Ambystoma mexicanum* salamander eye at 7 µm lateral resolution. The high lateral resolution of the instrument allows single cell-per-pixel acquisition of 15 µm-diameter retinal cells without dissociation from the tissue where they are closely packed.[97]

Sample preparation for MALDI-MSI

In initial MALDI single-cell imaging experiments,[138] matrix was simply applied in a single drop directly over the cells and quickly dried with heat. This sufficed for large frozen *A. californica* cells imaged at a 50 µm raster size; however, with the goal of imaging much smaller mammalian cells, MALDI-MSI has been pushed toward ever higher resolutions. Unfortunately, the lack of appropriate matrix application techniques has become a limiting factor and thus, is a focus of ongoing method development efforts. Conventional tissue-level wet application techniques fall short, either due to analyte delocalization, leading to losses in spatial resolution, or insufficient sensitivity resulting from poor analyte extraction. MALDI matrix sublimation, originally proposed by Hankin et al.,[147] is a promising method of matrix application for subcellular imaging since it produces uniform microcrystals on the sample surface and therefore provides good spatial resolution. With a subsequent reconstitution/recrystallization step, sensitivity is improved.[148] This effectively decouples the two functions of conventional matrix application—analyte extraction and matrix crystallization/analyte inclusion—thus allowing better control of each step. Also beneficial is the highly homogeneous, reproducible microcrystal formation, as well as the capability to extend the detectable masses to tens of kDa.[149] Another approach has been to modify the dimensions of the sample itself by thaw-mounting it on a stretchable material such as Parafilm-M and then physically enlarging its area prior to matrix application.[150-151] This can be done with tissue sections and cell cultures and not only enables single-cell measurements and MS/MS peptide sequencing, but original sample dimensions can also be reconstructed using a software tool.[152] Finally, it is worth noting that while alternative (non-organic) matrices such as gold nanoparticles[153] and functionalized metal nanoparticles[154] have not been reported for the MSI of individual cells or subcellular components, these particles are on the single-nanometer size scale and support analyte detection without formation of larger crystals; we expect to see these used for single cell MSI in the near future.

OTHER MASS SPECTROMETRIC SINGLE-CELL MEASUREMENT TECHNIQUES

Traditional optical systems used for focused laser probes in MALDI have been impressively refined for lateral submicron resolution and therefore subcellular imaging, but ultimately they are still diffraction-limited to approximately half their emission wavelength, which is on the scale of hundreds of nanometers. Fiber optic laser interfaces have been utilized for some time to desorb,[139, 155] ionize,[156] and photodissociate[157] analytes in conjunction with a variety of mass analyzers and this method of laser probe delivery presents an alternative approach to improving MSI resolution via near-field focusing techniques. In scanning near-field optical microscopy (SNOM), laser light is directed at a finely-sharpened metal tip that is placed within nanometers of the sample surface. This significantly enhances laser fluence delivered in the vicinity of the tip, allowing localized ablation from craters <200 nm in diameter and ~20 nm deep.[158] SNOM-MS can be performed at atmospheric pressure and ablated material (ions and neutrals) is sampled into the MS vacuum chamber with a closely-positioned orifice, after which additional ions may be generated from the abundant neutrals by electron impact ionization. A TOF-MS system equipped with this desorption/ionization apparatus allowed researchers to analyze atoms and molecules including acetylcholine or 2,5-dihydroxybenzoic acid.[159] Zhu, Zenobi and colleagues[17] have recently shown that SNOM-MS transfers approximately 10% of all ablated material into the mass spectrometer compared to the ~1% ion sampling efficiency of AP-MALDI, a significant improvement.

When elemental information is needed, the inductively-coupled plasma (ICP) ionization source[160] provides quantitative and sensitive (pg/g LOD)[161] elemental and isotopic data. ICP-MS data is not influenced by the sample matrix or ion signal suppression effects, even in complex and heterogeneous biological specimens.[162] By directing laser-ablated sample material into the plasma with a carrier gas such as argon, LA-ICP-MS has been successfully applied to tissue-level imaging studies and has been reviewed by Becker.[163] Recent work by this same group[98] has also shown that combining ICP-MS with a modified laser microdissection apparatus allows for practical imaging spatial resolutions of 3–5 µm and SNOM-focusing methods produce submicron-scale ablation,[164] which can be expected to improve resolution further, possibly to below 100 nm.[161] This research direction offers the exciting possibility of a highly sensitive, quantitative nanoscale elemental imaging capability at atmospheric pressure, conceivably even on live cells in tissue or culture.

Near-field sampling methods could also be advantageous when coupled with nanostructure-initiator mass spectrometry (NIMS), a matrix-free desorption/ionization method that relies on liquid “initiator”-filled nanopores in the substrate beneath the sample to desorb and ionize analytes. NIMS boasts impressive 700 ymol limits of detection in ideal conditions and a mass limit of 30 kDa.[165-166] It has been applied to biomolecular MSI at the tissue level to visualize cancer tumors,[167] and can be performed using either laser or ion microprobes, with the latter providing an ultimate lateral resolution of ~150 nm. Near-field laser focusing methods could bring laser probe-based NIMS down to a competitive size scale and also allow high-resolution NIMS MSI at atmospheric pressure.

For high throughput whole-cell measurements, mass cytometry is another clever microanalytical approach introduced recently by Bandura et al.[168] In mass cytometry, cells are first labeled with assorted multiatom elemental (e.g., lanthanide isotope) antibody tags which can number in the dozens. Cells are then suspended in solution, nebulized and fed into an ICP source which disintegrates them completely; the resulting discrete ion packets are then analyzed by an orthogonal TOF and metal ions are detected at high-speed to generate 10+ spectra per individual cell. This promising new instrument allows absolute quantitation of tens of tagged target molecules with virtually no channel crosstalk and high-throughput rates of (theoretically) 3000 cells/s.

CONCLUSIONS

Among the broad array of single-cell, spatially-resolved analysis techniques currently available, mass spectrometry imaging offers distinct advantages. It is capable of obtaining rich chemical information at the cellular level, and offers non-targeted specificity and multiplexed detection.[169] Continued method development and instrumentation advances represent a burgeoning analytical area that promises to rapidly increase the applicability of MS in the fields of biological and biomedical research as sensitivity, dynamic range and consequently, the variety of detectable biomolecules are all increased. The microsampling and imaging approaches discussed here comprise a diverse toolbox, effective for probing the composition of cells with various levels of breadth in chemical sensitivity and spatial resolution.

Subcellular MSI approaches predominantly use a variety of SIMS techniques. Dynamic SIMS offers high sensitivity with the best lateral resolution and has been especially useful for mapping the localization of compounds labeled with rare elements. This approach most notably allows researchers to determine how anti-cancer drugs and other compounds having therapeutic potential are distributed between and within the cells of humans and other multicellular organisms. Static SIMS, restricted traditionally to visualizing the distribution of small molecules and molecular fragments, has recently been augmented by the introduction of softer-ionization, higher-yield cluster ion sources and accompanying instrumental advances. As a result, greater molecular information, molecular depth profiling, and MS/MS identification of detected species is possible with traditionally-static SIMS instrumentation. Accordingly, this approach is now a rapidly advancing MSI platform with great potential for direct subcellular mapping of the localization of unlabeled biomolecules of interest. Although new single-cell sample preparation methods allow direct access to cell contents for molecular MSI, ion signal suppression effects continue to pose a major obstacle to thorough detection and mapping of cell composition. This issue is a major focus of development efforts. Newer primary ion sources being explored—argon cluster,[170] electrospray droplet impact,[171] massive gold cluster,[172] and high-brightness C_{60} plasma[173]—offer promising alternatives to the existing ion source repertoire and may provide advantages such as softer ionization, higher secondary ion yields, or smoother etching for 3-D analysis. Work by Matsuo and colleagues[174-176] with a high-energy (MeV) copper primary ion beam also presents the possibility of SIMS operation at atmospheric pressure and therefore, live-cell SIMS imaging, which would be an interesting and noteworthy development.

MALDI-MS is well-established for tissue-level imaging and has become almost routine for sensitive subcellular profiling experiments. For biological MSI, MALDI offers the advantages of a wide molecular mass range and soft ionization for high intact molecular ion yields. Recent advances in both sample preparation methodologies and high-resolution MSI instrumentation have enabled its application at single-cell and subcellular spatial resolutions. MALDI-MSI has progressed to the point where visualization of bioanalyte distributions can be made more routine, accessible, and informative at these length scales. Likewise, laser ablation-based techniques such as SNOM-MS, LA-ICP-MS and NIMS hold realistic potential to become highly sensitive and quantitative subcellular sampling platforms. These nontraditional approaches can operate under atmospheric conditions and therefore hold real promise for achieving the exciting ability to profile live cells.

REFERENCES

1. Scarcelli, G.; Yun, S. H., Confocal Brillouin microscopy for three-dimensional mechanical imaging. *Nat Photon* **2008,** *2* (1), 39-43.
2. Castaing, R.; Slodzian, G., Microanalyse par emission ionique secondaire. *J Microscopie* **1962,** *1*, 395-410.
3. Caprioli, R. M.; Farmer, T. B.; Gile, J., Molecular Imaging of Biological Samples: Localization of Peptides and Proteins Using MALDI-TOF MS. *Anal. Chem.* **1997,** *69* (23), 4751-4760.
4. Wiseman, J. M.; Ifa, D. R.; Song, Q.; Cooks, R. G., Tissue Imaging at Atmospheric Pressure Using Desorption Electrospray Ionization (DESI) Mass Spectrometry. *Angew. Chem. Int. Ed.* **2006,** *45* (43), 7188-7192.
5. Kertesz, V.; Ford, M. J.; Van Berkel, G. J., Automation of a Surface Sampling Probe/Electrospray Mass Spectrometry System. *Anal. Chem.* **2005,** *77* (22), 7183-7189.
6. Nemes, P.; Vertes, A., Atmospheric-pressure molecular imaging of biological tissues and biofilms by LAESI mass spectrometry. *J Vis Exp* **2010,** *43*, 1-4.
7. Laskin, J.; Heath, B. S.; Roach, P. J.; Cazares, L.; Semmes, O. J., Tissue imaging using nanospray desorption electrospray ionization mass spectrometry. *Anal. Chem.* **2011,** *84* (1), 141-148.
8. Liebl, H., Ion microprobe mass analyzer. *J. Appl. Phys.* **1967,** *38* (13), 5277-5283.
9. Schueler, B.; Sander, P.; Reed, D. A., A time-of-flight secondary ion microscope. *Vacuum* **1990,** *41* (7–9), 1661-1664.
10. Chughtai, K.; Heeren, R. M. A., Mass spectrometric imaging for biomedical tissue analysis. *Chem. Rev.* **2010,** *110*, 3237-3277.
11. Watrous, J. D.; Dorrestein, P. C., Imaging mass spectrometry in microbiology. *Nat Rev Micro* **2011,** *9* (9), 683-694.
12. Kaspar, S.; Peukert, M.; Svatos, A.; Matros, A.; Mock, H.-P., MALDI-imaging mass spectrometry – An emerging technique in plant biology. *Proteomics* **2011,** *11* (9), 1840-1850.
13. Sugiura, Y.; Setou, M., Imaging mass spectrometry for visualization of drug and endogenous metabolite distribution: Toward in situ pharmacometabolomes. *J Neuroimmune Pharmacol* **2010,** *5* (1), 31-43.
14. Solon, E. G.; Schweitzer, A.; Stoeckli, M.; Prideaux, B., Autoradiography, MALDI-MS, and SIMS-MS imaging in pharmaceutical discovery and development. *AAPS J* **2010,** *12* (1), 11-26.
15. Rubakhin, S.; Sweedler, J., *Mass Spectrometry Imaging: Principles and Protocols*. Humana Press, New York: 2010; Vol. 656.
16. Setou, M., *Imaging mass spectrometry : protocols for mass microscopy*. Springer: Tokyo, 2010.
17. Zhu, L.; Stadler, J.; Schmitz, T. A.; Krumeich, F.; Zenobi, R., Atmospheric pressure sampling for laser ablation based nanoscale imaging mass spectrometry: Ions or neutrals? *J Phys Chem C* **2011,** *115* (4), 1006-1013.
18. McCombie, G.; Knochenmuss, R., Enhanced MALDI ionization efficiency at the metal-matrix interface: Practical and mechanistic consequences of sample thickness and preparation method. *J. Am. Soc. Mass Spectrom.* **2006,** *17* (5), 737-745.
19. Galle, P., Sur une nouvelle methode d'analyse cellulaire utilisant le phenomene d'emission ionique secondaire. *Ann. Phys. Biol. Med.* **1970,** *42*, 83-94.
20. Lechene, C. P.; Luyten, Y.; McMahon, G.; Distel, D. L., Quantitative Imaging of Nitrogen Fixation by Individual Bacteria Within Animal Cells. *Science* **2007,** *317* (5844), 1563-1566.
21. Chandra, S.; Tjarks, W.; Lorey Ii, D. R.; Barth, R. F., Quantitative subcellular imaging of boron compounds in individual mitotic and interphase human glioblastoma cells with imaging secondary ion mass spectrometry (SIMS). *J. Microsc.* **2008,** *229* (1), 92-103.
22. Boxer, S. G.; Kraft, M. L.; Weber, P. K., Advances in Imaging Secondary Ion Mass Spectrometry for Biological Samples. *Ann Rev Biophys* **2009,** *38* (1), 53-74.
23. Setou, M.; Kurabe, N., Mass microscopy: High-resolution imaging mass spectrometry. *J. Electron Microsc.* **2011,** *60* (1), 47-56.
24. Carado, A.; Passarelli, M. K.; Kozole, J.; Wingate, J. E.; Winograd, N.; Loboda, A. V., C60 Secondary Ion Mass Spectrometry with a Hybrid-Quadrupole Orthogonal Time-of-Flight Mass Spectrometer. *Anal. Chem.* **2008,** *80* (21), 7921-7929.
25. Komatsu, M.; Murayama, Y.; Hashimoto, H., Protein fragment imaging using ink jet printing digestion technique. *Appl. Surf. Sci.* **2008,** *255* (4), 1162-1164.

26. Altelaar, A. F. M.; Minnen, J. v.; Jimenez, C. R.; Heeren, R. M. A.; Piersma, S. R., Direct Molecular Imaging of Lymnaea stagnalis Nervous Tissue at Subcellular Spatial Resolution by Mass Spectrometry. *Anal. Chem.* **2005,** *77*, 735-741.
27. Monroe, E. B.; Jurchen, J. C.; Lee, J.; Rubakhin, S. S.; Sweedler, J. V., Vitamin E Imaging and Localization in the Neuronal Membrane. *J. Am. Chem. Soc.* **2005,** *127* (35), 12152-12153.
28. McMahon, G.; Saint-Cyr, H. F.; Lechene, C.; Unkefer, C. J., CN− Secondary Ions Form by Recombination as Demonstrated Using Multi-Isotope Mass Spectrometry of 13C- and 15N-Labeled Polyglycine. *J. Am. Soc. Mass Spectrom.* **2006,** *17* (8), 1181-1187.
29. Kleinfeld, A. M.; Kampf, J. P.; Lechene, C., Transport of 13C-oleate in adipocytes measured using multi imaging mass spectrometry. *J. Am. Soc. Mass Spectrom.* **2004,** *15* (11), 1572-1580.
30. Chandra, S., Subcellular Imaging of Cells and Tissues with Dynamic Secondary Ion Mass Spectrometry. In *The Encyclopedia of Mass Spectrometry*, Gross, M. L.; Caprioli, R. M., Eds. Elsevier: 2010; pp 469-480.
31. CAMECA NanoSIMS 50/50L. SIMS Microprobe for Ultra Fine Feature Analysis. http://www.cameca.fr/instruments-for-research/nanosims.aspx (accessed 10/23/2011).
32. Kraft, M. L.; Weber, P. K.; Longo, M. L.; Hutcheon, I. D.; Boxer, S. G., Phase Separation of Lipid Membranes Analyzed with High-Resolution Secondary Ion Mass Spectrometry. *Science* **2006,** *313* (5795), 1948-1951.
33. Weber, P. K.; Graham, G. A.; Teslich, N. E.; Chan, W. M.; Ghosal, S.; Leighton, T. J.; Wheeler, K. E., NanoSIMS imaging of Bacillus spores sectioned by focused ion beam. *J. Microsc.* **2010,** *238* (3), 189-199.
34. Chandra, S., Studies of cell division (mitosis and cytokinesis) by dynamic secondary ion mass spectrometry ion microscopy: LLC-PK1 epithelial cells as a model for subcellular isotopic imaging. *J. Microsc.* **2001,** *204* (2), 150-165.
35. Anderton, C. R.; Lou, K.; Weber, P. K.; Hutcheon, I. D.; Kraft, M. L., Correlated AFM and NanoSIMS imaging to probe cholesterol-induced changes in phase behavior and non-ideal mixing in ternary lipid membranes. *Biochim Biophys Acta* **2011,** *1808* (1), 307-315.
36. Lau, K. H.; Christlieb, M.; SchrÖder, M.; Sheldon, H.; Harris, A. L.; Grovenor, C. R. M., Development of a new bimodal imaging methodology: A combination of fluorescence microscopy and high-resolution secondary ion mass spectrometry. *J. Microsc.* **2010,** *240* (1), 21-31.
37. Strick, R.; Strissel, P. L.; Gavrilov, K.; Levi-Setti, R., Cation–chromatin binding as shown by ion microscopy is essential for the structural integrity of chromosomes. *J Cell Biol* **2001,** *155* (6), 899-910.
38. Wedlock, L. E.; Wedlock, M. R. K.; Cliff, J. B.; Filgueira, L.; Saunders, M.; Berners-Price, S. J., Visualising gold inside tumour cells following treatment with an antitumour gold(I) complex. *Metallomics* **2011,** *3*, 917-925.
39. Chandra, S., 3D subcellular SIMS imaging in cryogenically prepared single cells. *Appl. Surf. Sci.* **2004,** *231-232*, 467-469.
40. Quintana, C.; Wu, T. D.; Delatour, B.; Dhenain, M.; Guerquin-Kern, J. L.; Croisy, A., Morphological and chemical studies of pathological human and mice brain at the subcellular level: Correlation between light, electron, and NanoSIMS microscopies. *Microsc. Res. Tech.* **2007,** *70* (4), 281-295.
41. Quintana, C.; Bellefqih, S.; Laval, J. Y.; Guerquin-Kern, J. L.; Wu, T. D.; Avila, J.; Ferrer, I.; Arranz, R.; Patiño, C., Study of the localization of iron, ferritin, and hemosiderin in Alzheimer's disease hippocampus by analytical microscopy at the subcellular level. *J. Struct. Biol.* **2006,** *153* (1), 42-54.
42. Azari, F.; Vali, H.; Guerquin-Kern, J. L.; Wu, T. D.; Croisy, A.; Sears, S. K.; Tabrizian, M.; McKee, M. D., Intracellular precipitation of hydroxyapatite mineral and implications for pathologic calcification. *J. Struct. Biol.* **2008,** *162* (3), 468-479.
43. Smith, D. R.; Chandra, S.; Barth, R. F.; Yang, W.; Joel, D. D.; Coderre, J. A., Quantitative imaging and microlocalization of boron-10 in brain tumors and infiltrating tumor cells by SIMS ion microscopy: Relevance to neutron capture therapy. *Cancer Res.* **2001,** *61* (22), 8179-8187.
44. Chandra, S.; Kabalka, G. W.; Lorey Ii, D. R.; Smith, D. R.; Coderre, J. A., Imaging of fluorine and boron from fluorinated boronophenylalanine in the same cell at organelle resolution by correlative ion microscopy and confocal laser scanning microscopy. *Clin. Cancer. Res.* **2002,** *8* (8), 2675-2683.
45. Berry, J. P.; Galle, P.; Chassoux, D.; Escaig, F.; Linarez-Cruz, L. G.; Lespinats, G., Mapping of intracellular halogenous molecules by low and high resolution SIMS microscopy. *Biol. Cell* **1992,** *74* (1), 93-98.
46. Chandra, S.; Morrison, G. H., Imaging ion and molecular transport at subcellular resolution by secondary ion mass spectrometry. *Int. J. Mass Spectrom. Ion Processes* **1995,** *143* (C), 161-176.

47. Ausserer, W. A.; Ling, Y. C.; Chandra, S.; Morrison, G. H., Quantitative imaging of boron, calcium, magnesium, potassium, and sodium distributions in cultured cells with ion microscopy. *Anal. Chem.* **1989,** *61* (24), 2690-2695.
48. Kabalka, G. W.; Shaikh, A. L.; Barth, R. F.; Huo, T.; Yang, W.; Gordnier, P. M.; Chandra, S., Boronated unnatural cyclic amino acids as potential delivery agents for neutron capture therapy. *Appl. Radiat. Isot.* **2011,** *69* (12), 1778-1781.
49. Kabalka, G. W.; Yao, M. L.; Marepally, S. R.; Chandra, S., Biological evaluation of boronated unnatural amino acids as new boron carriers. *Appl. Radiat. Isot.* **2009,** *67* (7-8 SUPPL.), S374-S379.
50. Lorey Ii, D. R.; Morrison, G. H.; Chandra, S., Dynamic secondary ion mass spectrometry analysis of boron from boron neutron capture therapy drugs in co-cultures: Single-cell imaging of two different cell types within the same ion microscopy field of imaging. *Anal. Chem.* **2001,** *73* (16), 3947-3953.
51. Chandra, S., Quantitative Imaging of Chemical Composition in Single Cells by Secondary Ion Mass Spectrometry: Cisplatin Affects Calcium Stores in Renal Epithelial Cells. In *Mass Spectrometry Imaging: Principles and Protocols*, 1 ed.; Rubakhin, S. S.; Sweedler, J. V., Eds. Humana Press: New York, 2010; pp 113-130.
52. Usami, N.; Furusawa, Y.; Kobayashi, K.; Lacombe, S.; Reynaud-Angelin, A.; Sage, E.; Wu, T. D.; Croisy, A.; Guerquin-Kern, J. L.; Le Sech, C., Mammalian cells loaded with platinum-containing molecules are sensitized to fast atomic ions. *Int. J. Radiat. Biol.* **2008,** *84* (7), 603-611.
53. Guerquin-Kern, J. L.; Hillion, F.; Madelmont, J. C.; Labarre, P.; Papon, J.; Croisy, A., Ultra-structural cell distribution of the melanoma marker iodobenzamide: Improved potentially of SIMS imaging in life sciences. *BioMed Eng Online* **2004,** *3*.
54. Clode, P. L.; Stern, R. A.; Marshall, A. T., Subcellular imaging of isotopically labeled carbon compounds in a biological sample by ion microprobe (NanoSIMS). *Microsc. Res. Tech.* **2007,** *70* (3), 220-229.
55. Zhang, D.-S.; Piazza, V.; Perrin, B. J.; Rzadzinska, A. K.; Poczatek, J. C.; Wang, M.; Prosser, H. M.; Ervasti, J. M.; Corey, D. P.; Lechene, C. P., Multi-isotope imaging mass spectrometry reveals slow protein turnover in hair-cell stereocilia. *Nature* **2012,** *481* (7382), 520-524.
56. Steinhauser, M. L.; Bailey, A. P.; Senyo, S. E.; Guillermier, C.; Perlstein, T. S.; Gould, A. P.; Lee, R. T.; Lechene, C. P., Multi-isotope imaging mass spectrometry quantifies stem cell division and metabolism. *Nature* **2012,** *481* (7382), 516-519.
57. Kraft, M. L.; Fishel, S. F.; Marxer, C. G.; Weber, P. K.; Hutcheon, I. D.; Boxer, S. G., Quantitative analysis of supported membrane composition using the NanoSIMS. *Appl. Surf. Sci.* **2006,** *252* (19), 6950-6956.
58. Kollmer, F., Cluster primary ion bombardment of organic materials. *Appl. Surf. Sci.* **2004,** *231-232*, 153-158.
59. Gunnarsson, A.; Kollmer, F.; Sohn, S.; Höök, F.; Sjövall, P., Spatial-resolution limits in mass spectrometry imaging of supported lipid bilayers and individual lipid vesicles. *Anal. Chem.* **2010,** *82* (6), 2426-2433.
60. Dubey, M.; Brison, J.; Grainger, D. W.; Castner, D. G., Comparison of Bi1+, Bi3+ and C60+ primary ion sources for ToF-SIMS imaging of patterned protein samples. *Surf. Interface Anal.* **2011,** *43* (1-2), 261-264.
61. Weibel, D.; Wong, S.; Lockyer, N.; Blenkinsopp, P.; Hill, R.; Vickerman, J. C., A C60 Primary Ion Beam System for Time of Flight Secondary Ion Mass Spectrometry: Its Development and Secondary Ion Yield Characteristics. *Anal. Chem.* **2003,** *75* (7), 1754-1764.
62. Nygren, H.; Malmberg, P.; Nilsson, M.; Kriegeskotte, C.; Arlinghaus, H. F., The cytochemistry of anaplastic thyroid tumour cells and differentiated thyrocytes analyzed by TOF-SIMS and depth profiling. *Appl. Surf. Sci.* **2008,** *255* (4), 1285-1288.
63. Breitenstein, D.; Rommel, C. E.; Möllers, R.; Wegener, J.; Hagenhoff, B., The Chemical Composition of Animal Cells and Their Intracellular Compartments Reconstructed from 3D Mass Spectrometry. *Angew. Chem. Int. Ed.* **2007,** *46* (28), 5332-5335.
64. Brison, J.; Benoit, D. S. W.; Muramoto, S.; Robinson, M.; Stayton, P. S.; Castner, D. G., ToF-SIMS imaging and depth profiling of HeLa cells treated with bromodeoxyuridine. *Surf. Interface Anal.* **2011,** *43* (1-2), 354-357.
65. Carado, A.; Kozole, J.; Passarelli, M.; Winograd, N.; Loboda, A.; Wingate, J., Cluster SIMS with a hybrid quadrupole time-of-flight mass spectrometer. *Appl. Surf. Sci.* **2008,** *255* (4), 1610-1613.
66. Rabbani, S.; Fletcher, J. S.; Lockyer, N. P.; Vickerman, J. C., Exploring subcellular imaging on the buncher-ToF J105 3D chemical imager. *Surf. Interface Anal.* **2011,** *43* (1-2), 380-384.
67. Hill, R.; Blenkinsopp, P.; Thompson, S.; Vickerman, J.; Fletcher, J. S., A new time-of-flight SIMS instrument for 3D imaging and analysis. *Surf. Interface Anal.* **2011,** *43* (1-2), 506-509.

68. Fletcher, J. S.; Rabbani, S.; Henderson, A.; Blenkinsopp, P.; Thompson, S. P.; Lockyer, N. P.; Vickerman, J. C., A New Dynamic in Mass Spectral Imaging of Single Biological Cells. *Anal. Chem.* **2008,** *80*, 9058-9064.
69. Fletcher, J. S.; Rabbani, S.; Henderson, A.; Lockyer, N. P.; Vickerman, J. C., Three-dimensional mass spectral imaging of HeLa-M cells – sample preparation, data interpretation and visualisation. *Rapid Commun. Mass Spectrom.* **2011,** *25* (7), 925-932.
70. Smith, D. F.; Robinson, E. W.; Tolmachev, A. V.; Heeren, R. M. A.; Paša-Tolić, L., C60 Secondary Ion Fourier Transform Ion Cyclotron Resonance Mass Spectrometry. *Anal. Chem.* **2011,** *83*, 9552–9556.
71. Passarelli, M. K.; Winograd, N., Lipid imaging with time-of-flight secondary ion mass spectrometry (ToF-SIMS). *Biochim Biophys Acta* **2011,** *1811* (11), 976-990.
72. Piehowski, P. D.; Carado, A. J.; Kurczy, M. E.; Ostrowski, S. G.; Heien, M. L.; Winograd, N.; Ewing, A. G., MS/MS Methodology To Improve Subcellular Mapping of Cholesterol Using TOF-SIMS. *Anal. Chem.* **2008,** *80* (22), 8662-8667.
73. Jerigova, M.; Biro, C.; Kirchnerova, J.; Chorvatova, A.; Chorvat, D.; Lorenc, D.; Velic, D., Chemical Imaging of Cardiac Cell and Tissue by Using Secondary Ion Mass Spectrometry. *Mol. Imag. Biol.* **2010**, 1-10.
74. Benabdellah, F.; Seyer, A.; Quinton, L.; Touboul, D.; Brunelle, A.; Laprévote, O., Mass spectrometry imaging of rat brain sections: Nanomolar sensitivity with MALDI versus nanometer resolution by TOF-SIMS. *Anal. Bioanal. Chem.* **2010,** *396* (1), 151-162.
75. Monroe, E. B.; Annangudi, S. P.; Hatcher, N. G.; Gutstein, H. B.; Rubakhin, S. S.; Sweedler, J. V., SIMS and MALDI MS imaging of the spinal cord. *Proteomics* **2008,** *8* (18), 3746-3754.
76. Ostrowski, S. G.; Van Bell, C. T.; Winograd, N.; Ewing, A. G., Mass Spectrometric Imaging of Highly Curved Membranes During Tetrahymena Mating. *Science* **2004,** *305* (5680), 71-73.
77. Kurczy, M. E.; Piehowski, P. D.; Van Bell, C. T.; Heien, M. L.; Winograd, N.; Ewing, A. G., Mass spectrometry imaging of mating Tetrahymena show that changes in cell morphology regulate lipid domain formation. *Proc. Natl. Acad. Sci. USA* **2010,** *107* (7), 2751-2756.
78. Ostrowski, S. G.; Kurczy, M. E.; Roddy, T. P.; Winograd, N.; Ewing, A. G., Secondary ion MS imaging to relatively quantify cholesterol in the membranes of individual cells from differentially treated populations. *Anal. Chem.* **2007,** *79* (10), 3554-3560.
79. Kurczy, M. E.; Kozole, J.; Parry, S. A.; Piehowski, P. D.; Winograd, N.; Ewing, A. G., Relative quantification of cellular sections with molecular depth profiling ToF-SIMS imaging. *Appl. Surf. Sci.* **2008,** *255* (4), 1158-1161.
80. Lanekoff, I.; Sjövall, P.; Ewing, A. G., Relative quantification of phospholipid accumulation in the PC12 cell plasma membrane following phospholipid incubation using TOF-SIMS imaging. *Anal. Chem.* **2011,** *83* (13), 5337-5343.
81. Uchiyama, Y.; Maxson, M. M.; Sawada, T.; Nakano, A.; Ewing, A. G., Phospholipid mediated plasticity in exocytosis observed in PC12 cells. *Brain Res.* **2007,** *1151*, 46-54.
82. Anderton, C. R.; Vaezian, B.; Lou, K.; Frisz, J. F.; Kraft, M. L., Identification of a lipid-related peak set to enhance the interpretation of TOF-SIMS data from model and cellular membranes. *Surf. Interface Anal.* **2011,** *44* (3), 322-333.
83. Breitenstein, D.; Rommel, C. E.; Stolwijk, J.; Wegener, J.; Hagenhoff, B., The chemical composition of animal cells reconstructed from 2D and 3D ToF-SIMS analysis. *Appl. Surf. Sci.* **2008,** *255* (4), 1249-1256.
84. Szakal, C.; Narayan, K.; Fu, J.; Lefman, J.; Subramaniam, S., Compositional Mapping of the Surface and Interior of Mammalian Cells at Submicrometer Resolution. *Anal. Chem.* **2011,** *83* (4), 1207-1213.
85. Henderson, A.; Fletcher, J. S.; Vickerman, J. C., A comparison of PCA and MAF for ToF-SIMS image interpretation. *Surf. Interface Anal.* **2009,** *41* (8), 666-674.
86. Tyler, B. J.; Takeno, M. M.; Hauch, K. D., Identification and Imaging of 15N labeled cells with ToF-SIMS. *Surf. Interface Anal.* **2011,** *43* (1-2), 336-339.
87. Nygren, H.; Malmberg, P., High-resolution imaging and proteomics of peptide fragments by TOF-SIMS. *Proteomics* **2010,** *10* (9), 1694-1698.
88. Piwowar, A.; Fletcher, J.; Lockyer, N.; Vickerman, J., Top-down approach to studying biological components using ToF-SIMS. *Surf. Interface Anal.* **2011,** *43* (1-2), 265-268.
89. Jones, E.; Lockyer, N.; Kordys, J.; Vickerman, J., Suppression and enhancement of secondary ion formation due to the chemical environment in static-secondary ion mass spectrometry. *J. Am. Soc. Mass Spectrom.* **2007,** *18* (8), 1559-1567.

90. Sostarecz, A. G.; Cannon Jr, D. M.; McQuaw, C. M.; Sun, S.; Ewing, A. G.; Winograd, N., Influence of molecular environment on the analysis of phospholipids by time-of-flight secondary ion mass spectrometry. *Langmuir* **2004,** *20* (12), 4926-4932.
91. Altelaar, A. F. M.; Klinkert, I.; Jalink, K.; de Lange, R. P. J.; Adan, R. A. H.; Heeren, R. M. A.; Piersma, S. R., Gold-enhanced biomolecular surface imaging of cells and tissue by SIMS and MALDI mass spectrometry. *Analytical Chemistry* **2006,** *78* (3), 734-742.
92. McDonnell, L. A.; Piersma, S. R.; Altelaar, A. F. M.; Mize, T. H.; Luxembourg, S. L.; Verhaert, P. D. E. M.; van Minnen, J.; Heeren, R. M. A., Subcellular imaging mass spectrometry of brain tissue. *J. Mass Spectrom.* **2005,** *40* (2), 160-168.
93. Piwowar, A. M.; Fletcher, J. S.; Kordys, J.; Lockyer, N. P.; Winograd, N.; Vickerman, J. C., Effects of cryogenic sample analysis on molecular depth profiles with TOF-secondary ion mass spectrometry. *Anal. Chem.* **2010,** *82* (19), 8291-8299.
94. Piehowski, P. D.; Kurczy, M. E.; Willingham, D.; Parry, S.; Heien, M. L.; Winograd, N.; Ewing, A. G., Freeze-etching and vapor matrix deposition for ToF-SIMS imaging of single cells. *Langmuir* **2008,** *24* (15), 7906-7911.
95. Mouhib, T.; Delcorte, A.; Poleunis, C.; Bertrand, P., Organic secondary ion mass spectrometry: Signal enhancement by water vapor injection. *J. Am. Soc. Mass Spectrom.* **2010,** *21* (12), 2005-2010.
96. Brummel, C. L.; Willey, K. F.; Vickerman, J. C.; Winograd, N., Ion beam induced desorption with postionization using high repetition femtosecond lasers. *Int. J. Mass Spectrom. Ion Processes* **1995,** *143*, 257-270.
97. Roy, M. C.; Nakanishi, H.; Takahashi, K.; Nakanishi, S.; Kajihara, S.; Hayasaka, T.; Setou, M.; Ogawa, K.; Taguchi, R.; Naito, T., Salamander retina phospholipids and their localization by MALDI imaging mass spectrometry at cellular size resolution. *J. Lipid Res.* **2011,** *52* (3), 463-470.
98. Becker, J. S.; Niehren, S.; Matusch, A.; Wu, B.; Hsieh, H. F.; Kumtabtim, U.; Hamester, M.; Plaschke-Schlütter, A.; Salber, D., Scaling down the bioimaging of metals by laser microdissection inductively coupled plasma mass spectrometry (LMD-ICP-MS). *Int. J. Mass spectrom.* **2010,** *294* (1), 1-6.
99. Chandra, S.; Bernius, M. T.; Morrison, G. H., Intracellular localization of diffusible elements in frozen-hydrated biological specimens with ion microscopy. *Anal. Chem.* **1986,** *58* (2), 493-496.
100. Steere, R. L., Electron Microscopy of Structural Detail in Frozen Biological Specimens. *J Biophys Biochem Cytol* **1957,** *3* (1), 45-60.
101. Chandra, S.; Morrison, G. H.; Wolcott, C. C., Imaging intracellular elemental distribution and ion fluxes in cultured cells using ion microscopy: a freeze-fracture methodology. *J. Microsc.* **1986,** *144* (1), 15-37.
102. Roddy, T. P.; Cannon, D. M.; Ostrowski, S. G.; Winograd, N.; Ewing, A. G., Identification of Cellular Sections with Imaging Mass Spectrometry Following Freeze Fracture. *Anal. Chem.* **2002,** *74* (16), 4020-4026.
103. Colliver, T. L.; Brummel, C. L.; Pacholski, M. L.; Swanek, F. D.; Ewing, A. G.; Winograd, N., Atomic and Molecular Imaging at the Single-Cell Level with TOF-SIMS. *Anal. Chem.* **1997,** *69* (13), 2225-2231.
104. Pacholski, M. L.; Cannon, D. M.; Ewing, A. G.; Winograd, N., Static time-of-flight secondary ion mass spectrometry imaging of freeze-fractured, frozen-hydrated biological membranes. *Rapid Commun. Mass Spectrom.* **1998,** *12* (18), 1232-1235.
105. Cliff, B.; Lockyer, N.; Jungnickel, H.; Stephens, G.; Vickerman, J. C., Probing cell chemistry with time-of-flight secondary ion mass spectrometry: development and exploitation of instrumentation for studies of frozen-hydrated biological material. *Rapid Commun. Mass Spectrom.* **2003,** *17* (19), 2163-2167.
106. Pegg, D. E., Principles of Cryopreservation. In *Cryopreservation and Freeze-Drying Protocols*, 2 ed.; G., D. J.; N., S. G., Eds. Humana Press: Totowa, NJ, 2007; Vol. 368, pp 39-57.
107. Lanekoff, I.; Kurczy, M. E.; Hill, R.; Fletcher, J. S.; Vickerman, J. C.; Winograd, N.; Sjövall, P.; Ewing, A. G., Time of Flight Mass Spectrometry Imaging of Samples Fractured In Situ with a Spring-Loaded Trap System. *Anal. Chem.* **2010,** *82* (15), 6652-6659.
108. Conlan, X. A.; Lockyer, N. P.; Vickerman, J. C., Is proton cationization promoted by polyatomic primary ion bombardment during time-of-flight secondary ion mass spectrometry analysis of frozen aqueous solutions? *Rapid Commun. Mass Spectrom.* **2006,** *20* (8), 1327-1334.
109. Chandra, S., Challenges of biological sample preparation for SIMS imaging of elements and molecules at subcellular resolution. *Appl. Surf. Sci.* **2008,** *255* (4), 1273-1284.
110. Berman, E.; Fortson, S.; Checchi, K.; Wu, L.; Felton, J.; Wu, K.; Kulp, K., Preparation of single cells for imaging/profiling mass spectrometry. *J. Am. Soc. Mass Spectrom.* **2008,** *19* (8), 1230-1236.

111. Malm, J.; Giannaras, D.; Riehle, M. O.; Gadegaard, N.; Sjövall, P., Fixation and Drying Protocols for the Preparation of Cell Samples for Time-of-Flight Secondary Ion Mass Spectrometry Analysis. *Anal. Chem.* **2009,** *81* (17), 7197-7205.
112. Sjövall, P.; Lausmaa, J.; Nygren, H.; Carlsson, L.; Malmberg, P., Imaging of Membrane Lipids in Single Cells by Imprint-Imaging Time-of-Flight Secondary Ion Mass Spectrometry. *Analytical Chemistry* **2003,** *75* (14), 3429-3434.
113. Kurczy, M. E.; Piehowsky, P. D.; Willingham, D.; Molyneaux, K. A.; Heien, M. L.; Winograd, N.; Ewing, A. G., Nanotome Cluster Bombardment to Recover Spatial Chemistry After Preparation of Biological Samples for SIMS Imaging. *J. Am. Soc. Mass Spectrom.* **2010,** *21* (5), 833-836.
114. Barnes, C. A.; Brison, J.; Robinson, M.; Graham, D. J.; Castner, D. G.; Ratner, B. D., Identifying Individual Cell Types in Heterogeneous Cultures Using Secondary Ion Mass Spectrometry Imaging with C60 Etching and Multivariate Analysis. *Analytical Chemistry* **2011,** *84* (2), 893-900.
115. Vaidyanathan, S.; Fletcher, J. S.; Goodacre, R.; Lockyer, N. P.; Micklefield, J.; Vickerman, J. C., Subsurface Biomolecular Imaging of Streptomyces coelicolor Using Secondary Ion Mass Spectrometry. *Anal. Chem.* **2008,** *80*, 1942-1951.
116. Lu, C.; Wucher, A.; Winograd, N., Molecular depth profiling of buried lipid bilayers using C60-secondary ion mass spectrometry. *Anal. Chem.* **2011,** *83* (1), 351-358.
117. Fletcher, J. S.; Lockyer, N. P.; Vaidyanathan, S.; Vickerman, J. C., TOF-SIMS 3D Biomolecular Imaging of Xenopus laevis Oocytes Using Buckminsterfullerene (C60) Primary Ions. *Analytical Chemistry* **2007,** *29*, 2199-2206.
118. Malmberg, P.; Kriegeskotte, C.; Arlinghaus, H. F.; Hagenhoff, B.; Holmgren, J.; Nilsson, M.; Nygren, H., Depth profiling of cells and tissues by using C60+ and SF5+ as sputter ions. *Appl. Surf. Sci.* **2008,** *255* (4), 926-928.
119. Sjövall, P.; Rading, D.; Ray, S.; Yang, L.; Shard, A. G., Sample Cooling or Rotation Improves C60 Organic Depth Profiles of Multilayered Reference Samples: Results from a VAMAS Interlaboratory Study. *J Phys Chem B* **2009,** *114* (2), 769-774.
120. Karas, M.; Bachmann, D.; Hillenkamp, F., Influence of the wavelength in high-irradiance ultraviolet laser desorption mass spectrometry of organic molecules. *Anal. Chem.* **1985,** *57* (14), 2935-2939.
121. Tanaka, K.; Waki, H.; Ido, Y.; Akita, S.; Yoshida, Y.; Yoshida, T.; Matsuo, T., Protein and polymer analyses up to m/z 100 000 by laser ionization time-of-flight mass spectrometry. *Rapid Commun. Mass Spectrom.* **1988,** *2* (8), 151-153.
122. Van Veelen, P. A.; Jiménez, C. R.; Li, K. W.; Wildering, W. C.; Geraerts, W. P. M.; Tjaden, U. R.; Van Der Greef, J., Direct peptide profiling of single neurons by matrix-assisted laser desorption-ionization mass spectrometry. *Org. Mass Spectrom.* **1993,** *28*, 1542-1546.
123. Jiménez, C. R.; Van Veelen, P. A.; Li, K. W.; Wildering, W. C.; Geraerts, W. P. M.; Tjaden, U. R.; Van der Greef, J., Neuropeptide expression and processing as revealed by direct matrix- assisted laser desorption ionization mass spectrometry of single neurons. *J. Neurochem.* **1994,** *62* (1), 404-407.
124. Li, K. W.; Hoek, R. M.; Smith, F.; Jiménez, C. R.; Van Der Schors, R. C.; Van Veelen, P. A.; Chen, S.; Van Der Greef, J.; Parish, D. C.; Benjamin, P. R.; Geraerts, W. P. M., Direct peptide profiling by mass spectrometry of single identified neurons reveals complex neuropeptide-processing pattern. *J. Biol. Chem.* **1994,** *269* (48), 30288-30292.
125. Garden, R. W.; Moroz, L. L.; Moroz, T. P.; Shippy, S. A.; Sweedler, J. V., Excess Salt Removal with Matrix Rinsing: Direct Peptide Profiling of Neurons from Marine Invertebrates Using Matrix-assisted Laser Desorption/Ionization Time-of-flight Mass Spectrometry. *J. Mass Spectrom.* **1996,** *31* (10), 1126-1130.
126. Jiménez, C. R.; Li, K. W.; Dreisewerd, K.; Spijker, S.; Kingston, R.; Bateman, R. H.; Burlingame, A. L.; Smit, A. B.; Van Minnen, J.; Geraerts, W. P. M., Direct mass spectrometric peptide profiling and sequencing of single neurons reveals differential peptide patterns in a small neuronal network. *Biochemistry (Mosc).* **1998,** *37* (7), 2070-2076.
127. Jing, J.; Sweedler, J. V.; Cropper, E. C.; Alexeeva, V.; Park, J. H.; Romanova, E. V.; Xie, F.; Dembrow, N. C.; Ludwar, B. C.; Weiss, K. R.; Vilim, F. S., Feedforward compensation mediated by the central and peripheral actions of a single neuropeptide discovered using representational difference analysis. *J. Neurosci.* **2010,** *30* (49), 16545-16558.
128. Proekt, A.; Vilim, F. S.; Alexeeva, V.; Brezina, V.; Friedman, A.; Jing, J.; Li, L.; Zhurov, Y.; Sweedler, J. V.; Weiss, K. R., Identification of a new neuropeptide precursor reveals a novel source of extrinsic modulation in the feeding system of Aplysia. *J. Neurosci.* **2005,** *25* (42), 9637-9648.

129. Sweedler, J. V.; Li, L.; Rubakhin, S. S.; Alexeeva, V.; Dembrow, N. C.; Dowling, O.; Jing, J.; Weiss, K. R.; Vilim, F. S., Identification and characterization of the feeding circuit-activating peptides, a novel neuropeptide family of Aplysia. *J. Neurosci.* **2002,** *22* (17), 7797-7808.

130. Floyd, P. D.; Li, L.; Rubakhin, S. S.; Sweedler, J. V.; Horn, C. C.; Kupfermann, I.; Alexeeva, V. Y.; Ellis, T. A.; Dembrow, N. C.; Weiss, K. R.; Vilim, F. S., Insulin prohormone processing, distribution, and relation to metabolism in Aplysia californica. *J. Neurosci.* **1999,** *19* (18), 7732-7741.

131. Bai, L.; Romanova, E. V.; Sweedler, J. V., Distinguishing endogenous d-amino acid-containing neuropeptides in individual neurons using tandem mass spectrometry. *Anal. Chem.* **2011,** *83* (7), 2794-2800.

132. Rubakhin, S. S.; Churchill, J. D.; Greenough, W. T.; Sweedler, J. V., Profiling Signaling Peptides in Single Mammalian Cells Using Mass Spectrometry. *Anal. Chem.* **2006,** *78* (20), 7267-7272.

133. Rubakhin, S. S.; Sweedler, J. V., Characterizing peptides in individual mammalian cells using mass spectrometry. *Nat Protoc* **2007,** *2* (8), 1987-1997.

134. Amantonico, A.; Urban, P. L.; Fagerer, S. R.; Balabin, R. M.; Zenobi, R., Single-cell MALDI-MS as an analytical tool for studying intrapopulation metabolic heterogeneity of unicellular organisms. *Anal. Chem.* **2010,** *82* (17), 7394-7400.

135. Miura, D.; Fujimura, Y.; Yamato, M.; Hyodo, F.; Utsumi, H.; Tachibana, H.; Wariishi, H., Ultrahighly sensitive in situ metabolomic imaging for visualizing spatiotemporal metabolic behaviors. *Anal. Chem.* **2010,** *82* (23), 9789-9796.

136. Rubakhin, S. S.; Sweedler, J. V., Quantitative Measurements of Cell−Cell Signaling Peptides with Single-Cell MALDI MS. *Anal. Chem.* **2008,** *80* (18), 7128-7136.

137. Rubakhin, S. S.; Garden, R. W.; Fuller, R. R.; Sweedler, J. V., Measuring the peptides in individual organelles with mass spectrometry. *Nat Biotech* **2000,** *18* (2), 172-175.

138. Rubakhin, S. S.; Greenough, W. T.; Sweedler, J. V., Spatial Profiling with MALDI MS: Distribution of Neuropeptides within Single Neurons. *Anal. Chem.* **2003,** *75* (20), 5374-5380.

139. Dreisewerd, K.; Schürenberg, M.; Karas, M.; Hillenkamp, F., Influence of the laser intensity and spot size on the desorption of molecules and ions in matrix-assisted laser desorption/ionization with a uniform beam profile. *Int. J. Mass Spectrom. Ion Processes* **1995,** *141* (2), 127-148.

140. Altelaar, A. F. M.; Taban, I. M.; McDonnell, L. A.; Verhaert, P. D. E. M.; de Lange, R. P. J.; Adan, R. A. H.; Mooi, W. J.; Heeren, R. M. A.; Piersma, S. R., High-resolution MALDI imaging mass spectrometry allows localization of peptide distributions at cellular length scales in pituitary tissue sections. *Int. J. Mass spectrom.* **2007,** *260* (2-3), 203-211.

141. Hillenkamp, F.; Unsöld, E.; Kaufmann, R.; Nitsche, R., Laser microprobe mass analysis of organic materials. *Nature* **1975,** *256* (5513), 119-120.

142. Spengler, B.; Hubert, M., Scanning microprobe matrix-assisted laser desorption ionization (SMALDI) mass spectrometry: instrumentation for sub-micrometer resolved LDI and MALDI surface analysis. *J. Am. Soc. Mass Spectrom.* **2002,** *13* (6), 735-748.

143. Bouschen, W.; Schulz, O.; Eikel, D.; Spengler, B., Matrix vapor deposition/recrystallization and dedicated spray preparation for high-resolution scanning microprobe matrix-assisted laser desorption/ionization imaging mass spectrometry (SMALDI-MS) of tissue and single cells. *Rapid Commun. Mass Spectrom.* **2010,** *24* (3), 355-364.

144. Koestler, M.; Kirsch, D.; Hester, A.; Leisner, A.; Guenther, S.; Spengler, B., A high-resolution scanning microprobe matrix-assisted laser desorption/ionization ion source for imaging analysis on an ion trap/Fourier transform ion cyclotron resonance mass spectrometer. *Rapid Commun. Mass Spectrom.* **2008,** *22* (20), 3275-3285.

145. Guenther, S.; Römpp, A.; Kummer, W.; Spengler, B., AP-MALDI imaging of neuropeptides in mouse pituitary gland with 5 μm spatial resolution and high mass accuracy. *Int. J. Mass spectrom.* **2011,** *305* (2–3), 228-237.

146. Harada, T.; Yuba-Kubo, A.; Sugiura, Y.; Zaima, N.; Hayasaka, T.; Goto-Inoue, N.; Wakui, M.; Suematsu, M.; Takeshita, K.; Ogawa, K.; Yoshida, Y.; Setou, M., Visualization of Volatile Substances in Different Organelles with an Atmospheric-Pressure Mass Microscope. *Anal. Chem.* **2009,** *81* (21), 9153-9157.

147. Hankin, J.; Barkley, R.; Murphy, R., Sublimation as a method of matrix application for mass spectrometric imaging. *J. Am. Soc. Mass Spectrom.* **2007,** *18* (9), 1646-1652.

148. Monroe, E. B.; Koszczuk, B. A.; Losh, J. L.; Jurchen, J. C.; Sweedler, J. V., Measuring salty samples without adducts with MALDI MS. *Int. J. Mass spectrom.* **2007,** *260* (2-3), 237-242.

149. Yang, J.; Caprioli, R. M., Matrix Sublimation/Recrystallization for Imaging Proteins by Mass Spectrometry at High Spatial Resolution. *Anal. Chem.* **2011,** *83* (14), 5728–5734.
150. Monroe, E. B.; Jurchen, J. C.; Koszczuk, B. A.; Losh, J. L.; Rubakhin, S. S.; Sweedler, J. V., Massively Parallel Sample Preparation for the MALDI MS Analyses of Tissues. *Anal. Chem.* **2006,** *78* (19), 6826-6832.
151. Tucker, K. R.; Lanni, E. J.; Serebryannyy, L. A.; Rubakhin, S. S.; Sweedler, J. V., Stretched Tissue Mounting for MALDI Mass Spectrometry Imaging. *Anal. Chem.* **2011,** *83* (23), 9181-9185.
152. Zimmerman, T.; Rubakhin, S.; Sweedler, J., MALDI Mass Spectrometry Imaging of Neuronal Cell Cultures. *J. Am. Soc. Mass Spectrom.* **2011,** *22* (5), 828-836-836.
153. Goto-Inoue, N.; Hayasaka, T.; Zaima, N.; Kashiwagi, Y.; Yamamoto, M.; Nakamoto, M.; Setou, M., The detection of glycosphingolipids in brain tissue sections by imaging mass spectrometry using gold nanoparticles. *J. Am. Soc. Mass Spectrom.* **2010,** *21* (11), 1940-1943-1943.
154. Taira, S.; Sugiura, Y.; Moritake, S.; Shimma, S.; Ichiyanagi, Y.; Setou, M., Nanoparticle-Assisted Laser Desorption/Ionization Based Mass Imaging with Cellular Resolution. *Anal. Chem.* **2008,** *80* (12), 4761-4766.
155. Cecchetti, W.; Polloni, R.; Maccioni, A. M.; Traldi, P., A simple instrumental approach for laser induced 'hard' evaporation of samples. *Org. Mass Spectrom.* **1986,** *21* (8), 517-518.
156. Hand, O. W.; Emary, W. B.; Winger, B. E.; Cooks, R. G., Depth profiling of multilayered samples and comparisons of secondary ion and laser desorption mass spectra in the same instrument. *Int. J. Mass Spectrom. Ion Processes* **1989,** *90* (2), 97-118.
157. Louris, J. N.; Brodbelt, J. S.; Cooks, R. G., Photodissociation in a quadrupole ion trap mass spectrometer using a fiber optic interface. *Int. J. Mass Spectrom. Ion Processes* **1987,** *75* (3), 345-352.
158. Stöckle, R.; Setz, P.; Deckert, V.; Lippert, T.; Wokaun, A.; Zenobi, R., Nanoscale atmospheric pressure laser ablation-mass spectrometry. *Anal. Chem.* **2001,** *73* (7), 1399-1402.
159. Kossakovski, D. A.; O'Connor, S. D.; Widmer, M.; Baldeschwieler, J. D.; Beauchamp, J. L., Spatially resolved chemical analysis with an NSOM-based laser desorption microprobe. *Ultramicroscopy* **1998,** *71* (1-4), 111-115.
160. Zoriy, M. V.; Becker, J. S., Near-field laser ablation inductively coupled plasma mass spectrometry: a novel elemental analytical technique at the nanometer scale. *Rapid Commun. Mass Spectrom.* **2009,** *23* (1), 23-30.
161. Becker, J. S.; Gorbunoff, A.; Zoriy, M.; Izmer, A.; Kayser, M., Evidence of near-field laser ablation inductively coupled plasma mass spectrometry (NF-LA-ICP-MS) at nanometre scale for elemental and isotopic analysis on gels and biological samples. *J. Anal. At. Spectrom.* **2006,** *21* (1), 19-25.
162. Zayed, A.; Shoeib, T.; Taylor, S. E.; Jones, G. D. D.; Thomas, A. L.; Wood, J. P.; Reid, H. J.; Sharp, B. L., Determination of Pt-DNA adducts and the sub-cellular distribution of Pt in human cancer cell lines and the leukocytes of cancer patients, following mono- or combination treatments, by inductively-coupled plasma mass spectrometry. *Int. J. Mass spectrom.* **2011,** *307* (1-3), 70-78.
163. Becker, J. S., Bioimaging of metals in brain tissue from micrometre to nanometre scale by laser ablation inductively coupled plasma mass spectrometry: State of the art and perspectives. *Int. J. Mass spectrom.* **2010,** *289* (2-3), 65-75.
164. Zoriy, M. V.; Kayser, M.; Becker, J. S., Possibility of nano-local element analysis by near-field laser ablation inductively coupled plasma mass spectrometry (LA-ICP-MS): New experimental arrangement and first application. *Int. J. Mass spectrom.* **2008,** *273* (3), 151-155.
165. Greving, M. P.; Patti, G. J.; Siuzdak, G., Nanostructure-Initiator Mass Spectrometry Metabolite Analysis and Imaging. *Anal. Chem.* **2010,** *83* (1), 2-7.
166. Northen, T. R.; Yanes, O.; Northen, M. T.; Marrinucci, D.; Uritboonthai, W.; Apon, J.; Golledge, S. L.; Nordstrom, A.; Siuzdak, G., Clathrate nanostructures for mass spectrometry. *Nature* **2007,** *449* (7165), 1033-1036.
167. Reindl, W.; Bowen, B. P.; Balamotis, M. A.; Green, J. E.; Northen, T. R., Multivariate analysis of a 3D mass spectral image for examining tissue heterogeneity. *Integr Biol* **2011,** *3* (4), 460-467.
168. Bandura, D. R.; Baranov, V. I.; Ornatsky, O. I.; Antonov, A.; Kinach, R.; Lou, X.; Pavlov, S.; Vorobiev, S.; Dick, J. E.; Tanner, S. D., Mass cytometry: Technique for real time single cell multitarget immunoassay based on inductively coupled plasma time-of-flight mass spectrometry. *Anal. Chem.* **2009,** *81* (16), 6813-6822.
169. Lin, Y.; Trouillon, R.; Safina, G.; Ewing, A. G., Chemical analysis of single cells. *Anal. Chem.* **2011,** *83* (12), 4369-4392.

170. Yamada, I.; Matsuo, J.; Toyoda, N.; Kirkpatrick, A., Materials processing by gas cluster ion beams. *Mater Sci Eng R Rep* **2001,** *34* (6), 231-295.
171. Sakai, Y.; Iijima, Y.; Mukou, S.; Hiraoka, K., Molecular depth profiling of polystyrene by electrospray droplet impact. *Surf. Interface Anal.* **2011,** *43* (1-2), 167-170.
172. Fernandez-Lima, F. A.; Post, J.; DeBord, J. D.; Eller, M. J.; Verkhoturov, S. V.; Della-Negra, S.; Woods, A. S.; Schweikert, E. A., Analysis of native biological surfaces using a 100 kV massive gold cluster source. *Anal. Chem.* **2011,** *83* (22), 8448-8453.
173. Ji, Q.; Chen, Y.; Ji, L.; Hahto, S.; Leung, K.-N.; Lee, T. G.; Moon, D. W., Development of C60 plasma ion source for time-of-flight secondary ion mass spectrometry applications. *Rev. Sci. Instrum.* **2008,** *79* (2), 02B309-02B309-4.
174. Yamada, H.; Nakata, Y.; Ninomiya, S.; Seki, T.; Aoki, T.; Tamura, J.; Matsuo, J., MeV-energy probe SIMS imaging of major components in washed and fractured animal cells. *Surf. Interface Anal.* **2011,** *43* (1-2), 363-366.
175. Yamada, H.; Ichiki, K.; Nakata, Y.; Ninomiya, S.; Seki, T.; Aoki, T.; Matsuo, J., MeV-energy probe SIMS imaging of major components in animal cells etched using large gas cluster ions. *Nucl Instrum Methods Phys Res B* **2010,** *268* (11-12), 1736-1740.
176. Nakata, Y.; Honda, Y.; Ninomiya, S.; Seki, T.; Aokic, T.; Matsuo, J., Matrix-free high-resolution imaging mass spectrometry with high-energy ion projectiles. *J. Mass Spectrom.* **2009,** *44* (1), 128-136.

FIGURES

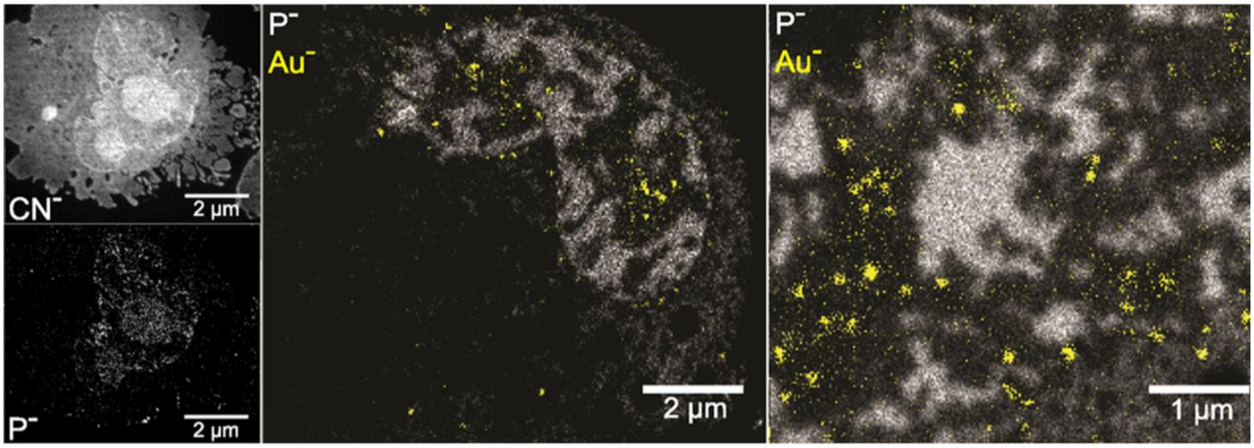

Figure 2.1: High resolution dynamic SIMS imaging reveals gold complex distribution within single human breast cancer cells. The CN^- ion (top left) reveals overall cellular structure while P^- (bottom left) shows nucleic acid distribution. In other cells after treatment with a gold-containing anticancer complex, superimposed Au^- and P^- images (center and right) indicate that the Au accumulates as ~200 nm aggregates in and around the nucleus, segregated clearly from the DNA. Adapted with permission from ref. [38], copyright 2011 The Royal Society of Chemistry.

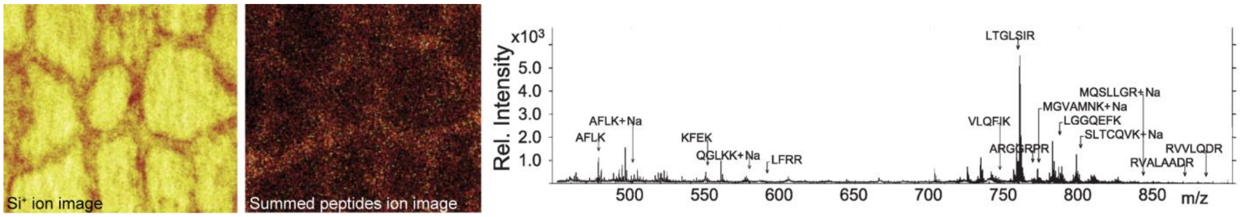

Figure 2.2: Static SIMS imaging of a large protein at cell-scale resolution. Thyroglobulin (660 kDa) in thyroid gland tissue is visualized using static matrix-enhanced SIMS after on-tissue trypsin digest. An Si^+ ion image (left) of sectioned tissue reveals cell morphology since removal of colloid within the cells exposes the underlying silicon substrate. Summed signals of the detected tryptic peptides generates an ion image (middle) indicating protein localization along the epithelial cell borders. A mass spectrum (right) from the tissue on the right shows labeled tryptic peptides in the *m/z* 450–900 range. Images are represented in false-color scale ranging from black (low signal) through red to yellow (high signal); field of view is 500 x 500 µm. Adapted with permission from ref. [87], copyright 2010, John Wiley and Sons.

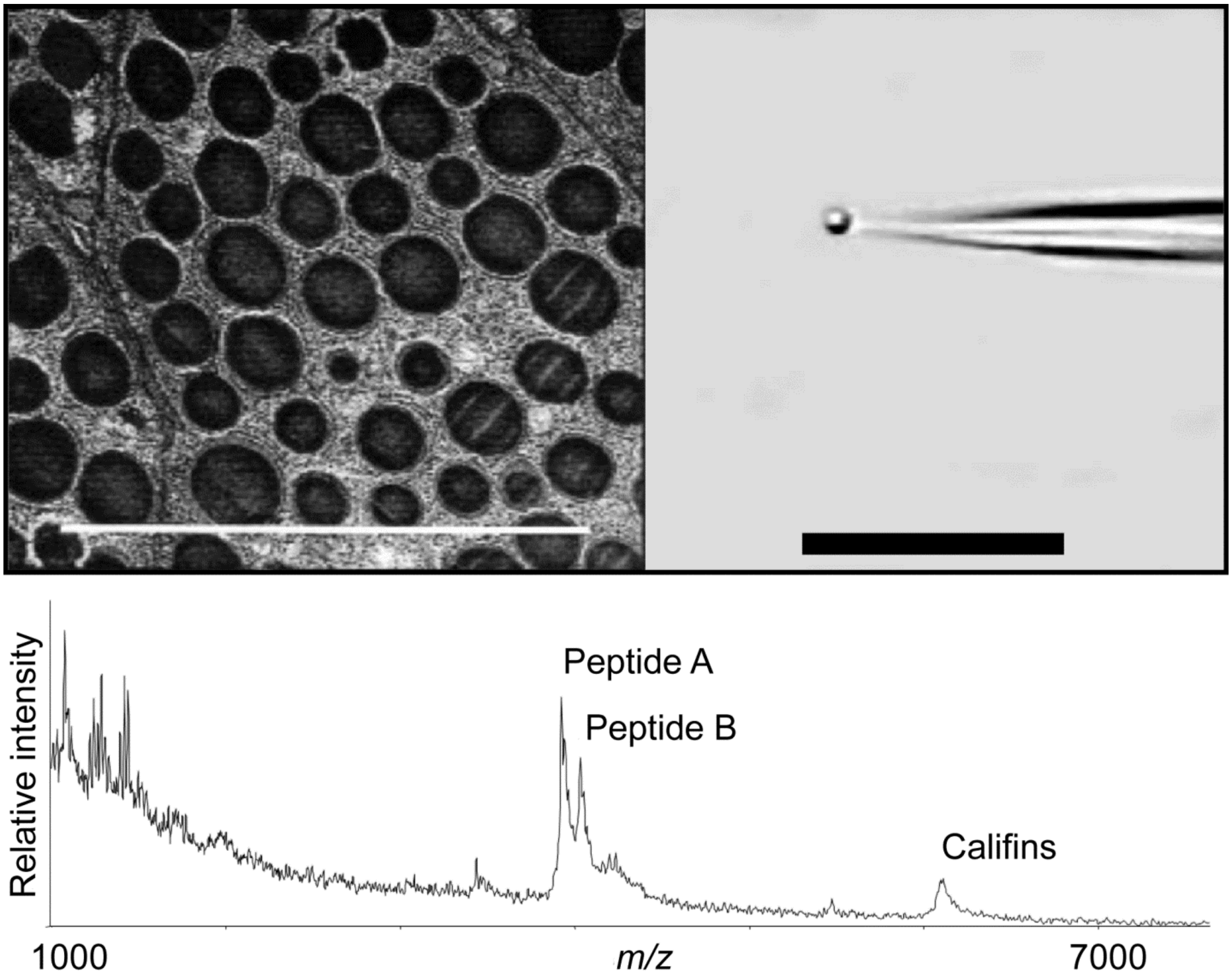

Figure 2.3: Single-organelle mass profiling with MALDI. Individual secretory granules from the *A. californica* atrial gland (left, TEM of tissue cross-section) are isolated manually using micropipette (right, video image) and prepared with matrix for MALDI-TOF analysis. Several peptides contained within the single granule are detected as shown in the mass spectrum (bottom). Scale bars are 10 µm. Adapted with permission from ref. [137], Macmillan Publishers Ltd: Nature Biotechnology, copyright 2000.

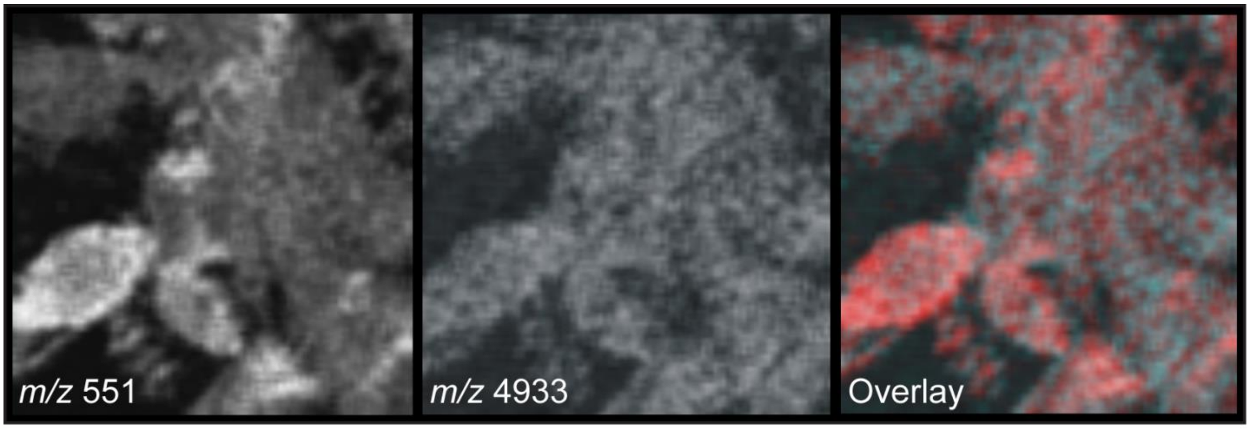

Figure 2.4: MALDI MSI at subcellular spatial resolution. MALDI analysis of cultured human renal cancer cells allows visualization of analytes across an extended *m/z* range relative to SIMS; vapor deposition of matrix permits 2 µm effective spatial resolution. Two ion images are overlaid (*m/z* 551 in red false color and *m/z* 4933 in greyscale) to reveal differences in the profiles of adjacent cells. Field of view shown is 100 x 100 µm. Adapted with permission from ref. [143], copyright 2010, John Wiley and Sons.

CHAPTER 3

BIOMOLECULAR IMAGING WITH C_{60}-SIMS: INSTRUMENTATION, MATRIX ENHANCEMENT, AND SINGLE CELL ANALYSIS

ACKNOWLEDGMENTS

This chapter is an adapted version of a completed manuscript written with coauthors S. J. B. Dunham, P. Nemes, S. S. Rubakhin, and J. V. Sweedler, submitted for publication on May 19, 2014, used here with permission from Springer, copyright 2014. P. Nemes contributed to initial instrument design, S. S. Rubakhin contributed to development of methods for cell isolation, culture, and preparation for SIMS imaging, and S. J. B. Dunham assisted with data acquisition. The work was supported by the Department of Energy Office of Biological and Environmental Research through grant DE SC0006642, and The National Resource for *Aplysia* funded by PHS grant P40 OD010952. The authors are very grateful for instrumental design and troubleshooting advice provided by Dr. Alexandre Loboda at AB SCIEX (presently at Fludigm Corporation) and support from the Winograd research group at Penn State University, Dr. Randall Pedder at Ardara Technologies, design suggestions by Dr. Zhen Li and Dr. Kevin Tucker, as well as precision machining by Michael Harland and Roger Smith at the Machine Shop of the School of Chemical Sciences at the University of Illinois at Urbana-Champaign. Cell dissection and culture assistance by Xiying Wang and Dr. Callie Croushore are also gratefully acknowledged.

INTRODUCTION

Mass spectrometry imaging (MSI) is a versatile analytical tool that enables multiplexed, non-targeted, and label-free molecular imaging of biological specimens.[1-3] MSI is commonly performed with a microprobe that is scanned across the surface of a sample to acquire mass spectra from multiple coordinates in a rectangular array; this data is then used to generate ion images in which each image pixel represents a position in the interrogated array, and the relative intensity of a selected ion is represented by the (false) color of each pixel.

Many microprobe types have now been developed for MSI, each offering unique advantages for particular studies. Focused laser beams are routinely used as microprobes in biological and biomedical tissue imaging experiments. Matrix-assisted laser desorption/ ionization (MALDI) mass spectrometry (MS) provides excellent detection limits, high spatial resolution (~50 µm typical), and an extended mass range—up to hundreds of kDa for MSI—allowing detection and imaging of protein distributions.[3-5] With advanced protocols in matrix deposition, MALDI also enables the measurement of peptides in single cells and organelles.[6-8] Nanostructure initiator MS, another laser microprobe-based approach, is capable of imaging with ~20 µm resolution for smaller biomolecules (*m/z* <1,500) in single cells, and can achieve yoctomole-range detection limits under ideal conditions.[9] Furthermore, the advent of ambient ion sources such as desorption electrospray ionization,[10-11] laser ablation electrospray ionization,[12-14] and liquid microjunctions,[15-16] have recently extended microprobe MSI to ordinary environmental conditions, enabling *in situ* analysis of biological samples, including live organisms.[16-19]

MSI with secondary ion mass spectrometry (SIMS)[20-21] is well-suited for single-cell and subcellular investigations. In state-of-the-art systems, SIMS utilizes ion microprobes that can be focused to submicron spots, achieving <100 nm lateral resolution,[22-23] currently unmatched by other MSI probe types. Ion probes also allow etching of sample surfaces with nanometer-scale precision, offering depth profiling and three-dimensional imaging with unsurpassed spatial resolution.[21, 24-25]

Innovations in instrumentation and methodology can further extend the imaging capability of SIMS to a broader range of biomolecules and biological specimens, especially if they meet several main challenges: improving molecular ionization efficiencies, providing softer ionization (reducing source fragmentation), reducing analyte suppression due to matrix effects,[26] and resolving isobaric compounds. Recently, identifications in biomolecular SIMS have greatly benefited from high mass resolution, mass accuracy, and tandem MS capabilities, enhancements that have been incorporated into several customized SIMS instruments reported recently.[27-29] Likewise, ion yields for intact molecules have been improved with the development of polyatomic or "cluster" primary ion sources such as Bi_3^+,[30] C_{60}^+,[31] and Ar_{2000}^+,[32] and signals can also be enhanced via laser post-ionization of sputtered neutrals,[33-34] gas cluster ion beam doping,[35] sample surface oxygen co-sputtering,[36] and chemical pretreatment of the sample with metal overlays[37-38] or organic matrixes (matrix-enhanced SIMS (ME-SIMS)).[39-42]

In addition to advances in instrumentation, new experimental protocols can further improve SIMS MSI. Interestingly, experimental methods that have been developed for "traditional" monatomic ion probes do not necessarily translate to cluster ion beams. For example, metal coatings enhanced the ionization of alkanes using Ga^+ and In^+ projectiles, but not with Bi_3^+ and C_{60}^+ probes.[43] Similar results were observed for C_{60}-SIMS of gold-coated peptides, other polymers, and small organic molecules.[44] On the other hand, 2,5-dihydroxybenzoic acid (DHB) matrix, mixed precisely in a 10:1 ratio with the peptide gramicidin S, yielded eightfold molecular ion signal enhancement when profiled by C_{60}-SIMS,[45] and signal enhancement was reported for intact lipids in brain tissue when coated with DHB in conjunction with a Bi_3^+ probe,[46] though these studies did not extend the work to ME-SIMS imaging. Thus, a targeted combination of instrumentation and methodology offers the potential to further aid biomolecular investigations using SIMS imaging.

Here we describe a new hybrid MALDI/C_{60}-SIMS quadrupole time-of-flight (Q-TOF) mass spectrometer and accompanying sample preparation methodologies to enable cell-scale molecular imaging, with a focus on a C_{60}-SIMS operation mode. We utilized the combined features of this customized instrument—high mass resolution, tandem MS, and a cluster primary ion for softer secondary ion generation—to extract molecular information from chemically and structurally complex biological samples generating high quality low-mass SIMS spectra. We demonstrated the imaging capabilities of the instrument using mammalian spinal cord samples and networks of cultured neurons from *Aplysia californica*. We also investigated the feasibility of matrix sublimation for ME-C_{60}-SIMS imaging of biological tissues, demonstrating that the signal intensity of intact lipid ions from spinal cord can be enhanced significantly with this treatment.

EXPERIMENTAL

Hybrid MALDI/C_{60}-SIMS Instrument Design

A commercial Q-TOF mass spectrometer (QSTAR XL, AB SCIEX, Framingham, MA, USA) was modified to construct the MALDI/SIMS hybrid mass spectrometer, based conceptually on previous work from the Winograd laboratory,[27] but with the addition of several features designed to optimize performance for our samples. The standard instrument configuration featured an ultraviolet (UV) MALDI source (oMALDI 2) equipped with an *x/y* translation stage and a camera for optical inspection of the sample, as well as a data acquisition/analysis software package (oMALDI Server v5.1 and Analyst v1.2, AB SCIEX). The QSTAR provides tandem

MS capability *via* collision-induced dissociation (CID) and high mass resolution (>10,000 FWHM).

The original MALDI source enclosure was precision-milled to accommodate a 20 kV C_{60} ion gun (Ionoptika, Manchester, UK) with an ~1 µm ultimate ion probe diameter, while preserving MALDI functionality. A partial schematic of the hybrid instrument is shown in **Figure 3.1a**, and the modifications are described as follows. The ion gun was supplemented with a differentially pumped and enclosed beam column designed for operation at intermediate vacuum (<10 mTorr), and positioned at a 30° incidence angle relative to the surface normal. The end of the ion gun was fitted with a custom-designed electrically floating tip to improve sampling efficiency, and a blanking circuit was constructed using a pulse generator (Model 4001, Global Specialties Instruments, Yorba Linda, CA, USA) to control the ion beam using the transistor-transistor logic (or TTL) signal that ordinarily triggers the nitrogen laser of the MALDI source. The original vacuum chamber of the QSTAR was extended with a set of two vacuum adapter blocks bridged with a flange adapter to fit and mechanically support the ion gun.

Secondary ions generated by C_{60}-SIMS and the primary ions generated by MALDI were extracted into the ion guide Q_0 of the QSTAR using an additional ion guide. A custom-designed rectilinear quadrupole (RLQ) ion guide (Ardara Technologies, Ardara, PA, USA) was installed between the sample plate and the front end of the Q_0, without any modification to the latter. The RLQ had an 8-mm inscribed diameter and 4.7 mm square rod electrodes, and was driven by a 2.8 MHz radiofrequency (RF) and DC power supplies (Ardara Technologies). The RLQ was further modified with removable front segments (shown in **Figure 3.2**) to facilitate frequent cleaning, ensuring robust performance. The adapter blocks incorporated vacuum gauge sensors and an additional turbomolecular pump that provided high vacuum (< 0.1 mTorr) in the source chamber, while electrical and gas feed-through ports for the RLQ were located on the flange adapter. The adapter blocks were designed in-lab by computer-aided design freeware (DraftSight v1, Dassault Systémes, Vélizy-Villacoublay, France) and precision milled from 6061 aluminum, and the flange adapter was designed and provided by Ardara Technologies. Adapter blocks were sealed with aluminum Conflat flanges (note that for this application, soft aluminum gaskets must be used in place of standard copper gaskets). Operational settings for the hybrid instrument in the positive ion mode for both MALDI and SIMS were optimized as follows: sample plate/orifice

+34 V, C_{60} tip +30 V, RLQ +24 V DC offset with 1100 V RF p-p amplitude, and Q_0 +20 V with 8 mTorr collisional focusing gas pressure.

Materials and Chemicals

HPLC-grade methanol and acetonitrile, glycerol, formic acid (~98%), renin substrate (porcine, >97%), poly(propylene glycol) standards (M_n ~425, 1,000, and 2,000), DHB (98%), methionine, and α-cyano-4-hydroxycinnamic acid 98% (CHCA) were purchased from Sigma-Aldrich (St. Louis, MO, USA); ammonium acetate (98%) was from Fisher Scientific (Waltham, MA, USA). Copper mesh grids were obtained from Ted Pella, Inc. (Redding, CA, USA). For cell culture and tissue section substrates, 4-in diameter circular wafers of silicon (100) (Silicon, Inc., Boise, ID) were scored and snapped to create tiles 1 × 1 cm^2 in area. To estimate the C_{60} beam sample currents that are reported here, a Faraday cup was improvised by drilling a 2 mm-diameter hole in the center of a standard 100-well stainless steel MALDI target (AB SCIEX). The sample plate was disconnected from the accelerating voltage and connected to a picoammeter *via* a shielded coaxial cable for measurements.

Biological Specimens

Adult male Long-Evans rats (Harlan, Indianapolis, IN, USA) were used for the vertebrate animal experiments. After rapid decapitation and dissection, intact spinal cord tissue was isolated and then frozen promptly in aluminum foil on dry ice and stored in a sealed bag at –80 ºC until use. Spinal cord sections, 12-µm-thick, were collected on a cryotome (3050S, Leica Biosystems, Germany) and thaw-mounted to clean silicon tiles, then warmed to room temperature (22–25 ºC) in a nitrogen-purged dry box prior to matrix application and/or direct analysis. Animal care protocols and procedures were approved by the UIUC Laboratory Animal Care Advisory Committee and fully comply with federal guidelines for the humane care and treatment of animals.

Aplysia californica (Mollusca, Gastropoda) were obtained from the University of Miami/NIH National Resource for *Aplysia* (Miami, FL, USA) and kept alive in an aquarium filled with chilled, circulated, and aerated sea water at –14 °C until used. Sea water was prepared in the lab using a synthetic sea salt mix (Instant Ocean, Aquarium Systems Inc., USA).

Prior to dissection, animals were anesthetized by injection of isotonic $MgCl_2$ (30–50% of body weight) into the body cavity, individual neurons were isolated from the buccal, abdominal, pleural and pedal ganglia of the molluscan central nervous system. These neurons were cultured on silicon tiles in plastic Petri dishes according to a procedure that we have established previously.[47] Cultures were allowed to develop for 24 h at room temperature, then prepared for MSI by either freeze drying or glycerol stabilization followed by rinsing, as described below.

For freeze drying, the culturing media was first substituted stepwise with 150 mM ammonium acetate (pH 7) in deionized (DI) water (Milli-Q filtration system; Millipore, Billerica, MA, USA) to remove inorganic salts from the extracellular environment. Most of this solution was then removed, leaving cells submerged in a minimal volume, and the Petri dish was then rapidly cooled by partial immersion in liquid nitrogen. Once the culturing solution was completely frozen, the Petri dish was transferred to a vacuum chamber and allowed to freeze-dry overnight. Cells were then rinsed by dipping the entire silicon substrate vertically into DI water for 1 s, followed by rapid drying with a stream of dry nitrogen gas, repeated in triplicate. The morphology of most cells was maintained throughout this procedure.

For glycerol stabilization, the culture media was substituted stepwise with mixture of 33% glycerol and 67% artificial seawater (v/v), and then decanted in ~1 s. The tiles were stored vertically overnight at ambient conditions, allowing excess solution to drain and evaporate. Stabilized cells were then rinsed by either rapid dips in DI water as described above, or by carefully applying microdroplets of DI water onto individual cells and then promptly aspirating the water using a micropipette tip. The latter technique was preferred as it generally resulted in less cell lysis and/or loss of neurites, and was used for the cells depicted in the optical and molecular images presented here.

Matrix Sublimation

The sublimation chamber apparatus and procedure were adapted from previous work described elsewhere.[48] The chamber was modified with a $25 \times 75\ \text{mm}^2$ aluminum foil boat affixed to the inner base surface with double-sided conductive copper tape as well as a $25 \times 75 \times 1\ \text{mm}^3$ thick stainless steel plate similarly affixed to the bottom face of the cold finger to improve thermal conductivity to the sample; the boat-to-plate distance was 20 mm. For each sublimation procedure, 350 mg of powdered DHB was added to the aluminum foil boat and distributed evenly. Samples on silicon tiles were first weighed on an ultra-microbalance (Cubis, Sartorius, Bohemia, NY, USA), then affixed to the stainless steel plate with conductive copper tape. The chamber was closed, placed in a heating mantle, pumped to intermediate vacuum (~10 mTorr), and the cold finger was then filled with iced water (~4 °C). After 5 min of temperature equilibration, the desired matrix coating was achieved by supplying 120 V to a heating mantle for 240–285 s. The chamber was then removed from the mantle, vented to room temperature air, and the sample promptly removed from the cold finger. The sample was weighed again to determine the amount of matrix applied (density estimated as total applied matrix mass/silicon tile area) before SIMS analysis.

SIMS Imaging Experiments

All SIMS MSI experiments were performed on the customized hybrid instrument described above. For the matrix enhancement experiments with spinal cord sections, the SIMS images were acquired in raster imaging mode with the following settings: 50 × 50 μm^2 step size, 60–850 atomic mass unit (AMU) detection mass window, 0.25 s/pixel dwell time, default TOF settings, and Q_1 ion guide transmission biased for intact lipids (10/20/70% at 70/200/400 AMU, respectively). The MALDI spine images were acquired with the laser set to 40 Hz at 60% relative power and a 100 × 100 μm^2 step size with otherwise identical parameters; smaller step sizes were found to generate lower quality images due to severe oversampling. Ion distribution images for the matrix enhancement experiments were acquired from consecutive tissue sections taken from a single spinal cord specimen and imaged in successive sessions in order to minimize systematic errors; n = 6 for untreated and 0.115 mg/cm^2-coated sections, and n = 5 for 0.016 and 0.181 mg/cm^2-coated sections. The C_{60}^+ probe was focused to a 40-µm diameter and produced 190 pA sample current. Mass calibration was performed for $In_{1\text{-}7}^+$ ions.

For the cell imaging experiments, the C_{60}^+ probe current was reduced to 50 pA with an ~15-µm diameter, and SIMS images were acquired by rastering the sample at a 10 × 10 μm^2 step size. Acquisition parameters were a 60–450 AMU detection window, 1 s/pixel dwell time, Q_1 biased to higher mass transmission (10/40/50% at 50/100/200 AMU respectively), and default TOF settings. Mass calibration was performed using $In_{1\text{-}7}^+$ ions, or Cu^+ and In^+ ions for the small metabolite tandem MS experiments. Imaging data was converted from the wiff to img format at 20 bins/AMU and imported to BioMap (Novartis, Switzerland) for further processing. Mass filters were ± 0.05 AMU and ion images were represented in false color, with black corresponding to zero and red to maximum signal intensity. Tandem MS experiments were performed in SIMS mode with 10–30 eV CID in argon collision gas.

RESULTS AND DISCUSSION

Characterization of the Hybrid Mass Spectrometer

Initially, the analytical performance of the hybrid mass spectrometer was systematically evaluated; ionization efficiency, mass resolution, capability for tandem MS, and spatial resolution were assessed for the MALDI-MS and C_{60}-SIMS operational modes. Since the original QSTAR ion path was left virtually unmodified beyond the source, downstream electrode settings required no optimization when switching between the two modes. The RF-only RLQ was used as an ion guide through the vacuum chamber adapter because RLQ guides provide a broad mass transmission window,[49] obviating the need to ramp RF amplitude synchronously with the subsequent Q_0 ion guide. The performance of the RLQ is characterized by the mass transmission profiles shown in **Figure 3.1b**, acquired by varying the RF voltage while measuring the ion signal for ions generated from a poly(propylene glycol) standard with a continuously-rastered laser probe. Transmission of larger ions (1–2 kDa) was greatest at the maximum accessible RF amplitude, 1,100 V peak-to-peak ($V_{p\text{-}p}$), which still provided efficient (>90% relative) transmission for the smaller ions. Thus the guide was operated at this fixed RF amplitude and 2.8 MHz frequency for all further experiments.

A differentially pumped interface was designed to suit different vacuum requirements that were imposed by the C_{60}^+ gun and the mass spectrometer. The commercial QSTAR originally operated with a low vacuum (1 Torr) MALDI source chamber to collisionally cool ions, and medium vacuum (~10 mTorr) in the ion guide Q_0 to collisionally focus them for transmission to the analyzer.[50] However, SIMS is incompatible with low and medium vacuum as the primary ion beam is defocused by collisions with gas.[27] At 10 mTorr, the mean free path of a C_{60}^+ ion is ~1 mm; thus, few intact projectiles reach the sample from a practical (>5 mm) working distance. To resolve this conflict, the adapter block was differentially pumped to maintain the sample chamber at high vacuum while collisional focusing was accomplished downstream with ~10 mTorr in the back half of the RLQ and throughout Q_0. Operation with intermediate source pressure (1–10 mTorr) was found to have no effect on C_{60}-SIMS performance until ~5 mTorr (data not shown), beyond which the ion signal intensity decreased, likely as a result of beam destruction.[27] To evaluate the effective spatial resolution in the SIMS mode, a copper mesh grid was imaged at a 10-µm step size, the highest spatial resolution offered by the MALDI sample stage. The reconstructed Cu^+ ion map showed a matching 10 µm effective lateral spatial resolution (**Figure 3.2**). The ion gun is capable of smaller (~1 µm ultimate diameter) probe dimensions, so we are currently implementing synchronized beam control using built-in raster plates to improve the lateral resolution by approximately an order of magnitude. A high mass resolution, >13,000 by FWHM, is also demonstrated on the adapted system with MALDI-MS analysis of renin substrate tetradecapeptide standard (shown in **Figure 3.2**).

The hybrid mass spectrometer provided complementary performance in C_{60}-SIMS and MALDI MSI modes. As the laser optics on the oMALDI source were unaffected by the instrumental modifications undertaken here, an ~100 × 200 μm^2 laser microprobe area was obtainable as on the original instrument. To evaluate the complementarity of SIMS and MALDI MSI by this hybrid instrument, tissue sections of rat spinal cord were imaged in each mode with DHB sublimed on the sample for MALDI MSI. The results are compared in **Figure 3.3**. The MS lipid profile spectra from the tissue gray matter show that MALDI generated a several times higher ion abundance for intact lipid ions (pseudomolecular and salt adduct) over SIMS for a comparable analysis area. The smaller probe size of SIMS enabled imaging with higher spatial resolution, improving the definition of small anatomical features such as the central canal and dorsal horns, which both show as intense localizations of PC(32:0), *m/z* 772. Also notable is that MALDI generated relatively fewer lipid fragments at *m/z* 713, 723, and 739, corresponding to the loss of trimethylamine observed in earlier investigations on mouse brain using a similar C_{60}-SIMS system.[51]

Imaging of Single Cells and Neuronal Networks

The hybrid mass spectrometer was utilized to uncover chemical differences between the soma and processes of individual neurons cultured from *A. californica*. Buccal neurons were placed on a silicon substrate in culturing solution for 1–2 days, where they formed processes (shown in **Figure 3.4**). Each step of the sample preparation workflow was judiciously assessed to ensure minimal chemical changes and avoid potential morphological alterations to the neurons before removing them from the culture solution and introducing the samples into vacuum for C_{60}-SIMS imaging. We previously found that fixation with formaldehyde and paraformaldehyde preserved cell morphology for SIMS imaging.[52] However, because this treatment chemically modifies the specimen, we explored alternative treatment options. Glycerol cell stabilization[6] has been used successfully and has also been found to preserve cell function[53] We also tried freeze drying, common to the typical SIMS workflow,[54-55] in an effort to avoid chemical modification of analytes. While freeze drying preserved cell somas, it destroyed their processes (data not shown), whereas the glycerol treatment preserved both. As alternatives, cryogenic techniques, such as frozen hydration[56] and critical-point drying,[57] may also preserve the fragile cell outgrowth. Here, glycerol stabilization was found to yield robust results, and was therefore adopted to prepare the cultured neurons for MSI.

C_{60}-SIMS imaging produced characteristic ion images of the distribution of several biomolecules in the cultured neurons. SIMS-generated ions were identified based on mass measurements and fragmentation behavior under CID. Representative identifications are presented for phosphocholine and α-tocopherol **Figure 3.5.** The tandem mass spectra recorded on these ions matched well with those published in the METLIN mass spectrometric metabolite database.[58] Phosphocholine was detected at *m/z* 184.08 as a fragment from the phospholipid head group of lipids, in agreement with other studies using SIMS.[47, 52, 59] This signal was particularly useful in highlighting localization of the cell membrane in our C_{60}-SIMS images. The ion of α-tocopherol, one form of vitamin E, was observed as $M^{\bullet+}$ at *m/z* 430.38. This membrane-localized, multi-functional nutrient fulfills roles in oxygen radical scavenging as well as modulation of signal transmission and gene expression,[60] thus it is an analyte of particular interest in this work. The C_{60}-SIMS ion images of phosphocholine and α-tocopherol were acquired from two cultured and glycerol-stabilized neurons (Figure 3). Neural processes are readily visible in the phosphocholine ion image, whereas α-tocopherol accumulated at the soma-neurite junctions. We previously reported comparable subcellular localization of α-tocopherol in similar *A. californica* neurons using a commercial TOF-SIMS instrument that was equipped with a Au^+ ion probe.[47] These combined results demonstrate that the hybrid mass spectrometer provides biomolecular images with high spatial resolution, serving as a powerful bioanalytical platform to help decipher the molecular architecture of single cells.

Attaining high mass resolution, the hybrid mass spectrometer resolved multiple isobaric ions by their nominal molecular mass throughout the *m/z* 100–300 range. Images often revealed different spatial distributions for these ion sets for *m/z* 103.98, 104.05, and 104.11, as shown in **Figure 3.4**. This observation highlights the importance of the high mass resolution SIMS provides and also suggests that some of these ions may correspond to biomolecules rather than nonspecific organic fragments. Moreover, useful biological information might be gleaned from them, provided they can be confidently identified. That task is made challenging by several factors: many metabolites will match a given nominal mass, some may be structural isomers, i.e., share an exact mass, and spectral complexity in this range will also be increased by fragments generated from larger biomolecules during the SIMS sputtering process. Approaches that offer high mass resolution, mass accuracy, and tandem MS capability, used in combination with a well-characterized biological model and existing metabolite databases such as METLIN,[58] have become valuable and provide a useful starting point for SIMS ion identification.[61]

We further stress the importance of distinguishing isobaric ions in high-fidelity SIMS imaging data to aid in bioanalytical discovery. This point is demonstrated for three isobars detected at a nominal mass of *m/z* 104. As the ion map at *m/z* 103.98 homogeneously distributed the entire sample area (**Figure 3.4**) and did not match any metabolites in METLIN, this signal was assigned as background and disregarded in further analysis. The other isobars at 104.11 and 104.05 exhibited characteristic images that correlated with the neuron structure, suggesting that they may be biologically relevant. An accurate-mass search in METLIN resulted in three possible metabolites for 104.11 Da with 10 mDa accuracy: choline, neurine, and valinol (2-amino-3-methyl-1-butanol). Likewise, seven matches were found as potential intact biomolecules for 104.05 Da, though none of these compounds seemed biologically feasible given the existing knowledge on *A. californica* neurons. Thus, we propose that this ion may instead be an organic fragment produced during sputtering. In agreement, this mass was recently assigned as a unique methionine fragment amongst 20 common metabolites identified by C_{60}-SIMS tandem MS.[61] To confirm these assignments, tandem MS was performed on the cultured neurons, with the resulting spectrum shown in **Figure 3.6**. Importantly, these experiments were conducted in SIMS mode since MALDI may generate different ions, and also because the addition of a matrix would complicate the low mass spectrum with additional matrix-related cluster, adduct, and fragment ions.

The tandem MS capability of the hybrid instrument facilitated the identification of ions. As the isobars at *m/z* 104 could not be isolated individually, the tandem MS spectrum on this mass represented a convolution of fragments from the three precursors. The abundant fragments observed at *m/z* 45.03, 58.07, and 60.08 closely match the tandem MS spectrum of choline reported in METLIN, supporting this assignment. Choline is also biologically the most likely of the three candidate compounds matching *m/z* 104.11 to be present in the cells as a metabolite or generated as a membrane lipid fragment. On the other hand, the expected smaller fragments of methionine—*m/z* 61.01 and 56.05—were not present. Furthermore, C_{60}-SIMS analysis of methionine standard yielded the MH^+ ion at *m/z* 150.05, along with multiple characteristic fragments including *m/z* 104.06, 61.01, and 56.05 (see **Figure 3.7**). Isolation and tandem MS of the *m/z* 104.06 fragment itself—essentially a pseudo MS^3 experiment in which SIMS source fragmentation provides MS^2—also yielded the expected smaller fragments at *m/z* 61.01 and 56.05 from the standard. The absence of these fragments in the tandem MS spectrum of *m/z* 104 acquired from the cells indicates that this ion was either not a methionine fragment, or that the abundance was too low to generate detectable fragments during pseudo-MS^3. Fragments observed at *m/z* 77.04 and 78.05 could not be assigned to either choline or the methionine fragment; these may be fragments of the third precursor ion *m/z* 103.98, which is likely an inorganic cluster ion based on elemental permutation calculations, and may originate from the cell culture solution (artificial seawater containing numerous inorganic salts). While the analysis of these ions did not yield complete identification here, it demonstrates how high mass resolution and tandem MS capability may be combined with existing databases to decipher convoluted chemical images.

The C_{60}-SIMS instrument offers an opportunity to evaluate cultured neural networks. When cultured in close proximity, *A. californica* neurons reconnect with processes to form a neural network, and by co-culturing specific cells such as sensory and motor neurons, simple neural circuits can be assembled and studied as a model of fundamental nervous system function.[62] Towards this goal, we cultured neural networks and imaged them using the C_{60}-SIMS modality of the platform, with results shown in **Figure 3.8**. The optical image revealed extensive neurite outgrowth, including visible intercellular connections between the neurons, and these connections were resolved in the SIMS ion images as well. Phosphocholine and choline were detected throughout the network, corresponding to the exposed cell membranes. In contrast, α-tocopherol accumulated at the cell somata at specific subcellular locations, in general agreement with recent SIMS data.[63] While additional work, including image normalization, is necessary to establish the biological significance of the molecular distributions observed here (*e.g.*, discern actual subcellular distributions from artifactual signal bias), these results demonstrate the capability of our new instrumentation, combined with existing biological knowledge, to interrogate the chemical nature of cultured neural networks.

ME-SIMS of Biological Tissue

To evaluate matrix-enhancement for C_{60}-SIMS imaging, DHB was applied *via* sublimation to mammalian spinal cord tissue sections. The spinal cord was selected as a specimen for this study since it has been well-characterized in previous MSI studies,[59, 64] has a distinctive anatomy consisting primarily of central gray matter mostly containing cell bodies and peripheral white matter populated with myelinated axons, and has a similar chemical composition axially, which allows comparisons between consecutive tissue sections. Vacuum sublimation was chosen for matrix deposition as this dry process avoids lateral analyte delocalization and also generates small crystals that do not preclude micron-scale lateral resolution.[48] The applied matrix amount was controlled by sublimation time and quantified as matrix density on the surface following an approach that was established elsewhere.[65] Three matrix densities were evaluated by C_{60}-SIMS imaging along with untreated sections. The overall results are shown in **Figure 3.9**.

Statistically significant enhancement of intact lipid signal amplitudes was achieved with a 0.12 mg/cm^2 sublimed matrix coating ($p < 0.05$ by one-tailed, heteroscedastic student's t-test), yielding an approximately threefold increase in signal for intact lipid ions such as $[M + K]^+$ ions of PC(32:0) and PC(34:1), shown here (**Figure 3.9**). The phosphocholine fragment appeared suppressed with all of the tested matrix treatments, possibly indicating reduced fragmentation of lipids by the primary beam in the presence of matrix. Heavier and lighter matrix coats (0.18 mg/cm^2 and 0.02 mg/cm^2, respectively) resulted in reduced signal relative to uncoated sections. The observation that this treatment appeared to enhance non-protonated molecular lipid ions suggests that signal enhancement in this case may come primarily from concentration of analytes at the sample surface rather than by proton donation in solid or gas phases. Although sublimation is a dry matrix application method, which is not expected to solvate analytes from a tissue section, some analyte migration may nevertheless occur, enabled by residual tissue moisture and/or brief water condensation on the sample prior to removal from the sublimation cold finger, similar to recrystallization steps employed elsewhere.[65] While the details of this enhancement mechanism are the subject of ongoing investigation, these results indicate that the combination of a C_{60} ion probe and matrix application provides significant signal enhancement.

CONCLUSIONS

The design details and performance characteristics of a hybrid MALDI/C_{60}-SIMS Q-TOF mass spectrometer have been presented, along with data demonstrating C_{60}-SIMS tissue and cell imaging capabilities of the new instrument, used specifically for investigating the chemical composition of cultured neurons and model neuronal networks. We have demonstrated how ambiguous small ions may be characterized by taking advantage of the high mass resolution (13,000 by FWHM) and tandem MS capabilities in conjunction with existing knowledge of the biological model and online MS databases. The compatibility of sublimed-matrix enhancement with a C_{60} microprobe was also demonstrated with *ca.* threefold signal enhancement for pseudomolecular lipid ions in mammalian nervous tissue.

Continuing work is focused on expanding the chemical information obtainable from single neurons and cultured neural networks via application of matrix-enhancement, dual SIMS imaging/MALDI profiling analysis, and tandem MS characterization of endogenous metabolites to discern them from nonspecific chemical background. Imaging spatial resolution will also be increased to the ion gun focus limit (~1 µm) by integrating precise electronic control of microprobe and/or sample position, and a secondary electron detector will be added for electron microscope functionality.

REFERENCES

1. Rubakhin, S.; Sweedler, J., A Mass Spectrometry Primer for Mass Spectrometry Imaging. In *Mass Spectrometry Imaging*, Rubakhin, S. S.; Sweedler, J. V., Eds. Humana Press: 2010; Vol. 656, pp 21-49.
2. Setou, M., *Imaging mass spectrometry: protocols for mass microscopy*. Springer: Tokyo, 2010.
3. Chughtai, K.; Heeren, R. M. A., Mass Spectrometric Imaging for Biomedical Tissue Analysis. *Chem. Rev.* **2010,** *110*, 3237-3277.
4. Schwamborn, K.; Caprioli, R. M., INNOVATION Molecular imaging by mass spectrometry - looking beyond classical histology. *Nat. Rev. Cancer* **2010,** *10* (9), 639-646.
5. Cornett, D. S.; Reyzer, M. L.; Chaurand, P.; Caprioli, R. M., MALDI imaging mass spectrometry: molecular snapshots of biochemical systems. *Nat. Methods* **2007,** *4* (10), 828-833.
6. Rubakhin, S. S.; Greenough, W. T.; Sweedler, J. V., Spatial Profiling with MALDI MS: Distribution of Neuropeptides within Single Neurons. *Anal. Chem.* **2003,** *75* (20), 5374-5380.
7. Rubakhin, S. S.; Garden, R. W.; Fuller, R. R.; Sweedler, J. V., Measuring the peptides in individual organelles with mass spectrometry. *Nat. Biotechnol.* **2000,** *18* (2), 172-175.
8. Rubakhin, S. S.; Sweedler, J. V., Quantitative Measurements of Cell−Cell Signaling Peptides with Single-Cell MALDI MS. *Anal. Chem.* **2008,** *80* (18), 7128-7136.
9. Greving, M. P.; Patti, G. J.; Siuzdak, G., Nanostructure-Initiator Mass Spectrometry Metabolite Analysis and Imaging. *Anal. Chem.* **2011,** *83* (1), 2-7.
10. Eberlin, L. S.; Ferreira, C. R.; Dill, A. L.; Ifa, D. R.; Cooks, R. G., Desorption electrospray ionization mass spectrometry for lipid characterization and biological tissue imaging. *Biochim. Biophys. Acta* **2011,** *1811* (11), 946-960.
11. Eberlin, L. S.; Ifa, D. R.; Wu, C.; Cooks, R. G., Three-Dimensional Vizualization of Mouse Brain by Lipid Analysis Using Ambient Ionization Mass Spectrometry. *Angew. Chem.-Int. Edit.* **2010,** *49* (5), 873-876.
12. Nemes, P.; Woods, A. S.; Vertes, A., Simultaneous Imaging of Small Metabolites and Lipids in Rat Brain Tissues at Atmospheric Pressure by Laser Ablation Electrospray Ionization Mass Spectrometry. *Anal. Chem.* **2010,** *82* (3), 982-988.
13. Nemes, P.; Barton, A. A.; Vertes, A., Three-Dimensional Imaging of Metabolites in Tissues under Ambient Conditions by Laser Ablation Electrospray Ionization Mass Spectrometry. *Anal. Chem.* **2009,** *81* (16), 6668-6675.
14. Shrestha, B.; Patt, J. M.; Vertes, A., In Situ Cell-by-Cell Imaging and Analysis of Small Cell Populations by Mass Spectrometry. *Anal. Chem.* **2011,** *83* (8), 2947-2955.
15. Laskin, J.; Heath, B. S.; Roach, P. J.; Cazares, L.; Semmes, O. J., Tissue Imaging Using Nanospray Desorption Electrospray Ionization Mass Spectrometry. *Anal. Chem.* **2011,** *84* (1), 141-148.
16. Watrous, J.; Roach, P.; Heath, B.; Alexandrov, T.; Laskin, J.; Dorrestein, P. C., Metabolic Profiling Directly from the Petri Dish Using Nanospray Desorption Electrospray Ionization Imaging Mass Spectrometry. *Anal. Chem.* **2013,** *85* (21), 10385-10391.
17. Nemes, P.; Vertes, A., Ambient mass spectrometry for in vivo local analysis and in situ molecular tissue imaging. *Trac-Trends Anal. Chem.* **2012,** *34*, 22-34.
18. Harris, G. A.; Galhena, A. S.; Fernandez, F. M., Ambient Sampling/Ionization Mass Spectrometry: Applications and Current Trends. *Anal. Chem.* **2011,** *83* (12), 4508-4538.
19. Ifa, D. R.; Wu, C. P.; Ouyang, Z.; Cooks, R. G., Desorption electrospray ionization and other ambient ionization methods: current progress and preview. *Analyst* **2010,** *135* (4), 669-681.
20. Boxer, S. G.; Kraft, M. L.; Weber, P. K., Advances in Imaging Secondary Ion Mass Spectrometry for Biological Samples. *Annu. Rev. Biophys.* **2009,** *38* (1), 53-74.
21. Lanni, E. J.; Rubakhin, S. S.; Sweedler, J. V., Mass spectrometry imaging and profiling of single cells. *J. Proteomics* **2012,** *75* (16), 5036-5051.
22. CAMECA NanoSIMS 50/50L. SIMS Microprobe for Ultra Fine Feature Analysis. http://www.cameca.fr/instruments-for-research/nanosims.aspx (accessed 4/3/2014).
23. Kollmer, F.; Paul, W.; Krehl, M.; Niehuis, E., Ultra high spatial resolution SIMS with cluster ions — approaching the physical limits. *Surf. Interface Anal.* **2012,** *45* (1), 312-314.
24. Fletcher, J. S.; Lockyer, N. P.; Vaidyanathan, S.; Vickerman, J. C., TOF-SIMS 3D Biomolecular Imaging of Xenopus laevis Oocytes Using Buckminsterfullerene (C60) Primary Ions. *Anal. Chem.* **2007,** *29*, 2199-2206.

25. Fletcher, J. S.; Vickerman, J. C.; Winograd, N., Label free biochemical 2D and 3D imaging using secondary ion mass spectrometry. *Curr. Opin. Chem. Biol.* **2011,** *15* (5), 733-740.

26. Jones, E.; Lockyer, N.; Kordys, J.; Vickerman, J., Suppression and enhancement of secondary ion formation due to the chemical environment in static-secondary ion mass spectrometry. *J. Am. Soc. Mass Spectrom.* **2007,** *18* (8), 1559-1567.

27. Carado, A.; Passarelli, M. K.; Kozole, J.; Wingate, J. E.; Winograd, N.; Loboda, A. V., C60 Secondary Ion Mass Spectrometry with a Hybrid-Quadrupole Orthogonal Time-of-Flight Mass Spectrometer. *Anal. Chem.* **2008,** *80* (21), 7921-7929.

28. Smith, D. F.; Robinson, E. W.; Tolmachev, A. V.; Heeren, R. M. A.; Paša-Tolić, L., C60 Secondary Ion Fourier Transform Ion Cyclotron Resonance Mass Spectrometry. *Anal. Chem.* **2011,** *83* (24), 9552-9557.

29. Fletcher, J. S.; Rabbani, S.; Henderson, A.; Blenkinsopp, P.; Thompson, S. P.; Lockyer, N. P.; Vickerman, J. C., A New Dynamic in Mass Spectral Imaging of Single Biological Cells. *Anal. Chem.* **2008,** *80*, 9058-9064.

30. Kollmer, F., Cluster primary ion bombardment of organic materials. *Appl. Surf. Sci.* **2004,** *231-232*, 153-158.

31. Boussofiane-Baudin, K.; Bolbach, G.; Brunelle, A.; Della-Negra, S.; Håkansson, P.; Le Beyec, Y., Secondary ion emission under cluster impact at low energies (5–60 keV); influence of the number of atoms in the projectile. *Nucl. Instr. Meth. Phys. Res. B* **1994,** *88* (1–2), 160-163.

32. Matsuo, J.; Okubo, C.; Seki, T.; Aoki, T.; Toyoda, N.; Yamada, I., A new secondary ion mass spectrometry (SIMS) system with high-intensity cluster ion source. *Nucl. Instr. Meth. Phys. Res. B* **2004,** *219–220* (0), 463-467.

33. Willingham, D.; Brenes, D. A.; Winograd, N.; Wucher, A., Investigating the fundamentals of molecular depth profiling using strong-field photoionization of sputtered neutrals. *Surf. Interface Anal.* **2011,** *43* (1-2), 45-48.

34. Winograd, N., Ion beams and laser postionization for molecule-specific imaging. *Anal. Chem.* **1993,** *65* (14), 622A-629A.

35. Wucher, A.; Tian, H.; Winograd, N., A mixed cluster ion beam to enhance the ionization efficiency in molecular secondary ion mass spectrometry. *Rapid Commun. Mass Spectrom.* **2014,** *28* (4), 396-400.

36. Liao, H.-Y.; Lin, K.-Y.; Kao, W.-L.; Chang, H.-Y.; Huang, C.-C.; Shyue, J.-J., Enhancing the Sensitivity of Molecular Secondary Ion Mass Spectrometry with C60+-O2+ Cosputtering. *Anal. Chem.* **2013,** *85* (7), 3781-3788.

37. Grade, H.; Cooks, R. G., Secondary ion mass spectrometry. Cationization of organic molecules with metals. *J. Am. Chem. Soc.* **1978,** *100* (18), 5615-5621.

38. Altelaar, A. F. M.; Klinkert, I.; Jalink, K.; de Lange, R. P. J.; Adan, R. A. H.; Heeren, R. M. A.; Piersma, S. R., Gold-Enhanced Biomolecular Surface Imaging of Cells and Tissue by SIMS and MALDI Mass Spectrometry. *Analytical Chemistry* **2005,** *78* (3), 734-742.

39. Wu, K. J.; Odom, R. W., Matrix-Enhanced Secondary Ion Mass Spectrometry: A Method for Molecular Analysis of Solid Surfaces. *Anal. Chem.* **1996,** *68* (5), 873-882.

40. Nicola, A.; Muddiman, D.; Hercules, D., Enhancement of ion intensity in time-of-flight secondary-ionization mass spectrometry. *J. Am. Soc. Mass Spectrom.* **1996,** *7* (5), 467-472.

41. Altelaar, A. F. M.; Luxembourg, S. L.; McDonnell, L. A.; Piersma, S. R.; Heeren, R. M. A., Imaging mass spectrometry at cellular length scales. *Nat. Protoc.* **2007,** *2* (5), 1185-1196.

42. Altelaar, A. F. M.; Taban, I. M.; McDonnell, L. A.; Verhaert, P. D. E. M.; de Lange, R. P. J.; Adan, R. A. H.; Mooi, W. J.; Heeren, R. M. A.; Piersma, S. R., High-resolution MALDI imaging mass spectrometry allows localization of peptide distributions at cellular length scales in pituitary tissue sections. *International Journal of Mass Spectrometry* **2007,** *260* (2–3), 203-211.

43. Wehbe, N.; Heile, A.; Arlinghaus, H. F.; Bertrand, P.; Delcorte, A., Effects of Metal Nanoparticles on the Secondary Ion Yields of a Model Alkane Molecule upon Atomic and Polyatomic Projectiles in Secondary Ion Mass Spectrometry. *Anal. Chem.* **2008,** *80* (16), 6235-6244.

44. Delcorte, A.; Yunus, S.; Wehbe, N.; Nieuwjaer, N.; Poleunis, C.; Felten, A.; Houssiau, L.; Pireaux, J. J.; Bertrand, P., Metal-Assisted Secondary Ion Mass Spectrometry Using Atomic (Ga+, In+) and Fullerene Projectiles. *Anal. Chem.* **2007,** *79* (10), 3673-3689.

45. Locklear, J. E.; Guillermier, C.; Verkhoturov, S. V.; Schweikert, E. A., Matrix-enhanced cluster-SIMS. *Appl. Surf. Sci.* **2006,** *252* (19), 6624-6627.

46. McDonnell, L. A.; Heeren, R. M. A.; de Lange, R. P. J.; Fletcher, I. W., Higher Sensitivity Secondary Ion Mass Spectrometry of Biological Molecules for High Resolution, Chemically Specific Imaging. *J. Am. Soc. Mass Spectrom.* **2006,** *17* (9), 1195-1202.
47. Monroe, E. B.; Jurchen, J. C.; Lee, J.; Rubakhin, S. S.; Sweedler, J. V., Vitamin E Imaging and Localization in the Neuronal Membrane. *J. Am. Chem. Soc.* **2005,** *127* (35), 12152-12153.
48. Hankin, J.; Barkley, R.; Murphy, R., Sublimation as a method of matrix application for mass spectrometric imaging. *J. Am. Soc. Mass Spectrom.* **2007,** *18* (9), 1646-1652.
49. Taormina, C. R.; Nicolette, E.; Pedder, R. E.; Novak, T. T. An Ion Guide Study: Quadrupoles, Rectilinear Quadrupoles, Hexapoles, and Octopoles. http://www.ardaratech.com/document-library/technical-notes/11-tn-3007-practical-quadrupole-theory-ion-guides. (Accessed online 2014/6/12.)
50. Loboda, A. V.; Krutchinsky, A. N.; Bromirski, M.; Ens, W.; Standing, K. G., A tandem quadrupole/time-of-flight mass spectrometer with a matrix-assisted laser desorption/ionization source: design and performance. *Rapid Commun. Mass Spectrom.* **2000,** *14,* 1047-1057.
51. Passarelli, M. K.; Winograd, N., Characterizing in situ Glycerophospholipids with SIMS and MALDI Methodologies. *Surf. Interface Anal.* **2011,** *43* (1-2), 269-271.
52. Tucker, K. R.; Li, Z.; Rubakhin, S. S.; Sweedler, J. V., Secondary Ion Mass Spectrometry Imaging of Molecular Distributions in Cultured Neurons and Their Processes: Comparative Analysis of Sample Preparation. *J. Am. Soc. Mass Spectrom.* **2012,** *23* (11), 1931-1938.
53. Miyamoto, M. D., Binomial analysis of quantal transmitter release at glycerol treated frog neuromuscular junctions. *J. Physiol.* **1975,** *250* (1), 121-142.
54. Galle, P., Sur une nouvelle methode d'analyse cellulaire utilisant le phenomene d'emission ionique secondaire. *Ann. Phys. Biol. Med.* **1970,** *42,* 83-94.
55. Ostrowski, S. G.; Van Bell, C. T.; Winograd, N.; Ewing, A. G., Mass Spectrometric Imaging of Highly Curved Membranes During Tetrahymena Mating. *Science* **2004,** *305* (5680), 71-73.
56. Rabbani, S.; Fletcher, J. S.; Lockyer, N. P.; Vickerman, J. C., Exploring subcellular imaging on the buncher-ToF J105 3D chemical imager. *Surf. Interface Anal.* **2011,** *43* (1-2), 380-384.
57. Tokareva, E. N.; Fardim, P.; Pranovich, A. V.; Fagerholm, H. P.; Daniel, G.; Holmbom, B., Imaging of wood tissue by ToF-SIMS: Critical evaluation and development of sample preparation techniques. *Appl. Surf. Sci.* **2007,** *253* (18), 7569-7577.
58. Smith, C. A.; O'Maille, G.; Want, E. J.; Qin, C.; Trauger, S. A.; Brandon, T. R.; Custodio, D. E.; Abagyan, R.; Siuzdak, G., METLIN: a metabolite mass spectral database. *Ther. Drug Monit.* **2005,** *27* (6), 747-751.
59. Monroe, E. B.; Annangudi, S. P.; Hatcher, N. G.; Gutstein, H. B.; Rubakhin, S. S.; Sweedler, J. V., SIMS and MALDI MS imaging of the spinal cord. *Proteomics* **2008,** *8* (18), 3746-3754.
60. Zingg, J.-M., Modulation of signal transduction by vitamin E. *Mol. Aspects Med.* **2007,** *28* (5–6), 481-506.
61. Fletcher, J.; Kotze, H.; Armitage, E.; Lockyer, N.; Vickerman, J., Evaluating the challenges associated with time-of-fight secondary ion mass spectrometry for metabolomics using pure and mixed metabolites. *Metabolomics* **2013,** *9* (3), 535-544.
62. Glanzman, D. L.; Kandel, E. R.; Schacher, S., Identified target motor neuron regulates neurite outgrowth and synapse formation of Aplysia sensory neurons in vitro. *Neuron* **1989,** *3* (4), 441-450.
63. Passarelli, M. K.; Ewing, A. G.; Winograd, N., Single-cell lipidomics: characterizing and imaging lipids on the surface of individual Aplysia californica neurons with cluster secondary ion mass spectrometry. *Anal. Chem.* **2013,** *85* (4), 2231-8.
64. Girod, M.; Shi, Y.; Cheng, J.-X.; Cooks, R. G., Desorption electrospray ionization imaging mass spectrometry of lipids in rat spinal cord. *J. Am. Soc. Mass Spectrom.* **2010,** *21* (7), 1177-1189.
65. Yang, J.; Caprioli, R. M., Matrix Sublimation/Recrystallization for Imaging Proteins by Mass Spectrometry at High Spatial Resolution. *Anal. Chem.* **2011,** *83* (14), 5728–5734.

FIGURES AND TABLES

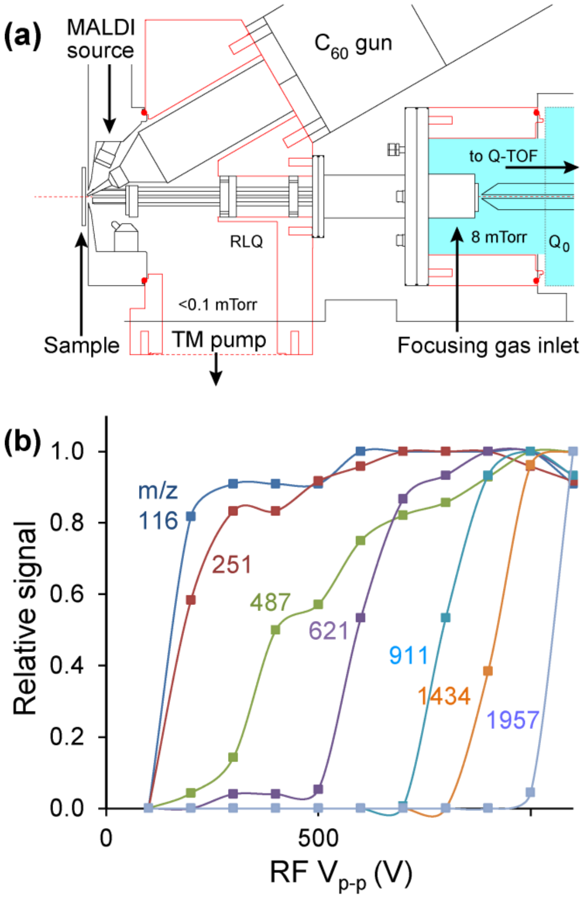

Figure 3.1: Schematic of the hybrid C_{60}-SIMS/MALDI mass spectrometer and RLQ transmission profiles. (a) Custom-designed adapter blocks (outlined in red) were installed to connect the C_{60}^{+} gun to the vacuum chamber, the standard UV-MALDI source, and the Q-TOF mass spectrometer. A rectilinear quadrupole (RLQ) ion guide was incorporated to transmit ions through the adapter into the ion guide Q_0. The enlarged source chamber was operated at high vacuum pressure (<0.1 mTorr) by an additional turbomolecular pump (TM Pump) that was mounted at the bottom of the adapter, while nitrogen gas (represented with blue) was introduced to the chamber surrounding the Q_0 for collisional focusing of ions. **(b)** Mass transmission profiles measured for the RLQ ion guide (2.8 MHz) confirmed the efficient transmission of ions across a broad range, approx. *m/z* 100–2,000, at 1,100 $V_{p\text{-}p}$ RF amplitude. Squares indicate measured data with connecting lines added as a visual guide. Used with permission from Springer, copyright 2014.

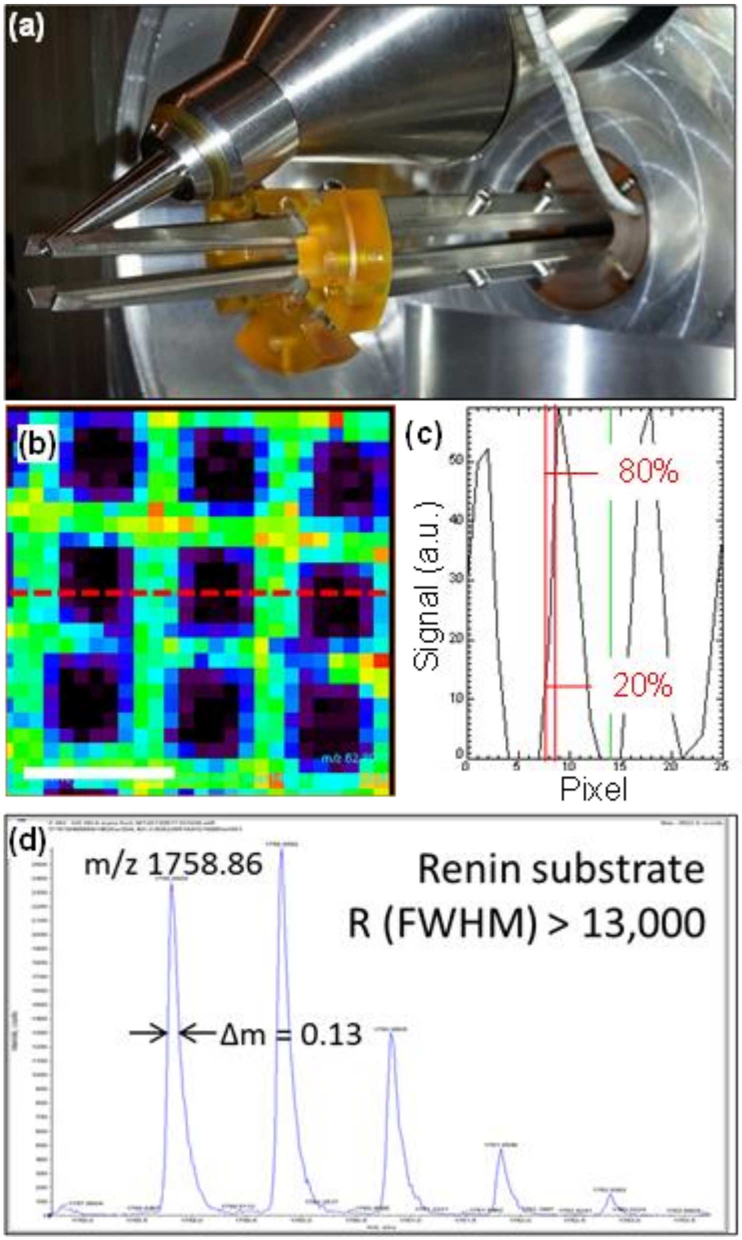

Figure 3.2: Modified QTOF MS detail and performance. (a) A close-up photograph of the inside of the adapted source chamber showing the ion gun and the segmented front end of the rectilinear quadrupole ion guide which can be removed for cleaning. **(b)** Ion image of Cu^+ (m/z 62.93) acquired from a copper mesh with 10 µm step size and ion probe diameter demonstrates similar achievable practical lateral spatial resolution in C_{60}-SIMS mode, determined by **(c)** a line scan across one edge of a Cu wire feature, in which 20-80% Cu^+ signal spans one pixel or 10 µm. (D) MALDI MS spectrum detail of renin substrate standard acquired on the adapted system demonstrates mass resolution R >13,000 at m/z 1759, calculated by the FWHM method. Used with permission from Springer, copyright 2014.

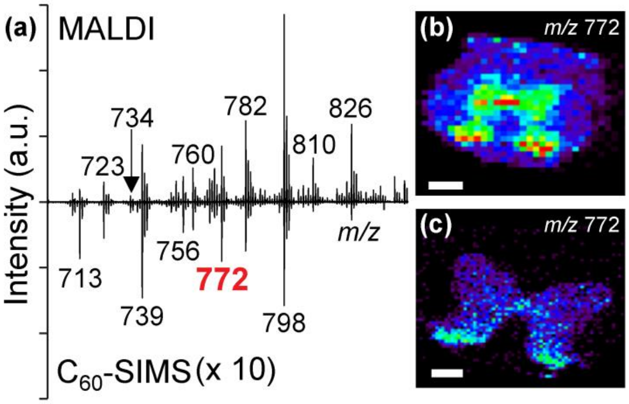

Figure 3.3. Imaging of a mammalian spinal cord in MALDI and C_{60}-SIMS modes using the hybrid Q-TOF mass spectrometer. **(a)** MS lipid profiles of central gray tissue matter acquired by MALDI (top) and SIMS (bottom, inverted and intensity scaled ×10) show similar overall ion composition from comparable tissue areas, with certain differences. MALDI yielded several-fold more intact lipid ions, including *m/z* 734 – PC(32:0) $[M + H]^+$, *m/z* 756 – PC(32:0) $[M + Na]^+$, *m/z* 760 – PC(34:1) $[M + H]^+$, 772 – PC(32:0) $[M + K]^+$, *m/z* 782 – PC(34:1) $[M + Na]^+$, and *m/z* 798 – PC(32:0) $[M + K]^+$. In comparison, SIMS generated relatively more fragments by trimethylamine loss including at *m/z* 713 – PC(32:0) $[M – N(CH_3)_3+K]^+$, *m/z* 723 – PC(34:1) $[M – N(CH_3)_3 + Na]^+$, and *m/z* 739 – PC(34:1) $[M – N(CH_3)_3 + K]^+$. Ions were assigned tentatively by mass match to previous work with similar tissue [51]. **(b)** MALDI-mode ion image of PC(32:0) $[M + K]^+$ at *m/z* 772 provided higher signal intensity and image contrast compared with **(c)** SIMS-mode image for the same ion. SIMS provided imaging higher spatial resolution, allowing improved definition of small anatomical features in the spinal cord such as the central canal and dorsal horns, which show higher relative PC(32:0) abundance. Decreasing MALDI step size resulted in significant oversampling and did not improve image quality. Scale bar = 500 µm. Used with permission from Springer, copyright 2014.

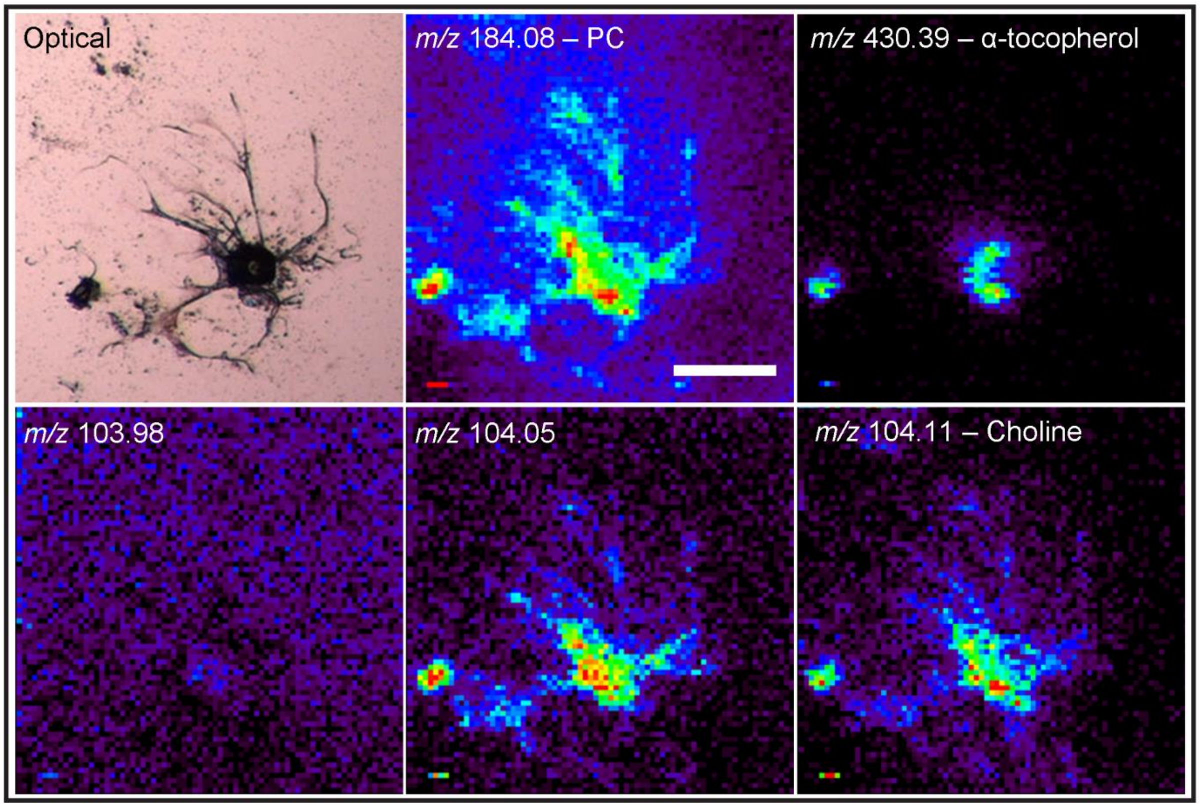

Figure 3.4: C_{60}-SIMS ion images of cultured *A. californica* neurons. Cells were cultured on silicon tiles and stabilized with glycerol substitution. Cell bodies and processes are apparent in the phosphocholine (PC) image (*m/z* 184.08, 0–200 counts), while α-tocopherol accumulated on the cell bodies (*m/z* 430.39, 0–50 counts). The isobaric ions *m/z* 103.98, 104.05 (0–60 counts), and 104.11 (bottom row, 0–60 counts) were detected with different distributions, assigned to background contaminant, nonspecific organic fragment, and choline, respectively. Scale bar = 200 µm. Used with permission from Springer, copyright 2014.

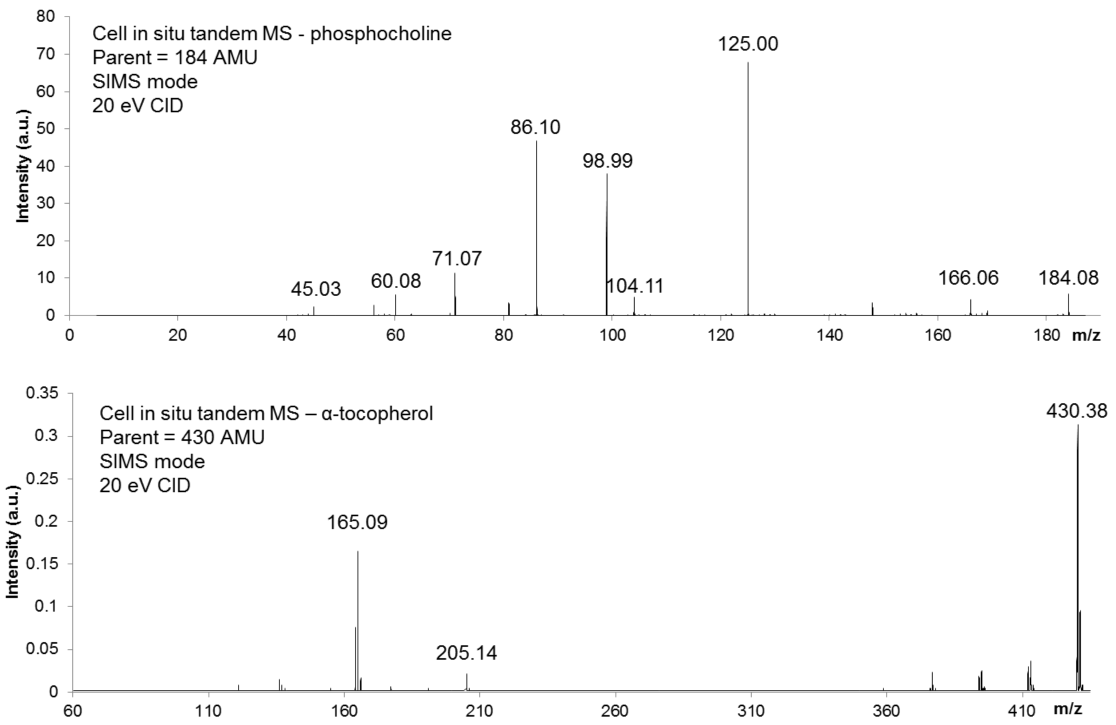

Figure 3.5: C_{60}-SIMS *in situ* tandem MS spectra of cell metabolites. Phosphocholine (top) and α-tocopherol (bottom) ion assignments are confirmed directly from cultured *A. californica* neurons. Characteristic ions are labeled in the spectra and match with the tandem MS spectra reported in the METLIN online database (http://metlin.scripps.edu/) Used with permission from Springer, copyright 2014.

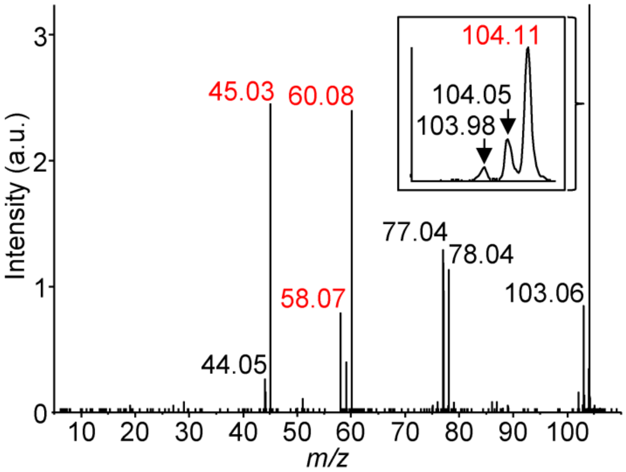

Figure 3.6: C_{60}-SIMS tandem mass spectrum of *m/z* 104 acquired from *A. californica* ganglion tissue. Several precursor ions are included in the isolation window (see the inset). The ion at *m/z* 104.11 was assigned to choline based on the precursor mass and characteristic fragment ions at *m/z* 45.03, 58.07 and 60.08 (red text). Used with permission from Springer, copyright 2014.

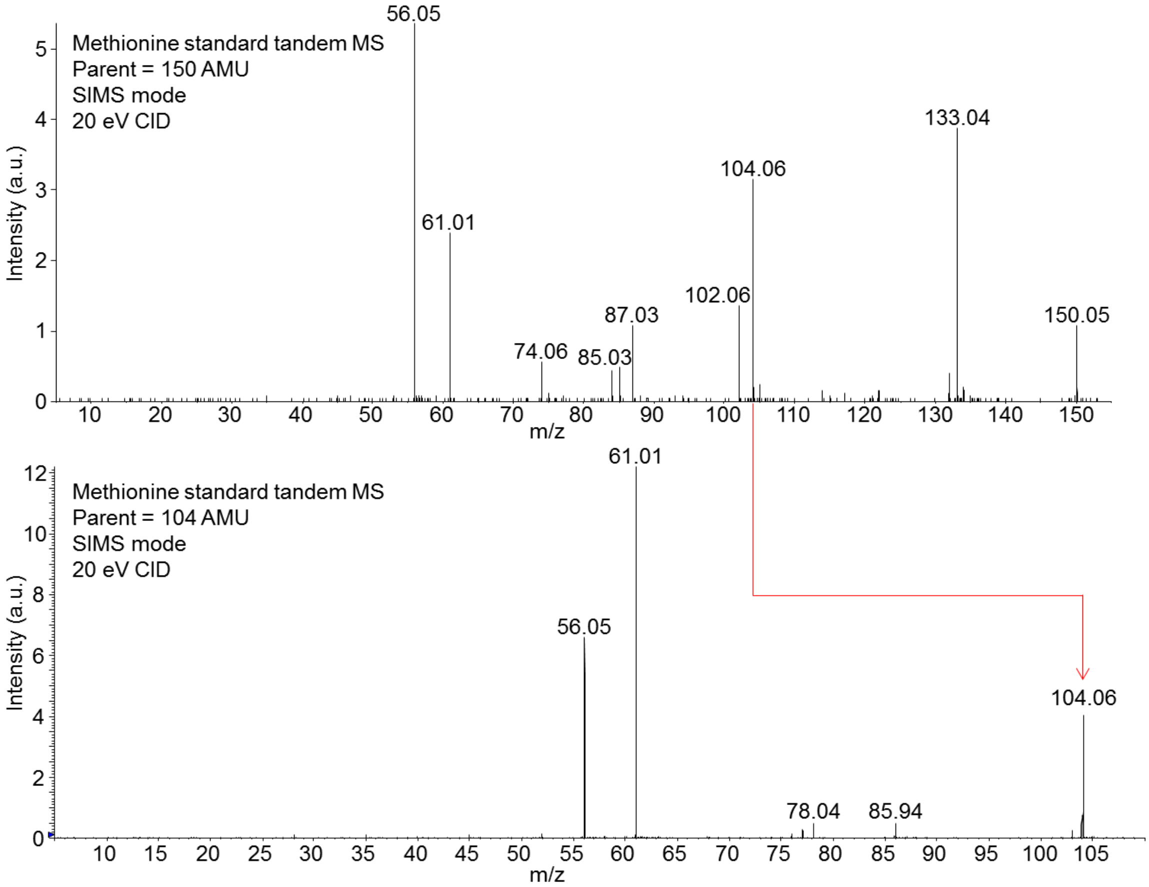

Figure 3.7: C_{60}-SIMS tandem MS spectra of methionine standard. Tandem MS of methionine standard MH^+ ion at *m/z* 151 (top) yields a fragmentation pattern matching that of the Metlin database spectrum. Tandem MS of characteristic fragment *m/z* 104.05 (bottom) generated by C_{60}-SIMS source fragmentation yields several of these smaller ions as well. Used with permission from Springer, copyright 2014.

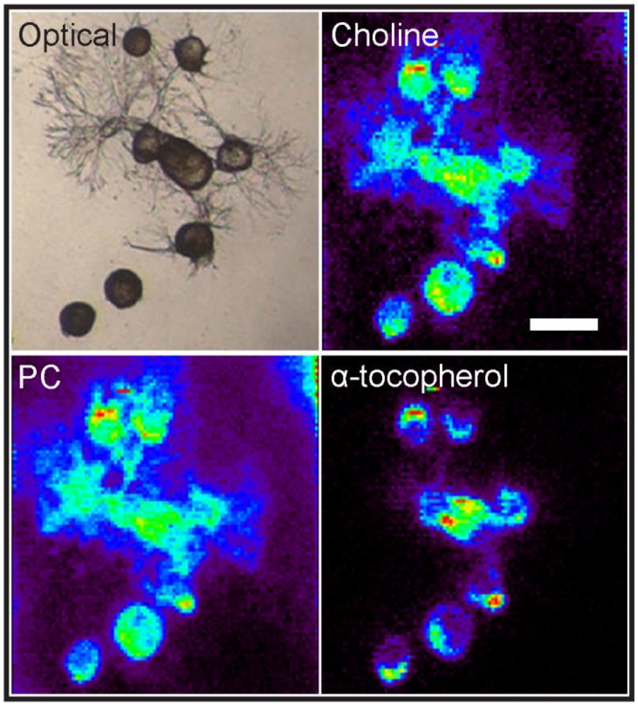

Figure 3.8: C_{60}-SIMS ion images of an *A. californica* neuronal network. Cells were cultured on a silicon tile and stabilized with glycerol. Outgrowth and interconnecting processes are visible in the optical image and correlate with the total ion and phosphocholine (PC, 0–400 counts) ion images, while α-tocopherol (0–150 counts) is concentrated to cell bodies and also shows subcellular localization. Scale bar = 200 µm. Used with permission from Springer, copyright 2014.

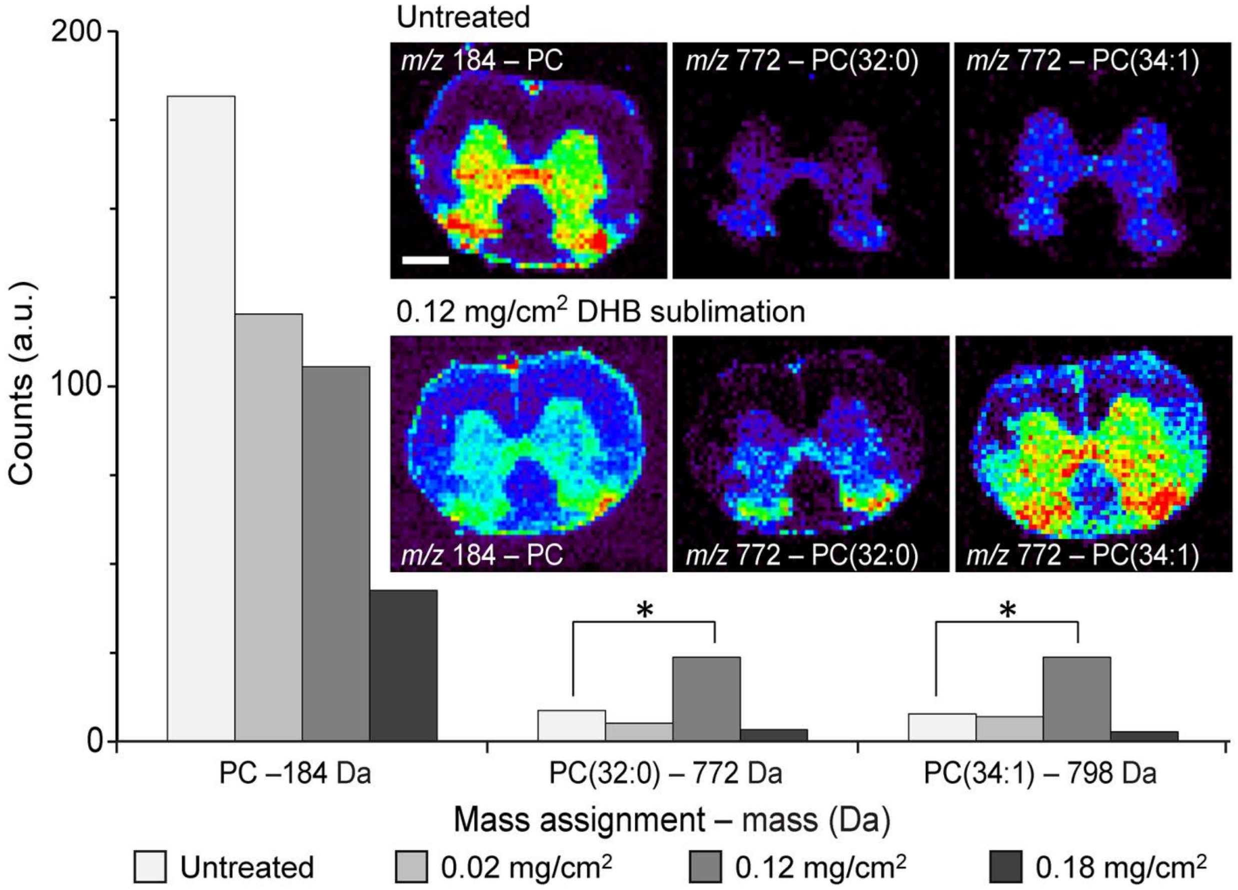

Figure 3.9: Results of matrix-enhanced C_{60}-SIMS imaging experiments using sublimed DHB on spinal cord tissue sections. The chart compares average peak counts detected in gray matter for a lipid phosphocholine (PC) fragment as well as putative PC(32:0) and PC(34:1), two intact lipids detected as $[M + K]^+$ adduct ions, from samples that were untreated or coated with one of three different matrix densities. Statistically significant ($p < 0.05$) intact lipid enhancement was achieved with a 0.12 mg/cm^2 sublimed matrix coating, indicated with asterisks. Inset shows representative ion images from uncoated and matrix-coated specimens; identical color scale is used for each pair of images for accurate comparison. Scale bar = 500 µm. Used with permission from Springer, copyright 2014.

CHAPTER 4

CORRELATED SINGLE CELL ANALYSIS WITH C_{60}^+ AND ELECTRON MICROPROBES

NOTES AND ACKNOWLEDGMENTS

This chapter presents unpublished results from a set of experiments to explore the utility of combining C_{60}-SIMS imaging with scanning electron microscopy for single cell analysis. This work was supported by the Department of Energy Office of Biological and Environmental Research through grant DE SC0006642, NIH through grant U54GM093342, and The National Resource for Aplysia funded by PHS grant P40 OD010952. Cell dissection and culture assistance by Xiying Yang, Stanislav Rubakhin, and Callie Croushore are also gratefully acknowledged, as well as SEM assistance by Scott Robinson.

INTRODUCTION

As outlined in Chapter 2, mass spectrometry imaging (MSI) is a powerful chemical imaging approach which allows multiple molecular analytes to be detected and mapped on a sample surface, including individual cells such as neurons as presented earlier (in Chapter 4) and in related publications.[1-3] However, SIMS alone does not provide information on physical surface topography or biological sample morphology which can be critical for correctly interpreting ion images. MSI is therefore often paired with complementary imaging techniques such as optical digital scanning, light microscopy with tissue staining,[4] and electron microscopy,[5-7] all of which can provide this information. Electron microscopy is particularly useful in conjunction with microscopic secondary ion mass spectrometry (SIMS) imaging since it can reliably match or exceed SIMS spatial resolution (routinely submicron and <50 nm in best conditions[8]) and also allows analysis of thick, opaque sample surfaces with minimal (or no) additional sample preparation in the case of scanning electron microscopy (SEM). Secondary electron detectors are routinely incorporated on commercial SIMS instruments since electron micrographs can be acquired using secondary electrons generated by the primary ion beam, and several recent reports have also demonstrated the usefulness of combining or correlating electron microscopy with SIMS imaging. For example, Carpenter *et al.* correlated SEM with SIMS images of single microbes from termite hindguts in order to follow isotopically-labeled cellulose digestion and track it to specific organisms.[5] More recently, Sjövall and colleagues correlated SIMS and SEM to detect drug molecule distributions in mouse ear tissue sections, utilizing SIMS to visualize drug distribution and SEM to resolve micron-scale layers, allowing precise localization of the drugs.[6] In another study, Wedlock et al. combined SIMS and energy-filtered transmission electron microscopy (EFTEM) to determine subcellular localization of a gold phosphine drug compound within treated tumor cells.[7] SIMS and TEM each provided some chemical and some physical information; the drug distribution was selectively visualized in SIMS by Au^- ions and in EFTEM by Au-characteristic inelastically scattered electrons, and combining the techniques provided cross-validation of results as well as additional information such as the location of proteins and nucleic acids by SIMS (using S^- and P^- ion images, respectively) and cell morphology by TEM.

Here the utility of combining C_{60}-SIMS and SEM is explored for single cell analysis applications, specifically on our MALDI/C_{60}-SIMS Q-TOF instrument which differs from commercial SIMS instruments in a number of important ways.[2] In addition to correlating images to enhance information yielded by a SIMS imaging experiment, we propose that SEM can also be useful in studying the SIMS ionization process itself. SIMS is an intrinsically destructive technique involving sputtering – removal of sample material upon each ion projectile impact – and as polyatomic primary ion sources allow use of high ion doses and resampling the same surface areas for molecular information, the consequences of this effect become more important. Projectile-surface interaction has been well investigated using simple mock samples,[9] but how does the ion sputtering process affect a complex “real world” biological specimen, and how might it differ with primary ion choice or other experimental parameters?

One highly touted feature of the C_{60}^+ projectile is its suitability for molecular depth profiling[9-10] (and by extension, 3D imaging[11]) owing to high molecular ion yields and low damage cross-section, *i.e.* that it “removes material faster than it damages the sample” in theory.[12] We therefore sought here to evaluate the practical capability of C_{60}-SIMS for molecular depth profiling of a single cell, in combination with subsequent SEM to visualize the effect of sustained C_{60}^+ ion bombardment on the sample. Results raise interesting questions about the nature of this process which may direct useful future experiments.

EXPERIMENTAL METHODS

Materials and chemicals

Silicon substrates were purchased from Silicon, Inc. (Boise, ID, USA) as 4 in.-diameter wafers of Si (100), rinsed in HPLC-grade methanol purchased from Sigma-Aldrich (St Louis, MO, USA), then scored, broken into 1 × 1 cm^2 tiles, and stored immersed in methanol before use.

Mass spectrometry

All MS imaging and depth profiling experiments were performed on a custom-built hybrid MALDI/C_{60}-SIMS Q-TOF MS instrument described in detail elsewhere,[2] operating in positive ion SIMS mode. This instrument features a pulsed nitrogen UV laser (6 mW max. avg. power, 337 nm emission wavelength) for laser desorption/ionization, a 20 kV DC C_{60} ion gun fitted to the same sample chamber to enable SIMS, a translational sample stage for MS imaging in either MALDI or SIMS mode, and quadrupole time-of-flight analyzers in orthogonal geometry enabling tandem MS *via* CID with Ar gas as well as high mass resolution (R > 10,000) in any mode of operation. SIMS images were acquired in step mode at 10 × 10 μm^2 pixel (step) size, 1 s accumulation/pixel, m/z 50-500, and Q_1 transmission set to 15/35/50% at 40/90/250 AMU, respectively. C_{60}^+ ion microprobe sample current was 100 pA and spot diameter was estimated at 15 µm. For single cell depth profiling, the C_{60} gun was set to the 1 mm beam aperture for a ~70 µm probe spot diameter and 430 pA sample current. SIMS spectral data was acquired with 1 s accumulation time, m/z 100-850, and Q_1 transmission set to 25/25/50% at 80/180/370 AMU, respectively. Laser ablation was performed with the UV laser set to 100% relative power (no attenuation) and 40 Hz firing rate.

Cell culture and stabilization

Aplysia californica were obtained from the University of Miami NIH National Resource for Aplysia (Miami, FL, USA). Dissection, cell isolation, and cell culture procedures used here are described elsewhere.[3] Cultures were allowed to incubate for 24 h on lab bench top at ~25° C, and then glycerol-stabilized prior to imaging as described elsewhere.[2]

Scanning electron microscopy

SEM was performed on a XL30 ESEM-FEG (Philips, Amsterdam, North Holland, Netherlands) operating at 5 kV electron beam energy, 2.0 nm spot size, and 7.5-10.0 mm working distance. Samples were sputter coated with ~5 nm Au prior to imaging. Analyzed areas were located by approximate position on the substrate and confidently identified by the characteristic square etch pattern generated by the C_{60} ion beam on the surface.

RESULTS & DISCUSSION

C_{60}-SIMS/SEM correlated imaging

The main goal of this work was to explore the correlation of C_{60}-SIMS with SEM for single cell analysis. One way to combine these approaches is to follow a SIMS imaging experiment with SEM of the same region; by precisely correlating molecular maps from SIMS with higher-resolution topographical maps acquired by SEM, chemical features can be associated with specific physical structures on or in the cells. Importantly, SIMS is an inherently destructive process which removes material from the sample surface during analysis, thus subsequent SEM imaging may also provide useful information about the nature of this interaction. **Figure 4.1** shows the combined results of such an experiment in which a cluster of several *A. californica* neurons were imaged sequentially by optical, SIMS, and then SEM. In contrast with the low-magnification optical image which provides little detail on the imaged cells, SEM clearly resolves the cells and also visualizes the SIMS-imaged region itself as a square feature where the substrate appears distinctly smoother and lighter, possibly due to removal of surface material by the ion probe. SIMS generated several useful ion images for molecular and fragment ions, including phosphocholine (m/z 184.08) and choline (m/z 104.11), two metabolites and lipid fragment ions which can serve as cell membrane markers. The distribution of these ions is similar here, but choline shows a unique area of concentration around one cell in the field of view. This might arise from an actual abundance of free choline at this location (rather than lipid-incorporated choline, which typically mirrors phosphocholine distribution on cells) or from isobaric interference by another ion with similar mass. α-tocopherol (m/z 430.38) also appears localized around this cell and especially concentrated in a small (~$20 \times 20\ \mu m^2$) region of the apparent cell body. α-tocopherol is one form of vitamin E and a lipophilic metabolite involved in many cell processes including cell repair, cell signaling modulation, and gene expression modulation,[13] thus visualizing its subcellular distribution may help to elucidate its role in these functions or others. Since the SIMS analysis region is clearly visible by SEM, it allows SIMS and SEM images to be precisely superimposed as shown in **Figure 4.2(a)**. A higher-magnification electron micrograph at the α-tocopherol hotspot (**Figure 4.2(b)**) shows that this signal is associated with a rough patch in the otherwise-smooth cell surface, possibly a region of cellular damage exposing intracellular material. **Figure 4.2(c)** shows a micrograph of the same region from the approximate incident angle of the C_{60}^+ ion beam; interestingly this damaged region is not visible from this angle, suggesting that the damage was not caused directly by the beam itself. One possibility is that this was the site of a soma-neurite junction which was damaged during preparation or analysis, and in that case the α-tocopherol hot-spot would be consistent with previous observations made by our group.[3]

Figure 3(a) shows physical detail of another cell in the SIMS-imaged sample region. The semispherical feature in the center may be the cell nucleus, and the larger flat encompassing feature may be the compressed remains of the cell cytoplasm. SEM reveals an irregular surface and micron-scale features within the putative cytoplasm region; these could be organelles. Superposition of the phosphocholine ion image and the lower-magnification electron micrograph (**Figure 4.3(b)**) shows localization primarily around the cell rather than on it, suggesting that the SEM-imaged surface is presenting intracellular material which has been exposed by the SIMS sputtering process.

Single cell SIMS depth profiling with supplemental SEM

To investigate the capability of C_{60}-SIMS (and specifically, SIMS on our hybrid QTOF MS) to acquire sub-surface molecular information e.g. for 3D imaging, a simple depth profiling experiment was performed. Since previous experiments indicated that C_{60} bombardment does actually damage the sample surface and reduce subsequent molecular ion signal, we also investigated the possibility of restoring signal with a simple surface “cleaning” using the LDI UV laser already available on the instrument. For this experiment, the DC C_{60}^+ probe was set to a high sample current (430 pA) and large spot diameter (70 µm) to generate large ion counts and a high etch rate. Calculated primary ion dose was 7E+13 C_{60}^+ ions/cm^2•s, 70-fold above the static limit and estimated to provide an etch rate of 50 nm/s based on similar work reported elsewhere.[14] The probe was centered on a single *A. californica* neuron cultured on Si wafer and unblanked in a stationary position for ~22 min total time. At 10 min the beam was blanked briefly and the entire cell was exposed to the laser for 30 s (100% power and 40 Hz firing rate), then the beam was reactivated for the remaining 10 min.

Results from this exploratory depth profiling experiment are shown in **Figure 4.4**, including depth profiles of several ions of interest and mass profiles at time points near the beginning, middle, and end of the experiment. The mass chromatograms (**Figure 4.4(a)**) serve as depth profiles, showing that total ion count (TIC) drops rapidly in the first ~1 min., decreasing more gradually by approx. 10× over the entire experiment. Identified molecular ions phosphocholine and α-tocopherol decrease even more rapidly at first – nearly 100× in the first 5 min. – although this is expected for membrane-localized compounds such as these, as the ion probe is estimated to etch through the ~5 nm-thick lipid bilayer in only 0.1 s assuming constant etch rate. Not all ions decrease during the profile, however; at ~7 min a slight increase in signal can be seen in the TIC and also for several individual ions including m/z 192.89, an unidentified ion shown here. This profile feature may correlate with a specific intracellular region which generates these ions abundantly for some reason, and characterization of the ions using tandem MS could help to explain this observation more confidently. Finally, a series of intense ions were observed to arise at the end of the experiment including m/z 672.72, shown here. These are likely substrate-derived ions based on isotope patterns which reflect the 92/5/3% characteristic stable isotope distribution of silicon (data not shown) as well as the repeating 59.97 Da unit mass which can be assigned to SiO_2 (m_{ex} = 59.9667). The chronological series of MS profiles (**Figure 4.4(b)**) also reflects these observations, and the appearance of substrate ions at approx. 15 min corresponds with an estimated 45 µm etch depth which is a reasonable number for the thickness of a ~100 µm-diameter cell lying flat on a surface. The baseline on these mass spectra decreases noticeably at the end of the experiment; this baseline is likely attributable to “nonspecific” organic fragments generated in the sputtering process, so the decrease can be attributed to the transition from organic cell material to inorganic substrate which is also indicated by concurrently-rising silicon cluster ions. Finally, it is interesting to note that membrane-specific ions (phosphocholine and α-tocopherol) were not detected at the bottom of the cell, where the lower lipid bilayer interfaces with the silicon substrate. It may be that sustained C_{60} bombardment thoroughly fragments these molecules before they can be ionized.

Exposure of the cell to UV laser light appeared to have little effect on the mass profiles. A slight uptick was observed in the counts of individual ions and TIC, but signal returned to pre-exposure levels within 1 min. This might be expected considering that laser desorption/ionization is a much harsher ionization method in comparison with MALDI, typically only generating elemental ions and very small fragment ions. Thus if laser fluence is high enough to induce removal of material by LDI, it is unlikely to remove the SIMS-damaged layer without generating more chemical damage of its own. A better alternative may be to clean with an IR-wavelength laser, as IR light is absorbed by water in the sample and has already been applied successfully for depth profiling of molecular ions, indicating that it can ablate material without completely destroying subsurface molecules.[15]

Following SIMS, the depth-profiled cell was imaged by SEM in order to investigate the physical effect of extensive C_{60}^+ bombardment. A large ablated region is apparent in the electron micrograph, shown in **Figure 4.5(a)**, with approx. 70 µm diameter which is consistent with previous probe size estimates. The underlying Si substrate has been clearly exposed in the center of this region, and a higher-magnification micrograph here (**Figure 4.5(b)**) reveals highly heterogeneous cell material and many similar 1-2 µm-diameter circular features at the cell-substrate interface and on the exposed silicon itself. The origin of these features is unknown: computer simulations suggest that lateral redistribution of sputtered material is occurs on the nm scale following projectile impact,[16] but the features observed here are several orders larger than that. Still, they could arise specifically from C_{60} sputtering of silicon by some yet-unexplained phenomenon, or they could originate from the biological (cell) sample.

FUTURE DIRECTIONS

C_{60}-SIMS was combined with SEM in order to enhance the information obtained from single cell analyses. In one experiment SIMS and SEM image data were precisely correlated, and superposition of chemical maps with higher-resolution electron micrographs allowed association of subcellular chemical features with micron-scale physical structures in the sample. In a separate experiment a chemical depth profile was performed on a single cell by C_{60}-SIMS; chemical features such as cell membrane and Si substrate were depth-resolved by characteristic ions, and subsequent SEM imaging allowed inspection of the cell post-profile. While numerous previous reports have demonstrated the utility of combining SIMS imaging with electron microscopy,[5-7, 17-19] this work uniquely applied SEM to investigate the physical effect of C_{60} bombardment on stabilized, cultured neurons. It also evaluated the combination of techniques specifically in conjunction with our new hybrid MALDI/C_{60}-SIMS Q-TOF MS, serving as a useful prelude to the (more involved) incorporation of SEM capability on the same instrument. While the chemical profile performed here was a simple exploratory procedure yielding low depth resolution due to a large, Gaussian ion probe, it demonstrates the feasibility (and limitations) of such experiments on our hybrid QTOF MS. To achieve more useful depth-resolved information, a more sophisticated approach is required in which layers of uniform thickness are removed by rastering the probe, crater-edge effects are addressed by cropping usable data, and the resulting voxels are corrected for a topographically-complex sample such as a cell. Depth profiling has also shown to benefit from frozen-hydrated sample preparation and cryogenic analysis conditions,[9] an advance which would require addition of a cryostage to the current MS system.

Future work can investigate the micron-scale crater features observed by SEM in the depth-profiled cell, and specifically whether such craters arise from C_{60} sputtering of clean silicon wafer in the absence of biological material. Additionally, while UV laser exposure did not appear to produce a significant “surface cleaning” effect after extensive SIMS analysis of a cell, a similar approach with an IR laser could be more effective. An IR laser could be installed on the existing QTOF MS (utilizing the same UV laser feedthrough with IR-compatible optics, or *via* addition of another feedthrough) for this purpose. Based on the usefulness of this combination, future plans for the SIMS instrument now include the addition of a secondary electron detector on the QTOF MS will allow SEM imaging in the same sample chamber. Although this system will not match performance (*e.g.* in spatial resolution, contrast) of the higher performance dedicated SEM such as the one used here, it will nevertheless enable new combined SIMS/SEM experiments such as interlaced imaging experiments where SEM is used to monitor sample morphology during SIMS acquisition.

REFERENCES

1. Yang, H.-J.; Sugiura, Y.; Ishizaki, I.; Sanada, N.; Ikegami, K.; Zaima, N.; Shrivas, K.; Setou, M., Imaging of lipids in cultured mammalian neurons by matrix assisted laser/desorption ionization and secondary ion mass spectrometry. *Surface and Interface Analysis* **2010,** *42* (10-11), 1606-1611.
2. Lanni, E. J.; Dunham, S. J. B.; Nemes, P.; Sweedler, J. V., Biomolecular Imaging with C60-SIMS: Instrumentation, Matrix Enhancement, and Single Cell Analysis. **2014,** *submitted for publication*.
3. Monroe, E. B.; Jurchen, J. C.; Lee, J.; Rubakhin, S. S.; Sweedler, J. V., Vitamin E Imaging and Localization in the Neuronal Membrane. *J Am Chem Soc* **2005,** *127* (35), 12152-12153.
4. Deutskens, F.; Yang, J.; Caprioli, R. M., High spatial resolution imaging mass spectrometry and classical histology on a single tissue section. *Journal of Mass Spectrometry* **2011,** *46* (6), 568-571.
5. Carpenter, K. J.; Weber, P. K.; Davisson, M. L.; Pett-Ridge, J.; Haverty, M. I.; Keeling, P. J., Correlated SEM, FIB-SEM, TEM, and NanoSIMS Imaging of Microbes from the Hindgut of a Lower Termite: Methods for In Situ Functional and Ecological Studies of Uncultivable Microbes. *Microscopy and Microanalysis* **2013,** *19* (06), 1490-1501.
6. Sjövall, P.; Greve, T. M.; Clausen, S. K.; Moller, K.; Eirefelt, S.; Johansson, B.; Nielsen, K. T., Imaging of Distribution of Topically Applied Drug Molecules in Mouse Skin by Combination of Time-of-Flight Secondary Ion Mass Spectrometry and Scanning Electron Microscopy. *Analytical Chemistry* **2014,** *86* (7), 3443-3452.
7. Wedlock, L. E.; Wedlock, M. R. K.; Cliff, J. B.; Filgueira, L.; Saunders, M.; Berners-Price, S. J., Visualising gold inside tumour cells following treatment with an antitumour gold(I) complex. *Metallomics* **2011,** *3*, 917-925.
8. Kollmer, F.; Paul, W.; Krehl, M.; Niehuis, E., Ultra high spatial resolution SIMS with cluster ions — approaching the physical limits. *Surface and Interface Analysis* **2012,** *45* (1), 312-314.
9. Winograd, N., Molecular depth profiling. *Surface and Interface Analysis* **2013,** *45* (1), 3-8.
10. Mao, D.; Wucher, A.; Winograd, N., Molecular Depth Profiling with Cluster Secondary Ion Mass Spectrometry and Wedges. *Analytical Chemistry* **2009,** *82* (1), 57-60.
11. Fletcher, J. S.; Vickerman, J. C.; Winograd, N., Label free biochemical 2D and 3D imaging using secondary ion mass spectrometry. *Current Opinion in Chemical Biology* **2011,** *15* (5), 733-740.
12. Weibel, D.; Wong, S.; Lockyer, N.; Blenkinsopp, P.; Hill, R.; Vickerman, J. C., A C60 Primary Ion Beam System for Time of Flight Secondary Ion Mass Spectrometry: Its Development and Secondary Ion Yield Characteristics. *Analytical Chemistry* **2003,** *75* (7), 1754-1764.
13. Zingg, J.-M., Modulation of signal transduction by vitamin E. *Mol Aspects Med* **2007,** *28* (5–6), 481-506.
14. Robinson, M. A.; Graham, D. J.; Castner, D. G., ToF-SIMS depth profiling of cells: Z-correction, 3D imaging, and sputter rate of individual NIH/3T3 fibroblasts. *Analytical Chemistry* **2012,** *84* (11), 4880-4885.
15. Nemes, P.; Barton, A. A.; Li, Y.; Vertes, A., Ambient Molecular Imaging and Depth Profiling of Live Tissue by Infrared Laser Ablation Electrospray Ionization Mass Spectrometry. *Analytical Chemistry* **2008,** *80* (12), 4575-4582.
16. Postawa, Z.; Rzeznik, L.; Paruch, R.; Russo, M. F.; Winograd, N.; Garrison, B. J., Depth profiling by cluster projectiles as seen by computer simulations. *Surface and Interface Analysis* **2011,** *43* (1-2), 12-15.
17. Palmquist, A.; Emanuelsson, L.; Sjövall, P., Chemical and structural analysis of the bone-implant interface by TOF-SIMS, SEM, FIB and TEM: Experimental study in animal. *Applied Surface Science* **2012,** *258* (17), 6485-6494.
18. Metzner, R.; Schneider, H. U.; Breuer, U.; Schroeder, W. H., Imaging Nutrient Distributions in Plant Tissue Using Time-of-Flight Secondary Ion Mass Spectrometry and Scanning Electron Microscopy. *Plant Physiology* **2008,** *147* (4), 1774-1787.
19. Ostrowski, S. G.; Van Bell, C. T.; Winograd, N.; Ewing, A. G., Mass Spectrometric Imaging of Highly Curved Membranes During Tetrahymena Mating. *Science* **2004,** *305* (5680), 71-73.

FIGURES

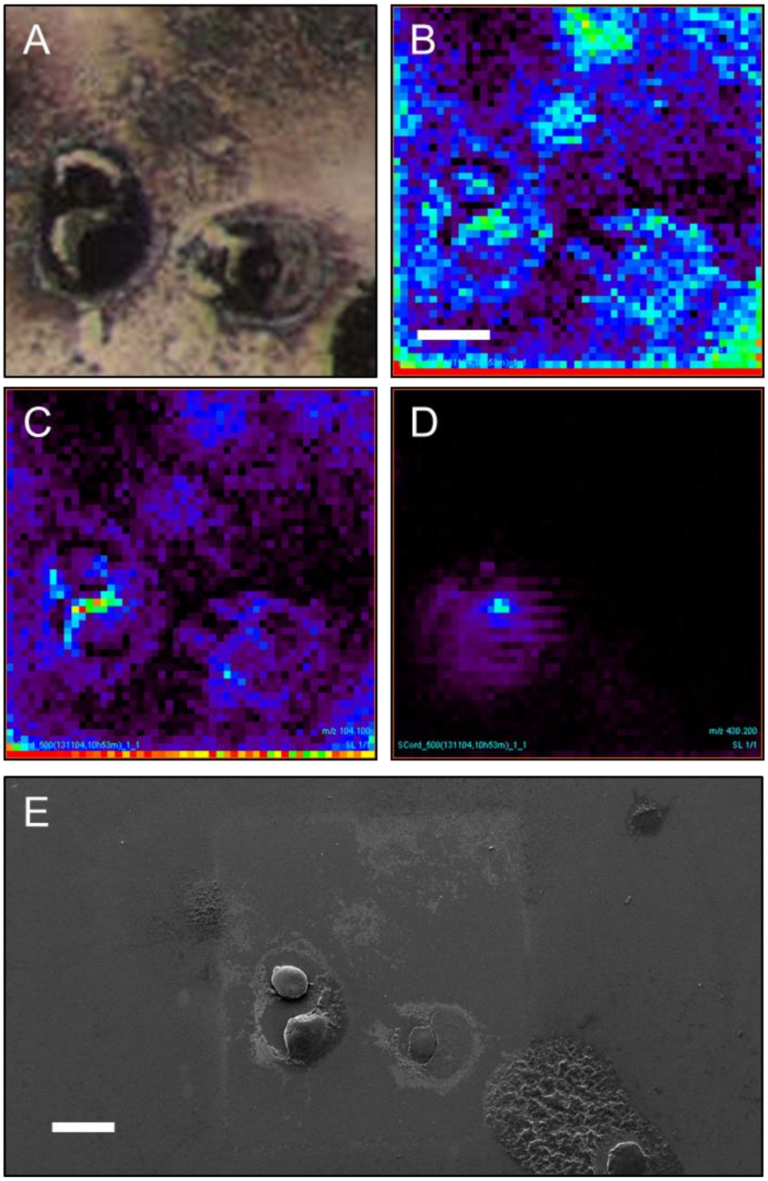

Figure 4.1: Correlated C_{60}-SIMS and SEM images of cultured *A. californica* neurons. A) Optical image (pre-SIMS) of three glycerol-stabilized neurons cultured in close proximity on Si wafer, scaled approximately to match ion images. SIMS ion images of B) phosphocholine (m/z 184.08), C) choline (m/z 104.11), and D) α-tocopherol (m/z 430.38) show molecular distributions on and around the cells. E) The same cells were subsequently sputter coated with Au and imaged by SEM at low magnification, where the SIMS-imaged area is visible as an altered square of substrate surface. Scale bars = 100 µm.

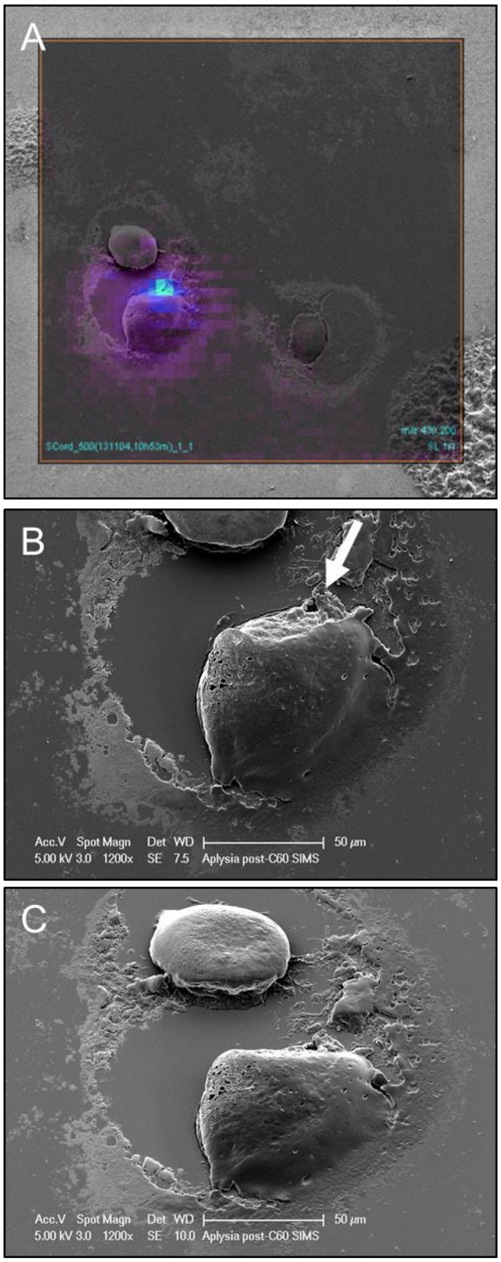

Figure 4.2: Correlation of subcell α-tocopherol localization with physical features. A) Ion image of α-tocopherol is aligned and superimposed with a low-magnification SEM image, allowing precise location of a concentrated "hot spot" within one cell of the three which were imaged. B) Higher-magnification SEM at this location shows subcell features associated with the chemical feature, indicated with arrow, which may correspond with a soma-neurite junction which was damaged and removed during the SIMS process. C) angled-stage SEM shows that subsurface material has been undermined from the adjacent cell from the direction of the incoming primary $C60^+$ beam.

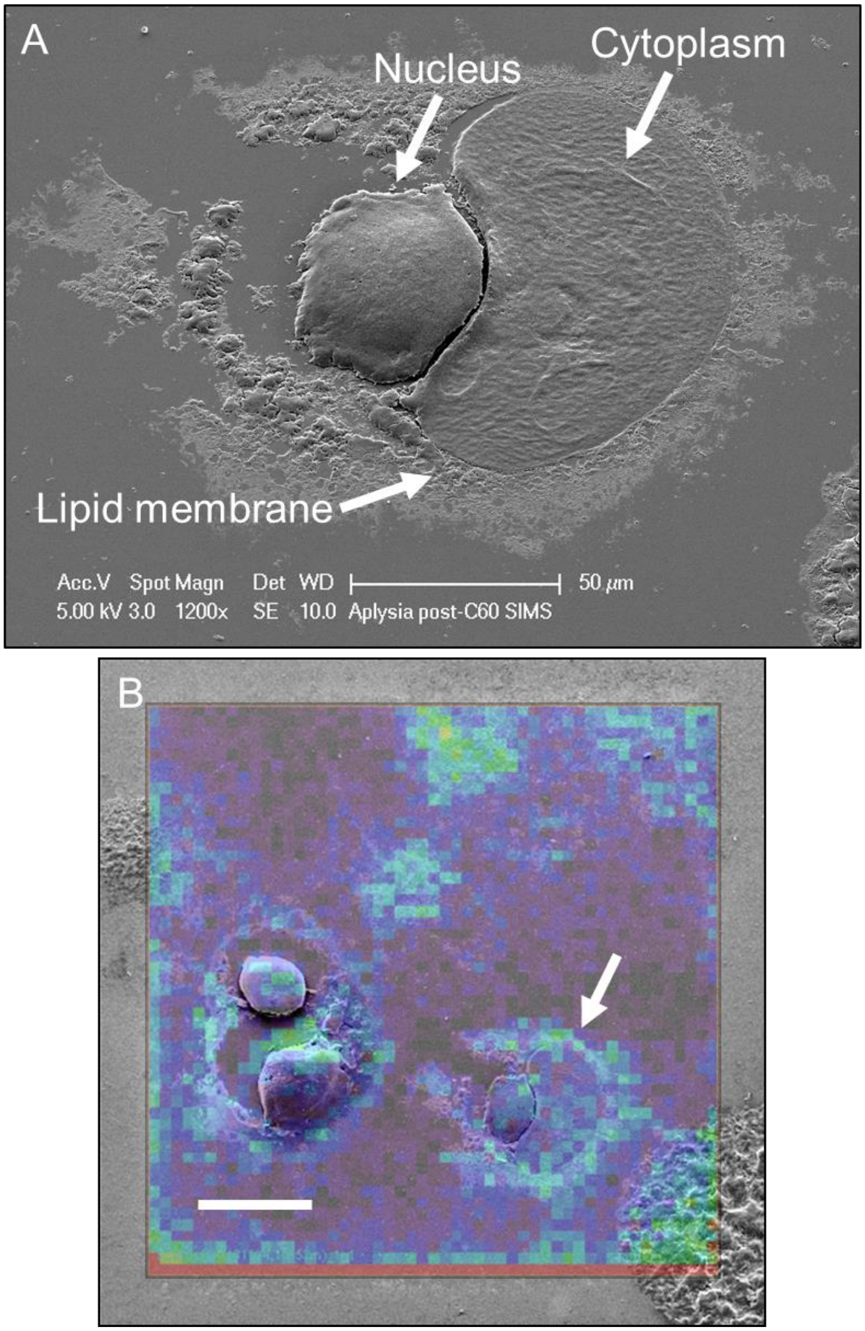

Figure 4.3: SEM reveals micron-scale features in SIMS-imaged cell. A) SEM image of a SIMS-imaged cell resolves micron-scale subcell features putatively identified as nucleus, cytoplasm with organelles, and outer lipid membrane. B) Phosphocholine ion image correlated with low-magnification SEM image shows localization of phosphocholine signal predominantly around the cell, supporting the assignment of this peripheral material as lipid-rich outer membrane. Scale bar = 100 µm.

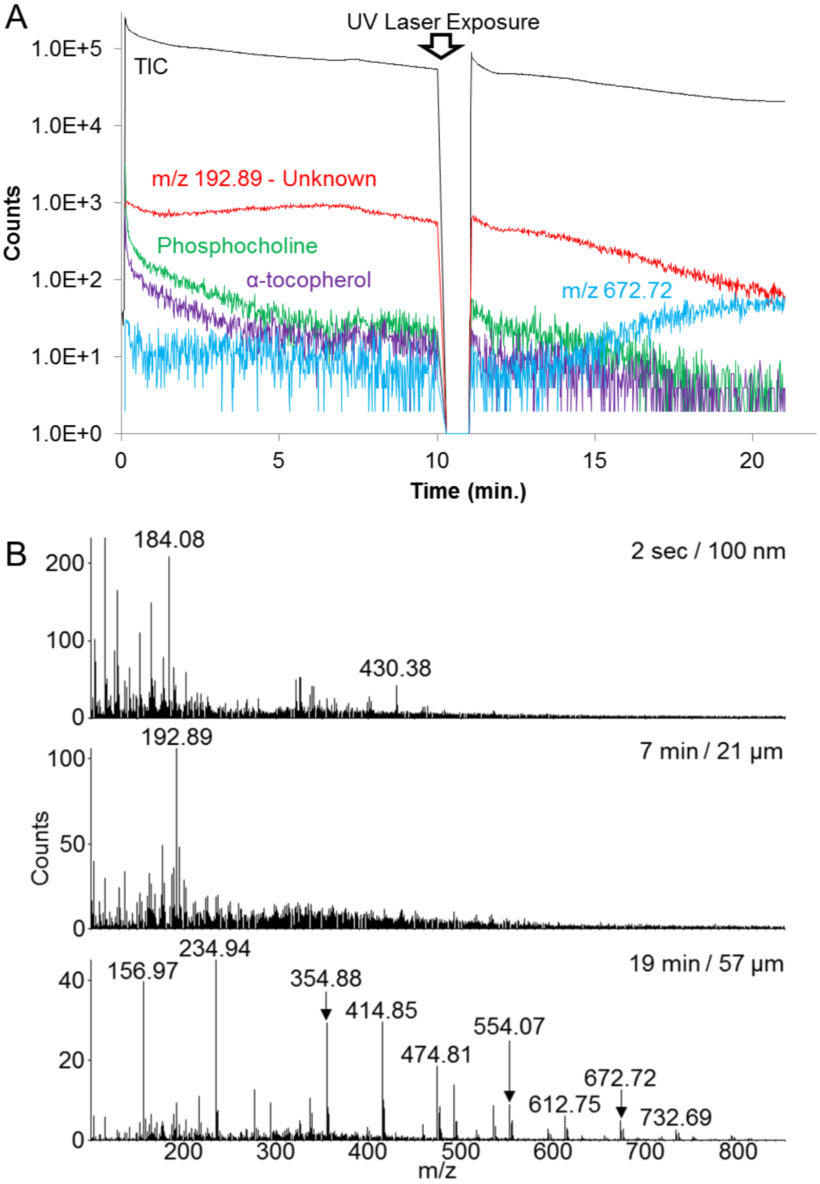

Figure 4.4: C_{60}-SIMS depth profiling of a single cell. A) Stacked mass chromatograms on semi-log plot represent chemical depth profiles of compounds including phosphocholine (m/z 184.08), α-tocopherol (m/z 430.38), unidentified ion m/z 192.89, and putative silicon substrate cluster ion m/z 672.72 acquired from a single neuron cultured on Si wafer. At 10 min. depth profiling was halted, the cell was exposed to UV laser light for ~30 sec, and then profiling was resumed. B) Mass spectra acquired at 2 s, 7 min., 19 min. during the profile experiment represent depth-specific chemical composition, estimated at 0.1, 21, and 57 μm respectively based on estimated ion dose and sputter rates reported in other similar work.[14]

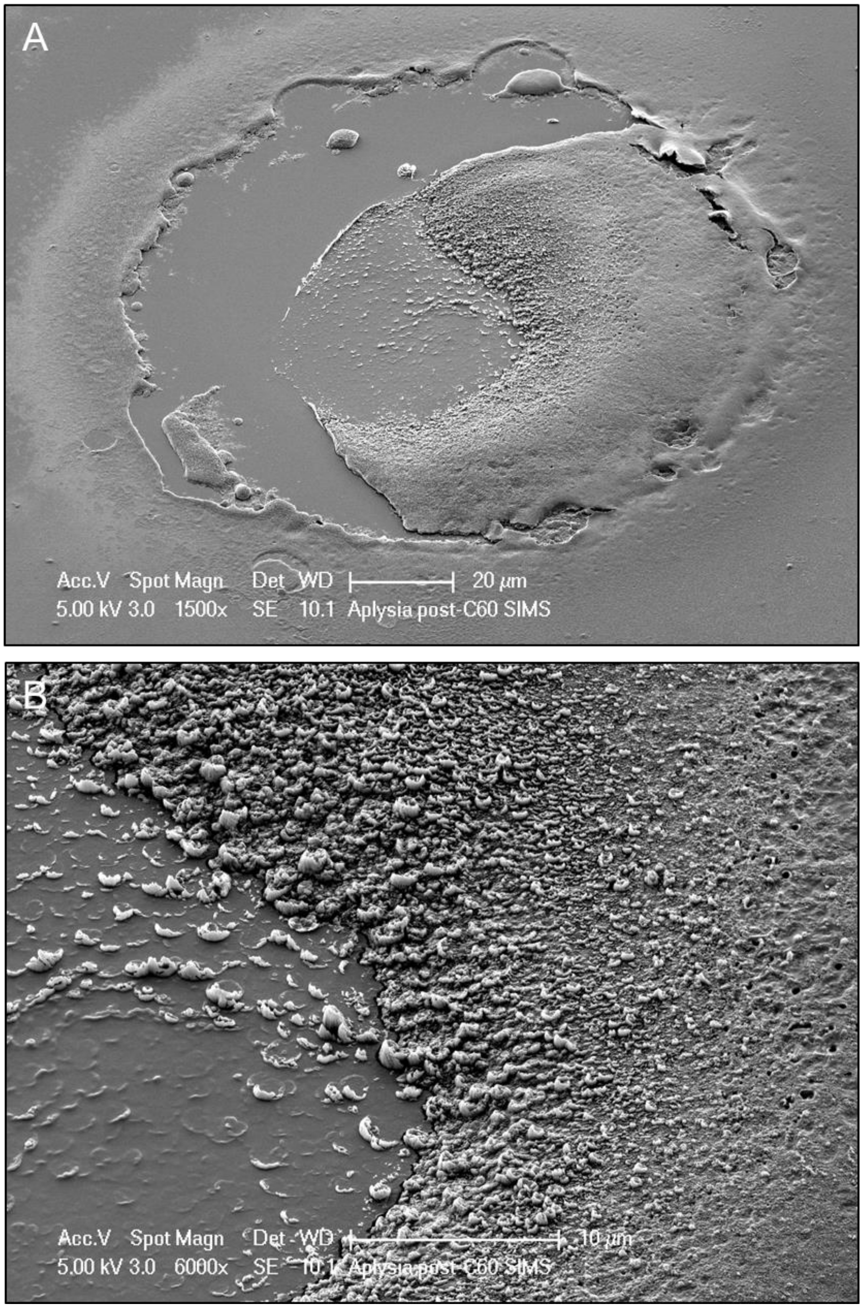

Figure 4.5: Post-depth profile SEM images show effect of C_{60} bombardment on cell material. A) Low-magnification micrograph of the entire cell shows a circular ablated area in the center with D ~ 50 µm, consistent with separate ion microprobe sizing experiments conducted with similar ion gun parameters. B) High-magnification micrograph at the center of the crater shows a heterogeneous consistency through the cell material as well as many <2 µm-sized circular features across both the ablated cell and Si substrate surfaces.

CHAPTER 5

CORRELATED IMAGING – A GRAND CHALLENGE IN CHEMICAL ANALYSIS

NOTES AND ACKNOWLEDGMENTS

This chapter was published as a "grand challenge" critical review article in *Analyst* **2013**, 138 (7), 1924-1939, and represents a joint effort between E. J. Lanni, J. V. Sweedler and collaborators R. N. Masyuko and P. W. Bohn at University of Notre Dame. E. J. Lanni contributed approximately half of the writing including the following sections: introduction, "specific approaches to biomolecular imaging," "challenges in MS imaging," "preliminaries – sample requirements," "sequential *vs*. parallel imaging," and "heterocorrelated imaging of lignocellulosic materials." The article is slightly modified and published here with permission, copyright 2013 The Royal Society of Chemistry. Support from the Department of Energy Office of Biological and Environmental Research through grant SC0006642 and NIH through P30 DA018310 is gratefully acknowledged.

INTRODUCTION

Chemical imaging can usefully be defined as "*the spatial (and temporal) identification and characterization of the molecular chemical composition, structure, and dynamics of any given sample.*"[1] Ideally this encompasses the ability to detect, identify, and visualize the spatial distribution of molecules, known or unknown, over multiple size scales, with arbitrary time resolution, and with single-molecule detection limits. Scientists use chemical imaging to address a wide variety of problems – visualizing the arrangement of atoms patterned on a surface at nanometer scale,[2] the molecular contents of single cells at sub-micrometer scale,[3] and colorless gases released into Earth's atmosphere by cities on the kilometer scale.[4] While none of these imaging applications comes close to fulfilling the above ideal, analytical techniques have been developed in imaging modes that permit access to a considerable fraction of this "chemical imaging space". Now researchers are beginning to invest substantial effort in learning how to combine different imaging modalities, thus amplifying the information-gathering power of imaging experiments.

Chemical imaging involves probing a sample, then detecting a signal that provides spatial and temporal information about the chemical state. Images are usually acquired either by an encoding/decoding operation, as in optical imaging, or by rastering sample and probe past one another. Imaging probes come in a stunning array of interactions – bombarding the sample with photons, charged particles, atoms, or sound waves, for example. Readout can involve detection of these agents, whether they are similar to the incident probe (fluorescence microscopy), or not (photoacoustic microscopy[5]), or reading out the interaction of proximal probes, as in atomic force microscopy, AFM. Chemical imaging can also be accomplished by addition of labels or contrast agents which either generate a detectable event independently, *e.g.* positron emitters for tomography, PET, and radionuclides for autoradiography, or enhance information from an external probe, *e.g.* fluorescent tags in fluorescence imaging and microbubbles for ultrasound.[6] The specific combination of probe and readout define the capabilities, limitations, and therefore useful applications of chemical imaging techniques. From these underlying principles emerge important secondary characteristics such as spatial and temporal resolution, sample penetration depth, sensitivity, multiplex capability, sample preparation requirements, destructiveness, chemical specificity, and information content. One of the principal aims of correlated imaging is to carefully mix and match the imaging tools so that these secondary characteristics can be optimized across the combined imaging platforms.

Since all possible combinations of chemical imaging techniques and applications constitute a vast subject area, here the focus is limited to correlated chemical imaging of molecules in bioanalytical research. Emphasis is placed on how combining suitable, complementary imaging techniques circumvents specific limitations and provides advantages to the researcher. General themes in correlated imaging will be illustrated by reference to correlated mass spectrometric and confocal Raman imaging.

Specific approaches to biomolecular imaging

Biological organisms are chemically, spatially, and temporally complex, exhibiting diversity in size, structure, shape, and concentration spanning orders of magnitude. Chemical and structural features change on time scales ranging from years of organismal life to the millisecond time-frame of a nerve cell's action potential.[7] Understanding how biological systems function and malfunction ultimately requires integration of information across all of these scales, a challenging task where chemical imaging plays a critical role, especially at the microscopic level.

One of the first applications of light microscopy was by Anton van Leeuwenhoek who examined single cells in the first biomolecular microscopic imaging experiment.[8] Probing a sample with incoherent white light and observing what is transmitted or reflected reports principally on morphology, but adaptations of the basic principle can yield chemical information. For example, in fluorescence microscopy a molecule of interest is tagged with an organic dye, protein, or quantum dot, which can then be excited to yield the spatial distribution of the probe. Because fluorophores can be engineered for specific excitation and emission wavelengths and also designed with affinity for particular biomolecules, fluorescence microscopy has become a powerful method for visualizing specific molecular species. Many other imaging methods, such as autoradiography,[9] positron emission tomography (PET),[10] and ultrasound biomicroscopy (UBM),[11] achieve chemical specificity in a similar targeted manner.

How can molecular imaging be performed on biological systems *de novo*, or when a reliable tagging approach does not exist?[12] In this case imaging techniques must deliver information to allow for broad initial chemical survey, while retaining chemical specificity and structural detail for identification of unknowns. Two techniques – mass spectrometry and Raman spectroscopy – serve as excellent imaging platforms for this purpose. Functioning on distinct principles, they provide uniquely information-rich chemical images and complementary advantages. For example, Raman microscopy is non-invasive and non-destructive, so the integrity of the sample is preserved for the MS imaging, thus accessing the high chemical specificity inherent in mass measurement with MS, which however, is inherently destructive. We will use these two techniques to illustrate the challenges and opportunities in correlated imaging.

Mass Spectrometric Imaging

In contemporary practice even high molecular weight biomolecules can be volatilized, ionized, and detected, making MS a robust technique for non-targeted biochemical analysis of tissue samples and single cells.[13] Furthermore, highly-accurate mass assignments and tandem MS (fragmentation) experiments can greatly amplify the information about the identity and structure of compounds, such as peptides. Performing MS with a microprobe, such as a focused laser or primary ion beam, allows different regions of a chemically heterogeneous sample to be chemically profiled.[14] Rastering the microprobe automatically across an area of interest, *i.e.* microprobe-mode mass spectrometric imaging (MSI), yields a chemical map of the region. Each position in the array constitutes a "pixel" in the resulting image and contains a full mass spectrum. Alternatively, microscope-mode MSI involves probing the entire field of view simultaneously with a defocused probe, then preserving spatial information by transmitting the ions to a position-sensitive detector *via* a stigmatic mass spectrometer.[15, 16] Optimal representation of the data remains a significant challenge. It is typically visualized by filtering the spectral data to display the localization of specific ions, resulting in an ion image. A single MSI experiment can generate a separate ion image from each distinct ion within the scanned mass range, and typically tens to hundreds of ions are detected depending on sample complexity and the resolving power of the mass analyzer(s). Nevertheless, the richness of the data, especially when tandem MS^n experiments are performed, allows more powerful means to visualize the data.

Probe choice has a profound effect on MSI data content and quality, especially in terms of ions observed, sensitivity, and spatial resolution. The most common probes used are ultraviolet lasers for laser desorption ionization (LDI)[17, 18] or matrix-assisted LDI (MALDI)[13, 19-21] and focused ion beams for secondary ion mass spectrometry (SIMS),[22-27] though many other viable probe types exist including desorption electrospray ionization (DESI),[28-32] capillary-controlled liquid microjunctions (LMJ),[29, 33-36] laser-ablation electrospray ionization (LAESI),[29, 37-40] and laser ablation with post-ionization by inductively-coupled plasma (LA-ICP).[41-43] An overview and comparison of these MSI probe types is given in **Table 5.1.**

MALDI is a relatively soft (non-fragmenting) ion generation scheme which offers excellent mass range (to MDa),[44] high sensitivity,[45] and µm-scale probe diameters in custom instrumentation.[46] SIMS employs probes with diameters as small as 20 nm [47] suitable for cell- and subcellular imaging, albeit with a harsher ionization mechanism leading to lower sensitivity (higher detection limits) particularly for intact biomolecules. Conveniently, ion beams can also serve to etch away surface layers, such as the contamination from culture medium with cultured cells,[48, 49] making it possible to produce three-dimensional images.[50-52] DESI involves bombarding a sample surface with charged solvent droplets. In comparison to MALDI and SIMS, it provides lower lateral resolution (>35 µm)[53] in exchange for a softer ionization mechanism, which is more amenable to ionization of intact biomolecules. DESI is also performed at ambient conditions rather than in vacuum, a useful feature enabling direct analysis of live biological samples.[54]

Raman Microscopy

In vibrational Raman spectroscopy the frequency spectrum of inelastically-scattered light is measured to obtain information about the functional groups present in a sample.[55] Because a large number of cellular constituents are Raman-active to some degree, Raman spectroscopy offers broad, non-targeted detection of biomolecules in complex matrices, *e.g.* cells, tissues, and biofilms, with chemical specificity relating to structure – as opposed to molecular identity in MS. Moreover, by employing resonance Raman spectroscopy (RRS) and surface-enhanced Raman spectroscopy (SERS), sensitivity can be enhanced dramatically, even yielding single-molecule detection under ideal circumstances.[56]

Similar to MSI, a focused laser is raster scanned across a sample to produce chemical images where each pixel is composed of a full Raman spectrum. Both Raman and IR images provide information on the spatial distribution of the components of a sample, with the intensity of each component related to its abundance. This makes it possible to elucidate quantitative sample component measurements[160] and distributions.[57] In contrast with MSI, Raman spectroscopy is both nondestructive and amenable to ambient conditions. Thus, it is well-suited to live cell imaging.[58] Furthermore, carrying out confocal Raman microscopy (CRM) offers many additional advantages such as 3D and subsurface sample imaging capability, sub-µm (diffraction-limited) lateral resolution, and reduced autofluorescence background by confining the region of excitation and analysis to a small volume.[55] Alternatively, the development of spatially offset Raman spectroscopy (SORS) has afforded subsurface analysis of turbid materials at greater depths than CRM. Based on acquiring Raman spectra at spatial positions offset from the incident laser, the acquired spectra allow signal contributions from the surface and the subsurface layers to be separated, thereby producing pure Raman spectra from the subsurface layers.[59, 60] Because the overpowering Raman and fluorescence signals that arise from the surface can be suppressed, it is feasible to image at depths in the mm range in SORS.

Scanning vs. Fourier Image Formation

2D images showing the spatial distributions of analytes can be acquired in two different ways.

In traditional optical microscopy, images are obtained by focusing light onto an object, measuring the field that is scattered or diffracted, and then processing the information to obtain a spatial map of the distribution of components. Alternatively, the sample and source may be rastered relative one another to produce point by point maps. In the first method, Fourier imaging, the entire object is illuminated, and the resultant scattered/transmitted light is collected by a lens system and transferred to a detector. The collection lens system performs a Fourier transform on the characteristic radiation from the sample to extract spatial frequency information from the object after which it undergoes an inverse Fourier transform to form the image.[61, 62] This method is maximally efficient, because the collected light contains information from each point on the sample.

In scanning based imaging, light is tightly focused to a small spot on the surface. Spectral information is acquired from each spatial location, and images are constructed by rastering, while recording spectra at each position. After collection the multispectral data can be reconstructed in various ways to form an image.[63] Scanned images usually require longer acquisition times, since the time required is proportional to the number of pixels in the image.

Introduction to Correlated Imaging

Because all individual imaging approaches have natural limitations, correlating information acquired from complementary experiments, such as MS (LDI or SIMS) and vibrational spectroscopy (Raman or IR), has the potential to provide more complete information about complex spatial distributions of chemical and molecular components than that available from either technique in isolation.

While single-technique chemical imaging is well developed, experiments correlating information from independent imaging approaches are just beginning to appear. For example, synchrotron FTIR and ToF-SIMS microspectroscopies were coupled in a recent study of steatotic liver tissue.[64] Images acquired from combining these two techniques showed the distribution of lipids and other tissue components and distinctively revealed differences between normal and steatotic tissue. In another study, images of tissue from a cirrhosis liver were acquired using a multi-modal platform consisting of TOF-SIMS coupled to both Synchrotron FTIR and synchrotron UV- microspectroscopies, *viz.* **Figure 5.1**.[65] In both studies, the images provide multimodal chemical information along with the spatial distribution of cellular components, which holds great promise for early diagnosis. In another report, a multi-modal imaging system, comprised of LDI-MS, Raman and fluorescence microspectroscopies, was used to explore a single-cell algae (*Euglena gracilis*), yielding detailed information about the internal structure and chemical composition of cells. Images of individual algal cells provided information on the content and distribution of photosynthetic molecules and phospholipids.[66] Raman and mass spectrometric imaging have also been applied in environmental/geological research. CRM and SIMS images from the same sample at the same location were successfully acquired in a study of Akilia supracrustal rocks, allowing the presence and physical and molecular composition of apatite-based graphitic inclusions in the rocks to be confirmed.[67] In an art conservation application, FTIR, SIMS were combined with x-ray (SEM-EDX) imaging to identify the mineral content and map their spatial distribution on fragments of African wood art.[68] Finally, in our laboratories, CRM and SIMS-MS imaging were combined to study processed samples of *Miscanthus x gigenteus*. These images provide detailed information on the spatial distribution of cell wall components, and correlating Raman and mass spectra from specific spatial locations allow assignment of intracellular globular structures to hemicellulose-rich lignin complexes, an assignment which could not be made definitively from either image alone.[17]

Outline of the Article

The remainder of this article begins by focusing on MS and Raman imaging, identifying their characteristic capabilities and weaknesses. Using these as examples the generic challenges in multispectral image correlation are described. Finally, opportunities for advancing the state-of-the-art are identified and discussed.

CHALLENGES AND OPPORTUNITIES IN MS AND RAMAN IMAGING

Challenges in Mass Spectrometric Imaging

MSI is unique in providing comprehensive molecular maps as a basis to study biological systems. In practice, however, a number of challenges present themselves, many relating to the central problem of ionizing and detecting low-abundance analytes in complex chemical environments which often interfere with measurement.

Sample Preparation

MSI techniques generally impose stringent sample preparation requirements which must be met, while preserving as much of the original spatial chemical information as possible. Flat samples avoid topographically-induced signal artifacts;[69] thus tissues are typically frozen, thin-sectioned (<20 µm thickness), and thaw-mounted to a flat substrate for analysis. In the case of vacuum MALDI and SIMS sources, ion extraction prefers a conductive substrate; often a metal plate or indium tin oxide-coated microscope slide, the latter permitting transmission light microscopy as well. The vacuum requirement of conventional MALDI and SIMS presents an additional challenge in high-spatial resolution work, since biological samples with high water content may collapse and disrupt native structure upon vacuum desiccation. Chemical fixation,[70, 71] stabilization with glycerol,[71, 72] and cryogenic methods such as freeze-drying and frozen-hydrated preparation [52, 73] have all been successfully used to address this issue.

Since MSI is a form of surface analysis, sample preparation may also include steps to uncover subsurface features of interest, especially the case for SIMS which probes only the top few nanometers of the sample.[74] Freeze-fracturing cells is one effective way to accomplish this,[75] and in-source manipulation methods offer effective alternatives. Polyatomic “cluster” primary ion beams such as C_{60} or Ar_{2000} excel at removing material while causing little sample damage,[76, 77] thus serving as effective etching tools to interrogate cell contents.[78] Similarly, orthogonal fast ion beam milling can shave off nanometer-scale layers of material between imaging scans.[79]

Sensitivity and Ion Suppression

MS provides excellent sensitivity, down to zeptomole LODs with optimized sample preparation.[45] However, since MSI is necessarily performed *in situ* to preserve spatiochemical features, optimization is more difficult and cannot include means to simplify a complex mixture – although notably, a liquid microjunction probe does allow separation prior to electrospray ionization.[36] As a result, MSI detection limits are reduced in practice due to ion suppression,[80] arising from co-desorption of compounds such as inorganic salts or easily-ionized molecules such as glycerophospholipids,[81] potentially producing false negatives in MSI. It also complicates quantitation in MSI, since ion intensity may not accurately report analyte concentration in this case. One way to reduce ion suppression is to remove interfering compounds while taking care to leave analytes of interest undisturbed, and various chemical rinses, including ammonium salt solutions,[82] water and organic solvent rinses,[83] have been devised to accomplish this. Care must be taken to avoid analyte loss or delocalization during rinsing, and additional method optimization, such as pH adjustment, is helpful in some cases.[84]

LDI benefits greatly from addition of a matrix which assists in desorption and/or ionization of the sample, and this can be true for SIMS as well.[21, 27] The best known and most versatile examples are the organic laser-absorbing compounds for MALDI, but a similar effect can be achieved with metal coatings,[18] derivatized nanoparticles,[85] and nanostructured substrates.[86, 87] Selecting the most effective matrix for a given specimen is certainly a challenge, but in MSI it is equally important to optimize extraction (high sensitivity) without significant chemical delocalization (loss of spatial information). Unfortunately these two goals compete; pneumatic spray of organic matrices [72] offers superior sensitivity while drier applications such as sublimation preserve small spatial features by generating a uniform coat of µm-sized crystals.[88] Preparation can be improved by separating extraction and crystallization steps,[89, 90] but optimizing both sensitivity and spatial resolution remains a challenge.

Spatial Resolution

SIMS is capable of high resolution (<100 nm) chemical imaging with monatomic ion sources, but these typically yield few intact molecular ions. In contrast, polyatomic cluster ion sources, including C_{60}, Bi_3, and Au_{400}, greatly enhance molecular ion yields and now rival monatomic sources in focus as well.[21, 47, 91, 92] Likewise laser ablation probes can reach essentially diffraction-limited focus [46, 93] and near-field enhancement approaches can surpass this limit.[94] Given the substantial progress in MSI microprobe quality, spatial resolution is now limited largely by the ability to detect sufficient ion counts,[95] a challenge related closely to sample preparation and detection limits. Also, increasing spatial resolution leads to longer acquisition times and larger data volumes, so at high resolution datasets become prohibitively large, unless the imaged region is decreased accordingly.

Chemical Specificity: Mass Accuracy and Resolution

MS is a highly chemically-selective detection platform, but it is not without limits. One such limit is mass accuracy; nominal (integer) or low-accuracy mass assignments leave the identity of the detected ion highly ambiguous, whereas a small mass error (*e.g.* ±0.0001 Da) provides an accurate mass from which the exact elemental composition of the ion can be inferred.[96] The accuracy of mass measurements depends critically on the available MS analyzer, working mass range, and sometimes sampling conditions, and completely unambiguous elemental formulae are often not obtainable. Chemical interference, a second limit to the chemical specificity of MS detection, arises when peaks from two or more ions overlap and cannot be distinguished. The consequence of chemical interference in MSI experiments is that an ion filter will sum all of the overlapping peaks and display them as a single image, thus concealing potentially important chemical complexity. This problem can be mitigated to some degree by MS instrumentation, *i.e.* higher resolution analyzers such as Orbitrap and FT-ICR yield narrower peaks and decrease (improve) the mass difference that can be resolved. "Adequate" mass resolution is difficult to define, since this depends entirely on the masses and mass differences of the analytes of interest, but several recent publications have demonstrated the importance of resolving nearly-isobaric species in MSI experiments, especially among lipids, metabolites, and other small molecules.[78, 97] In some cases, several distinct biomolecules are perfectly isobaric, and in this case identification depends on additional steps to separate and identify the ions, such as ion mobility chromatography [98] or tandem MS.[99]

Data Processing and Analysis

MS images can produce up to hundreds of gigabytes of data, and continuing improvements to effective spatial resolution as well as three-dimensional imaging capability stand to further increase dataset size. Thus, one challenge is to compress the data without losing useful spectral information, and another is to automate data processing to efficiently discern significant spatiochemical features against a rich chemical background.[100] Workflows typically involve spectral refinement (smoothing, baseline correction, peak alignment or binning), image refinement (pixel normalization or spatial denoising), and classification of image regions into anatomically- or chemically-distinct regions.[101] Classification is achieved by clustering or multivariate approaches, such as principal component analysis, k-means clustering, and maximum autocorrelation factorization,[102-104] which allows informative segmentation maps of the analyzed region to be constructed that may reveal distinct chemical regions and colocalization of chemical species. Despite this progress MS image processing remains complex, time-consuming, computationally intensive, and prone to image artifacts,[105] so additional work is needed to build an efficient and reliable pipeline for it.

Challenges in Raman Imaging

Because vibrational Raman spectroscopy provides chemical functional group information, it does not require labeling to generate image contrast. Thus, it non-destructive and requires little or no sample preparation. Raman signals are not affected by water, which scatters only weakly, making it well suited to study biological samples. Performing Raman spectroscopy in a confocal microscope allows image acquisition at high spatial resolution in all three dimensions. Confocal Raman microscopy (CRM) is, thus, a tool with applications in both plant[106] and biomedical[107] research. An overview and comparison of different approaches to vibrational imaging is given in **Table 5.2**.

SERS Imaging

While Raman microscopy is rich in information about the composition and spatial distribution of analytes in heterogeneous materials, Raman scattering is an inherently weak process (*ca*. 1 scattered photon in 10^9 incident photons), resulting in long imaging times and limiting its application to sample abundant components. Thus, there is strong interest in methods to enhance sensitivity, such as surface-enhanced Raman spectroscopy (SERS), where the apparent Raman cross-section is enhanced by many orders of magnitude by placing it in close proximity to a nanoparticle or a roughened noble metal surface.[108, 109] The signal enhancement is attributed, in part, to the strong electromagnetic fields that are generated upon excitation of local surface plasmon resonances (LSPR). Population-averaged SERS enhancements are typically in the range of 10^3-10^6, while individual molecule enhancements as high as 10^{14} can be achieved under the right conditions, rendering Raman comparable to fluorescence in sensitivity.[110] SERS can be exploited in imaging experiments,[111] and, being non-invasive, it is attractive for biological and biomedical applications. Over the years SERS imaging has been applied to cancer research studies,[107, 112] *in vivo* imaging studies,[113] medical diagnostics,[114] bacteria and biofilms[110] and biological processes in cells.[89] SERS has achieved great successful at probing intracellular components and processes, however, SERS has not yet proven capable of probing the nucleus, because the nuclear membrane pores are too small to admit nanoparticles. In addition to its sensitivity advantages, the metallic features responsible for SERS can quench the autofluorescence ubiquitous in biological experiments. However, because SERS intensities vary strongly with nanoscopic details of the molecular environment, it is difficult to make quantitative comparisons of SERS signals between sample sites.[115] Another challenge to employing SERS imaging is the need for a metallic substrate. Great effort has been invested in extending SERS beyond metallic nanoparticle substrates.[116] One advance is tip-enhanced Raman scattering (TERS),[117, 118] in which the Raman signal is enhanced by the intense fields generated at a tip that can be rastered over the sample. TERS experiments combine scanning probe microscopy features with SERS to provide spatial, structural and chemical information. The major advantage of TERS is that the enhanced Raman signals are confined to a small area in the immediate surrounding the tip, which is typically much smaller than a diffraction-limited laser focal spot, thus enabling imaging with nm-scale lateral resolution.[119, 120] However, the Raman signal in TERS is still weak, primarily because the sampled region (20-50 nm diameter) is small. To circumvent these difficulties, Tian *et al.* recently developed a novel set of enhancement media based on SiO_2-shell-Au/Ag core nanoparticles. These structures show great promise, since they combine the spatial localization available from TERS with the ability to bring the enhancement medium to the sample under a wide range of environmental conditions.[121]

Spatial Resolution

Spatial resolution in Raman microscopy is primarily determined by the wavelength of light, λ, numerical aperture of the objective, $NA = n \sin\theta$, and the refractive index of the medium, n. Abbe theory gives the minimum distance Δx between two adjacent points that can be resolved by a microscope. When the objective and condenser NAs are identical it is defined by the two-point Rayleigh resolution criterion, [122, 123]

$$\Delta x = \frac{0.61\lambda}{NA} \tag{5.1}$$

Raman imaging is primarily implemented in a scanning confocal configuration, which rejects signal contributions out of the focal plane, resulting in higher axial resolution compared to conventional microscopy. The depth resolution of a confocal microscope is,[123]

$$\Delta z = \frac{4.4 n\lambda}{2\pi (NA)^2} \tag{5.2}$$

thus being determined by the physical properties of the sample and the efficiency of the collection and imaging optics. In practice, axial resolution is degraded by spherical aberration, and the actual resolution realized is typically less than the theoretical value. Clearly, high NA objectives, imaging in a high index medium, *e.g.* oil, and employing shorter wavelengths all improve spatial resolution, with best results being on the order of ~ λ/2 (~200 nm). Enhanced spatial resolution in Raman imaging can also be obtained by TERS; in a recent communication, a λ/60 resolution was reported in TERS imaging study of carbon nanotubes.[124] Near-field scanning optical microscopy and Raman spectroscopy has also been combined to achieve high spatial resolution imaging. For example, 100 nm resolution was reported in a DNA imaging study.[125] In addition, standard Raman experiments can be modified by spatial oversampling followed by deconvolution to enhance the spatial resolution.[126]

Information content

Image formation in CRM entails collecting spectra at a spatial location (pixel) on a sample, which upon processing yields a map of chemical functional groups identified by their characteristic fingerprint vibrations.[127-129] Unfortunately, while this is an efficient method to analyze small datasets, it is not suitable for large image data sets having subtle molecular variability within the image. These datasets require much more sophisticated chemometric tools, in order to extract all the information present in the CRM image.

Chemometrics – essentially "*the entire process whereby data, e.g. numbers in a table, are transformed into information used for decision making*,"[130] – is a powerful adjunct in Raman imaging, since each pixel represents an entire spectrum. Chemometric tools can extract subtle relationships hidden in the complex chemical and physical phenomena represented in spectral datasets.[131, 132] Pattern recognition tools, which dominate usage in chemical analysis, can further be grouped into unsupervised and supervised leaning approaches. Unsupervised learning techniques, such as principal component analysis (PCA) and hierarchal cluster analysis (HCA), work well for initial analysis of Raman images, as they seek to identify data clustering without *a priori* conditions.

In PCA, the variation present in a data matrix is decomposed and represented using a small number of factors - the principal components – chosen to expose the underlying basis for the observed behavior. Frequently, PCA is implemented, and the principal component values for a large number of samples are plotted in an *n*-dimensional space in order to identify common responses. HCA, on the other hand, examines abstract inter-point distances between samples and represents that information in a two-dimensional dendrogram, in which clusters of data can be identified by eye. The dendrograms are created through an iterative process of sample-specific cluster joining, which is repeated until only one cluster remains. The distances between clusters give information on variations in the data, thereby identifying those data subsets that are most alike, *i.e.* are clustered. PCA has become a staple in Raman spectroscopy and imaging generally,[131, 133-135] while HCA is a common approach used in biological Raman imaging.[136-138]

Supervised learning approaches are designed to construct models, which are used to classify samples. Unlike, unsupervised models, these approaches excel when there is significant *a priori* information about the sample. A set of known samples, the training set, is used to establish the number of classes and how the different classes are distinguished from each other. Validation diagnostics are critical in order to assess the reliability and quality of the model and the sensitivity to the various parameters within the model. Sample tools are designed to determine the relationship between different samples and identify any unusual samples, while the variable tools are used to also determine the relationship between the different variables and identify any outlying variables.[130] Two frequently used examples of supervised learning techniques are K-Nearest neighbor (KNN) and Soft Independent Modeling of Class Analogies (SIMCA). In KNN, the class of the unknown sample is considered to be the class of the samples that are found nearest to it in multi-dimensional space.[130] KNN's ability to identify samples is a powerful tool that has been used in the identification of counterfeit drugs.[139] SIMCA, models are designed based on the shape and position of an object formed by the samples within an abstract row space to define the class. PCA is used for modeling the object formed by an individual class. Classes are represented in multi-dimensional space, and samples are classified by determining the spatial region in which the samples belong.

CORRELATING MSI AND CRM

Preliminaries – Sample Requirements

Additional challenges arise when correlating two spectral imaging modes; we will illustrate the generic problems by considering the specific issues raised when CRM and MSI are combined. These begin with sample preparation, where fortunately the requirements are not mutually exclusive. CRM and MSI both perform best with thin (<20 µm), flat specimens; tissue samples must be sectioned and mounted to a substrate for analysis. Glass microscope slides are convenient, since they allow additional optical microscopy to be performed, *e.g.* to map the specimen morphologically with stains, afterwards. Because MALDI and SIMS ion sources both depend on a uniform electric field for ion extraction, conductive indium tin oxide (ITO)-coated slides are typically used, and fortuitously ITO does not interfere with Raman measurements.[140] Since the samples are introduced to vacuum for MS analysis, biological specimens must be fixed and dried or otherwise stabilized, *e.g.* by frozen hydration or glycerol addition, beforehand. Chemical fixation methods, such as ethanol or formaldehyde treatment, are Raman-compatible for some samples, although care must be exercised, especially for protein components where chemical cross-linking can affect α-helix and β-sheet specific vibrations.[141] MSI may benefit from additional chemical treatments depending on the experiment. Typically these involve either chemical washes to reduce ion suppression or chemical coatings, *e.g.* organic matrices, metal plasma, or nanoparticles, to enhance sensitivity. Many such treatments have yet to be tested for compatibility with Raman imaging, though we have previously shown that in some cases they are not only compatible but in fact mutually beneficial.[140]

General Technical Challenges

To fully exploit the possibilities inherent in correlated imaging, a number of technical challenges must be addressed. These stem from the fact that the experiments are performed sequentially and because experimental capabilities and conditions differ between MSI and CRM. Three major experimental concerns for the particular case of MS-Raman imaging are spatial registry, sample integrity, and dynamic range differences.

Digital image correlation[142] is typically applied to pairs of images before and after application of a small perturbation, thus yielding information about the differential response to the perturbation. When the perturbation is in the temporal domain, raster-scan image correlation spectroscopy can be used to produce image data in which each differential pixel represents information offset in time by the raster period.[143] Of more utility are ideas borrowed from generalized image cross-correlation spectroscopy (ICCS).[144] In ICCS, fluctuations between two differently-labeled species are correlated in both space and time using the generalized correlation function, $g_{ab}^{(2)} = \langle \delta I_a(x,y) \delta I_b(x+\xi, y+\eta) \rangle$, where $\delta I_{a,b}$ are the intensity fluctuations corresponding to labels *a* and *b*, which might be mass and vibrational frequency in MS-CRM correlations. Of course, ICCS is optimally applied only when the labels can be observed simultaneously under exactly the same conditions, a requirement which clearly cannot be met in the MS-Raman experiment. To address this problem Todd and coworkers developed a semiautomated analytical image correlation approach and specifically addressed the correlation of optical (*i.e.* morphological) and SIMS data in images presenting both regular and irregular features, differentially tagged according to their chemical (atomic) composition.[145] They addressed both the image registration problem, by devising a relative positioning scheme, and the differential (between SIMS and optical refraction) sensitivity issue to produce a semi-automated system to identify complementary optical and MS image features.

In order to implement these approaches to image correlation spatial registry must be achieved between the two image acquisition modes. A method that is adaptable to both MSI and CRM identifies the exact regions of interest (ROIs) on the sample,[17] and a structural landmark can be used to achieve spatial registry. In our previous work on lignocellulosic materials spatial landmarks were established with a bright field microscopy image, and based on the optical image, a grid of 50-100 µm pitch (typical) for LDI-MS was defined and used as a fiducial reference to establish a small number (ROIs) for study by SIMS and CRM imaging.

While great emphasis is placed on the spatial registry, it is just as important to ensure that the orientation of the sample is maintained to minimize scaling issues arising from sample rotation. This is an issue that can be solved by an index notation along with the spatial registry feature to ensure the sample is placed on the same scale while imaging using both techniques. While the obvious concern from an imaging perspective would be that the images would not be identical, rotation has the ability to produce results that produce apparent chemical differences based on sample orientation. An example of this arises in Raman experiments with functional groups presenting signals that are excitation laser polarization-dependent.[146] Finally, different techniques invariably produce images with different characteristic pixel sizes, leading to image dilation uncertainties. For images obtained with comparable, but not equal, pixel sizes, such as are obtained by SIMS and CRM, the image pattern classification scheme described below offers the potential to harmonize information. Unfortunately when the pixel sizes are very different, as they are in MALDI-MSI and CRM, there is little that can be done *ex post facto*. In this case it is better to work to make the pixel sizes more closely commensurate, for example by reducing the focal diameter of the MALDI laser.

Another area of concern is the differing dynamic ranges of the image acquisition techniques. For example, mass spectrometry can be sensitive, especially when compared to unenhanced Raman experiments. As a result data acquired from MS and native Raman can present significant variations feature acquisition, rendering correlation challenging. Features which may lie in the middle of the dynamic range of one technique might not be detectable by the other. In the MSI-CRM example, increasing the sensitivity of CRM, for example by using SERS, could alleviate the problem, but thorough cross-validation experiments with painstakingly fabricated serially diluted reference standards would be needed.

Sequential vs. Parallel Imaging

Heterocorrelated imaging is, of necessity, nearly always sequential, which raises the problem of sample registration and regions of interest (ROIs). Accurately locating and addressing the ROI for the downstream imaging experiment (MSI, in our case) can be achieved through the use of mutually-detectable fiducial marks in the specimen or coordinate landmarks printed on the substrate, as described above.[147] Any misalignment of ROIs between the two imaging systems must be corrected post-acquisition, and of course misidentification essentially dictates re-imaging. Thus, although sequential imaging is the straightforward approach, in the absence of highly specialized instrumentation it introduces extra challenges and potential sources of error which must be addressed.

Parallel image acquisition with a hybrid Raman/mass spectrometer is another solution to address the issues inherent in sequential imaging. In fact, some of the challenges associated with incorporating a confocal Raman microscope (CRM) into a mass spectrometer have already been addressed, at least indirectly. Methods for delivering focused laser radiation into the source for LDI while minimally perturbing ion extraction optics critical to MS sensitivity have been developed, the relevant result being that two geometries – transmission [46] and reflection,[93] both orthogonal to the surface – allow nearly diffraction-limited focus on a sample surface. The high-numerical aperture objective lens required for these configurations is also suitable for both delivering the excitation laser and also efficiently collecting Raman scattered light from a sample, thus a single lens with proper transmission and aberration characteristics could fulfill all three roles.

One possible configuration for such a transmission-mode hybrid CRM/MS instrument is shown in **Figure 5.2**. In this system MS is performed by either UV LDI or C_{60} SIMS depending on sample and imaging requirements, *e.g.* lateral and depth resolution. LDI is accomplished coaxially in transmission-mode through a vacuum window and transparent sample substrate, in a geometry originally demonstrated by Hillencamp *et al.* [46] and more recently implemented by the Caprioli group for tissue imaging.[148] C_{60} primary ions for SIMS are delivered at 45° to the sample surface. Probes are aligned and fixed in position, and imaging is accomplished by rastering the sample on an X/Y translational stage with sub-µm precision in either continuous motion or discrete point mode, depending on sensitivity and time requirements. Ions generated from either source are extracted with a low voltage electric field into a (QTOF) system capable of tandem MS with CID, similar to the dual-source QTOF design reported by Carado *et al*.[149] In a novel extension of this previous work, CRM can be performed here in backscatter mode using the same objective lens employed to focus the UV LDI laser, allowing both excitation lasers to be focused to <1 µm at the sample. Z-axis piezoelectric devices could then be used to allow confocal access to various depths for 3D imaging.

Although data acquisition would still be sequential in the sense that the Raman spectrum would be acquired at each pixel before (destructive) probing by MS, properly aligned probes would yield Raman and MS data automatically spatially co-registered at each pixel without the need for physical markers or post-acquisition correction. Previous heterocorrelated imaging involved manual comparison of images, but with such automatically registered CRM/MSI one might think about combining mass and Raman spectra into a single hybrid spectrum for each pixel. This would open new possibilities for statistical analysis and image or sample classification based on the complete coherent assembly of mass spectrometric and light scattering information, potentially a powerful new tool in tissue, cell, or organelle-level profiling. Another advantage offered by such an instrument is that CRM could be used to conduct a relatively rapid (100 msec/pixel) chemical survey scan to identify particularly appealing ROIs before a lengthier (>1 sec/pixel) MSI scan is initiated, supplementing the reflected visible light image typically used for sample positioning within an MS source.

Heterocorrelated Imaging of Lignocellulosic Materials. We have recently applied a heterocorrelated chemical imaging approach utilizing CRM and MSI in order to characterize biofuel feedstock at subcellular spatial resolution, as shown in **Figure 5.3**.[44] *Miscanthus x giganteus* is a fast-growing grass that generates high mass yield at low cost, so it is an appealing alternative to corn as a biofuel source. However, polysaccharides, cellulose, and hemicellulose must first be freed from the lignin matrix of the cell walls before they can be hydrolyzed and fermented. Thus, elucidating how these molecules are distributed within the plant's cells, and how various chemical treatments extract them, are critical questions for optimizing *Miscanthus* biofuel processing methods. To accomplish this, LDI, SIMS and CRM were incorporated into a combined study of processed *Miscanthus*. After optimizing the methods individually[18, 84] in order to visualize lignin and saccharide distributions within cross-sections at µm-scale spatial resolution, LDI, SIMS and CRM were performed sequentially on a common vascular bundle region of a processed plant. ROIs were identified and registered using fiducial landmarks on the sample, allowing precise alignment of the images. As a result, the compounds of interest could be detected by both Raman scattering, with lignin-related bands at 1607 and 1630 cm^{-1}, and SIMS, with characteristic ions at *m/z* 95, corresponding to a $C_6H_5OH_2^+$ fragment ions of lignin, for cross-validating chemical images.

Interestingly, completely new information was available from the correlated imaging experiments. As shown in **Figure 5.4**, the processed *Miscanthus* samples exhibit a globular mass associated with the interior cell walls. Examination of the Raman spectrum in these regions revealed a band at 478 cm^{-1}, characteristic of lignin-hemicellulose complexes. While the cell walls show characteristic cellulose and lignin bands where these components are colocated, Raman bands characteristic of hemicelluloses, another major component of cell walls, are not visible, either because the hemicelluloses in *Miscanthus* cell walls exhibit intrinsically weak Raman scattering, or because their abundance is low. To probe this further, SIMS images were acquired at the same positions. The distribution maps of fragment ions corresponding to lignin (*m/z* 95, $C_6H_5OH_2^+$) and cellulose (*m/z* 105, $C_4H_9O_3^+$) were found to overlap in the cell wall regions, consistent with the CRM images. Detailed analysis of the mass spectra from the globular mass region shows that the intensities of two ions increase significantly: *m/z* 133 ($C_5H_9O_4^+$), a fragment ion from pentose, and *m/z* 181 ($C_6H_{12}O_6H^+$), assigned to either a hexose fragment ion or a pentose cluster ion. Because pentose is the scaffold of hemicellulose, the increased signal intensity of pentose fragment ions from the wall-associated globular structures confirms the tentative assignment made from the CRM image. In this manner hemicellulose was found to be localized primarily with lignin as globular structures within the cells, and CRM was subsequently used to show that NaOH treatment delignifies cells from the inside first without disturbing the cellulose.[106]

Critical Challenges for the Future

It is clear that combining information acquired from two complementary experiments, such as mass spectrometric imaging (LDI/SIMS) and Raman microscopy, has the potential to provide chemical information that may not be available from either method alone. MS and Raman experiments are performed in different experimental environments and the performance levels of the experiments differ significantly in quantitative analysis. Therefore, realizing the full potential of correlating disparate imaging tools requires effort in two stages. First, the performance of each technique must be optimized in isolation. Then careful design of an image correlation strategy must take into account sample registration, differences in instrumental operating characteristics, such as dynamic range, spatial resolution, and depth probed, and chemometric strategies for extracting maximal chemical information from the images acquired.

Raman and MS imaging experiments provide complementary information, with Raman experiments providing functional group information, and mass spectrometry giving accurate mass information that can enable identification of molecular ion species. However, Raman imaging can achieve spatial resolution ~1 μm, while LDI is typically implemented at ≥ 25 μm laser spot sizes, making image cross-correlation difficult. SIMS has better spatial resolution (< 1 μm under optimal conditions), so on the basis of image resolution alone SIMS is a better imaging partner for CRM. However, SIMS sacrifices access to high mass ions that are so informative in biological samples. In static mode, where MS and Raman images are acquired asynchronously, the image data can be correlated off-line by mask-pattern cross-correlation,[125] using, for example, the LDI mass spectrum as a mask for the development of Raman and SIMS cross-correlated images. Considering a mask consisting of $N_x \times N_y$ pixels, the cross-correlation can be obtained by moving the mask over the image, calculating the cross-correlation coefficient, S_{ij}, as a function of the spatial position in the image,

$$S_{ij} = \sum_{k=-N_y/2}^{N_y/2} \sum_{m=-N_x/2}^{N_x/2} \left[I_{mask}\left(m+N_x/2, k+N_y/2\right) - \langle I_{mask}\rangle\right]\left[I_{image}\left(i+m, j+k\right) - \langle I_{image}\rangle\right] \tag{5.3}$$

To validate these derived images, three formal spaces: the pattern space, **P**, mask space, **M**, and classification space, **C**, must be constructed and analyzed in such a way that all of the mathematical distortions which exist between MS and CRM images can be corrected computationally allowing accurate mathematical cross-correlation. These distortions are (a) dilation (change of scale), (b) rotation and translation, which can potentially be addressed by the landmark registration approach described above, and (c) dynamic range, which can be addressed by varying the relative CRM/MS signal intensities, *vide infra*. Although one can manually correlate the image features, the capacity to do this over large sample spaces is compromised in complex biological samples. For these more challenging situations, a classification algorithm can be implemented. Identifying the subset, **P′**, of **P** which most closely matches the mask, permits a multidimensional classification space to be defined by eqn. (5). Minimizing the classification matrix identifies the location of the feature encoded in the mask, **M**:

$$\boldsymbol{C}\left(r_i,c_j\right) = \left[\sum_{i,j}\left(\boldsymbol{M}\left(r,c\right) - \boldsymbol{P}'\left(r_i,c_j\right)\right)^2\right]^{1/2} \tag{5.4}$$

Finally, one of the major advantages of MS techniques is the high sensitivity they afford while Raman techniques are greatly hampered by low sensitivity, thus Raman techniques are not efficient tools for the study of systems with low concentration. The weaker sensitivity of Raman scattering compared to MS can be improved by the use of nanoparticle enhanced SERS and the SHINERS technique[121] which has been shown to afford superior performance compared regular SERS, but again quantitative comparisons will require careful validation with serially diluted samples.

CONCLUSIONS

Correlating information from independent image acquisition platforms constitutes a grand challenge problem in modern chemical analysis. In this article we have considered some of the generic technical challenges associated with correlated imaging and illustrated them with specific reference to MS-Raman correlated imaging. The range of possible operating modes and specific optimization procedures is large, meaning that achieving optimal experimental design is critical. For maximal utilization of multimodal imaging data it is crucial to develop efficient solutions for cross-platform sample registry, to address image distortion effects (dilation, rotation/translation, dynamic range effect) and to implement optimal chemometric strategies for post-acquisition processing. Generically, these issues can be addressed either by fusing disparate image data sets across space and time or by building instruments that allow true simultaneous image acquisition. The effort to do either is significant, yet, it is sure to be handsomely repaid, as the information that can be extracted from correlated images can greatly exceed what it is possible to learn from single imaging tools used in isolation.

REFERENCES

1. N. B. Jackson, *Visualizing Chemistry: The Progress and Promise of Advanced Chemical Imaging*, The National Academies Press, Washington, DC, 2006.
2. D. M. Eigler and E. K. Schweizer, *Nature*, **1990**, 344, 524-526.
3. E. B. Monroe, J. C. Jurchen, J. Lee, S. S. Rubakhin and J. V. Sweedler, *J. Am. Chem. Soc.*, **2005**, 127, 12152-12153.
4. K. L. Mays, P. B. Shepson, B. H. Stirm, A. Karion, C. Sweeney and K. R. Gurney, *Environ. Sci. Technol.*, **2009**, 43, 7816-7823.
5. L. V. Wang and S. Hu, *Science*, **2012**, 335, 1458-1462.
6. A. Greco, M. Mancini, S. Gargiulo, M. Gramanzini, P. P. Claudio, A. Brunetti and M. Salvatore, *J. Biomed. Biotechnol.*, **2012**, 2012.
7. L. Squire, *Fundamental neuroscience*, Elsevier / Academic Press, 2008.
8. A. Leewenhoeck, *Philosophical Transactions*, **1684**, 14, 568-574.
9. E. G. Solon, A. Schweitzer, M. Stoeckli and B. Prideaux, *AAPS Journal*, **2010**, 12, 11-26.
10. T. E. Peterson and H. C. Manning, *J. Nucl. Med. Technol.*, **2009**, 37, 151-161.
11. M. A. Pysz, S. S. Gambhir and J. K. Willmann, *Clin. Radiol.*, **2010**, 65, 500-516.
12. J. E. Shaw, R. F. Epand, R. M. Epand, Z. Li, R. Bittman and C. M. Yip, *Biophys. J.*, **2006**, 90, 2170-2178.
13. S. S. Rubakhin, E. V. Romanova, P. Nemes and J. V. Sweedler, *Nat Meth*, **2011**, 8, S20-S29.
14. T. Zimmerman, S. Rubakhin and J. Sweedler, *J. Am. Soc. Mass Spectrom.*, **2011**, 22, 828-836-836.
15. S. L. Luxembourg, T. H. Mize, L. A. McDonnell and R. M. A. Heeren, *Anal. Chem.*, **2004**, 76, 5339-5344.
16. A. F. M. Altelaar, I. M. Taban, L. A. McDonnell, P. D. E. M. Verhaert, R. P. J. de Lange, R. A. H. Adan, W. J. Mooi, R. M. A. Heeren and S. R. Piersma, *Int. J. Mass spectrom.*, **2007**, 260, 203-211.
17. L. Zhen, C. Li-Qiang, J. V. Sweedler and P. W. Bohn, *Anal. Chem.*, **2010**, 82, 2608-2611.
18. Z. Li, P. W. Bohn and J. V. Sweedler, *Bioresour. Technol.*, **2010**, 101, 5578-5585.
19. N. Goto-Inoue, T. Hayasaka, N. Zaima and M. Setou, *BBA Molec. Cell Biol. Lipids*, **2011**, 1811, 961-969.
20. E. H. Seeley, K. Schwamborn and R. M. Caprioli, *J. Biol. Chem.*, **2011**, 286, 25459-25466.
21. A. Heile, D. Lipinsky, N. Wehbe, A. Delcorte, P. Bertrand, A. Felten, L. Houssiau, J. J. Pireaux, R. De Mondt, L. Van Vaeck and H. F. Arlinghaus, *Appl. Surf. Sci.*, **2008**, 255, 941-943.
22. J. C. Vickerman, *Analyst*, **2011**, 136, 2199-2217.
23. M. L. Steinhauser, A. P. Bailey, S. E. Senyo, C. Guillermier, T. S. Perlstein, A. P. Gould, R. T. Lee and C. P. Lechene, *Nature*, **2012**, 481, 516-519.
24. L. E. Wedlock, M. R. K. Wedlock, J. B. Cliff, L. Filgueira, M. Saunders and S. J. Berners-Price, *Metallomics*, **2011**, 3, 917-925.
25. M. K. Passarelli and N. Winograd, *BBA Molec. Cell Biol. Lipids*, **2011**, 1811, 976-990.
26. H. Nygren and P. Malmberg, *Proteomics*, **2010**, 10, 1694-1698.
27. L. A. McDonnell, S. R. Piersma, A. F. M. Altelaar, T. H. Mize, S. L. Luxembourg, P. D. E. M. Verhaert, J. van Minnen and R. M. A. Heeren, *J. Mass Spectrom.*, **2005**, 40, 160-168.
28. M. Girod, Y. Shi, J.-X. Cheng and R. G. Cooks, *J. Am. Soc. Mass Spectrom.*, **2010**, 21, 1177-1189.
29. C. Wu, A. L. Dill, L. S. Eberlin, R. G. Cooks and D. R. Ifa, *Mass Spectrom. Rev.*, **2012**, 218-243.
30. C. Wu, D. R. Ifa, N. E. Manicke and R. G. Cooks, *Analyst*, **2010**, 135, 28-32.
31. J. M. Wiseman, D. R. Ifa, Y. Zhu, C. B. Kissinger, N. E. Manicke, P. T. Kissinger and R. G. Cooks, *Proc. Nat. Acad. Sci.*, **2008**, 105, 18120-18125.
32. V. Kertesz and G. J. Van Berkel, *Rapid Commun. Mass Spectrom.*, **2008**, 22, 2639-2644.
33. J. Laskin, B. S. Heath, P. J. Roach, L. Cazares and O. J. Semmes, *Anal. Chem.*, **2011**, 84, 141-148.
34. G. J. Van Berkel, V. Kertesz, K. A. Koeplinger, M. Vavrek and A.-N. T. Kong, *J. Mass Spectrom.*, **2008**, 43, 500-508.
35. O. S. Ovchinnikova, V. Kertesz and G. J. Van Berkel, *Rapid Commun. Mass Spectrom.*, **2011**, 25, 3735-3740.
36. V. Kertesz and G. J. Van Berkel, *Anal. Chem.*, **2010**, 82, 5917-5921.
37. P. Nemes and A. Vertes, *Journal of Visualized Experiments*, **2010**, 1-4.
38. P. Nemes, A. S. Woods and A. Vertes, *Anal. Chem.*, **2010**, 82, 982-988.
39. P. Nemes, A. A. Barton, Y. Li and A. Vertes, *Anal. Chem.*, **2008**, 80, 4575-4582.
40. P. Nemes and A. Vertes, *Anal. Chem.*, **2007**, 79, 8098-8106.
41. B. Wu and J. S. Becker, *Int. J. Mass spectrom.*, **2011**, 307, 85-91.

42. B. Wu and J. S. Becker, *Int. J. Mass spectrom.*, **2012**, 323–324, 34-40.
43. J. S. Becker, S. Niehren, A. Matusch, B. Wu, H. F. Hsieh, U. Kumtabtim, M. Hamester, A. Plaschke-Schlütter and D. Salber, *Int. J. Mass spectrom.*, **2010**, 294, 1-6.
44. A. Aksenov and M. Bier, *J. Am. Soc. Mass Spectrom.*, **2008**, 19, 219-230.
45. J. Sjödahl, M. Kempka, K. Hermansson, A. Thorsén and J. Roeraade, *Anal. Chem.*, **2005**, 77, 827-832.
46. F. Hillenkamp, E. Unsöld, R. Kaufmann and R. Nitsche, *Nature*, **1975**, 256, 119-120.
47. F. Kollmer, W. Paul, M. Krehl and E. Niehuis, *Surf. Interf. Anal.*, **2012**, *45* (1), 312-314.
48. J. Brison, D. S. W. Benoit, S. Muramoto, M. Robinson, P. S. Stayton and D. G. Castner, *Surf. Interf. Anal.*, **2011**, 43, 354-357.
49. M. E. Kurczy, P. D. Piehowsky, D. Willingham, K. A. Molyneaux, M. L. Heien, N. Winograd and A. G. Ewing, *J. Am. Soc. Mass Spectrom.*, **2010**, 21, 833-836.
50. J. S. Fletcher, N. P. Lockyer, S. Vaidyanathan and J. C. Vickerman, *Anal. Chem.*, **2007**, 29, 2199-2206.
51. D. Mao, A. Wucher, D. A. Brenes, C. Lu and N. Winograd, *Anal. Chem.*, **2012**, 84, 3981-3989.
52. M. A. Robinson, D. J. Graham and D. G. Castner, *Anal. Chem.*, **2012**, 84, 4880-4885.
53. D. I. Campbell, C. R. Ferreira, L. S. Eberlin and R. G. Cooks, *Anal. Bioanalyt. Chem.*, **2012**, 1-10.
54. J. I. Zhang, N. Talaty, A. B. Costa, Y. Xia, W. A. Tao, R. Bell, J. H. Callahan and R. G. Cooks, *Int. J. Mass spectrom.*, **2011**, 301, 37-44.
55. T. Dieing, *Confocal Raman Microscopy*, Springer, Berlin, 2011.
56. S. Nie and S. R. Emory, *Science*, **1997**, 275, 1102-1106.
57. R. Mendelsohn, H. C. Chen, M. E. Rerek and D. J. Moore, *J. Biomed. Opt.*, **2003**, 8, 185-190.
58. K. Klein, Alexander M. Gigler, T. Aschenbrenner, R. Monetti, W. Bunk, F. Jamitzky, G. Morfill, Robert W. Stark and J. Schlegel, *Biophys. J.*, **2012**, 102, 360-368.
59. N. Stone, K. Faulds, D. Graham and P. Matousek, *Anal. Chem.*, **2010**, 82, 3969-3973.
60. N. Stone, M. Kerssens, G. R. Lloyd, K. Faulds, D. Graham and P. Matousek, *Chemical Science*, **2011**, 2, 776-780.
61. A. Caprihan, E. Fukushima, A. D. Rosato and M. Kos, *Rev. Sci. Instrum.*, **1997**, 68, 4217-4220.
62. C. S. Yelleswarapu, S. R. Kothapalli and D. Rao, *Optics Communications*, **2008**, 281, 1876-1888.
63. M. D. Schaeberle, H. R. Morris, J. F. Turner and P. J. Treado, *Anal. Chem.*, **1999**, 71, 175A-181A.
64. F. Le Naour, M.-P. Bralet, D. Debois, C. Sandt, C. Guettier, P. Dumas, A. Brunelle and O. Laprévote, *Plos One*, **2009**, 4, 1-10.
65. V. W. Petit, M. Réfrégiers, C. Guettier, F. Jamme, K. Sebanayakam, A. Brunelle, O. Laprévote, P. Dumas and F. Le Naour, *Anal. Chem.*, **2010**, 82, 3963-3968.
66. P. L. Urban, T. Schmid, A. Amantonico and R. Zenobi, *Anal. Chem.*, **2011**, 83, 1843-1849.
67. K. D. McKeegan, A. B. Kudryavtsev and J. W. Schopf, *Geology*, **2007**, 35, 591-594.
68. V. Mazel, P. Richardin, D. Touboul, A. Brunelle, P. Walter and O. Laprévote, *Anal. Chim. Acta*, **2006**, 570, 34-40.
69. J. L. S. Lee, I. S. Gilmore, M. P. Seah, A. P. Levick and A. G. Shard, *Surf. Interf. Anal.*, **2012**, 44, 238-245.
70. J. Malm, D. Giannaras, M. O. Riehle, N. Gadegaard and P. Sjövall, *Anal. Chem.*, **2009**, 81, 7197-7205.
71. K. R. Tucker, Z. Li, S. Rubakhin and J. V. Sweedler, *J. Am. Soc. Mass Spectrom.*, **2012**, 23, 1931-1938.
72. E. B. Monroe, S. P. Annangudi, N. G. Hatcher, H. B. Gutstein, S. S. Rubakhin and J. V. Sweedler, *Proteomics*, **2008**, 8, 3746-3754.
73. S. Chandra, M. T. Bernius and G. H. Morrison, *Anal. Chem.*, **1986**, 58, 493-496.
74. K. E. Ryan, E. J. Smiley, N. Winograd and B. J. Garrison, *Appl. Surf. Sci.*, **2008**, 255, 844-846.
75. S. Chandra, G. H. Morrison and C. C. Wolcott, *J. Microsc.*, **1986**, 144, 15-37.
76. J. S. Fletcher, N. P. Lockyer and J. C. Vickerman, *Surf. Interf. Anal.*, **2006**, 38, 1393-1400.
77. J. S. Fletcher, S. Rabbani, A. M. Barber, N. P. Lockyer and J. C. Vickerman, *Surf. Interf. Anal.*, **2013**, 45, 273-276.
78. S. Rabbani, J. S. Fletcher, N. P. Lockyer and J. C. Vickerman, *Surf. Interf. Anal.*, **2011**, 43, 380-384.
79. C. Szakal, K. Narayan, J. Fu, J. Lefman and S. Subramaniam, *Anal. Chem.*, **2011**, 83, 1207-1213.
80. E. A. Jones, N. P. Lockyer, J. Kordys and J. C. Vickerman, *J. Am. Soc. Mass Spectrom.*, **2007**, 18, 1559-1567.
81. J. O. Lay, J. Gidden, R. Liyanage, B. Emerson and B. Durham, *Lipid Technol.*, **2012**, 24, 36-40.
82. P. M. Angel, J. M. Spraggins, H. S. Baldwin and R. Caprioli, *Anal. Chem.*, **2012**, 84, 1557-1564.
83. R. Lemaire, M. Wisztorski, A. Desmons, J. C. Tabet, R. Day, M. Salzet and I. Fournier, *Anal. Chem.*, **2006**, 78, 7145-7153.

84. M. Shariatgorji, P. Kallback, L. Gustavsson, N. Schintu, P. Svenningsson, R. J. A. Goodwin and P. E. Andren, *Anal. Chem.*, **2012**, 84, 4603-4607.
85. S. Taira, Y. Sugiura, S. Moritake, S. Shimma, Y. Ichiyanagi and M. Setou, *Anal. Chem.*, **2008**, 80, 4761-4766.
86. R. Calavia, F. E. Annanouch, X. Correig and O. Yanes, *J. Proteom.*, **2012**, 75, 5061-5068.
87. B. N. Walker, J. A. Stolee, D. L. Pickel, S. T. Retterer and A. Vertes, *J. Phys. Chem. C*, **2010**, 114, 4835-4840.
88. J. Hankin, R. Barkley and R. Murphy, *J. Am. Soc. Mass Spectrom.*, **2007**, 18, 1646-1652.
89. J. Yang and R. M. Caprioli, *Anal. Chem.*, **2011**, 83, 5728–5734.
90. E. B. Monroe, B. A. Koszczuk, J. L. Losh, J. C. Jurchen and J. V. Sweedler, *Int. J. Mass spectrom.*, **2007**, 260, 237-242.
91. D. Weibel, S. Wong, N. Lockyer, P. Blenkinsopp, R. Hill and J. C. Vickerman, *Anal. Chem.*, **2003**, 75, 1754-1764.
92. M. Dubey, J. Brison, D. W. Grainger and D. G. Castner, *Surf. Interf. Anal.*, **2011**, 43, 261-264.
93. B. Spengler and M. Hubert, *J. Am. Soc. Mass Spectrom.*, **2002**, 13, 735-748.
94. B. Dutoit, D. Zeisel, V. Deckert and R. Zenobi, *J. Phys. Chem. B*, **1997**, 101, 6955-6959.
95. P. D. Piehowski, A. M. Davey, M. E. Kurczy, E. D. Sheets, N. Winograd, A. G. Ewing and M. L. Heien, *Anal. Chem.*, **2009**, 81, 5593-5602.
96. A. Godfrey and A. Brenton, *Anal. Bioanal. Chem.*, **2012**, 404, 1159-1164.
97. D. Smith, K. Aizikov, M. Duursma, F. Giskes, D.-J. Spaanderman, L. McDonnell, P. O'Connor and R. Heeren, *J. Am. Soc. Mass Spectrom.*, **2011**, 22, 130-137.
98. Y. Xuan, A. J. Creese, J. A. Horner and H. J. Cooper, *Rapid Commun. Mass Spectrom.*, **2009**, 23, 1963-1969.
99. L. Bai, E. V. Romanova and J. V. Sweedler, *Anal. Chem.*, **2011**, 83, 2794-2800.
100. J. D. Watrous, T. Alexandrov and P. C. Dorrestein, *J. Mass Spectrom.*, **2011**, 46, 209-222.
101. E. A. Jones, S.-O. Deininger, P. C. W. Hogendoorn, A. M. Deelder and L. A. McDonnell, *J. Proteom.*, **2012**, 75, 4962-4989.
102. A. Henderson, J. S. Fletcher and J. C. Vickerman, *Surf. Interf. Anal.*, **2009**, 41, 666-674.
103. G. McCombie, D. Staab, M. Stoeckli and R. Knochenmuss, *Anal. Chem.*, **2005**, 77, 6118-6124.
104. T. Alexandrov, M. Becker, S.-O. Deininger, G. n. Ernst, L. Wehder, M. Grasmair, F. von Eggeling, H. Thiele and P. Maass, *Journal of Proteome Research*, **2010**, 9, 6535-6546.
105. S.-O. Deininger, D. Cornett, R. Paape, M. Becker, C. Pineau, S. Rauser, A. Walch and E. Wolski, *Anal. Bioanalyt. Chem.*, **2011**, 401, 167-181.
106. L.-Q. Chu, R. Masyuko, J. V. Sweedler and P. W. Bohn, *Bioresour. Technol.*, **2010**, 101, 4919-4925.
107. M. D. Schaeberle and V. F. Kalasinsky, *Anal. Chem.*, **1996**, 68, 1829.
108. D. L. Jeanmaire and R. P. Vanduyne, *J. Electroanal. Chem.*, **1977**, 84, 1-20.
109. C. L. Haynes, A. D. McFarland and R. P. van Duyne, *Anal. Chem.*, **2005**, 77, 338A-346A.
110. N. P. Ivleva, M. Wagner, H. Horn, R. Niessner and C. Haisch, *Anal. Chem.*, **2008**, 80, 8538-8544.
111. K. Kneipp and H. Kneipp, *Chem. Rev.*, **1999**, 99, 2957.
112. S. Lee, H. Chon, M. Lee, J. Choo, S. Y. Shin, Y. H. Lee, I. J. Rhyu, S. W. Son and C. H. Oh, *Biosens. Bioelectron.*, **2009**, 24, 2260-2263.
113. R. Liu, J.-f. Liu, X.-x. Zhou and G.-b. Jiang, *Trends Anal. Chem.*, **2011**, 30, 1462-1476.
114. T. Vo-Dinh, F. Yan and M. B. Wabuyele, *Surface-Enhanced Raman Scattering: Physics and Applications*, **2006**, 103, 409-426.
115. M. E. Hankus, L. Honggang, G. J. Gibson and B. M. Cullum, *Anal. Chem.*, **2006**, 78, 7535-7546.
116. T. Zhong-Qun, R. Bin, L. Jian-Feng and Y. Zhi-Lin, *Chem. Commun.*, **2007**, 2007, 3514-3534.
117. R. M. Stockle, Y. D. Suh, V. Deckert and R. Zenobi, *Chem. Phys. Lett.*, **2000**, 318, 131-136.
118. P. Sungho, Y. Pengxiang, P. Corredor and M. J. Weaver, *J. Am. Chem. Soc.*, **2002**, 124, 2428.
119. S. L. Carrier, C. M. Kownacki and Z. D. Schultz, *Chem. Commun.*, **2011**, 47, 2065-2067.
120. B. Pettinger, G. Picardi, R. Schuster and G. Ertl, *Single Mol.*, **2002**, 3, 285-294.
121. J. F. Li, Y. F. Huang, Y. Ding, Z. L. Yang, S. B. Li, X. S. Zhou, F. R. Fan, W. Zhang, Z. Y. Zhou, D. Y. Wu, B. Ren, Z. L. Wang and Z. Q. Tian, *Nature*, **2010**, 464, 392-395.
122. N. J. Everall, *Analyst*, **2010**, 135, 2512-2522.
123. C.-B. Juang, L. Finzi and C. J. Bustamante, *Rev. Sci. Instrum.*, **1988**, 59, 2399.
124. L. G. Cancado, A. Hartschuh and L. Novotny, *J. Raman Spec.*, **2009**, 40, 1420-1426.
125. V. Deckert, D. Zeisel, R. Zenobi and T. Vo-Dinh, *Anal. Chem.*, **1998**, 70, 2646-2650.

126. S. Schlucker, S. W. Huffman and I. W. Levin, *Biomedical Vibrational Spectroscopy and Biohazard Detection Technologies*, **2004**, 5321, 157-163.
127. N. B. Colthup, L. H. Daly and S. E. Wiberley, *Introduction to infrared and Raman spectroscopy*, Boston : Academic Press, 1990.
128. P. Larkin, *Infrared and Raman spectroscopy : principles and spectral interpretation*, Amsterdam ; Boston : Elsevier, 2011.
129. D. Lin-Vien, *The Handbook of infrared and raman characteristic frequencies of organic molecules*, Boston : Academic Press, 1991.
130. K. R. Beebe, R. J. Pell and M. B. Seasholtz, *Chemometrics : a practical guide*, New York : Wiley, 1998.
131. H. Shinzawa, K. Awa, W. Kanematsu and Y. Ozaki, *J. Raman Spec.*, **2009**, 40, 1720-1725.
132. L. Wei-Qi, J. Jian-Hui, Y. Hai-Feng, V. Ozaki, S. Guo-Li and Y. Ru-Qin, *Anal. Chem.*, **2006**, 78, 6003-6011.
133. C. Eliasson, J. Engelbrektsson, A. Lorén, J. Abrahamsson, K. Abrahamsson and M. Josefson, *Chemometr. Intell. Lab. Syst.*, **2006**, 81, 13-20.
134. C. A. Hayden and M. D. Morris, *Appl. Spectrosc.*, **1996**, 50, 708-714.
135. S. Sasic, *Appl. Spectrosc.*, **2007**, 61, 239-250.
136. A. K. Kniggendorf, T. W. Gaul and M. Meinhardt-Wollweber, *Appl. Spectrosc.*, **2011**, 65, 165-173.
137. F. Draux, C. Gobinet, J. Sulé-Suso, A. Trussardi, M. Manfait, P. Jeannesson and G. D. Sockalingum, *Anal. Bioanal. Chem.*, **2010**, 397, 2727-2737.
138. A. Tfayli, C. Gobinet, V. Vrabie, R. Huez, M. Manfait and O. Piot, *Appl. Spectrosc.*, **2009**, 63, 564-570.
139. K. Dégardin, Y. Roggo, F. Been and P. Margot, *Anal. Chim. Acta*, **2011**, 705, 334-341.
140. B. Nie, R. N. Masyuko and P. W. Bohn, *Analyst*, **2012**, 137, 1421-1427.
141. A.-K. Kniggendorf, T. W. Gaul and M. Meinhardt-Wollweber, *Microsc. Res. Tech.*, **2011**, 74, 177-183.
142. A. Kasper, E. Bartsch and H. Sillescu, *Langmuir*, **1998**, 14, 5004-5010.
143. E. Gielen, N. Smisdom, B. De Clercq, M. Vandeven, R. Gijsbers, Z. Debyser, J. M. Rigo, J. Hofkens, Y. Engelborghs and M. Ameloot, *J. Fluoresc.*, **2008**, 18, 813-819.
144. A. Nohe, E. Keating, C. Loh, M. T. Underhill and N. O. Petersen, *Faraday Discuss.*, **2004**, 126, 185-195.
145. T. G. Schaaff, J. M. McMahon and P. J. Todd, *Anal. Chem.*, **2002**, 74, 4361-4369.
146. S. Fischer, K. Schenzel, K. Fischer and W. Diepenbrock, *Macromolecular Symposia*, **2005**, 223, 41-56.
147. K. H. Lau, M. Christlieb, M. SchrÖder, H. Sheldon, A. L. Harris and C. R. M. Grovenor, *J. Microsc.*, **2010**, 240, 21-31.
148. A. Zavalin, E. M. Todd, P. D. Rawhouser, J. Yang, J. L. Norris and R. M. Caprioli, *J. Mass Spectrom.*, **2012**, 47, 1473-1481.
149. A. Carado, M. K. Passarelli, J. Kozole, J. E. Wingate, N. Winograd and A. V. Loboda, *Anal. Chem.*, **2008**, 80, 7921-7929.
150. H. L. Kotze, E. G. Armitage, J. S. Fletcher, A. Henderson, K. J. Williams, N. P. Lockyer and J. C. Vickerman, *Surf. Interf. Anal.*, **2012**.
151. P. D. Piehowski, A. J. Carado, M. E. Kurczy, S. G. Ostrowski, M. L. Heien, N. Winograd and A. G. Ewing, *Anal. Chem.*, **2008**, 80, 8662-8667.
152. R. Stöckle, P. Setz, V. Deckert, T. Lippert, A. Wokaun and R. Zenobi, *Anal. Chem.*, **2001**, 73, 1399-1402.
153. Y. Coello, A. D. Jones, T. C. Gunaratne and M. Dantus, *Anal. Chem.*, **2010**, 82, 2753-2758.
154. G. J. Van Berkel and V. Kertesz, *Anal. Chem.*, **2006**, 78, 4938-4944.
155. M. Offroy, Y. Roggo, P. Milanfar and L. Duponchel, *Anal. Chim. Acta*, **2010**, 674, 220-226.
156. C. S. Colley, S. G. Kazarian, P. D. Weinberg and M. J. Lever, *Biopolymers*, **2004**, 74, 328-335.
157. C. L. Evans, E. O. Potma, M. Puoris'haag, D. Cote, C. P. Lin and X. S. Xie, *Proc. Natl. Acad. Sci. USA*, **2005**, 102, 16807-16812.
158. J. X. Cheng and X. S. Xie, *J. Phys. Chem. B*, **2004**, 108, 827-840.
159. M. D. Duncan, J. Reintjes and T. J. Manuccia, *Opt. Lett.*, **1982**, **7**, 350-352.
160. M. V. Schulmerich, M. K. Gelber, H. A. Azam, S. K. Harrison, J. McKinney, D. Thompson, B. Owen, L. S. Kull, R. Bhargava, *Anal. Chem.* **2013**, 85, 11376-11381.

FIGURES AND TABLES

Probe	**Typical lateral resolution (µm)**	**Max. lateral resolution (µm)**	**Accessible chemical information**	**Advantages**	**Disadvantages**
SIMS	1-5[26, 27]	0.02[47]	Lipids,[25] peptides,[26, 27] metabolites,[150] characteristic molecular fragments,[151] elements,[24] isotopes[23]	Highest attainable lateral MSI resolution, ion beam etching capability allows high resolution depth profiling, 3D imaging	Harder ionization (*vs* MALDI, ESI), mass range limited to <2.5 kDa[27], expensive instrumentation, requires vacuum-compatible samples
MALDI	25-200[72]	0.6[93]	Lipids,[19] metabolites,[13] peptides,[13, 21] proteins[20]	Excellent high mass range, broadly applicable across many biomolecule classes	Matrix application complicates low-mass spectrum (< 500 Da), may reduce lateral resolution
LDI	25-100[17]	0.2[152]	Metabolites, characteristic ion fragments,[18] elements, isotopes	No sample pretreatment, performed on standard MALDI instrumentation	<1 kDa mass range limit, harder ionization (*vs* MALDI, ESI)
LA-ICP	12-160[43]	4[42]	Elements, isotopes[42]	Atmospheric pressure sampling, excellent sampling efficiency	Hard ionization limits chemical information
LA-ESI	200[29]	10[153]	Lipids, metabolites, small drug molecules[29]	Atmospheric pressure sampling, no sample pretreatment	Mass range limited to <1 kDa by laser ablation process
DESI	200[29]	40[32]	Lipids, metabolites, small drug molecules[29]	Atmospheric pressure sampling, no sample pretreatment	Low spatial resolution
LMJ	400-700[34, 154] / 100 (non-contact mode[35])	15[33]	Lipids,[33] metabolites, small drug molecules[34, 36]	Atmospheric pressure sampling, no sample pretreatment, potential for in-line sample processing[36]	Low typical spatial resolution, microjunction stability varies with tissue type & condition

Table 5.1: Performance comparison of some common MSI microprobes.

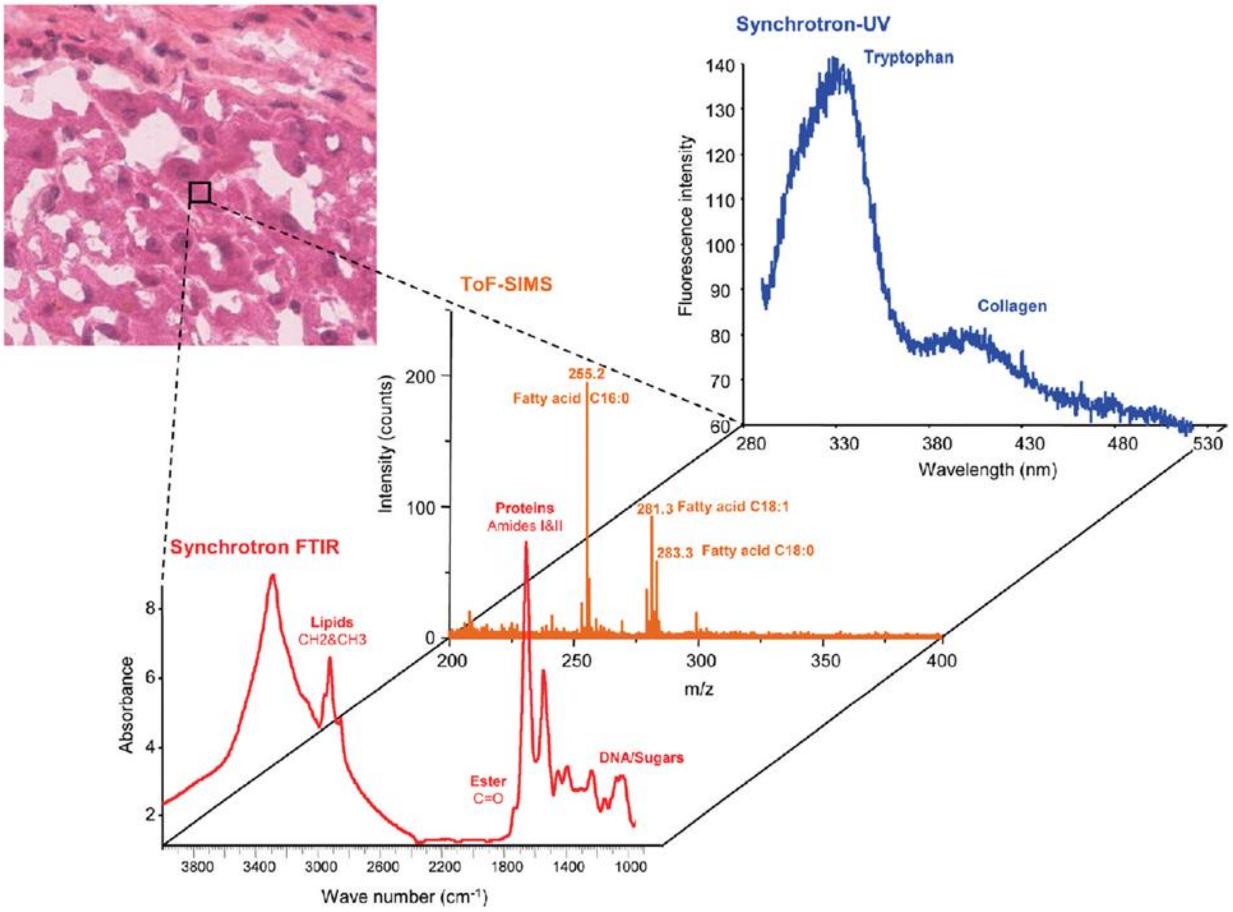

Figure 5.1: **Illustration of the combination of multimodal microspectroscopies from a single small region of liver tissue.** The spectra represent multimodal data – synchrotron FTIR, TOF-SIMS, and synchrotron UV absorption – from a single region, pixel, of a liver sample. Multimodal spectra such as these presage heterocorrelated images in which every pixel in the image contains multiple spectra spatially registered and optimally scaled for high value added post-processing. Adapted and reprinted with permission from ref. [65], copyright 2010 American Chemical Society.

Technique	**Lateral resolution**	**Chemical information**	**Advantages**	**Limitations**	**References**
IR	Diffraction limited ~λ/2 (2.5-25μm)	Molecular	Label free, non-invasive imaging	Low resolution due to long IR wavelengths; strong interference from water absorption	155, 156
Raman	Diffraction limited ~ λ/2	Molecular	Label free, non-invasive imaging; Raman signals are not affected by water therefore is suitable for biological samples; better spatial resolution than IR due to the use of shorter wavelengths	Low sensitivity; long experimental acquisition times; experiments require high powers that can lead to thermal damage	63, 106, 107
SERS	Diffraction limited ~ λ/2	Molecular	Higher sensitivity leading to faster image acquisition; metal nanoparticles can quench autofluorescence that is common with biological samples	Poor reproducibility; SERS is substrate dependent therefore not applicable to all samples	112-114
TERS		Molecular	Higher sensitivity than native Raman and is not limited to a metal substrate; label free analysis; sub-diffraction limited spatial resolution due to the size of the probe	Area of enhanced signal is very small	119, 124
CARS	Lateral 0.40μm-0.30μm axial ~1.5 μm	molecular and cellular structural	Label free, non-invasive imaging; high sensitivity compared to native Raman accesses video-rate imaging at modest laser powers; 3-D sectioning capabilities enable depth imaging of thick tissues and cells	High costs of implementing the set-up	157-159

Table 5.2: Comparison of Vibrational Imaging Techniques

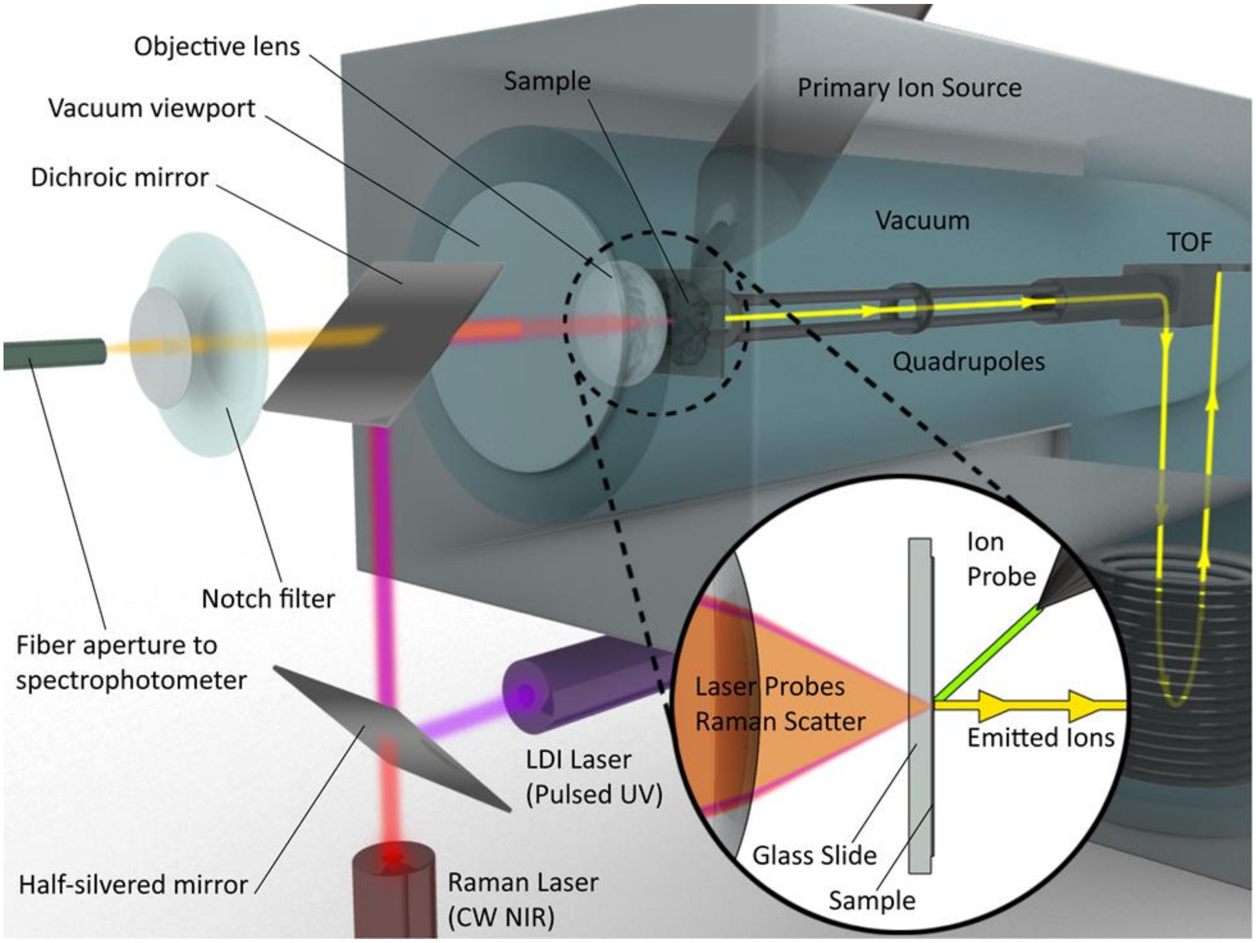

Figure 5.2: **Concept schematic of a hybrid CRM-QTOF LDI/C$_{60}$-SIMS chemical imaging instrument.** One potential arrangement of sample, optics and mass analyzer is shown. While not truly simultaneous, this instrument provides the ability to probe the sample with both imaging modalities without moving the sample between instruments and hence provides enhanced temporal and spatial registration between the imaging approaches. Adapted with permission from R. N. Masyuko, E. J. Lanni, J. V. Sweedler, and P. W. Bohn, *Analyst* **2013**, 138 (7), 1924-1939, copyright 2013 The Royal Society of Chemistry.

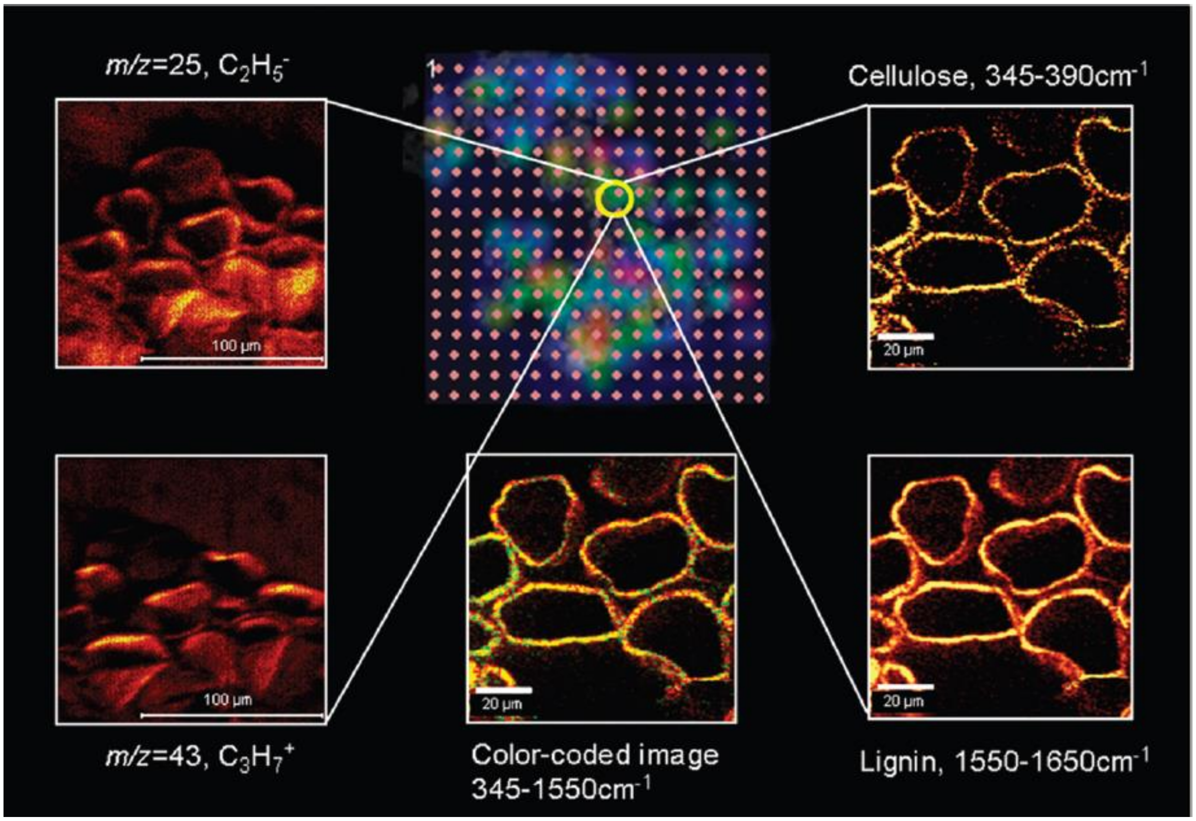

Figure 5.3: **Overview of LDI/SIMS/CRM heterocorrelated imaging applied to lignocellulosic materials.** The LDI-MS grid (center top) is color-coded, corresponding to the intensity of m/z = 45 ions obtained by laser desorption-ionization excitation spots on 100 µm centers. The yellow circle highlights the spot where high resolution imaging was performed by both negative (m/z = 25, C_2H^-, top left) and positive (m/z = 43, $C_3H_7^+$, bottom left) ion SIMS, as well as CRM, characterized by the cellulose band, 345–390 cm^{-1} (top right), and the lignin band, 1550–1650 cm^{-1} (bottom right). (Bottom center) Composite CRM image combining information from both cellulose (green) and lignin (yellow) bands. Adapted with permission from ref. [17], Copyright 2010 American Chemical Society.

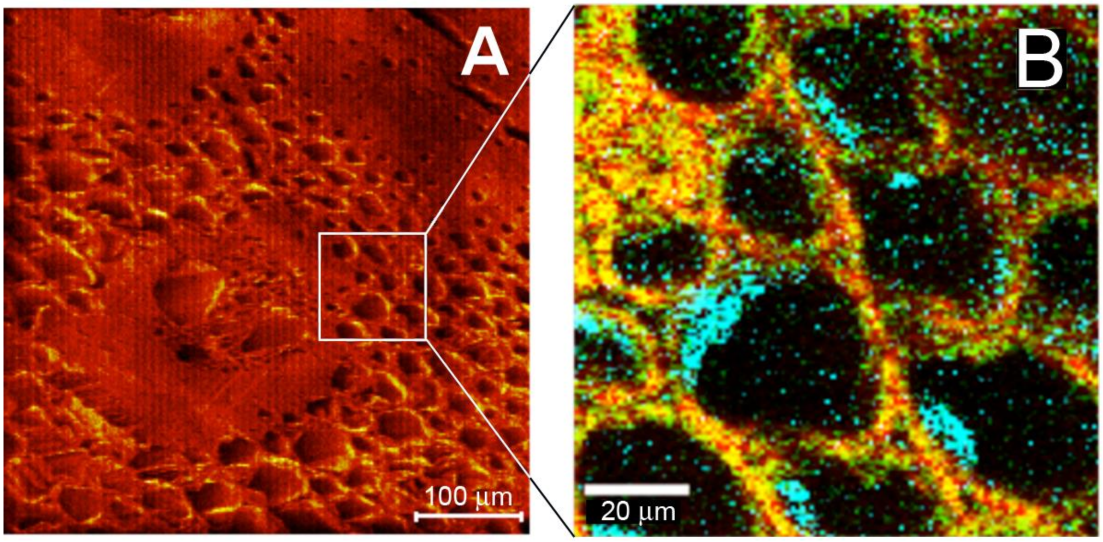

Figure 5.4: Correlation of the negative ion SIMS image (A) and CRM image (B) from the vascular bundle region of processed Miscanthus. Color-coded CRM image; red = lignin, 1550–1650 cm−1, green = cellulose, 345–390 cm−1, and blue = lignin-hemicellulose (460–500 cm−1) complex. Adapted with permission from Ref. [17], Copyright 2010 American Chemical Society.

CHAPTER 6

SPATIAL ORGANIZATION OF PSEUDOMONAS AERUGINOSA BIOFILMS PROBED BY COMBINED MATRIX-ASSISTED LASER DESORPTION IONIZATION MASS SPECTROMETRY AND CONFOCAL RAMAN MICROSCOPY

NOTES AND ACKNOWLEDGMENTS

This chapter was published as an original research article in *Analyst* **2014**, *in press*, DOI: 10.1039/C4AN00435C, coauthored by R. N. Masyuko, C. M. Driscoll, J. D. Shrout, J. V. Sweedler, and P. W. Bohn. The article is adapted and reprinted here with permission from the Royal Society of Chemistry, copyright 2014. E. J. Lanni performed all mass spectrometric analyses yielding data presented in figures 4, 5, S3, S4, and table 1, along with accompanying descriptions and discussion. R. N. Masyuko contributed confocal Raman spectroscopy and imaging and authored the majority of the manuscript (excluding MS results and discussion), and C. M. Driscoll performed *P. aeruginosa* cell and biofilm culturing. Funding for this work from Department of Energy Office of Biological and Environmental Research through grant DE SC0006642 is gratefully acknowledged.

INTRODUCTION

Biofilm bacteria are encased in a self-produced matrix formed by extracellular polymeric substances (EPS), which make up most of the biofilm organic matter by mass.[1] EPS are comprised of complex mixtures of macromolecules, such as proteins, polysaccharides, nucleic acids, lipids and amphiphilic polymers.[2-3] The nature of the EPS is not only complex, but dynamic; the molecules within the EPS are known to interact with each other and promote various functions such as biofilm formation, structural stabilization, sequestration of nutrients and water, and protection of the embedded microbes from environmental perturbations.[3] Acting in concert with the functions of the EPS, bacteria within biofilms form a complex microbial community that can exhibit primitive homeostasis, a circulatory system, and metabolic cooperativity,[4] often conveying beneficial effects for the population.

Biofilms themselves can be either beneficial or harmful to humans; they are beneficial in biotechnology applications, such as wastewater treatment[5] and chemical production, *e.g.* through fermentation in biofilm-based bioreactors.[6] On the other hand, bacteria within biofilms can be up to 1000 times more resistant to antibacterial treatments than planktonic cells.[7] Recent studies have inferred that antimicrobial resistance in biofilms is multifactorial, being ascribed to a combination of mechanisms.[8] In addition, consistent with the obvious phenotypic differences, biofilm bacteria show different gene expression profiles than planktonic bacteria[9-10] and respond differently to environmental perturbations than their planktonic counterparts.[11]

Pseudomonas aeruginosa is a Gram-negative bacterium that is ubiquitous in the natural environment and is present in many engineered systems.[12-14] A factor linked to *P. aeruginosa* biofilm formation is the inter-cellular signaling cascade known as quorum sensing (QS),[15-16] which is mediated by two acyl homoserine lactone (AHL) QS systems, *las* and *rhl*, each system having its own signal synthase, signal receptor and AHL signal transmission system. The signals for the *las* and *rhl* systems are 3-(oxo-dodecanoyl)-homoserine lactone and the N-butaryl-homoserine lactone.[16-17] *P. aeruginosa* is known to cause infections in burn wound patients,[18] patients with cancer,[19] HIV,[20] and cystic fibrosis,[21] with AHL quorum sensing linked with several pathogenic traits.[22] In most cases, biofilm-related behavior of *P. aeruginosa* is strongly associated with its pathogenic effects.[23] Yet questions remain concerning the spatial and dynamic expression of AHL quorum sensing *in vivo*—the uniform quorum sensing response(s) observed in studies of planktonic cultures can be markedly less uniform when considering *P. aeruginosa* strain or surface growth differences.[24-27]

Clearly, the ability to distinguish bacterial cells along a path - from initially surface-adhered planktonic cells, through the formation of microcolonies to encasement in an extracellular polymeric matrix that signals a fully developed biofilm - is of utmost importance, and methods based on molecular composition exhibit great promise in the management of biofilms, whether in the environment or in a health care context. While pathogenic microorganisms are typically identified using biochemical tests, these can take days to complete,[28] and it is essential to characterize not only the bacteria but the deleterious biofilms. Biofilm formation in *P. aeruginosa* can be analyzed through a combination of molecular genetics, phenotype characterization and signaling pathway analysis.[29-31] However, given the complex nature of biofilms, techniques with multiplex analysis capabilities, such as mass spectrometry and vibrational spectroscopy, are alternatives with great potential. Microspectroscopies can be used for rapid identification and characterization of complex microbial systems, while mass spectrometric and vibrational imaging modalities can provide additional information on the spatial distribution of characteristic molecular constituents that define a biofilm and its behavior. Furthermore, these two approaches are well-matched; vibrational spectroscopy provides a global analysis of the sample at the level of chemical functional groups, while mass spectroscopy identifies the biofilm constituents.

Vibrational Raman and infrared spectroscopies are non-destructive, label-free techniques that provide functional group information on a large number of cellular components. While the strong absorption of water in the mid-IR limits its usage to specialized applications such attenuated total reflectance IR microscopy in this spectral region, Raman spectroscopy is not affected by water, because it scatters weakly. With these natural advantages, Raman spectroscopy has been used to probe a wide range of both prokaryotic and eukaryotic cells,[32-34] to characterize bacteria and biofilms,[35-39] including medically relevant bacteria,[40] and for structural analysis of cellular components.[41] Raman scattering coupled with confocal microscopy affords three dimensional imaging at high spatial resolution and has been utilized for single cell mapping and analysis.[37, 42]

Mass spectrometry (MS) is a nearly ideal complement to Raman imaging, because it yields highly specific chemical information – molecular weight – of sample components which can be ionized. Ions can be further characterized by structural analysis through tandem MS experiments, which is especially useful for identifying unknown species and confirming mass assignments. The selection of ion source significantly affects the molecular classes that can be ionized and defines the physical process of ion generation; direct ionization from solid surfaces is possible with microprobe ion sources such as focused lasers, *e.g.* matrix-assisted laser desorption/ionization, MALDI, and ion beams, *e.g.* secondary ion mass spectrometry, SIMS,[43] which enables *MS profiling* – sampling of micro-scale regions on a large sample surface to obtain spatially specific chemical information. Taken a step further, multiple MS profiles can be acquired in a rectangular array of points over an extended area. This technique, known as *MS imaging* (MSI), maps the distribution of all detected ions within a specified area. Each MS profile is treated as a single pixel in the MSI experiment, and ion images are generated by defining pixel brightness to indicate the relative intensity of a selected ion at that position in the sample. MSI is a powerful, multiplex, and label-free imaging technique which can visualize many molecules which are not easily labeled, notably lipids and other small metabolites. Thanks to these characteristics, MSI is now employed routinely in biological and clinical research fields at macroscopic (tissue-level) [44] and microscopic (cell/subcell) size scales,[45] including in microbiology where it has been used to study interspecies metabolic interactions,[46] biofilm secretion,[47] and subcellular molecular distributions [48] among other applications.[49]

In the present study, static biofilms prepared from both wild-type *P. aeruginosa* and an isogenic QS mutant deficient for both AHL signal production and rhamnolipid secretion are spatially analyzed using both confocal Raman microscopy (CRM) and MALDI MSI. Raman and MS spectral profiles and images acquired from the biofilm are compared to those of the corresponding planktonic cells in order to examine the changes in composition associated with biofilm formation. While the wild-type *P. aeruginosa* biofilms show the presence of glycolipids and increased protein excretion, analysis of the QS deficient cells do not show any of these changes. In fact, the molecular composition is similar for both planktonic and biofilm growth conditions. Combining CRM and MSI allows data to be cross validated, as well as providing complementary chemical information.[50-51] CRM detects molecular classes that are not efficiently ionized by MS, while MSI can resolve multiple rhamnolipid species[52-53] in the wild-type biofilm which give rise to a single peak in the Raman spectrum. Confirmation of their identities by *in situ* tandem MS shows that rhamnolipid congeners exhibit different distributions across the biofilm surface, a feature which may relate to their functions and/or expression within the biofilm.

EXPERIMENTAL

Biofilm preparation

Pseudomonas aeruginosa ATCC strain 15692 and an isogenic QS mutant deficient for AHL production and for rhamnolipid excretion (Δ*las*Δ*rhlI*) [54] were used in all experiments. Cells were grown overnight at 30°C using sterilized FAB medium[55] with 150 µL of 1.2 M filter-sterilized glucose as a carbon source to an optical density (OD) of 1.0 at 600 nm. The FAB medium contained the following components: $(NH_4)_2SO_4$ (2 g L^{-1}), Na_2HPO_4. $2H_2O$ (6 g L^{-1}), KH_2PO_4 (3 g L^{-1}), NaCl (3 g L^{-1}), $MgCl_2$(93 mg L^{-1}), $CaCl_2$(11 mg L^{-1}) and trace metals solution (1 ml L^{-1}). The trace metals solution contained $CaSO_4$. $2H_2O$ (200 mg L^{-1}), $FeSO_4$.7H2O (200 mg L^{-1}), $MnSO_4.H_2O$ (20 mg L^{-1}), $CuSO_4$. $5H_2O$ (20 mg L^{-1}), $ZnSO_4$. $7H_2O$ (20 mg L^{-1}), $CoSO_4.7H_2O$ (10 mg L^{-1}), $NaMoO_4$. H_2O (10 mg L^{-1}), H_3BO_3 (5 mg L^{-1}). Planktonic cells were centrifuged and washed three times in phosphate buffered saline (PBS) then placed on (100) silicon for both Raman and MS analysis. Biofilms were grown on 2 cm x 2 cm pieces of (100) Si placed at the bottom of Petri dishes. For biofilm growth, the cell culture solution was deposited onto the Si wafers at the bottom of the Petri dish, and additional growth medium with 450 μL of 1.2 M glucose was added at a volume ratio of 1:49 (cell culture: growth medium). Biofilms were allowed to develop at 30 °C for 72 h. Extra growth medium was pipetted from the Petri dish and the silicon-supported biofilms were dried at 25 °C for 12 h in a sterile environment prior to analysis. Additional samples were prepared on Au-coated (100) Si for Raman analysis in order to expose any peaks that might overlap and be obscured by the strong $\nu($Si-O) band from SiO_2. Gold-coated substrates were prepared by thermally evaporating a 3 nm Cr adhesion layer followed by 100 nm of Au onto a clean (100) Si wafer.

Confocal Raman Measurements

Raman spectra were acquired at 300 K using a confocal Raman microscope (Alpha 300R, WITec GmbH, Germany) equipped with a focused Nd:YAG laser operating at the second harmonic frequency (λ = 532 nm) and a 60x, coverslip-corrected Nikon water-immersion objective (NA=1.0). Laser radiation was delivered via a single mode optical fiber through a dichroic beam splitter into the microscope objective and focused onto the sample. The scattered Raman radiation was collected by the same objective and focused into a 50 μm diameter multi-mode fiber connected to a UHTS 300 spectrometer equipped with a 600 groove mm^{-1} grating and a back-illuminated CCD camera (Newton DU970 N-BV, Andor Inc., cooled to -65 °C). Each Raman spectrum was recorded by accumulating 100 spectra at an integration time of 0.5 s each at 15 mW incident laser power. On each sample, individual Raman spectra were collected at 25 spatial locations and averaged to produce representative spectra for that sample. Raman images were acquired by recording a full Raman spectrum at every pixel (150 x 150 array for a total of 22,500 spectra per image) over the desired surface area at an integration time of 100 ms. The step sizes (not spatial resolution) for the images reported in this work are 33 nm, 170 nm and 210 nm for Figures 6.3(a), 6.3(b), and 6.3(c) respectively. Raman images showing the distribution of various constituents were calculated by integrating the area under the corresponding Raman band. WITec software was used for Raman data analysis. Raman spectra were baseline corrected using a fourth order polynomial function.

Mass Spectrometry Measurements

For all MALDI MS experiments, biofilms and planktonic cell samples were grown or deposited on uncoated silicon wafers and dried as described in the Biofilm Preparation section, then processed by applying a 1-2 nm thick Au layer to the surface with a Desk II TSC sputter coater (Denton Vacuum, Moorestown, NJ, USA) run for 6 s at 40% power and 65 mTorr of Ar. The biofilm-coated silicon wafers were then affixed with double-sided conductive tape (Electrical Tape, 3M, St. Paul, MN, USA) to a custom stainless steel MALDI target modified with a shallow cutout to precisely level the silicon wafer surface with the plate face, a step which was critical to obtaining high quality mass spectra from the biofilms. All MS experiments were performed on an Ultraflextreme MALDI-TOF/TOF MS (Bruker Daltonics, Billerica, MA, USA) set to reflectron/positive ion mode with matrix suppression disabled, using a frequency-tripled Nd:YAG Smartbeam II laser. Imaging experiments were performed with *m/z* range 20-1000, "medium" laser size (~100 μm probe diam. estimated by matrix ablation), 1000 Hz frequency, 200 shots/position, and 500 μm step/pixel size. Quadratic calibration was performed using K^+ and Au_n^+ cluster ions. Tandem MS (TOF/TOF) experiments were performed in post-source decay mode (without CID), and laser power was adjusted for each parent ion to maximize fragmentation. Data was processed using flexAnalysis v3.4 and flexImaging v3.0; ion filters were ±0.25 Da and images were RMS-normalized. Mixed rhamnolipid standard (95%, Aldrich) was purchased from Sigma Aldrich (St. Louis, MO, USA).

RESULTS AND DISCUSSION

Confocal Raman Analysis

P. aeruginosa biofilms grown under static conditions on Si and Au-coated Si wafers were initially analyzed using Raman microspectroscopy. Fluorescence images (shown in **Figure 6.1**) confirmed that biofilms grown on both Au and Si were similar. The specific Raman spectra observed here represent an ensemble of signals that arise from the molecular vibrations of individual cell components, integrating over lipids, proteins, nucleic acids and carbohydrates. Raman measurements for both wild type and mutant strains were performed in water. Autofluorescence, which is ubiquitous in biological materials, is significantly reduced in water, thus substantially reducing the background. Also the refractive index of water, $n = 1.33$, is close to that of bacterial cells and media, thereby minimizing refraction-induced image distortion effects. Finally, water efficiently dissipates the heat generated from laser irradiation, thus limiting potential thermal damage to the samples. Thus, the ability to perform confocal Raman imaging in water yields substantial experimental advantages in comparison to infrared vibrational imaging. Raman spectra of *P. aeruginosa* wild type and QS-mutant planktonic cells and biofilms were acquired between 100 cm^{-1} and 3600 cm^{-1}, however, the studies reported here concentrate on vibrational bands found in the fingerprint region 600 – 1800 cm^{-1}. Outside this range, C-H stretching vibrations in the range 2750 - 3050 cm^{-1} dominate spectra. Although these bands carry important information about cell membrane fluidity,[56-57] this information is of less interest here.

Figure 6.2 compares the Raman spectrum in the vibrational fingerprint region from planktonic cells, **Figure 6.2(a)**, to that of a biofilm grown from the same planktonic cells, **Figure 6.2(b)**. The Raman spectrum of wild type *P. aeruginosa* in the planktonic state, **Figure 6.2(a)**, exposes vibrational bands that belong to the basic biological building blocks of the cell, with the nucleotide bases dominating under the conditions used here. The Raman spectrum reveals a series of DNA/RNA base vibrations that are well defined, the strongest of these being the characteristic thymine out-of-plane C-O bending vibration at ~747 cm^{-1}, along with the guanine and adenine ring breathing vibrations observed in a well-defined high intensity band at 1585 cm^{-1}.[58] Strong bands at 1126 cm^{-1} and 1310 cm^{-1} along with the medium intensity band at 1336 cm^{-1} are assigned to cytosine and the adenine ring breathing vibration,[59] and a weaker band at 783 cm^{-1} represents the ring distortions from both cytosine and uracil with a contribution from the O-P-O symmetric vibrational stretch.[41, 60] The spectrum also shows bands that belong to proteins, carbohydrates and lipids that are significantly weaker than the DNA/ RNA bands. Protein bands at 1170 cm^{-1} and 1223 cm^{-1} are assigned to tyrosine C-H in plane bending vibrations and amide III vibrations,[61] and the band at 1358 cm^{-1} arises from the indole ring stretch of tryptophan. The band at 1448 cm^{-1} is representative of CH_2 scissoring deformation vibrations that arise from proteins, carbohydrates and lipids.[59]

Upon biofilm formation, dramatic changes occur in the spectrum, **Figure 6.2(b)**. Biofilms cultivated on bare Si exhibit a greatly reduced SiO_2 background (915-1015 cm^{-1}), presumably because biofilms at 72 h are much thicker than the < 1 μm confocal depth of the CRM. In addition, the strong DNA/RNA-related bands at 747 (thymine), 1126 (cytosine), and

1310 cm^{-1} (adenine) are all greatly diminished or disappear altogether. The only DNA/ RNA contributions remaining in the biofilm spectrum are very weak bands at 792 cm^{-1} attributed to cytosine and uracil ring stretching vibrations and a 1507 cm^{-1} band assigned to adenine. The strong band at 1585 cm^{-1} is reduced in strength and a new band at 1601 cm^{-1} grows in. In addition, narrow bands with peaks centered at 999 cm^{-1} and 1030 cm^{-1} appear as well as smaller bands centered at 1068 cm^{-1}, 1097 cm^{-1}, 1155 cm^{-1} and 1197 cm^{-1}. Most striking is the intense peak at 999 cm^{-1} attributed to symmetric ring breathing vibrations in phenylalanine and tryptophan, indicative of proteins.[62] Other bands characteristic of proteins are the broad band at 1175-1235 cm^{-1} that can be attributed to C-H in plane bending vibrations in tyrosine and phenylalanine, amide III and $C-C_6H_5$ stretching vibrations[61] and the two bands at 617 cm^{-1} and 1601 cm^{-1} arising from in plane ring breathing deformation and C=C stretching vibrations in phenylalanine.[62] The presence of these bands shows that the composition of the biofilm is different than that of the planktonic cells. More specifically, the contribution from proteins is significantly increased, as indicated by the relative intensities of the protein-characteristic bands compared to those derived from DNA/RNA, unlike planktonic cells where DNA/RNA peaks are dominant. These observations are consistent with the growth of a relatively thick biofilm, which dilutes the contribution of cellular nucleotide-derived peaks. The changes shown in the relative intensities of nucleic acid and protein bands in the planktonic and biofilm spectra in this case are consistent with other studies that have shown that bacteria produce more RNA when entering the logarithmic growth phase. This contrasts with a decrease in RNA levels and increase in protein when bacteria slow their growth and enter the stationary phase, a change that is reflected in the Raman bands characteristic of nucleotide-bases.[63-64] These observations also reflect the RNA increases associated with the growth cycle of bacteria described previously by Herbert.[65]

The important band at 1030 cm^{-1}, as well as bands at 1068 cm^{-1}, 1095 cm^{-1}and 1155 cm^{-1}, lie in the carbohydrate region of the spectrum, and are observed in the wild type biofilm spectrum, **Figure 6.2(b)**, but not in the spectrum from the planktonic cells, **Figure 6.2(a)**. These are classified as C-O stretching (1030 cm^{-1}), C-C and C-O stretching (1068 cm^{-1}), C-O-C glycosidic link symmetric ring breathing (1095 cm^{-1}) and C-C and C-O asymmetric ring breathing (1155 cm^{-1}) vibrations.[58-60] In the context of *Pseudomonas*-derived biofilms, these bands suggest the presence of rhamnolipids,[66] a specific class of glycolipids known to be secreted by *Pseudomonas* species concurrently with biofilm formation,[67-68] an assignment confirmed via MS. Comparison of representative microspectra from a *Pseudomonas* wild-type biofilm, **Figure 6.2(b)** with a mixed rhamnolipid standard shows that the standard has contributions from common Raman bands at 1030 cm^{-1}, 1068 cm^{-1}, and 1155 cm^{-1} characteristic of the sugar moieties, as described above, and consistent with the presence of rhamnolipids in the biofilm matrix. Confirming the assignment of these bands to rhamnolipids, the MS data below not only show the presence of rhamnolipids, but allow their assignment to individual congeners. **Figure 6.3** shows representative microspectra from the isogenic QS Δ*las*Δ*rhlI* mutant, a strain which is also deficient for rhamnolipid production, since QS is required for rhamnolipid production.[69] **Figure 6.3(a)** shows planktonic cell spectra, and **Figure 6.3(b)** shows spectra for the QS (rhamnolipid-deficient) mutant obtained using the conditions used to grow biofilms from the wild-type strain. The first striking feature in comparison to **Figure 6.2**, is that the DNA/RNA bands at 747, 1126, 1310, 1447, and 1585 cm^{-1} present in the planktonic cell spectrum are also observed in the 72 h spectrum, *i.e.* sufficient time for biofilm development in the wild-type, **Figure 6.2(b)**. In addition, the rhamnolipid bands clearly observed at ~1030 cm^{-1}, 1068 cm^{-1} and 1155 cm^{-1} in **Figure 6.2(b)** are absent in **Figure 6.3(b)**. Both indicate that biofilm development is hindered, or even completely absent, in the QS mutant.

To further elucidate the compositional and structural changes accompanying biofilm formation, Raman images in different scattering windows were acquired and are shown in **Figure 6.4(a)** for planktonic cells and **Figure 6.4(b)** for the biofilm. The image in **Figure 6.4(a)**, assembled from *v(*C-H) stretching vibrations in the 2800-3050 cm^{-1} window (representative of all organic matter), was acquired from *P. aerguinosa* wild-type planktonic cells on a surface and shows distinct cell bodies, ostensibly in different orientations. To show the distribution of the different molecular species on the biofilm surface, Raman images were constructed from 2800-3050 cm^{-1} (all organic matter), 1560-1620 (proteins), and 1010-1165 cm^{-1} (carbohydrates and glycolipids), as shown in **Figure 6.5**. A composite image showing the distribution of glycolipid and carbohydrate molecular components 1010-1165 cm^{-1} scattering (blue) and protein 1560-1620 cm^{-1} scattering (red) is shown in **Figure 6.4(b)**. This image is clearly dominated by scattering from secreted metabolites on the surface. **Figure 6.4(c)** shows a cross-sectional image in the *x-z* orientation of a biofilm assembled from 2800-3050 cm^{-1} (red) showing distribution of all organic components, 1560-1620 cm^{-1} (blue) representing protein species and 725-775 cm^{-1} (green), the latter region capturing the 747 cm^{-1} band assigned to thymine, meaning that this component is representative of DNA components found within the cell. The cross-sectional image clearly shows that the cell-derived nucleotide components are not visible on the surface of the biofilm but rather are found deep within the biofilm, below the protein/carbohydrate-rich EPS matrix. This observation is consistent with bacterial cells constituting a relatively small portion of the biofilm mass.

Mass Spectrometry

MALDI MS is commonly performed by coating the sample surface with a solution of organic acid, but here a thin coating of gold was used as the matrix, *i.e.* metal-enhanced LDI, or "MetA-LDI",[70-71] which typically limits mass range to < 1 kDa and thus excludes analysis of intact proteins but also yields several advantages for this work, *e.g.* virtually no matrix interference below *m/z* 1000, internal calibration on Au_n^+ cluster ions in the same range, and a highly uniform, easily-reproducible coating. Au thickness was initially optimized by coating and imaging rhamnolipid standard dried on silicon (**Figure 6.6**) which showed that the thinnest possible uniform coating, *ca*. 2 nm thick, yields the strongest signal. On biofilms prepared here, this preparation routinely allowed detection of over two hundred ions within *m/z* 20-1,000 per microprobe location (image pixel) on the sample. The focus of this work was on profiling rhamnolipids as discussed below, but other known *P. aeruginosa* primary and secondary metabolites are also likely detected within this mass range and can therefore be studied using the same approach in future work.

Typical single pixel spectra of *P. aeruginosa* wild-type biofilm, wild-type planktonic cells, and QS mutant biofilm are shown in **Figure 6.7**. Notably, major spectral features detected exclusively in the wild-type biofilm include several ions in the *m/z* 350-800 range which are identified as rhamnolipid salt adducts based initially on mass match with previous analyses of *P. aeruginosa* bulk extracts by MALDI [72] and LC-ESI MS.[73] To confirm these mass assignments, *in situ* tandem MS was performed, and spectra were matched with expected molecular fragments as well as spectra acquired from rhamnolipid standards (spectra shown in **Figure 6.8**).[74] Nine unique putative rhamnolipid species were detected on the wild-type biofilm and of these, six were detected with sufficient intensity for confirmation by tandem MS; ion identification data are listed in **Table 6.1** using standard rhamnolipid nomenclature.[73]

While this is a small fraction of the many dozens of molecular species reported for *P.*

aeruginosa in total,[73] it is in good agreement with the subset previously detected from extracts by MALDI MS.[72] It has been shown that the rhamnolipid profile can vary greatly with bacterial strain and growth conditions,[75] thus it is reasonable to assert that the particular *P. aeruginosa* strain and conditions studied here did not produce the other rhamnolipid species in significant (detectable) abundance. Furthermore, the MS data confirm and extend the conclusions drawn from the differences in Raman scattering highlighted between **Figures 6.1 and 6.2**. The assignment of Raman bands at 1030 cm^{-1}, 1068 cm^{-1} and 1155 cm^{-1} to rhamnolipids is confirmed by MS identification of a series of specific congeners from the rhamnolipid family.

MALDI MS imaging of the wild-type *P. aeruginosa* biofilm allowed visualization of specific rhamnolipids, which generally exhibited a heterogeneous distribution over the sample surface. Furthermore, while the individual rhamnolipid distributions share some resemblance, they are not identical; for example, monorhamnolipid Rha-C8-C10 (m/z 499.4) and dirhamnolipid Rha-Rha-C10-C12 (m/z 701.6) ion images shown in **Figure 6.9** show overlapping but distinct distributions, with exclusive regions of localization in the opposite corners of the substrate. Dirhamnolipids have been shown to act as chemoattractants in swarming motility of *P. aeruginosa*, while monorhamnolipids do not,[76] so the differential distributions observed here may relate to these unique roles in biofilm development. Furthermore, the genes responsible for mono- and dirhamnolipid synthesis (*rhlB* and *rhlC*, respectively) are located in different operons and synthesis of dirhamnolipids occurs by addition of a second rhamnose to existing monorhamnolipids. Thus, the observed difference in spatial distributions could arise from temporal differences in expression during biofilm growth and maturation.[73] Another interesting feature of the wild-type biofilm is the association of small light-colored regions with localization of dirhamnolipid Rha-Rha-C10-C12, but not monorhamnolipid Rha-C8-C10; the nature of these features is not understood and is currently under investigation.

CONCLUSIONS

CRM and MSI have been combined to characterize chemical composition and structure in samples of *P. aeruginosa* – both planktonic cells and biofilms, as well as the changes that accompany biofilm formation when comparing a wild type to a QS (Δ*las*Δ*rhlI*) mutant strain incapable of producing either rhamnolipids or the homo-serine lactones used in quorum sensing. Raman analysis of wild type planktonic cells reveal spectra that are dominated by DNA/RNA-related spectral features – bands that are almost completely absent in the biofilm. Instead biofilms produce spectra that are dominated by rhamnolipids, secreted as part of the biofilm formation process, and by a co-secreted protein/peptide component. In contrast, the QS mutant exhibits very similar spectra to the planktonic cells after 72 h under the same conditions used to obtain the wild-type biofilms. The straightforward interpretation of these observations posits the formation of a thick (relative to the sampling depth of the CRM) biofilm after 72 h in the wild type cells, but not in the QS mutant. MALDI MS profiling was applied to obtain more chemically specific information on the variety of rhamnolipids present; nine putative rhamnolipid species were detected in the wild-type biofilm, six of which could be confirmed by tandem MS. Furthermore, MS imaging revealed that rhamnolipid distributions were heterogeneous across the wild-type biofilm, consistent with the variegation observed at higher spatial resolution in the biofilm Raman image, **Figure 6.3(b)**, and also showed differences which may relate to differential expression and/or function of specific congeners and homologs within the rhamnolipid class; future work will further elucidate this observation and characterize temporal changes during biofilm development.

References

1. Jenkinson, H. F.; Lappin-Scott, H. M., Biofilms adhere to stay. *Trends Microbiol.* **2001,** *9* (1), 9-10.
2. Flemming, H. C., Biofouling in water systems - cases, causes and countermeasures. *Appl. Microbiol. Biotechnol.* **2002,** *59* (6), 629-640.
3. Branda, S. S.; Vik, A.; Friedman, L.; Kolter, R., Biofilms: the matrix revisited. *Trends Microbiol.* **2005,** *13* (1), 20-26.
4. Lopez, D.; Vlamakis, H.; Kolter, R., Biofilms. *Cold Spring Harbor Perspectives in Biology* **2010,** *2* (7).
5. Rodgers, M.; Wu, G. X.; Zhan, X. M., Nitrogen and phosphorus removal from domestic strength synthetic wastewater using an alternating pumped flow sequencing batch biofilm reactor. *J. Environm. Qual.* **2008,** *37* (3), 977-982.
6. Qureshi, N.; Annous, B. A.; Ezeji, T. C.; Karcher, P.; Maddox, I. S., Biofilm reactors for industrial bioconversion processes: employing potential of enhanced reaction rates. *Microbial Cell Factories* **2005,** *4.*
7. Nickel, J. C.; Ruseska, I.; Wright, J. B.; Costerton, J. W., Tobramycin Resistance of Pseudomonas-Aeruginosa Cells Growing as a Biofilm on Urinary Catheter Material. *Antimicrob. Agents Chemother.* **1985,** *27* (4), 619-624.
8. Drenkard, E., Antimicrobial resistance of Pseudomonas aeruginosa biofilms. *Microbes and Infection* **2003,** *5* (13), 1213-1219.
9. Schuster, M.; Lostroh, C. P.; Ogi, T.; Greenberg, E. P., Identification, timing, and signal specificity of Pseudomonas aeruginosa quorum-controlled genes: a transcriptome analysis. *J. Bacteriol.* **2003,** *185* (7), 2066-2079.
10. Wagner, V. E.; Bushnell, D.; Passador, L.; Brooks, A. I.; Iglewski, B. H., Microarray analysis of Pseudomonas aeruginosa quorum-sensing regulons: Effects of growth phase and environment. *J. Bacteriol.* **2003,** *185* (7), 2080-2095.
11. Costerton, J. W.; Lewandowski, Z.; Caldwell, D. E.; Korber, D. R.; Lappinscott, H. M., Microbial Biofilms. *Annual Review of Microbiology* **1995,** *49*, 711-745.
12. Dias, F. F.; Bhat, J. V., Microbial Ecology of Activated Sludge .I. Dominant Bacteria. *Applied Microbiology* **1964,** *12* (5), 412-&.
13. Jorgensen, K. S.; Pauli, A. S. L., Polyphosphate Accumulation among Denitrifying Bacteria in Activated-Sludge. *Anaerobe* **1995,** *1* (3), 161-168.
14. Szewzyk, U.; Szewzyk, R.; Manz, W.; Schleifer, K. H., Microbiological safety of drinking water. *Ann. Rev. Microbiol.* **2000,** *54*, 81-127.
15. Davies, D. G.; Parsek, M. R.; Pearson, J. P.; Iglewski, B. H.; Costerton, J. W.; Greenberg, E. P., The involvement of cell-to-cell signals in the development of a bacterial biofilm. *Science* **1998,** *280* (5361), 295-298.
16. Parsek, M. R.; Greenberg, E. P., Quorum sensing signals in development of Pseudomonas aeruginosa biofilms. *Biofilms* **1999,** *310*, 43-55.
17. Brint, J. M.; Ohman, D. E., Synthesis of Multiple Exoproducts in Pseudomonas-Aeruginosa Is under the Control of Rhlr-Rhli, Another Set of Regulators in Strain Pao1 with Homology to the Autoinducer-Responsive Luxr-Luxi Family. *J. Bacteriol.* **1995,** *177* (24), 7155-7163.
18. Hsueh, P. R.; Teng, L. J.; Yang, P. C.; Chen, Y. C.; Ho, S. W.; Luh, K. T., Persistence of a multidrug-resistant Pseudomonas aeruginosa clone in an intensive care burn unit. *J. Clin. Microbiol.* **1998,** *36* (5), 1347-1351.
19. Hachem, R. Y.; Chemaly, R. F.; Ahmar, C. A.; Jiang, Y.; Boktour, M. R.; Abou Rjaili, G.; Bodey, G. P.; Raad, I. I., Colistin is effective in treatment of infections caused by multidrug-resistant Pseudomonas aeruginosa in cancer patients. *Antimicrob. Agents Chemother.* **2007,** *51* (6), 1905-1911.
20. Ashorn, P.; Moss, B.; Weinstein, J. N.; Chaudhary, V. K.; Fitzgerald, D. J.; Pastan, I.; Berger, E. A., Elimination of Infectious Human-Immunodeficiency-Virus from Human T-Cell Cultures by Synergistic Action of Cd4-Pseudomonas Exotoxin and Reverse-Transcriptase Inhibitors. *Proc. Natl. Acad. Sci. USA* **1990,** *87* (22), 8889-8893.
21. Romling, U.; Fiedler, B.; Bosshammer, J.; Grothues, D.; Greipel, J.; Vonderhardt, H.; Tummler, B., Epidemiology of Chronic Pseudomonas-Aeruginosa Infections in Cystic-Fibrosis. *J. Infect. Dis.* **1994,** *170* (6), 1616-1621.
22. Passador, L.; Cook, J. M.; Gambello, M. J.; Rust, L.; Iglewski, B. H., Expression of *Psuedomonas aeruginosa* virulence genes requires cell-to-cell communication. *Science* **1993,** *260* (5111), 1127-1130.

23. Costerton, J. W.; Stewart, P. S.; Greenberg, E. P., Bacterial biofilms: A common cause of persistent infections. *Science* **1999,** *284* (5418), 1318-1322.

24. Morris, J. D.; Hewitt, J. L.; Wolfe, L. G.; Kamatkar, N. G.; Chapman, S. M.; Diener, J. M.; Courtney, A. J.; Leevy, W. M.; Shrout, J. D., Imaging and Analysis of Pseudomonas aeruginosa Swarming and Rhamnolipid Production. *Appl. Environ. Microbiol.* **2011,** *77*, 8310-8317.

25. Kamatkar, N.; Shrout, J., Surface hardness impairment of quorum sensing and swarming for Pseudomonas aeruginosa. *PLoS One* **2011,** *6*, e20888.

26. Chugani, S.; Kim, B.; Phattarasukol, S.; Brittnacher, M.; Choi, S.; Harwood, C.; Greenberg, E., Strain-dependent diversity in the Pseudomonas aeruginosa quorum-sensing regulon. *Proc Natl Acad Sci U S A.* **2012,** *109*, E2823-E2831.

27. Pamp, S.; Tolker-Nielsen, T., Multiple roles of biosurfactants in structural biofilm development by Pseudomonas aeruginosa. *J. Bacteriol.* **2007,** *189*, 2531-2539.

28. Latour, X.; Corberand, T. S.; Laguerre, G.; Allard, F.; Lemanceau, P., The composition of fluorescent pseudomonad populations associated with roots is influenced by plant and soil type. *Appl. Environ. Microbiol.* **1996,** *62* (7), 2449-2456.

29. Camilli, A.; Bassler, B. L., Bacterial small-molecule signaling pathways. *Science* **2006,** *311* (5764), 1113-1116.

30. Davey, M. E.; O'toole, G. A., Microbial biofilms: from ecology to molecular genetics. *Microbiol. Mol. Biol. Rev.* **2000,** *64* (4), 847-+.

31. O'Toole, G. A.; Kolter, R., Initiation of biofilm formation in Pseudomonas fluorescens WCS365 proceeds via multiple, convergent signalling pathways: a genetic analysis. *Mol. Microbiol.* **1998,** *28* (3), 449-461.

32. Zhang, X.; Roeffaers, M. B. J.; Basu, S.; Daniele, J. R.; Fu, D.; Freudiger, C. W.; Holtom, G. R.; Xie, X. S., Label-Free Live-Cell Imaging of Nucleic Acids Using Stimulated Raman Scattering Microscopy. *Chemphyschem* **2012,** *13* (4), 1054-1059.

33. Yue, S. H.; Cardenas-Mora, J. M.; Chaboub, L. S.; Lelievre, S. A.; Cheng, J. X., Label-Free Analysis of Breast Tissue Polarity by Raman Imaging of Lipid Phase. *Biophys. J.* **2012,** *102* (5), 1215-1223.

34. Barhoumi, A.; Halas, N. J., Label-Free Detection of DNA Hybridization Using Surface Enhanced Raman Spectroscopy. *J. Am. Chem. Soc.* **2010,** *132* (37), 12792-12793.

35. Jarvis, R. M.; Goodacre, R., Characterisation and identification of bacteria using SERS. *Chem. Soc. Rev.* **2008,** *37* (5), 931-936.

36. Harz, A.; Rosch, P.; Popp, J., Vibrational Spectroscopy-A Powerful Tool for the Rapid Identification of Microbial Cells at the Single-Cell Level. *Cytom. A* **2009,** *75A* (2), 104-113.

37. Huang, W. E.; Griffiths, R. I.; Thompson, I. P.; Bailey, M. J.; Whiteley, A. S., Raman microscopic analysis of single microbial cells. *Anal. Chem.* **2004,** *76* (15), 4452-4458.

38. Ivleva, N. P.; Wagner, M.; Horn, H.; Niessner, R.; Haisch, C., Raman microscopy and surface-enhanced Raman scattering (SERS) for in situ analysis of biofilms. *J. Biophoton.* **2010,** *3* (8-9), 548-556.

39. Sandt, C.; Smith-Palmer, T.; Pink, J.; Brennan, L.; Pink, D., Confocal Raman microspectroscopy as a tool for studying the chemical heterogeneities of biofilms in situ. *J. Appl. Microbiol.* **2007,** *103* (5), 1808-1820.

40. Maquelin, K.; Kirschner, C.; Choo-Smith, L. P.; van den Braak, N.; Endtz, H. P.; Naumann, D.; Puppels, G. J., Identification of medically relevant microorganisms by vibrational spectroscopy. *J. Microbiol. Methods* **2002,** *51* (3), 255-271.

41. Overman, S. A.; Aubrey, K. L.; Reilly, K. E.; Osman, O.; Hayes, S. J.; Serwer, P.; Thomas, G. J., Conformation and interactions of the packaged double-stranded DNA genome of bacteriophage T7. *Biospectroscopy* **1998,** *4* (5), S47-S56.

42. Krafft, C.; Knetschke, T.; Siegner, A.; Funk, R. H. W.; Salzer, R., Mapping of single cells by near infrared Raman microspectroscopy. *Vib Spectrosc* **2003,** *32* (1), 75-83.

43. Rubakhin, S.; Sweedler, J., A Mass Spectrometry Primer for Mass Spectrometry Imaging. In *Mass Spectrometry Imaging*, Rubakhin, S. S.; Sweedler, J. V., Eds. Humana Press: 2010; Vol. 656, pp 21-49.

44. Chughtai, K.; Heeren, R. M. A., Mass Spectrometric Imaging for Biomedical Tissue Analysis. *Chemical Reviews* **2010,** *110* (5), 3237-3277.

45. Lanni, E. J.; Rubakhin, S. S.; Sweedler, J. V., Mass spectrometry imaging and profiling of single cells. *Journal of Proteomics* **2012,** *75* (16), 5036-5051.

46. Phelan, V. V.; Liu, W.-T.; Pogliano, K.; Dorrestein, P. C., Microbial metabolic exchange - the chemotype-to-phenotype link. *Nat Chem Biol* **2012,** *8* (1), 26-35.

47. Blaze M. T, M.; Aydin, B.; Carlson, R. P.; Hanley, L., Identification and imaging of peptides and proteins on Enterococcus faecalis biofilms by matrix assisted laser desorption ionization mass spectrometry. *Analyst*

2012, *137* (21), 5018-5025.

48. Vaidyanathan, S.; Fletcher, J. S.; Goodacre, R.; Lockyer, N. P.; Micklefield, J.; Vickerman, J. C., Subsurface Biomolecular Imaging of Streptomyces coelicolor Using Secondary Ion Mass Spectrometry. *Analytical Chemistry* **2008,** *80* (6), 1942-1951.
49. Watrous, J. D.; Dorrestein, P. C., Imaging mass spectrometry in microbiology. *Nat Rev Micro* **2011,** *9* (9), 683-694.
50. Masyuko, R.; Lanni, E.; Sweedler, J.; Bohn, P., *Analyst* **2013,** *138*, 1924-1939.
51. Li, Z.; Chu, L.; Sweedler, J.; Bohn, P., *Anal. Chem.* **2010,** *82*, 2608-2611.
52. Zhang, L.; Veres-Schalnat, T. A.; Somogyi, A.; Pemberton, J. E.; Maier, R. M., Fatty Acid Cosubstrates Provide beta-Oxidation Precursors for Rhamnolipid Biosynthesis in Pseudomonas aeruginosa, as Evidenced by Isotope Tracing and Gene Expression Assays. *Appl. Environ. Microbiol.* **2012,** *78* (24), 8611-8622.
53. Lebron-Paler, A.; Pemberton, J. E.; Becker, B. A.; Otto, W. H.; Larive, C. K.; Maier, R. M., Determination of the acid dissociation constant of the biosurfactant monorhamnolipid in aqueous solution by potentiometric and spectroscopic methods. *Anal. Chem.* **2006,** *78* (22), 7649-7658.
54. Shrout, J. D.; Chopp, D. L.; Just, C. L.; Hentzer, M.; Givskov, M.; Parsek, M. R., The impact of quorum sensing and swarming motility on Pseudomonas aeruginosa biofilm formation is nutritionally conditional. *Mol. Microbiol.* **2006,** *62* (5), 1264-1277.
55. Heydorn, A.; Nielsen, A. T.; Hentzer, M.; Sternberg, C.; Givskov, M.; Ersboll, B. K.; Molin, S., Quantification of biofilm structures by the novel computer program COMSTAT. *Microbiology-Uk* **2000,** *146*, 2395-2407.
56. Haase, A.; Arlinghaus, H. F.; Tentschert, J.; Jungnickel, H.; Graf, P.; Mantion, A.; Draude, F.; Galla, S.; Plendl, J.; Goetz, M. E.; Masic, A.; Meier, W.; Thunemann, A. F.; Taubert, A.; Luch, A., Application of Laser Postionization Secondary Neutral Mass Spectrometry/Time-of-Flight Secondary Ion Mass Spectrometry in Nanotoxicology: Visualization of Nanosilver in Human Macrophages and Cellular Responses. *ACS Nano* **2011,** *5* (4), 3059-3068.
57. Pei, B.; Chen, J. W., More ordered, convex ganglioside-enriched membrane domains: The effects of GM(1) on sphingomyelin bilayers containing a low level of cholesterol. *J. Biochem.* **2003,** *134* (4), 575-581.
58. Notingher, I.; Verrier, S.; Romanska, H.; Bishop, A. E.; Polak, J. M.; Hench, L. L., In situ characterisation of living cells by Raman spectroscopy. *Spectroscopy-an International Journal* **2002,** *16* (2), 43-51.
59. Harz, M.; Rosch, P.; Peschke, K. D.; Ronneberger, O.; Burkhardt, H.; Popp, J., Micro-Raman spectroscopic identification of bacterial cells of the genus Staphylococcus and dependence on their cultivation conditions. *Analyst* **2005,** *130* (11), 1543-1550.
60. Neugebauer, U.; Schmid, U.; Baumann, K.; Ziebuhr, W.; Kozitskaya, S.; Deckert, V.; Schmitt, M.; Popp, J., Towards a detailed understanding of bacterial metabolism - Spectroscopic characterization of Staphylococcus epidermidis. *Chemphyschem* **2007,** *8* (1), 124-137.
61. Uzunbajakava, N.; Lenferink, A.; Kraan, Y.; Willekens, B.; Vrensen, G.; Greve, J.; Otto, C., Nonresonant Raman imaging of protein distribution in single human cells. *Biopolymers* **2003,** *72* (1), 1-9.
62. Puppels, G. J.; Garritsen, H. S. P.; Segersnolten, G. M. J.; Demul, F. F. M.; Greve, J., Raman Microspectroscopic Approach to the Study of Human Granulocytes. *Biophys. J.* **1991,** *60* (5), 1046-1056.
63. Manoharan, R.; Ghiamati, E.; Chadha, S.; Nelson, W. H.; Sperry, J. F., Effect of cultural conditions on deep UV resonance Raman-spectra of bacteria. *Appl. Spectrosc.* **1993,** *47* (12), 2145-2150.
64. Maquelin, K.; Choo-Smith, L. P.; van Vreeswijk, T.; Endtz, H. P.; Smith, B.; Bennett, R.; Bruining, H. A.; Puppels, G. J., Raman spectroscopic method for identification of clinically relevant microorganisms growing on solid culture medium. *Anal. Chem.* **2000,** *72* (1), 12-19.
65. Herbert, D., Chemical Composition of Microorganisms as a Function of their Environment. *Symp. Soc. Gen. Microbiol.* **1961**, 391-416.
66. Jadhav, M.; Kalme, S.; Tamboli, D.; Govindwar, S., Rhamnolipid from Pseudomonas desmolyticum NCIM-2112 and its role in the degradation of Brown 3REL. *J. Basic Microbiol.* **2011,** *51*, 385-396.
67. Boles, B. R.; Thoendel, M.; Singh, P. K., Rhamnolipids mediate detachment of Pseudomonas aeruginosa from biofilms. *Mol. Microbiol.* **2005,** *57* (5), 1210-1223.
68. Davey, M. E.; Caiazza, N. C.; O'Toole, G. A., Rhamnolipid surfactant production affects biofilm architecture in Pseudomonas aeruginosa PAO1. *J. Bacteriol.* **2003,** *185* (3), 1027-1036.
69. Pearson, J. P.; Pesci, E. C.; Iglewski, B. H., Roles of Pseudomonas aeruginosa las and rhl quorum-sensing systems in control of elastase and rhamnolipid biosynthesis genes. *J. Bacteriol.* **1997,** *179* (18), 5756-5767.
70. Altelaar, A. F. M.; Klinkert, I.; Jalink, K.; de Lange, R. P. J.; Adan, R. A. H.; Heeren, R. M. A.; Piersma, S.

R., Gold-Enhanced Biomolecular Surface Imaging of Cells and Tissue by SIMS and MALDI Mass Spectrometry. *Analytical Chemistry* **2005,** *78* (3), 734-742.

71. Li, Z.; Bohn, P. W.; Sweedler, J. V., Comparison of sample pre-treatments for laser desorption ionization and secondary ion mass spectrometry imaging of *Miscanthus giganteus*. *Bioresour. Technol.* **2010,** *101* (14), 5578-5585.
72. Price, N. P. J.; Ray, K. J.; Vermillion, K.; Kuo, T.-M., MALDI-TOF mass spectrometry of naturally occurring mixtures of monorhamnolipids and dirhamnolipids. *Carbohydrate Research* **2009,** *344* (2), 204-209.
73. Abdel-Mawgoud, A.; Lépine, F.; Déziel, E., Rhamnolipids: diversity of structures, microbial origins and roles. *Appl Microbiol Biotechnol* **2010,** *86* (5), 1323-1336.
74. de Koster, C. G.; Vos, B.; Versluis, C.; Heerma, W.; Haverkamp, J., High-performance thin-layer chromatography/fast atom bombardment (tandem) mass spectrometry of Pseudomonas rhamnolipids. *Biological Mass Spectrometry* **1994,** *23* (4), 179-185.
75. Rikalovic, M.; Abdel-Mawgoud, A.; Déziel, E.; Gojgic-Cvijovic, G.; Nestorovic, Z.; Vrvic, M.; Karadzic, I., Comparative Analysis of Rhamnolipids from Novel Environmental Isolates of Pseudomonas aeruginosa. *J Surfact Deterg* **2013,** *16* (5), 673-682.
76. Tremblay, J.; Richardson, A.-P.; Lépine, F.; Déziel, E., Self-produced extracellular stimuli modulate the Pseudomonas aeruginosa swarming motility behaviour. *Environmental Microbiology* **2007,** *9* (10), 2622-2630.

FIGURES AND TABLES

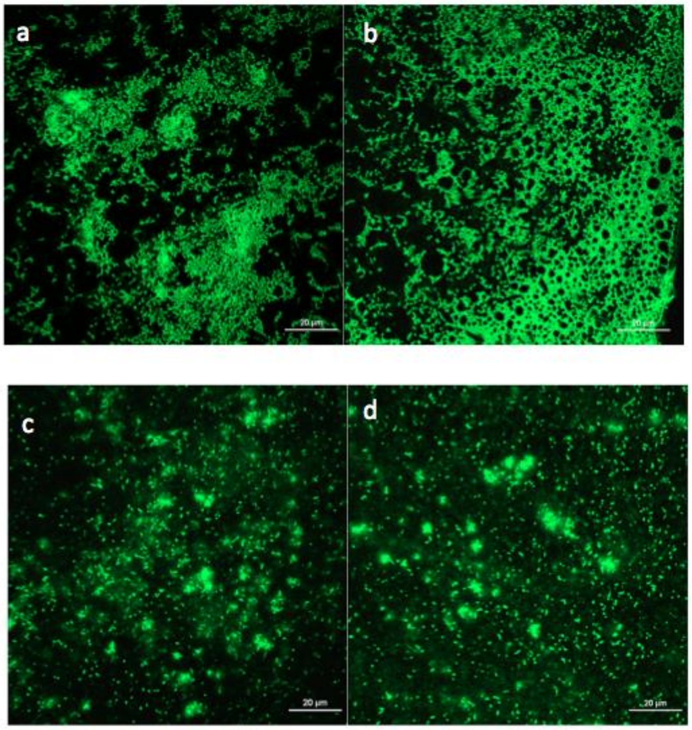

Figure 6.1: Fluorescence microscopy comparison of biofilms grown on different substrates. Fluorescence images of wild type biofilms on bare silicon wafer (a) and on gold-coated silicon wafer (b) and mutants prepared under biofilm conditions on bare silicon wafer (c) and gold-coated silicon wafer (d) . Biofilms were stained with SYTO 24. Adapted with permission from R. N. Masyuko, E. J. Lanni, C. M. Driscoll, J. D. Shrout, J. V. Sweedler, and P. W. Bohn, *Analyst* **2014**, *in press*, DOI: 10.1039/C4AN00435C. Copyright 2014 Royal Society of Chemistry.

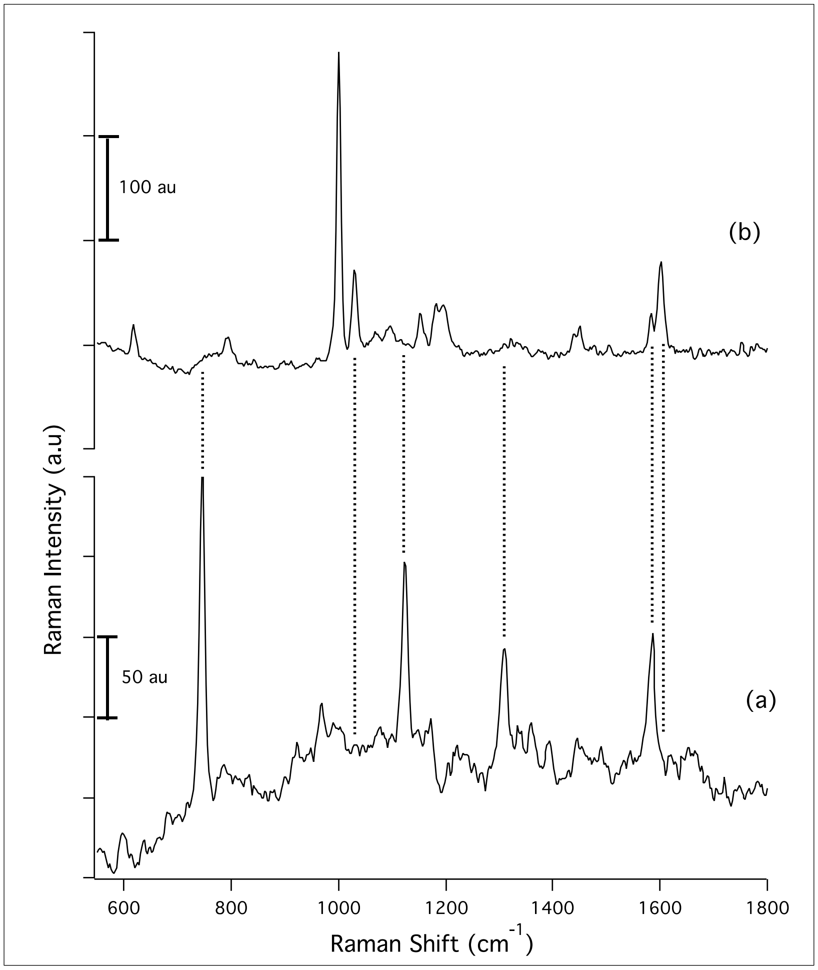

Figure 6.2: Raman microspectra of wild type *Pseudomonas aeruginosa*. (a) Planktonic cells, as deposited on Au-coated Si substrate. **(b)** Biofilm after 72 h formation on uncoated Si. Raman spectra are baseline corrected using a fourth order polynomial function. Vertical dashed lines added to aid comparison between spectra. Adapted with permission from R. N. Masyuko, E. J. Lanni, C. M. Driscoll, J. D. Shrout, J. V. Sweedler, and P. W. Bohn, *Analyst* **2014**, *in press*, DOI: 10.1039/C4AN00435C. Copyright 2014 Royal Society of Chemistry.

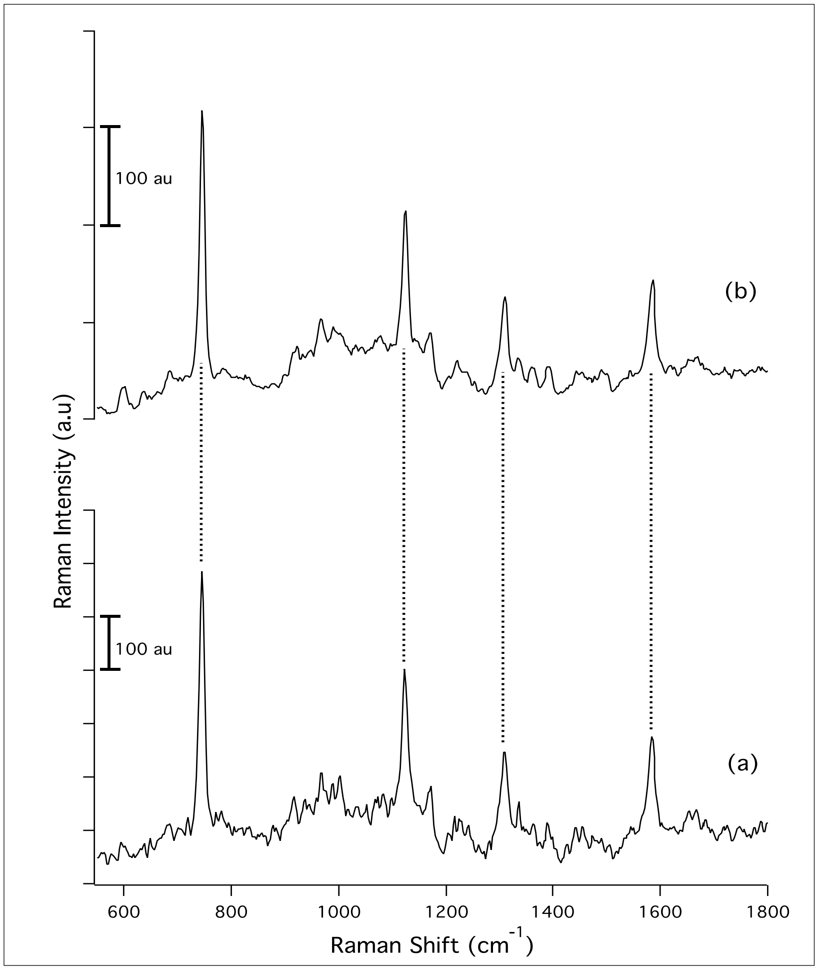

Figure 6.3: Raman microspectra of Δ*las*Δ*rhlI* mutant (MH710) *Pseudomonas aeruginosa*. (a) Planktonic cells as deposited on Au-coated Si substrate. **(b)** Same cells after 72 h in conditions supporting biofilm formation in the wild type. Raman spectra are baseline corrected using a fourth order polynomial function. Vertical dashed lines added to aid comparison between spectra. Adapted with permission from R. N. Masyuko, E. J. Lanni, C. M. Driscoll, J. D. Shrout, J. V. Sweedler, and P. W. Bohn, *Analyst* **2014**, *in press*, DOI: 10.1039/C4AN00435C. Copyright 2014 Royal Society of Chemistry.

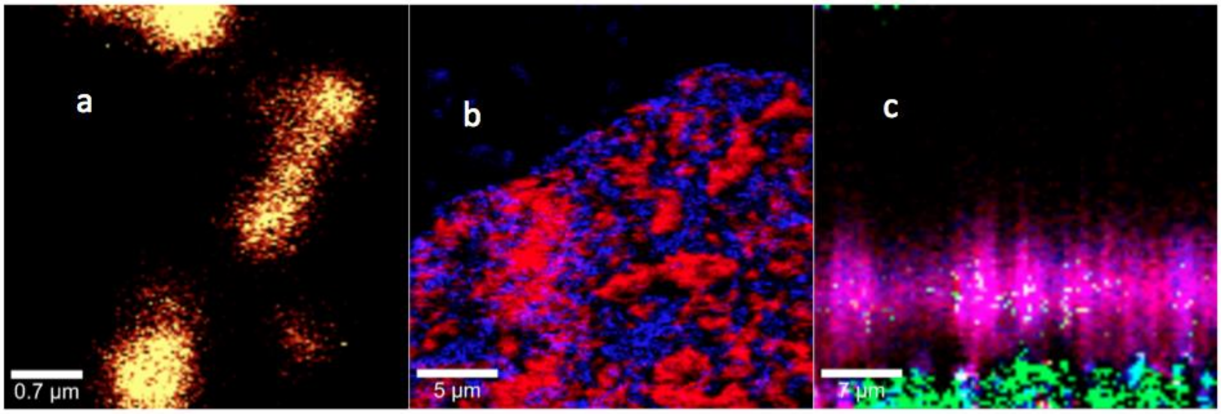

Figure 6.4: Composite Raman images of different *Pseudomonas aeruginosa* samples. **(a)** Plan view image of planktonic cells constructed from scattering in the region 2800-3050 cm^{-1}. Scale bar 0.7 µm. **(b)** Plan view image of a biofilm constructed from a combination of bands in the regions 1560-1620 cm^{-1} (red) and 1010-1165 cm^{-1} (blue), characteristic of protein and carbohydrate scattering, respectively. Scale bar 5 µm. (c) Depth profile of the biofilm in the *x*-*z* plane constructed from 2800-3050 cm^{-1} (red), 1560-1620 cm^{-1} (blue) and 725-775 cm^{-1} (green). Scale bar 7 µm. Adapted with permission from R. N. Masyuko, E. J. Lanni, C. M. Driscoll, J. D. Shrout, J. V. Sweedler, and P. W. Bohn, *Analyst* **2014**, *in press*, DOI: 10.1039/C4AN00435C. Copyright 2014 Royal Society of Chemistry.

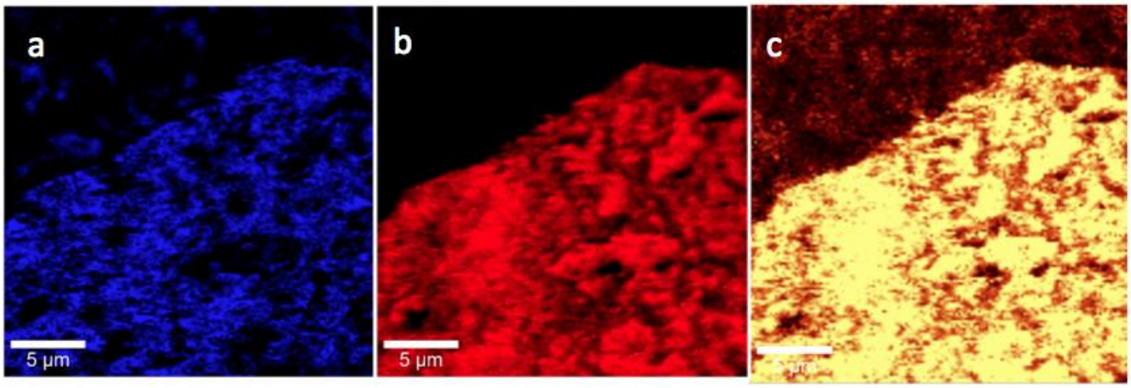

Figure 6.5: CRM images of biofilm. Confocal Raman images showing the distribution of carbohydrates and glycolipids (1010 -1165cm^{-1}) , blue (a), proteins (1560-1620 cm^{-1}), red (b), and all organic matter (2800-3050 cm^{-1}) yellow (c). Adapted with permission from R. N. Masyuko, E. J. Lanni, C. M. Driscoll, J. D. Shrout, J. V. Sweedler, and P. W. Bohn, *Analyst* **2014**, *in press*, DOI: 10.1039/C4AN00435C. Copyright 2014 Royal Society of Chemistry.

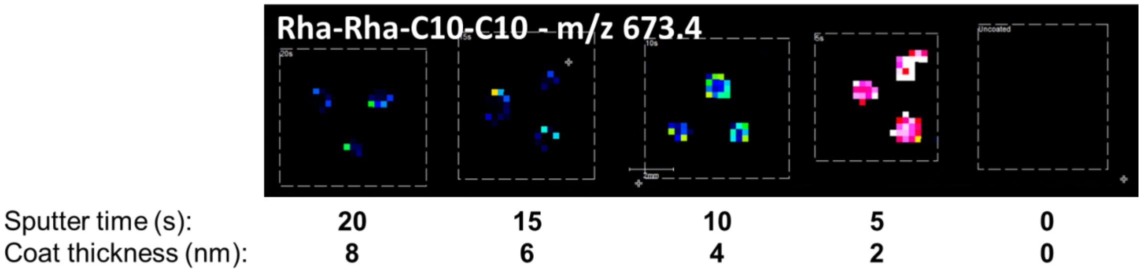

Figure 6.6: Optimization of Au sputter coat thickness for MALDI MSI. Rhamnolipid standard was spotted on silicon wafer substrates and sputter-coated for 0-20 seconds, corresponding to a 0-8 nm-thick Au coating. The ion image of the predominant rhamnolipid species Rha-Rha-C10-C10 (shown here) shows greatest signal with the thinnest (~2 nm) coating. Adapted with permission from R. N. Masyuko, E. J. Lanni, C. M. Driscoll, J. D. Shrout, J. V. Sweedler, and P. W. Bohn, *Analyst* **2014**, *in press*, DOI: 10.1039/C4AN00435C. Copyright 2014 Royal Society of Chemistry.

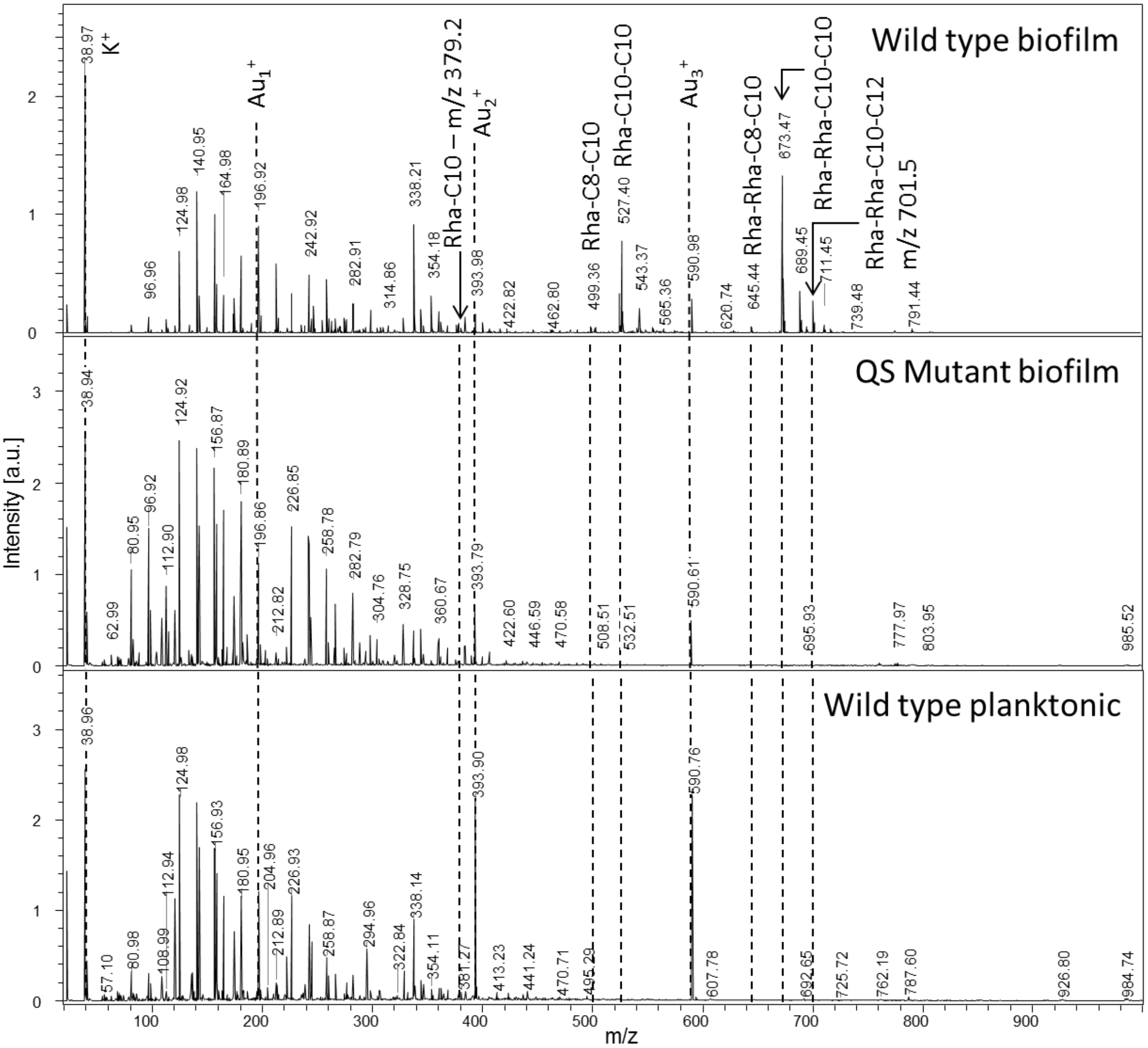

Figure 6.7: MALDI MS profiles of *P. aeruginosa.* Representative MALDI MS single-pixel spectra of *P. aeruginosa* wild-type biofilm (*top*), QS mutant biofilm (*center*), and wild-type planktonic cells (*bottom*). Rhamnolipid-derived ions are detected exclusively in the wild-type biofilm. Adapted with permission from R. N. Masyuko, E. J. Lanni, C. M. Driscoll, J. D. Shrout, J. V. Sweedler, and P. W. Bohn, *Analyst* **2014**, *in press*, DOI: 10.1039/C4AN00435C. Copyright 2014 Royal Society of Chemistry.

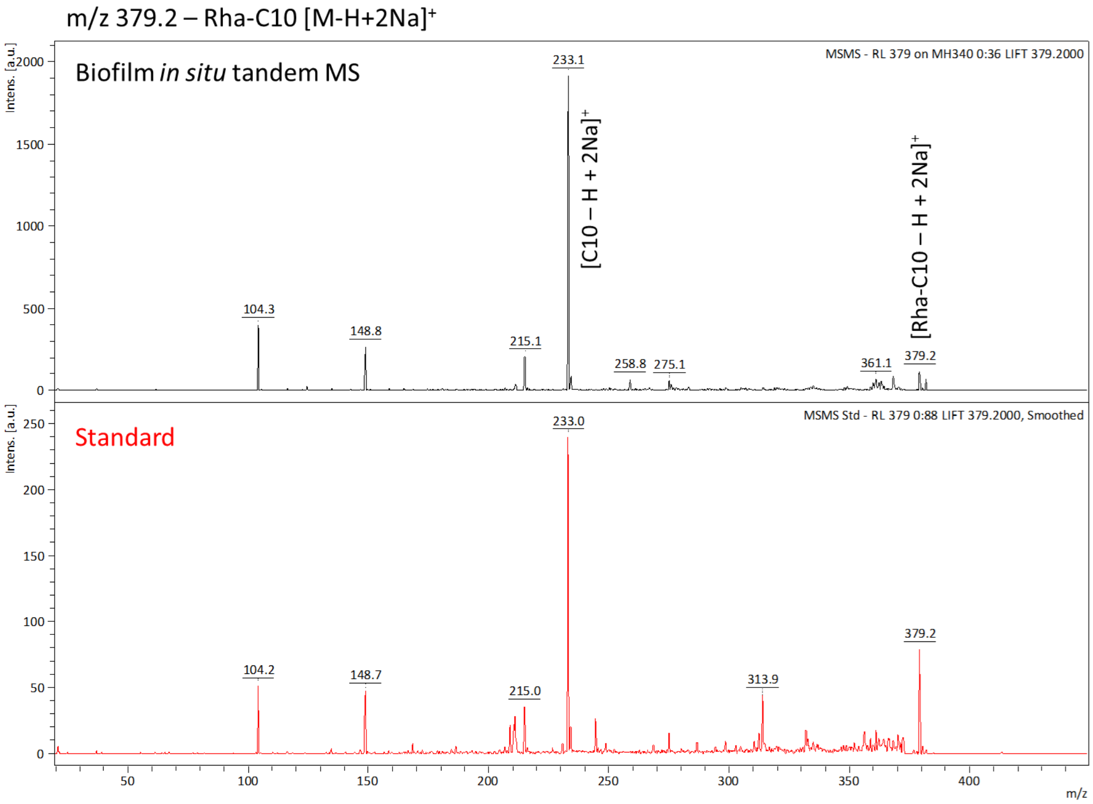

Figure 6.8: Rhamnolipid identification by MALDI tandem MS. Tandem MS spectra for rhamnolipid-related ions, acquired *in situ* by MALDI-TOF/TOF MS on wild type *P. aeruginosa* biofilm (top) and from mixed rhamnolipid standard (bottom), confirm mass assignments. Characteristic fragments are matched to and in agreement with previous MS/MS analyses (see ref. [66] – de Koster et al. (1994) Bio Mass Spec 23, 179 and ref. [26] – Moree et al. (2012) PNAS 109, 13811). Additional unassigned fragments may arise from post-source decay-specific fragmentation pathways not produced in CID and/or fragmentation of other nearly isobaric ions which were necessarily included in the parent isolation window. Adapted with permission from R. N. Masyuko, E. J. Lanni, C. M. Driscoll, J. D. Shrout, J. V. Sweedler, and P. W. Bohn, *Analyst* **2014**, *in press*, DOI: 10.1039/C4AN00435C. Copyright 2014 Royal Society of Chemistry.

m/z 499.3 – Rha-C8-C10 [M+Na]$^+$

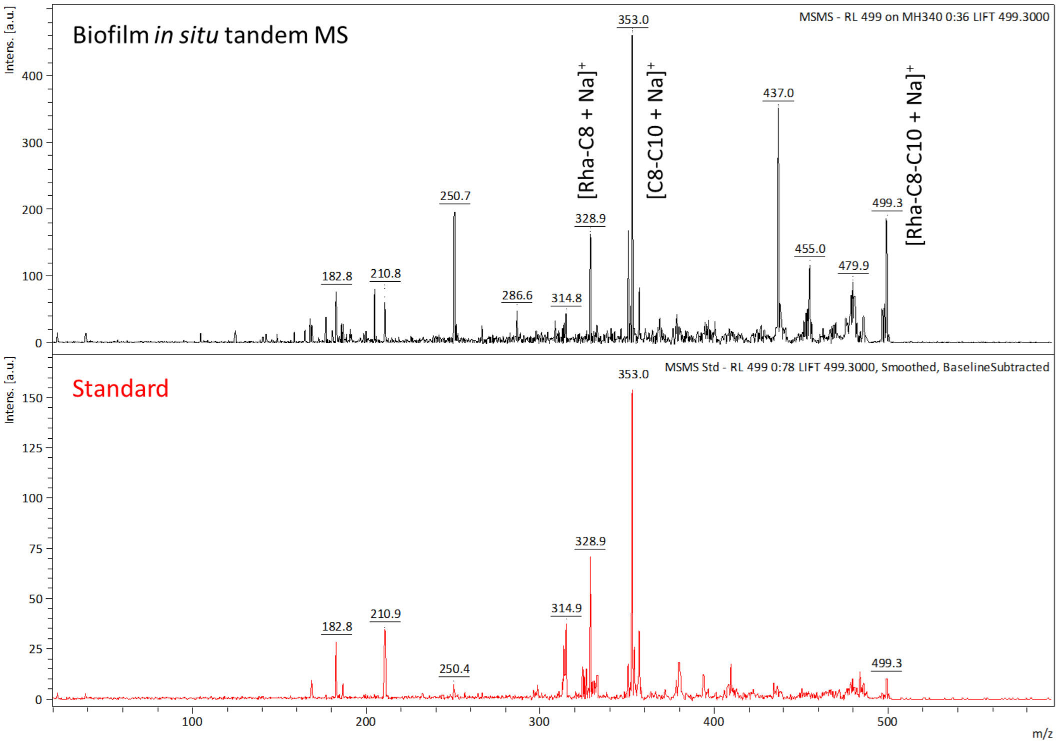

m/z 527.3 – Rha-C10-C10 [M+Na]$^+$

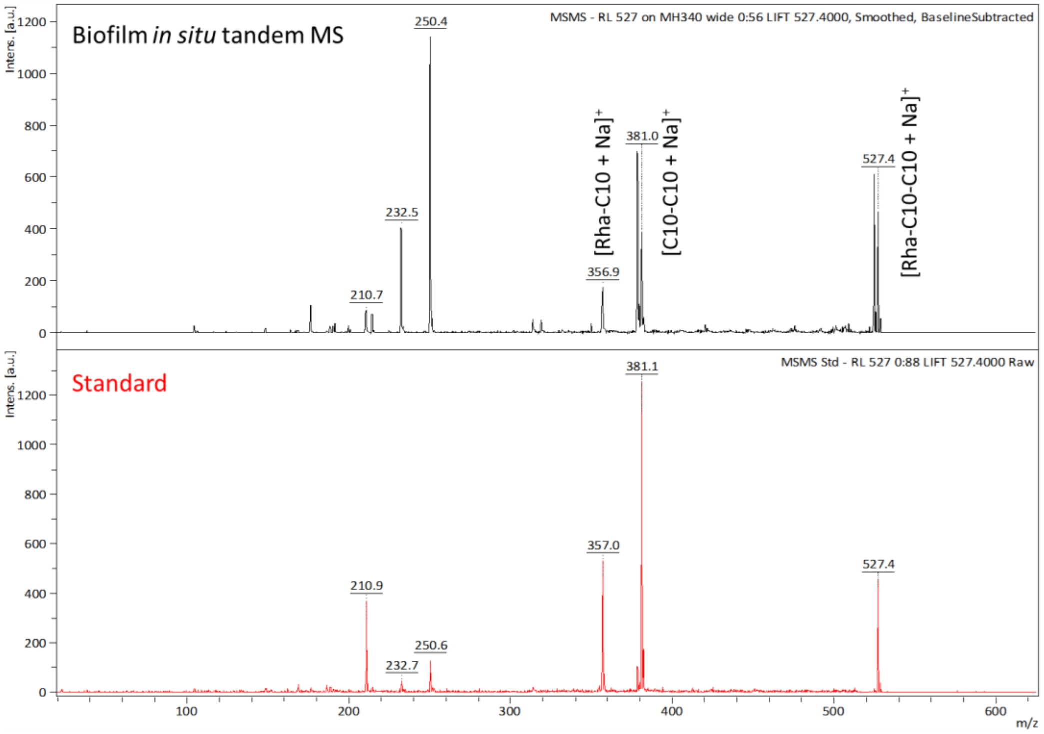

Figure 6.8 (continued)

m/z 645.3 – Rha-Rha-C8-C10 $[M+Na]^+$

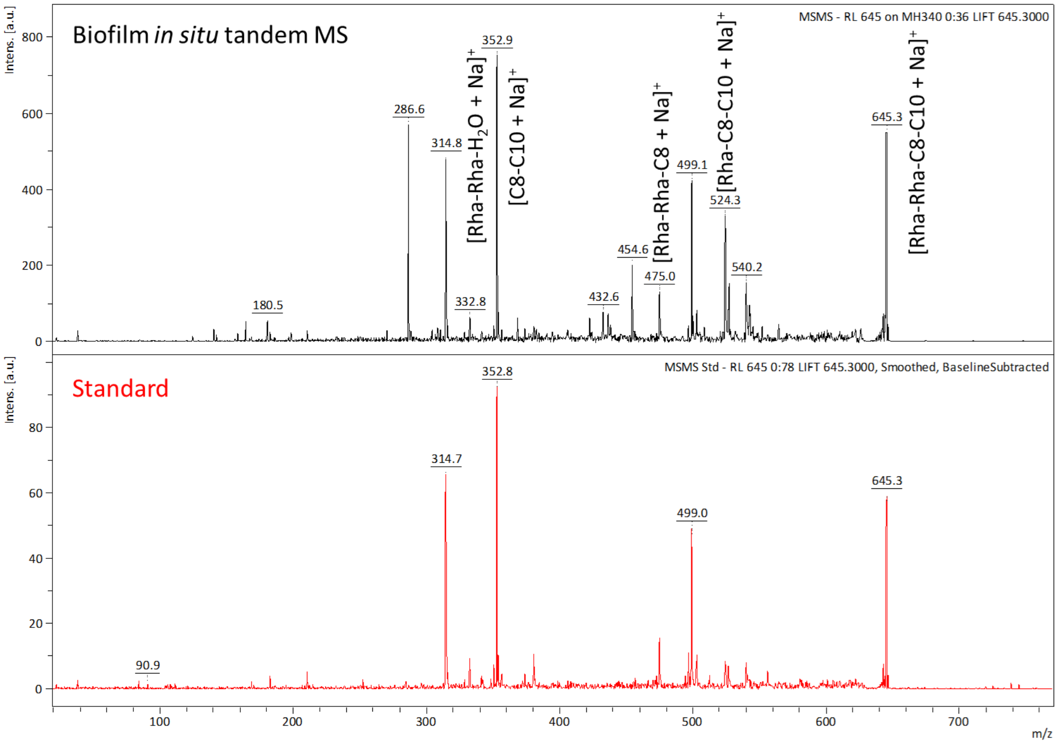

m/z 673.4 – Rha-Rha-C10-C10 $[M+Na]^+$

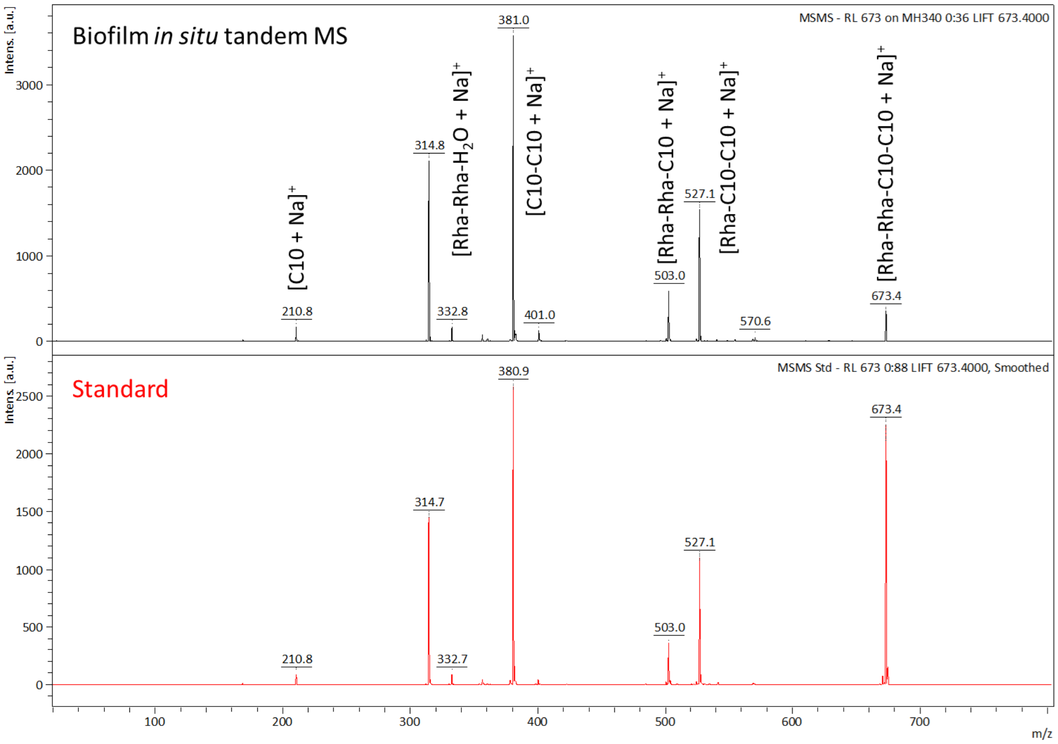

Figure 6.8 (continued)

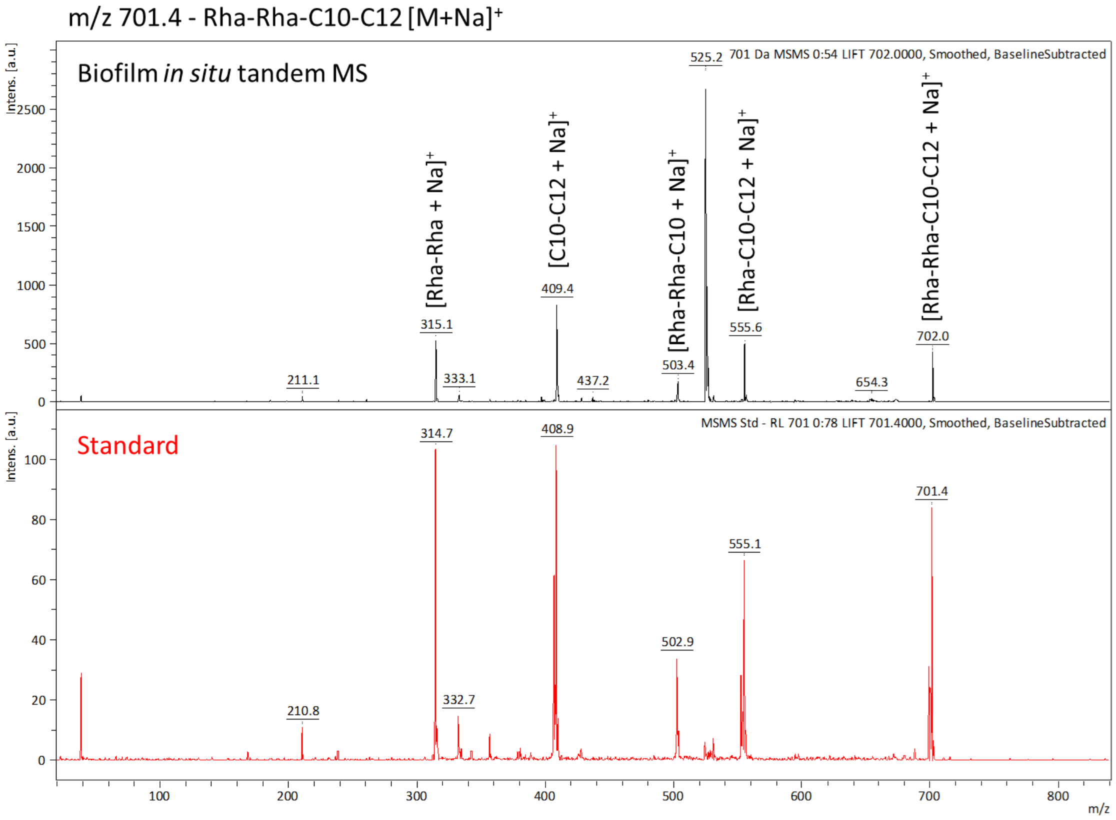

Figure 6.8 (continued)

Compound	**Molecular Formula**	**$[M+Na]^+$ theor.**	**$[M+Na]^+$ obs.**	**MS/MS confirmation**
Rha-C10	$C_{16}H_{30}O_7$	379.2*	379.2*	Y
Rha-C8-C10	$C_{24}H_{44}O_9$	499.3	499.4	Y
Rha-Rha-C10	$C_{22}H_{40}O_{11}$	503.3	503.4	
Rha-C10-C10	$C_{26}H_{48}O_9$	527.3	527.4	Y
Rha-C10-C12:1	$C_{28}H_{50}O_9$	553.3	553.4	
Rha-C10-C12	$C_{28}H_{52}O_9$	555.4	555.5	
Rha-Rha-C8-C10	$C_{30}H_{54}O_{13}$	645.3	645.4	Y
Rha-Rha-C10-C10	$C_{32}H_{58}O_{13}$	673.4	673.5	Y
Rha-Rha-C10-C12	$C_{34}H_{62}O_{13}$	701.4	701.5	Y

Table 6.1: **Rhamnolipid species detected on *P. aeruginosa* wild type biofilm and successfully identified by *in situ* tandem MS.** *Rha-C10 detected as $[M\text{-}H+2Na]^+$ Adapted with permission from R. N. Masyuko, E. J. Lanni, C. M. Driscoll, J. D. Shrout, J. V. Sweedler, and P. W. Bohn, *Analyst* **2014**, *in press*, DOI: 10.1039/C4AN00435C. Copyright 2014 Royal Society of Chemistry.

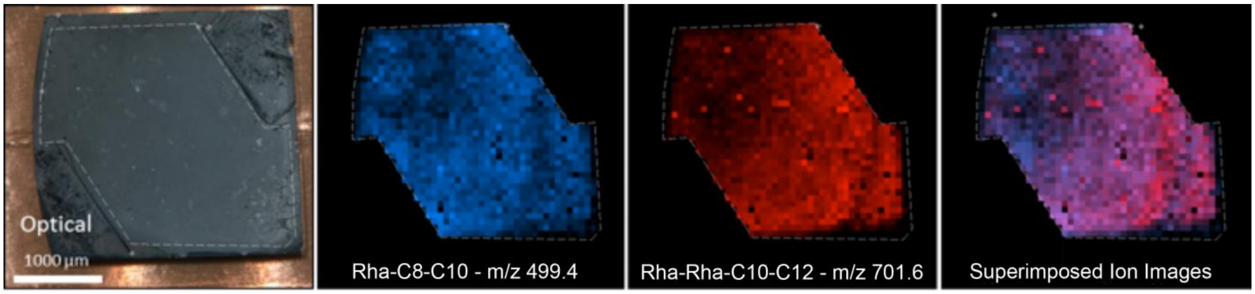

Figure 6.9: MALDI MSI of rhamnolipid distributions in biofilm. *P. aeruginosa* wild type biofilm optical (*left*) and rhamnolipid ion (*center and right*) images with Rha-C8-C10 (blue) and Rha-Rha-C10-C12 (red) color coded, scale bar 1 mm. Superposition of the mono- and dirhamnolipid reveals non-uniform distribution patterns, and dirhamnolipid Rha-Rha-C10-C12 also appear highly localized to small biofilm features. Adapted with permission from R. N. Masyuko, E. J. Lanni, C. M. Driscoll, J. D. Shrout, J. V. Sweedler, and P. W. Bohn, *Analyst* **2014**, *in press*, DOI: 10.1039/C4AN00435C. Copyright 2014 Royal Society of Chemistry.

CHAPTER 7

MALDI-GUIDED SIMS: MULTISCALE IMAGING OF METABOLITES IN BACTERIAL BIOFILMS

NOTES AND ACKNOWLEDGMENTS

This chapter is adapted and used with permission from a manuscript submitted for publication on June 2, 2014, coauthored by R. N. Masyuko, C. M. Driscoll, J. T. Aerts, J. D. Shrout, P. W. Bohn, and J. V. Sweedler. E. J. Lanni developed MSI sample preparation protocols, performed MALDI and SIMS imaging, MALDI tandem MS, and authored the manuscript. R. N. Masyuko and C. M. Driscoll prepared biofilm samples, and J. T. Aerts performed CE-ESI-MS and MS/MS experiments. Funding provided by the Department of Energy Office of Biological and Environmental Research through grant DE SC0006642 and NIH through grant U54GM093342 is gratefully acknowledged. SIMS imaging was performed in the Center for Microanalysis of Materials, University of Illinois at Urbana-Champaign, partially supported by the U.S. Department of Energy through grant DEFG02-91-ER45439.

INTRODUCTION

Mass spectrometry imaging (MSI) is an analytical approach which enables multiplex, label-free, and non-targeted chemical imaging of surfaces.[1-3] These features make it a useful tool for visualizing spatially heterogeneous chemical environments, especially for small molecules in biological systems, such as drugs and metabolites which can otherwise be difficult to reliably label and to distinguish from structurally similar compounds. MSI is commonly performed by scanning a microprobe over the sample surface and acquiring mass spectra at thousands of discrete positions in a rectangular array. Hundreds of unique ions are routinely detected per spectrum, and any of these signals may be used to generate an ion image representing relative abundance of the ionized compound across the analyzed region.

MSI can utilize many different microprobes including focused lasers for matrix-assisted laser desorption/ionization (MALDI)[4,5] and focused ion beams for secondary ion mass spectrometry (SIMS).[6-8] These techniques are complementary in that MALDI affords excellent detection limits and broad mass range extending to tens of kDa (in practice for MSI), while SIMS provides the highest lateral spatial resolution and nanometer-scale depth resolution,[9] but with a more limited, (typically sub-kDa) mass range. MALDI requires chemical modification of the sample surface to enhance the yields of non-volatile high molecular weight species to useful levels; this is often accomplished by applying a dissolved organic compound, which subsequently dries and crystallizes on the surface, but alternative matrices exist such as sputtered metal coatings.[10,11] SIMS does not require matrix but can nevertheless benefit from similar treatments, including metal coatings.[10-12] Combined MALDI and SIMS imaging has been utilized recently for multi-scale chemical mapping of nervous tissue,[13,14] single cultured neurons,[13] and biofuel feedstock grass.[12]

Microscopic MSI allows multiplex visualization of unlabeled analytes at cell- and subcell-size scales,[15] but it also involves trade-offs: sampled surface area (per pixel) and detected ions decrease quadratically with probe diameter, while pixel count and therefore data file size and acquisition time increase quadratically with spatial resolution. In practice, the experimental time increase may even be larger than quadratic because one often acquires greater number of laser/ion shots to make up for the smaller amount of material present in the smaller pixel size. These issues equate to practical limitations; large samples cannot be imaged entirely at high resolution in reasonable timeframes, so microscopic regions of interest (ROIs) must be specified first by some other means. Optical image correlation is often used for MSI of tissue sections, but this approach depends on well-understood anatomy and obvious morphological features such as the white and gray matter of brain tissue. Immunohistological stains have also been applied prior to MSI in order to enhance the information content of the optical image,[16] but this requires having details on a specific marker of interest, and also requires immersion of the sample in liquid washes and stain(s) which result in chemical modification and analyte delocalization on the microscopic scale. Thus for samples which lack visible and well-defined anatomy, new techniques are needed for directing microscopic MSI experiments to selected areas of chemical interest.

Here we develop MALDI-guided SIMS, wherein a full-sample chemical map is first acquired by MALDI MS, and this map is used to direct high resolution SIMS imaging at microscopic regions of interest. A metal-assisted preparation is utilized for compatibility with both ion imaging methods, and the surface is undersampled by MALDI in order to leave unperturbed surface for subsequent SIMS imaging. Laser ablation spots are visualized in SIMS images and used to precisely specify microscopic ROIs. The larger laser ablation volume yields substantially higher ion counts, enabling *in situ* ion identification with tandem MS on the same sample subsequent to imaging.

We apply MALDI-guided SIMS to cultured biofilms of the opportunistic pathogen *Pseudomonas aeruginosa* in order to visualize secondary metabolites which are involved in biofilm growth and cellular signaling. These compounds are detected as intact pseudomolecular ions for the first time by SIMS and confirmed by *in situ* tandem MS as well as by capillary electrophoresis electrospray ionization (CE-ESI) tandem MS of bulk biofilm extracts. While MALDI MSI has yielded informative "colony-scale" images[17,18] and SIMS imaging has been applied to obtain exquisite cell-scale chemical information[19-22] in previous microbiological studies, the unique sequential combination of MALDI and SIMS utilized here guides high-resolution imaging rationally and also enables this information to be placed within the macroscopic spatial context of the biofilm.

EXPERIMENTAL METHODS

Materials and Chemicals

Mixed rhamnolipid "R-95 Rhamnolipid" (95%, Aldrich^{CPR}), 2-heptyl-3-hydroxy-4(1H)-quinolone (*Pseudomonas* quinolone signal, PQS), and 2-heptyl-4-quinolone (HHQ) standards were purchased from Sigma-Aldrich (St Louis, MO, USA) and dissolved in methanol for MS experiments. Silicon substrates for biofilm growth were purchased as 4 in-diameter wafers of Si (100) from Silicon, Inc. (Boise, ID, USA), scored with a diamond scribe, and broken to yield 2 × 2 cm^2 tiles before use. Solvents and buffer ingredients for CE-MS were purchased from Sigma-Aldrich and mixtures were prepared in lab.

Biofilm Growth

Two *Pseudomonas aeruginosa* strains were used in this work: ATCC strain 15692 ("wild type") and Δ*lasI*Δ*rhlI* mutant[23] ("QS mutant") which is deficient in homoserine lactone production *i.e.* has disabled quorum sensing. Cell suspensions were grown at 30°C overnight in FAB culture medium[24] with a filter-sterilized glucose carbon source (150 µL of 1.2 M glucose solution per 6 mL culture) and then transferred to Petri dishes. Cell suspension in the Petri dishes was diluted 50× with culture medium, allowed 1 min. for initial cell attachment, and then silicon tiles were fully submerged in the mixture. Static biofilms were permitted to grow for 72 h at 30 °C. Growth medium was then removed from the Petri dishes by pipette and the biofilms were allowed to air dry completely prior to preparation for MSI analysis.

Mass Spectrometry Imaging

Sputter coating was performed using a Desk II TSC sputter coater equipped with a gold target (Denton Vacuum, Moorestown, NJ, USA) operated at 64 mTorr Ar pressure, 40% power, and six seconds of application time. MALDI MS was performed on an UltrafleXtreme MALDI-TOF/TOF MS (Bruker Daltonics, Billerca, MA, USA) in positive ion mode, reflectron enabled, acquiring m/z 20-1000, and equipped with a frequency-tripled Nd:YAG laser focused to approx. 100 µm probe diameter and triggered at 1000 Hz. Quadratic mass calibration was performed with K^+ and Au_n^+ cluster ions detected from the prepared sample. MS/MS (TOF/TOF) was performed by post-source decay without CID, adjusting laser power to optimize fragmentation for individual ions of interest. Data were processed using FlexAnalysis v3.4 and FlexImaging v3.0; ion filters are m/z ±0.25 and images are normalized to total ion count (TIC). SIMS imaging was performed on a TRIFT III (Physical Electronics, Chanhassen, MN, USA) TOF MS using a 22 kV Au^+ primary ion source yielding *ca.* 2 nA sample current and a 500 nm probe spot diameter. Images were acquired in the static SIMS regime, *i.e.* with primary beam flux $< 1\times 10^{12}$ primary ions / cm^2. Control and data processing were performed using WinCadence v4.4 software. Calibration was performed with H^+, Na^+, K^+, and Au_n^+ cluster ions. Optical images of samples were acquired with a Perfection V300 Photo flatbed scanner (Epson, Suwa, Nagano, Japan).

For MALDI-guided SIMS experiments, bacterial biofilms were first cultured and dried on silicon as described above. A thin layer of gold *ca.* 2 nm was applied to the sample and then an optical reference image was acquired. To load the samples into the MALDI TOF MS, they were first mounted in an “MTP AB adapter” MALDI target on a custom-made stainless steel plate and then affixed with double-sided conductive Cu-backed tape. The steel plate was milled to produce a recessed area matching the height of the mounted sample (silicon substrate plus tape) in order to level the sample surface with the MALDI target surface; this was critical for obtaining high quality MS spectra. The entire sample surface was then imaged by MALDI MS at 500 or 1000 µm pitch, 500 shots per position. MALDI ion images were inspected and used to select regions of interest (ROIs) for microscopic SIMS analysis. The sample was transferred to the SIMS instrument with care taken to maintain orientation. A SIMS "survey" was then acquired in mosaic mapping mode in which a relatively large (typically 4×4 mm^2) area was imaged quickly at low resolution (16×16 µm^2 pixel size) by stitching multiple small and fast (1 s accumulation time) ion images together; yielding images with low signal and contrast, but sufficient to visualize MALDI ablation marks for sample navigation and correlation with MALDI images. High resolution SIMS images (typically 150×150 µm^2 FOV and 0.6×0.6 µm^2 pixel size) were then acquired at ROIs specified from the MALDI map and subsequent SIMS survey.

CE-ESI MS/MS Biofilm Extract Analysis

CE–ESI MS/MS was performed as reported previously[25] using either an Impact HD or a maXis 4G Qq-ToF mass spectrometer (Bruker Daltonics, Billerica, MA) operated in positive and negative ion modes. Biofilm extracts were prepared by collecting *ca.* 1 mg dried biofilm from the silicon substrate with a clean razor blade, depositing the film into a microcentrifuge vial, adding 20 µL of extraction solution (50/50 (v/v) MeOH:H_2O + 0.5% AcOH), shaking vigorously for 2 min, then centrifuging for 5 min at 2,000 × g. 6 nL supernatant was loaded into the capillary per run, using a capillary length of 65–70 cm and a separation potential of 15 kV. For negative ion mode analysis, CE was performed using a background electrolyte composed of 20 mM ammonium bicarbonate, and a sheath liquid of 60% (v/v) isopropanol and 200 µM ammonium bicarbonate which was delivered at 600 nL per minute. Instrument calibration was performed using sodium acetate clusters in negative ion mode. Molecular features were assigned with high confidence through matching of tandem mass spectral data from the endogenous substances with those found at publicly available mass spectral databases (Metlin[26]).

RESULTS

MALDI-directed SIMS imaging enables the specification of ROIs for high resolution MSI on specimens which lack a characteristic anatomy, as in the bacterial biofilms studied here. A schematic of the overall workflow is shown in **Figure 7.1**. Dried biofilm samples were first sputter-coated with a 1-2 nm-thick Au film for metal-assisted (MetA) MS, providing signal enhancement for small molecules (effective to approx. < 1000 Da) with multiple additional advantages: mutual compatibility with both LDI and SIMS, no reduction in lateral resolution due to diffusion of analytes during solvent application or due to matrix particle size, minimal low-mass chemical background, monoisotopic Au_n^+ peaks for internal calibration, improved sample conductance to mitigate sample charging effects in SIMS, and optical transparency facilitating sample navigation and optical imaging after application. The Au coat thickness was optimized using mixed rhamnolipid standard spotted on Si wafer and found to give over tenfold signal enhancement for $[M+Na]^+$ ions (shown in **Figure 7.2**).

MS microprobes are inherently destructive, so a challenge in MALDI-guided SIMS is to acquire the MALDI image while leaving most of the sample surface unperturbed for subsequent SIMS imaging. This was accomplished by undersampling *i.e.* setting pixel size and array pitch to a length much larger than the microprobe diameter. The effect of this technique is apparent in **Figure 7.3**, showing selected results from a *P. aeruginosa* wild type (WT) biofilm analysis. MALDI imaging was performed in this experiment with a 1 mm pitch and 100 µm laser microprobe diameter, obtaining a coarse chemical map for multiple biologically-related ions including 2-heptyl-3-hydroxyquinolone, *Pseudomonas* quinolone signal (PQS, MH^+ at m/z 260.17), shown in **Figure 7.3B**. The laser ablation spots are clearly visible in the SIMS total ion image shown in **Figure 7.3C** as a decrease in overall signal, likely due to removal of the signal-enhancing metal coating, and these features form an array which can be used to navigate the sample and to select ROIs for SIMS imaging precisely positioned in relation to the MALDI data. In the ROI selected here, microscopic SIMS images show differential distribution of quinolones PQS and 2-heptyl-4-quinolone (HHQ, MH^+ at m/z 244.17). In addition to the MS/MS analyses discussed below, the assignment of these ions is confirmed by co-localization of ion fragments characteristic of their respective quinolone molecular classes, as shown in **Figure 7.4**).[27]

While mass profiles varied between and within individual biofilms, up to nine mono- and di-rhamnolipids and seven quinolone compounds were consistently detected in *P. aeruginosa* WT biofilms. All nine putative rhamnolipids were confirmed by CE-ESI-MS/MS analysis of bulk WT biofilm extract (results shown in **Figure 7.5**) while six of the nine could be confirmed directly from the biofilm by *in situ* MALDI-MS/MS as we reported recently[28] in comparison with standards and in agreement with previously published fragmentation analysis.[29]

Rhamnolipids were predominantly detected as sodium adducts ($[M+Na]^+$ and sometimes $[M-H+2Na]^+$) by both MALDI and SIMS and as deprotonated pseudomolecular ions by ESI, consistent with previous work.[30] Similarly, all seven putative quinolones were confirmed by CE-ESI-MS/MS (shown in **Figure 7.5**) while HHQ, PQS, and NHQ were also confirmed by *in situ* MALDI-MS/MS (spectra shown in **Figure 7.6**). Quinolones were detected as primarily MH^+ ions (and $[M-H]^-$ ions with ESI) which is consistent with previous ESI MS work,[27] and formation of these ions in SIMS was also confirmed with quinolone standards (PQS and HHQ; others were not available), both of which yielded primarily MH^+ ions after metal enhancement (as shown in **Figure 7.7**). Several pairs of known quinolones are isobaric, including PQS and 4-hydroxy-2-heptylquinoline-N-oxide (HQNO), but these were discerned by MS/MS fragmentation patterns.[27] In the case of PQS and HQNO at m/z 260, *in situ* MALDI-MS/MS yielded predominantly PQS-related fragments (m/z 175, 188) and little or no contribution from HQNO (m/z 159, 172). Detectable quantities of HQNO were observed with CE-MS/MS from a biofilm extract; our lack of detection of this compound by MALDI and SIMS may indicate that HQNO is localized below MALDI and SIMS sampling depth within the biofilm, or that low levels (below our MSI detection limits) are uniformly distributed on the surface. **Table 7.1** compiles the MALDI MS, SIMS, and CE-ESI MS data acquired from WT *P. aeruginosa* biofilms. The standard rhamnolipid notation used here is detailed elsewhere.[31]

Comparison of wild-type and quorum-sensing mutant *P. aeruginosa* biofilms

WT and QS mutant *P. aeruginosa* biofilms were compared using MALDI-guided SIMS to characterize spatiochemical differences arising from a disabled QS system, and results are shown in **Figure 7.8**. These biofilms were gold-coated and imaged by MALDI in a single experiment to minimize preparation- and instrument-related variation. MALDI images show high abundance of major rhamnolipids Rha-Rha-C_{10}-C_{10} and Rha-C_{10}-C_{10} (both detected as $[M+Na]^+$ at m/z 673.38 and 527.32, respectively) distributed uniformly across the WT biofilm and completely absent in the QS mutant biofilm. SIMS images reflect these observations on the microscopic scale; rhamnolipids are uniformly distributed in the WT biofilm, but they are not detected in the QS mutant biofilm. In contrast, quinolones are highly heterogeneous within and between both samples. HHQ shows comparable abundance overall between biofilms in the MALDI image, though a macroscopic region of relatively high abundance can be seen to follow the growth contour of the QS mutant. The HHQ SIMS image at this feature likewise shows higher overall signal as well as “hot spots” of intense localization in aggregated clusters of <10 µm features, while the WT biofilm SIMS image shows lower overall abundance and smaller, less intense localizations without the aggregate features. Another prominent quinolone, 2-nonyl-4-quinolone (NHQ, MH^+ at m/z 272.20), exhibits sparse localizations in MALDI images of both biofilms, and appears to co-localize with HHQ in the microscopic aggregates. Lower resolution mosaic SIMS images acquired around the specified ROIs on these biofilms (shown in **Figure 7.9**) indicate that these aggregates are abundant across the surface of the QS mutant biofilm in the selected area, while not observed at all with the WT. In contrast, PQS shows higher abundance on the WT biofilm in the MALDI image, and this is also reflected in the selected SIMS ROIs which show less PQS on the QS mutant relative to the other quinolones.

DISCUSSION

MALDI-guided SIMS imaging enables visualization of molecular distributions on both cell (microscopic) and population (macroscopic) size scales. This approach is demonstrated here with *P. aeruginosa* in order to visualize chemical features associated with growth and cellular signaling. *P. aeruginosa* is an opportunistic pathogen known for organizing into biofilms – thin layers of bacteria adhered to a surface and embedded in self-produced extracellular polymeric matrix – which impart numerous survival advantages.[32-34] Biofilm development is regulated *via* cell-to-cell chemical signaling which includes quorum sensing (QS),[35] utilizing several classes of secondary metabolites such as homoserine lactones,[36] quinolones,[37] rhamnolipids,[38] and phenazines.[39] This chemical language is expansive – *P. aeruginosa* produces over fifty distinct quinolone compounds alone[27] – and also highly complex, as a single metabolite may play several distinct roles in biofilm development.[37] Functional characterization is incomplete for most of these compounds, so there is a great deal yet to be elucidated about their meaning during biofilm growth and homeostasis.

MALDI-guided SIMS imaging allows several interesting observations to be made about *P. aeruginosa* biofilm composition based on the optical, low-resolution MALDI, and high-resolution SIMS images. MALDI MS images showed heterogeneous macroscopic distributions of many biomolecules including PQS as shown in **Figure 7.3B**, which appear to follow biofilm growth contours, at least partially. PQS production varies with cell density and population maturity,[40] thus the observed distribution may reflect temporal changes in production during biofilm growth and expansion. SIMS analysis directed at a region of high PQS abundance reveals a punctate microscopic distribution for PQS (**Figure 7.3D**), concentrated in µm-scale features. These features could be clusters of cells exposed at the surface of the biofilm or aggregations of membrane vesicles which have been shown to contain ~90% of the PQS produced by *P. aeruginosa*.[41] Several other quinolones were typically also detected along with PQS, and interestingly these quinolones were not always co-localized; **Figure 7.3E** shows a region where HHQ was observed to be similarly punctate but distributed differently. HHQ is the direct precursor to PQS,[42] released by cells and taken back up by others for PQS production,[27] therefore the features observed in the HHQ SIMS image may represent pockets of secreted HHQ. HHQ is also an autoinducer,[43] so local concentration around producing cells in the biofilm may increase production further *via* positive feedback. The differential distributions of HHQ and PQS observed here also raise the possibility of cell specialization within a biofilm population, a phenomenon known to occur with other biofilm-producing microbes such as *B. subtilis,* but not yet reported with *P. aeruginosa.*[44]

Several of the differences observed between the WT and QS mutant *P. aeruginosa* strains studied here fit well with what is known about their genomes. The QS mutant is a Δ*lasI*Δ*rhlI* strain which is incapable of synthesizing N-3-oxo-dodecanoyl-L-HSL (3-oxo-C_{12}-HSL) and N-butyryl-L-HSL (C_4-HSL), two “master regulator” signals controlling the *P. aeruginosa* QS systems *las* and *rhl* respectively.[36] One expected effect of these mutations is complete lack of rhamnolipid production,[23] a change which is clearly visualized in both the MALDI and SIMS ion images of rhamnolipids Rha-Rha-C_{10}-C_{10} and Rha-C_{10}-C_{10}. Quinolone biosynthesis is also regulated by these signals indirectly in a competitive manner; 3-oxo-C_{12}-HSL promotes PQS production while C_4-HSL suppresses it.[36] Thus the reduced PQS levels detected in the QS mutant biofilm may arise from loss of *las* promotion, with residual PQS produced by promotion from other signaling pathways, as the *las* system is not the dominant driver of PQS biosynthesis under certain growth conditions.[45]

The changes observed in HHQ and NHQ distributions are not as easily explained, partly because they are more subtle, and partly because these quinolones are not as well-characterized as PQS, so the effect of the Δ*lasI*Δ*rhlI* mutations on their abundance and distribution is less easily interpreted. The microscopic quinolone aggregations observed in the QS mutant biofilm could arise from lack of rhamnolipid production; rhamnolipids act as a surfactant which can mobilize cells[38] and solubilize quinolones in the biofilm,[46] so secreted quinolones or cells may aggregate more extensively without them. Another possible explanation is that PQS is required for production of the membrane vesicles which ordinarily transmit quinolones and other metabolites between cells,[41] so decreased PQS levels may result in reduced vesicular production and consequently a local buildup of other quinolones around the cells of origin. Current work is focused on elucidating the role of these quinolones and others in *P. aeruginosa* biofilm using MALDI-guided SIMS and Raman imaging.

CONCLUSIONS

We have developed a sequentially-combined chemical imaging approach wherein an undersampled MALDI MS image is used to guide microscopic SIMS imaging experiments to chemically-interesting regions of interest on the same sample. This combination of complementary microprobes conveys numerous advantages in an MSI experiment, including: (1) specification of microscopic ROIs from a chemical map rather than an optical image; (2) spatially registered macro- and microscopic chemical images of a single sample; (3) generation of a fiducial grid for sample navigation in SIMS; and (4) MALDI tandem MS capability for *in situ* ion characterization. Applied to bacterial biofilms of *P. aeruginosa*, this allowed detection and visualization of multiple secondary metabolites including rhamnolipid surfactants and quinolone signaling molecules which heretofore have not been reported by SIMS. The combination of SIMS and MALDI revealed both macroscopic and cell-scale chemical heterogeneity across the biofilms for these analytes and can be applied to other samples where similar multi-scale complexity exists, such as tissue sections. Additionally, while a single metal-enhanced preparation was utilized in this work for compatibility with both MALDI and SIMS, future work will include applying traditional MALDI matrix in a microdroplet array in order to extend mass range to include detection of proteins and other macromolecules of interest.

REFERENCES

1. Rubakhin, S.; Sweedler, J., A Mass Spectrometry Primer for Mass Spectrometry Imaging. In *Mass Spectrometry Imaging*, Rubakhin, S. S.; Sweedler, J. V., Eds. Humana Press: 2010; Vol. 656, pp 21-49.
2. Chughtai, K.; Heeren, R. M. A., Mass Spectrometric Imaging for Biomedical Tissue Analysis. *Chemical Reviews* **2010,** *110* (5), 3237-3277.
3. Setou, M., *Imaging mass spectrometry : protocols for mass microscopy*. Springer: Tokyo, 2010; p x, 262 p.
4. Gusev, A. I.; Vasseur, O. J.; Proctor, A.; Sharkey, A. G.; Hercules, D. M., Imaging of thin-layer chromatograms using matrix-assisted laser desorption/ionization mass spectrometry. *Analytical Chemistry* **1995,** *67* (24), 4565-4570.
5. Caprioli, R. M.; Farmer, T. B.; Gile, J., Molecular Imaging of Biological Samples: Localization of Peptides and Proteins Using MALDI-TOF MS. *Analytical Chemistry* **1997,** *69* (23), 4751-4760.
6. Castaing, R.; Slodzian, G., Microanalyse par emission ionique secondaire. *J Microscopie* **1962,** *1*, 395-410.
7. Galle, P., Sur une nouvelle methode d'analyse cellulaire utilisant le phenomene d'emission ionique secondaire. *Ann. Phys. Biol. Med.* **1970,** *42*, 83-94.
8. Boxer, S. G.; Kraft, M. L.; Weber, P. K., Advances in Imaging Secondary Ion Mass Spectrometry for Biological Samples. *Annual Review of Biophysics* **2009,** *38* (1), 53-74.
9. Mao, D.; Brenes, D. A.; Lu, C.; Wucher, A.; Winograd, N., Temperature effects of sputtering of Langmuir–Blodgett multilayers. *Surface and Interface Analysis* **2013,** *45* (1), 65-67.
10. Altelaar, A. F. M.; Klinkert, I.; Jalink, K.; de Lange, R. P. J.; Adan, R. A. H.; Heeren, R. M. A.; Piersma, S. R., Gold-Enhanced Biomolecular Surface Imaging of Cells and Tissue by SIMS and MALDI Mass Spectrometry. *Analytical Chemistry* **2005,** *78* (3), 734-742.
11. Delcorte, A.; Bour, J.; Aubriet, F.; Muller, J. F.; Bertrand, P., Sample Metallization for Performance Improvement in Desorption/Ionization of Kilodalton Molecules: Quantitative Evaluation, Imaging Secondary Ion MS, and Laser Ablation. *Analytical Chemistry* **2003,** *75* (24), 6875-6885.
12. Li, Z.; Bohn, P. W.; Sweedler, J. V., Comparison of sample pre-treatments for laser desorption ionization and secondary ion mass spectrometry imaging of Miscanthus giganteus. *Bioresource Technology* **2010,** *101* (14), 5578-5585.
13. Yang, H.-J.; Sugiura, Y.; Ishizaki, I.; Sanada, N.; Ikegami, K.; Zaima, N.; Shrivas, K.; Setou, M., Imaging of lipids in cultured mammalian neurons by matrix assisted laser/desorption ionization and secondary ion mass spectrometry. *Surface and Interface Analysis* **2010,** *42* (10-11), 1606-1611.
14. Monroe, E. B.; Annangudi, S. P.; Hatcher, N. G.; Gutstein, H. B.; Rubakhin, S. S.; Sweedler, J. V., SIMS and MALDI MS imaging of the spinal cord. *Proteomics* **2008,** *8* (18), 3746-3754.
15. Lanni, E. J.; Rubakhin, S. S.; Sweedler, J. V., Mass spectrometry imaging and profiling of single cells. *Journal of Proteomics* **2012,** *75* (16), 5036-5051.
16. Chaurand, P.; Schwartz, S. A.; Billheimer, D.; Xu, B. J.; Crecelius, A.; Caprioli, R. M., Integrating Histology and Imaging Mass Spectrometry. *Analytical Chemistry* **2004,** *76* (4), 1145-1155.
17. Blaze M. T, M.; Aydin, B.; Carlson, R. P.; Hanley, L., Identification and imaging of peptides and proteins on Enterococcus faecalis biofilms by matrix assisted laser desorption ionization mass spectrometry. *Analyst* **2012,** *137* (21), 5018-5025.
18. Watrous, J.; Roach, P.; Alexandrov, T.; Heath, B. S.; Yang, J. Y.; Kersten, R. D.; van der Voort, M.; Pogliano, K.; Gross, H.; Raaijmakers, J. M.; Moore, B. S.; Laskin, J.; Bandeira, N.; Dorrestein, P. C., Mass spectral molecular networking of living microbial colonies. *Proceedings of the National Academy of Sciences* **2012**.
19. Dekas, A. E.; Poretsky, R. S.; Orphan, V. J., Deep-Sea Archaea Fix and Share Nitrogen in Methane-Consuming Microbial Consortia. *Science* **2009,** *326* (5951), 422-426.
20. Lechene, C. P.; Luyten, Y.; McMahon, G.; Distel, D. L., Quantitative Imaging of Nitrogen Fixation by Individual Bacteria Within Animal Cells. *Science* **2007,** *317* (5844), 1563-1566.
21. Thiel, V.; Toporski, J.; Schumann, G.; Sjövall, P.; Lausmaa, J., Analysis of archaeal core ether lipids using Time of Flight-Secondary Ion Mass Spectrometry (ToF-SIMS): Exploring a new prospect for the study of biomarkers in geobiology. *Geobiology* **2007,** *5* (1), 75-83.
22. Vaidyanathan, S.; Fletcher, J. S.; Goodacre, R.; Lockyer, N. P.; Micklefield, J.; Vickerman, J. C., Subsurface Biomolecular Imaging of Streptomyces coelicolor Using Secondary Ion Mass Spectrometry. *Analytical Chemistry* **2008,** *80* (6), 1942-1951.

23. Shrout, J. D.; Chopp, D. L.; Just, C. L.; Hentzer, M.; Givskov, M.; Parsek, M. R., The impact of quorum sensing and swarming motility on Pseudomonas aeruginosa biofilm formation is nutritionally conditional. *Molecular Microbiology* **2006,** *62* (5), 1264-1277.
24. Heydorn, A.; Nielsen, A. T.; Hentzer, M.; Sternberg, C.; Givskov, M.; Ersbøll, B. K.; Molin, S., Quantification of biofilm structures by the novel computer program comstat. *Microbiology* **2000,** *146* (10), 2395-2407.
25. Nemes, P.; Rubakhin, S. S.; Aerts, J. T.; Sweedler, J. V., Qualitative and quantitative metabolomic investigation of single neurons by capillary electrophoresis electrospray ionization mass spectrometry. *Nat. Protocols* **2013,** *8* (4), 783-799.
26. Smith, C. A.; O'Maille, G.; Want, E. J.; Qin, C.; Trauger, S. A.; Brandon, T. R.; Custodio, D. E.; Abagyan, R.; Siuzdak, G., METLIN: a metabolite mass spectral database. *Therapeutic drug monitoring* **2005,** *27* (6), 747-751.
27. Lépine, F.; Milot, S.; Déziel, E.; He, J.; Rahme, L. G., Electrospray/mass spectrometric identification and analysis of 4-hydroxy-2-alkylquinolines (HAQs) produced by Pseudomonas aeruginosa. *Journal of the American Society for Mass Spectrometry* **2004,** *15* (6), 862-869.
28. Masyuko, R. N.; Lanni, E. J.; Driscoll, C. M.; Shrout, J. D.; Sweedler, J. V.; Bohn, P. W., Spatial Organization of Pseudomonas Aeruginosa Biofilms Probed by Correlated Matrix-Assisted Laser Desorption Ionization Mass Spectrometry and Confocal Raman Microscopy. **2014,** *Submitted for publication*.
29. de Koster, C. G.; Vos, B.; Versluis, C.; Heerma, W.; Haverkamp, J., High-performance thin-layer chromatography/fast atom bombardment (tandem) mass spectrometry of Pseudomonas rhamnolipids. *Biological Mass Spectrometry* **1994,** *23* (4), 179-185.
30. Price, N. P. J.; Ray, K. J.; Vermillion, K.; Kuo, T.-M., MALDI-TOF mass spectrometry of naturally occurring mixtures of monorhamnolipids and dirhamnolipids. *Carbohydrate Research* **2009,** *344* (2), 204-209.
31. Abdel-Mawgoud, A.; Lépine, F.; Déziel, E., Rhamnolipids: diversity of structures, microbial origins and roles. *Appl Microbiol Biotechnol* **2010,** *86* (5), 1323-1336.
32. Flemming, H.-C.; Wingender, J., The biofilm matrix. *Nat Rev Micro* **2010,** *8* (9), 623-633.
33. Costerton, J. W.; Stewart, P. S.; Greenberg, E. P., Bacterial biofilms: A common cause of persistent infections. *Science* **1999,** *284* (5418), 1318-1322.
34. Drenkard, E., Antimicrobial resistance of Pseudomonas aeruginosa biofilms. *Microbes and Infection* **2003,** *5* (13), 1213-1219.
35. Davies, D. G.; Parsek, M. R.; Pearson, J. P.; Iglewski, B. H.; Costerton, J. W.; Greenberg, E. P., The involvement of cell-to-cell signals in the development of a bacterial biofilm. *Science* **1998,** *280* (5361), 295-298.
36. Juhas, M.; Eberl, L.; Tümmler, B., Quorum sensing: the power of cooperation in the world of Pseudomonas. *Environmental Microbiology* **2005,** *7* (4), 459-471.
37. Huse, H.; Whiteley, M., 4-Quinolones: Smart Phones of the Microbial World. *Chemical Reviews* **2010,** *111* (1), 152-159.
38. Tremblay, J.; Richardson, A.-P.; Lépine, F.; Déziel, E., Self-produced extracellular stimuli modulate the Pseudomonas aeruginosa swarming motility behaviour. *Environmental Microbiology* **2007,** *9* (10), 2622-2630.
39. Dietrich, L. E. P.; Price-Whelan, A.; Petersen, A.; Whiteley, M.; Newman, D. K., The phenazine pyocyanin is a terminal signalling factor in the quorum sensing network of Pseudomonas aeruginosa. *Molecular Microbiology* **2006,** *61* (5), 1308-1321.
40. Diggle, S. P.; Winzer, K.; Chhabra, S. R.; Worrall, K. E.; Cámara, M.; Williams, P., The Pseudomonas aeruginosa quinolone signal molecule overcomes the cell density-dependency of the quorum sensing hierarchy, regulates rhl-dependent genes at the onset of stationary phase and can be produced in the absence of LasR. *Molecular Microbiology* **2003,** *50* (1), 29-43.
41. Mashburn, L. M.; Whiteley, M., Membrane vesicles traffic signals and facilitate group activities in a prokaryote. *Nature* **2005,** *437* (7057), 422-425.
42. Diggle, S. P.; Cornelis, P.; Williams, P.; Cámara, M., 4-Quinolone signalling in Pseudomonas aeruginosa: Old molecules, new perspectives. *International Journal of Medical Microbiology* **2006,** *296* (2–3), 83-91.
43. Diggle, S. P.; Matthijs, S.; Wright, V. J.; Fletcher, M. P.; Chhabra, S. R.; Lamont, I. L.; Kong, X.; Hider, R. C.; Cornelis, P.; Cámara, M.; Williams, P., The Pseudomonas aeruginosa 4-Quinolone Signal Molecules

HHQ and PQS Play Multifunctional Roles in Quorum Sensing and Iron Entrapment. *Chemistry & Biology* **2007,** *14* (1), 87-96.

44. López, D.; Kolter, R., Extracellular signals that define distinct and coexisting cell fates in Bacillus subtilis. *FEMS Microbiology Reviews* **2010,** *34* (2), 134-149.
45. Schafhauser, J.; Lepine, F.; McKay, G.; Ahlgren, H. G.; Khakimova, M.; Nguyen, D., The stringent response modulates 4-hydroxy-2-alkylquinoline (HAQ) biosynthesis and quorum sensing hierarchy in Pseudomonas aeruginosa. *Journal of Bacteriology* **2014,** *Published ahead of print*.
46. Calfee, M. W.; Shelton, J. G.; McCubrey, J. A.; Pesci, E. C., Solubility and Bioactivity of the Pseudomonas Quinolone Signal Are Increased by a Pseudomonas aeruginosa-Produced Surfactant. *Infection and Immunity* **2005,** *73* (2), 878-882.

FIGURES AND TABLES

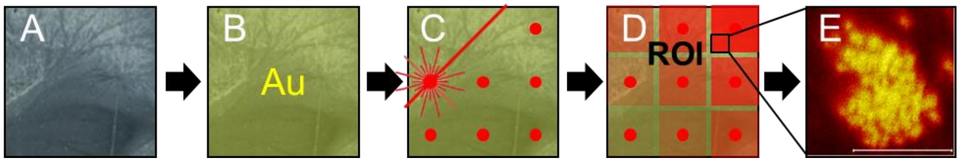

Figure 7.1. Workflow schematic of a MALDI-guided SIMS experiment, illustrating: (A) sample preparation to meet vacuum MS requirements (must be flat, dry, and mounted to a conductive or semi-conductive substrate), (B) surface chemical treatment for ion enhancement, (C) undersampling MALDI MS image acquisition across the specimen surface, (D) specification of ROIs for SIMS analysis based on the MALDI chemical map, and (E) SIMS imaging at microscopic ROIs. Adapted with permission from American Chemical Society, copyright 2014.

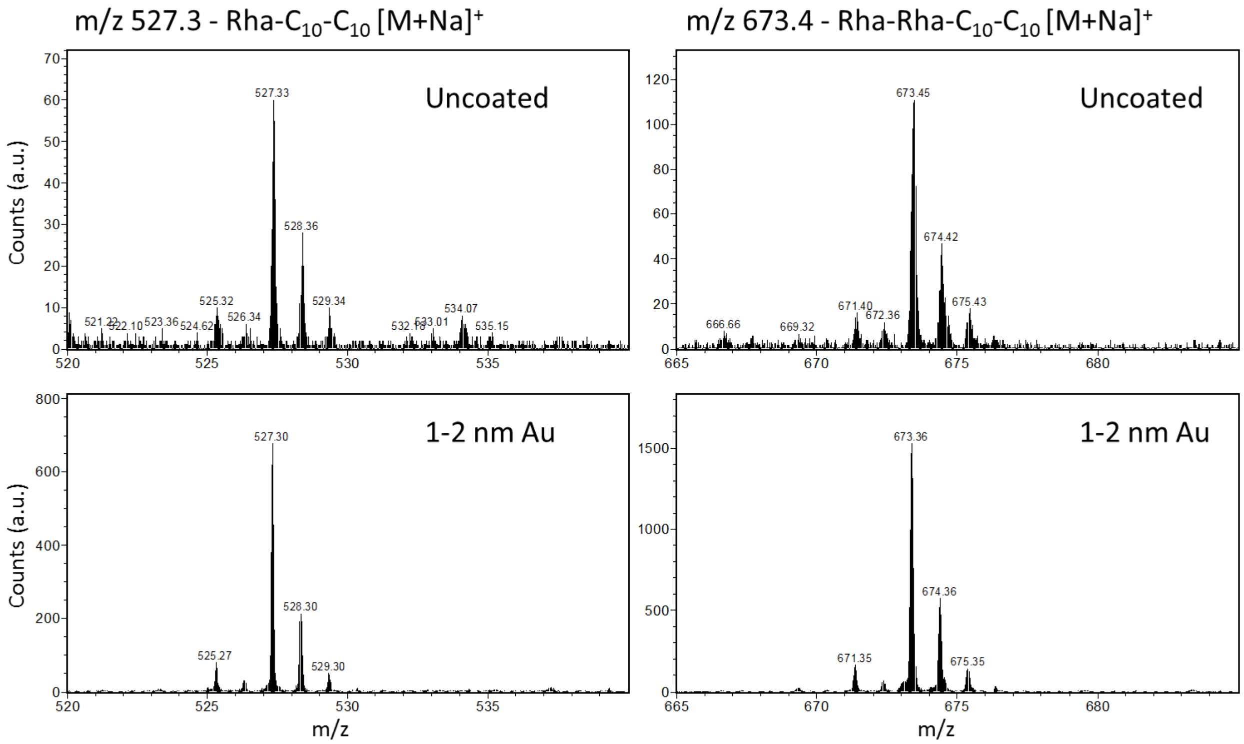

Figure 7.2: Rhamnolipid enhancement with Au MetA-SIMS. Dried drops of mixed rhamnolipid standard on Si wafers were analyzed by SIMS with no treatment *i.e.* "uncoated" (top row) and after sputter-coating with 1-2 nm Au (bottom row). For each sample a 600 × 600 μm^2 raster window was centered in the droplet and acquired for 15 min in positive ion mode, and then all pixels were summed to produce the spectra shown. Rhamnolipids are detected primarily as [M+Na]$^+$, and signal is enhanced by *ca.* 10× in the MetA-SIMS samples compared to the uncoated samples, as shown here with two representative species. Adapted with permission from American Chemical Society, copyright 2014.

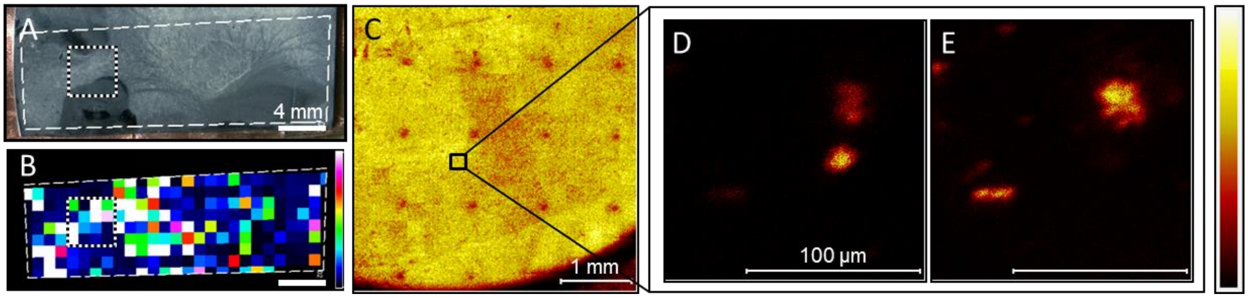

Figure 7.3. Selected results from MALDI-guided SIMS of *P. aeruginosa* wild-type biofilm. (A) Optical and (B) MALDI ion image of quinolone PQS (m/z 260.17) are acquired, and an ROI (dotted white box) is selected for further analysis (scale bars = 4 mm). (C) A mosaic-mode SIMS total ion image reveals laser ablation marks in the sample, and these positions are correlated with the MALDI ion image to select a microscopic ROI (black box, scale bar = 1 mm). High-resolution SIMS imaging at the ROI reveals µm-scale localization of (D) PQS (m/z 260.17) and (E) HHQ (m/z 244.17) on the biofilm (scale bars = 100 µm). Adapted with permission from American Chemical Society, copyright 2014.

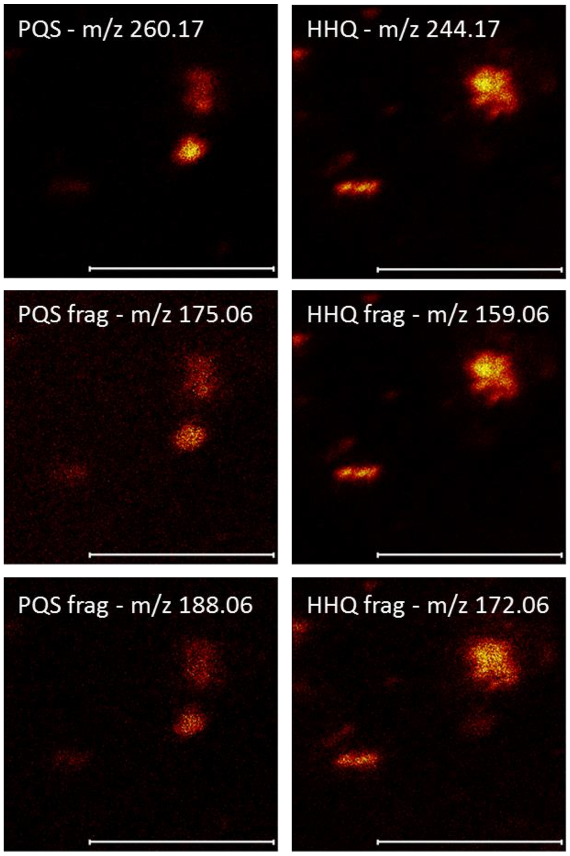

Figure 7.4: Co-localization of quinolone MH$^+$ pseudomolecular ions with characteristic fragments. Ions at m/z 260.17 and 244.17 are assigned to MH$^+$ of quinolones PQS (*left*) and HHQ (*right*), respectively. These quinolones generate unique characteristic fragments,[1] also detected here by CE-ESI-MS/MS and MALDI-MS/MS, which are observed to co-localize with the respective MH$^+$ ions here, confirming the mass assignments. Scale bars = 100 µm. Adapted with permission from American Chemical Society, copyright 2014.

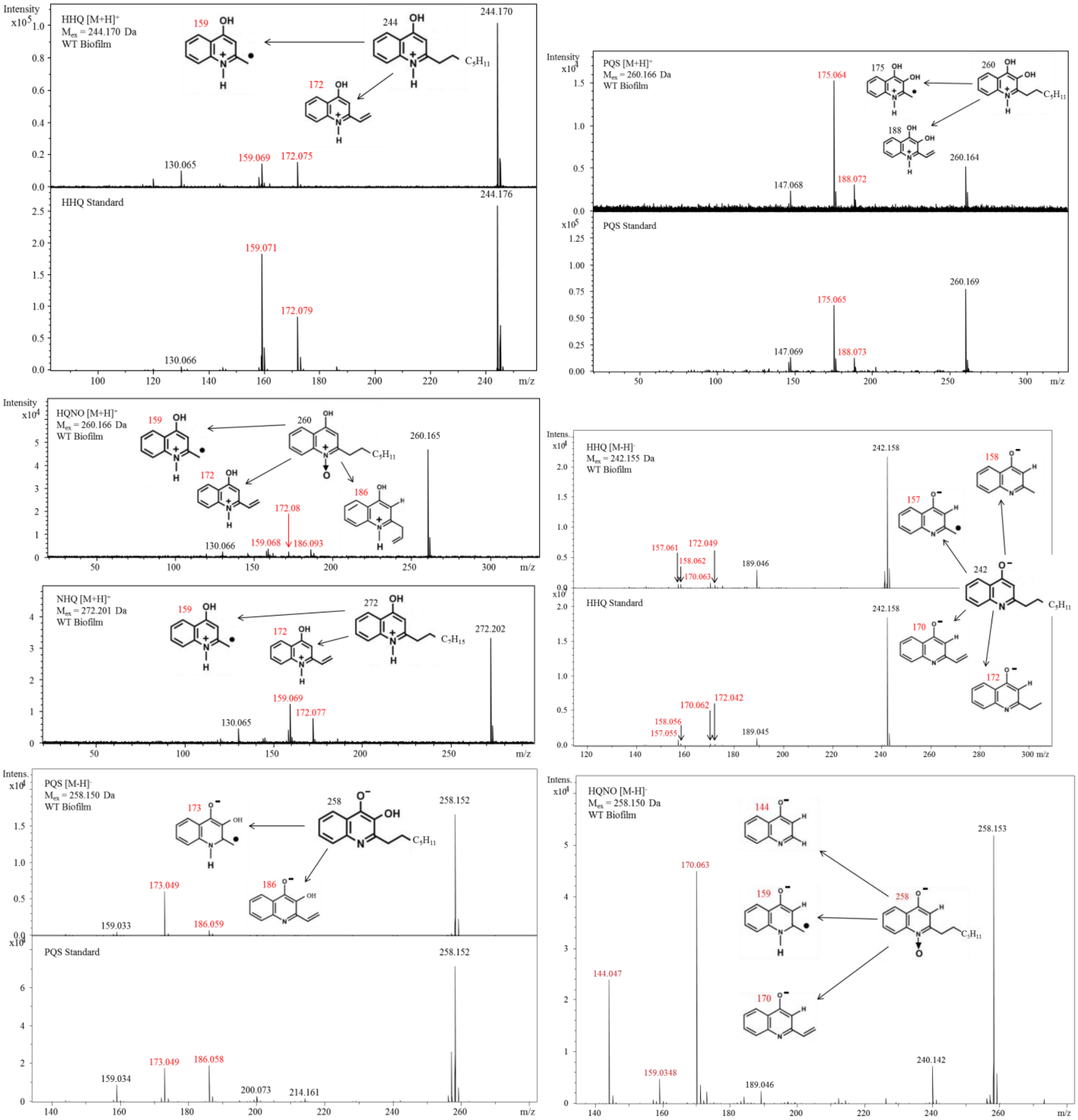

Figure 7.5: CE-ESI-MS/MS of WT *P. aeruginosa* biofilm extract. A WT biofilm was scraped into extraction solution, shaken and centrifuged, then 6 nL supernatant was separated by CE, ionized by ESI, and tandem MS (CID) was performed on putative analytes of interest, generating the spectra shown above as labeled. PQS and HHQ quinolone standards and mixed rhamnolipid standard were run under identical conditions for comparison, also shown. Parent ion masses and fragmentation patterns match with previous reports[27,30] and with publicly available mass spectral databases *e.g.* Metlin.[26] Adapted with permission from American Chemical Society, copyright 2014.

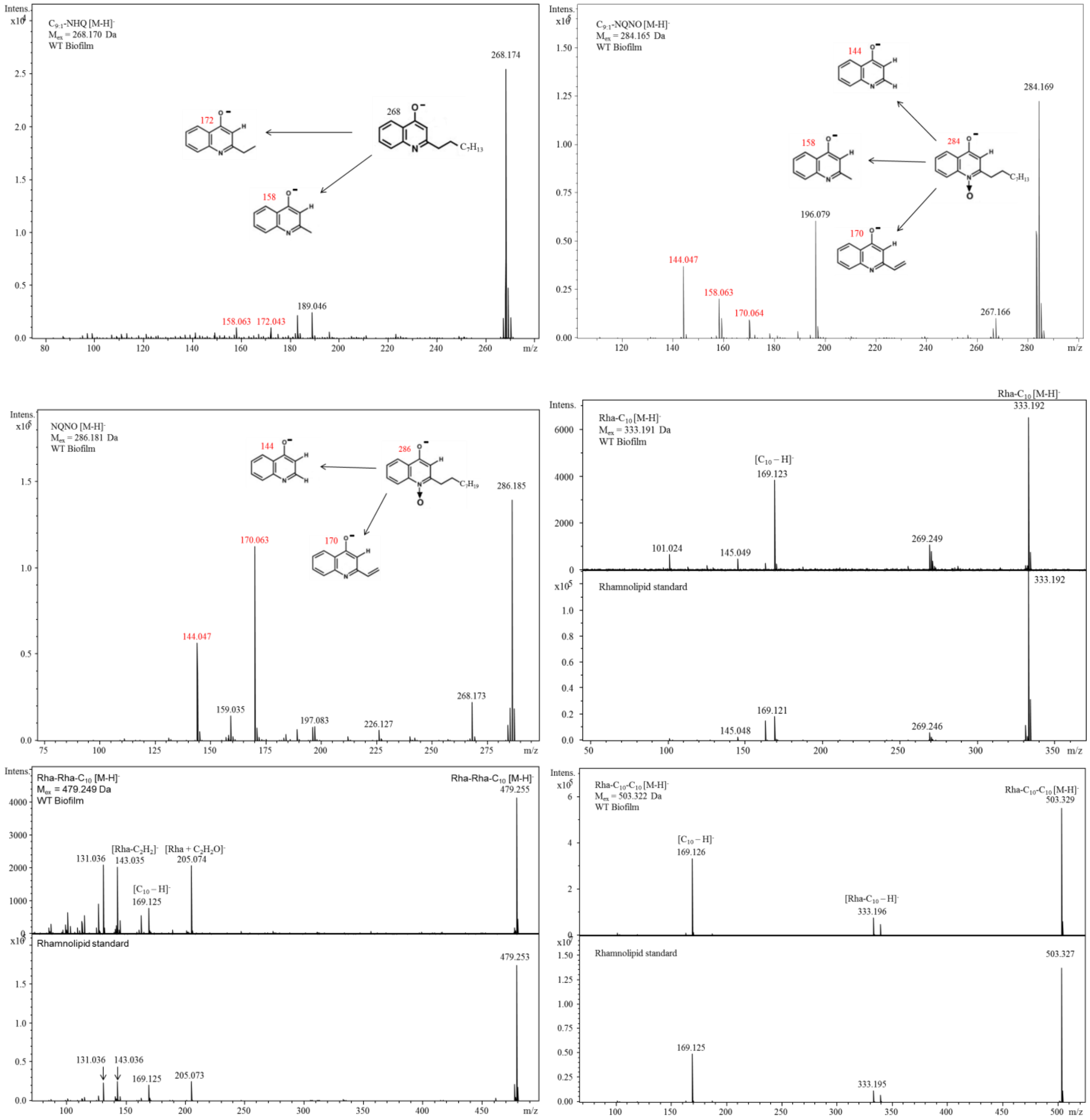

Figure 7.5 (continued)

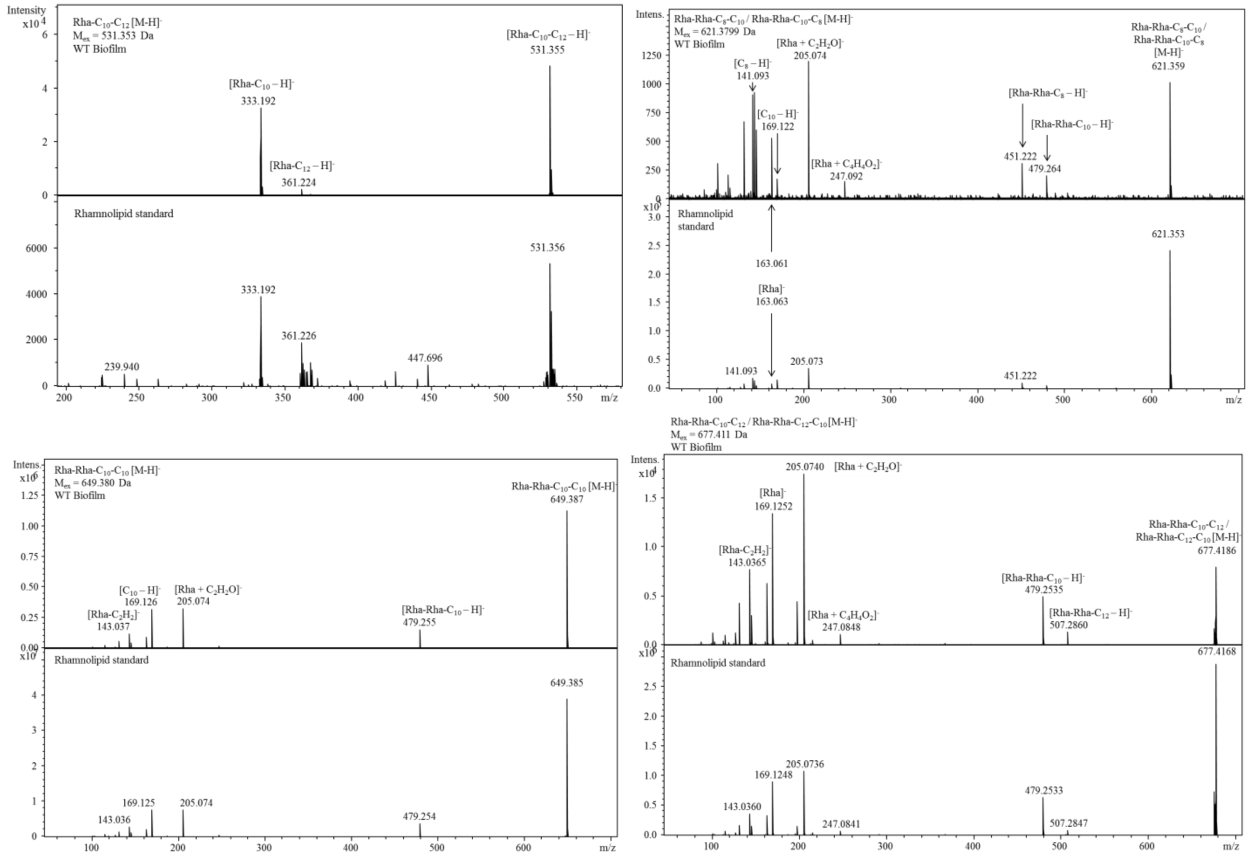

Figure 7.5 (continued)

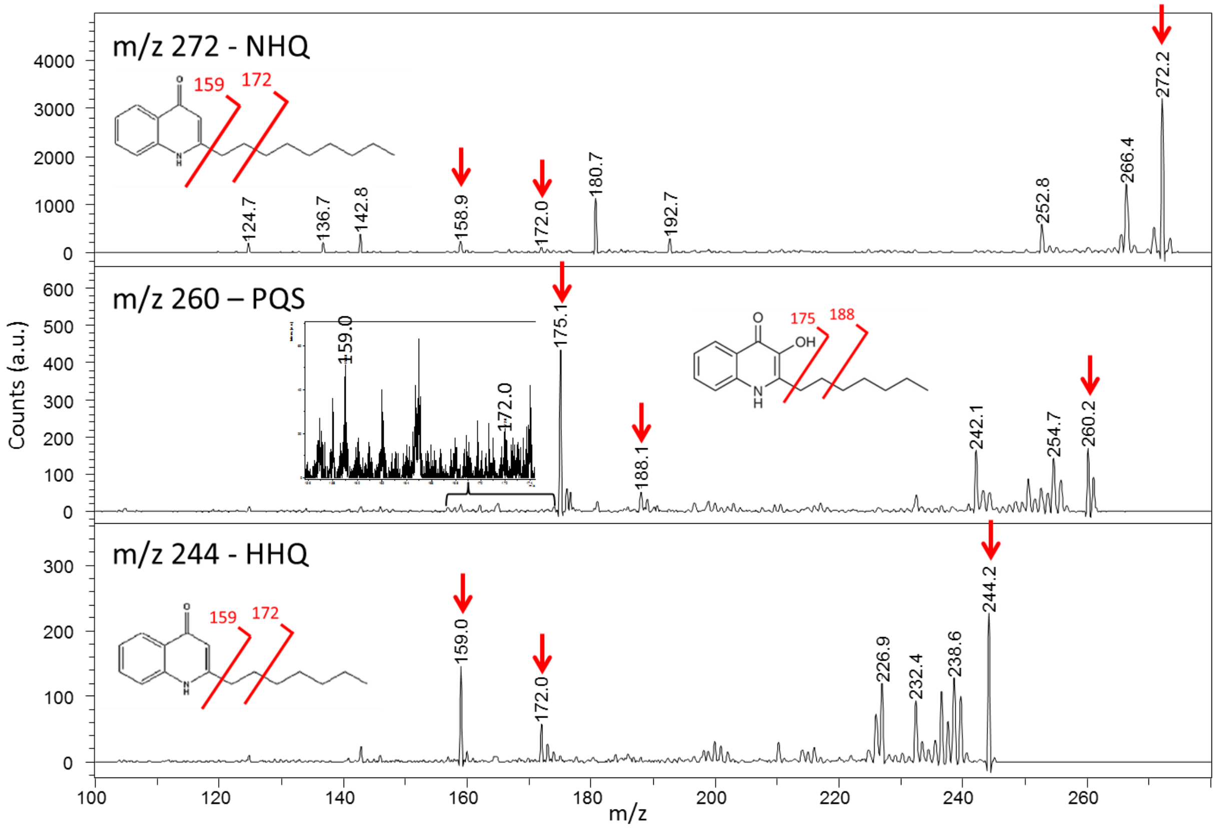

Figure 7.6: *In situ* MALDI-MS/MS of quinolones. Following imaging experiments, a WT *P. aeruginosa* biofilm was reloaded into the MALDI MS and the previously-acquired MALDI ion images were used to direct MS/MS experiments to regions of high putative quinolone concentration. Resulting spectra for NHQ, PQS, and HHQ show characteristic fragment ions confirming each assignment. The PQS spectrum shows little or no detected fragments at m/z 159/172 (inset), which would be characteristic of the isobaric quinolone HQNO. Additional unassigned fragment ions in each spectrum may be generated uniquely by the post-source decay fragmentation mechanism utilized here (in contrast with CID, used in previous work)[1] Adapted with permission from American Chemical Society, copyright 2014.

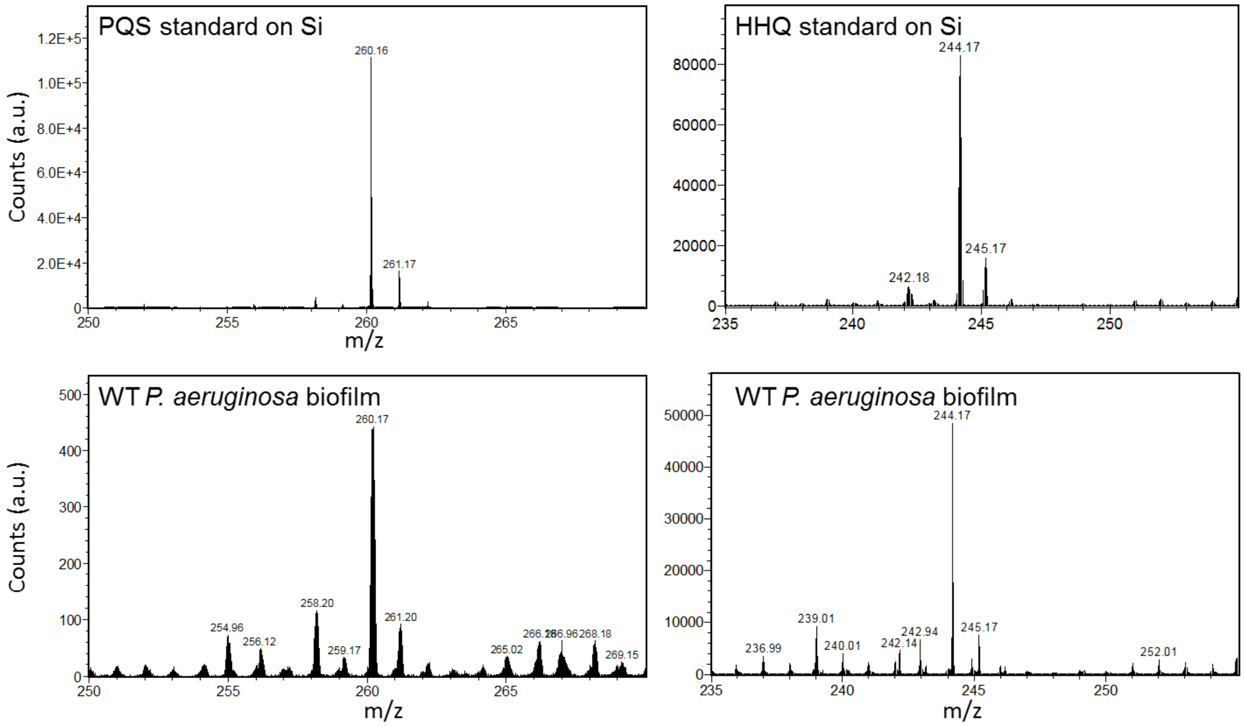

Figure 7.7: Quinolone MH$^+$ detection by Au MetA-SIMS. Dried drops of PQS and HHQ standards on Si wafer (top) and WT *P. aeruginosa* biofilm profiles (bottom) yield ions at the expected monoisotopic mass MH$^+$ for PQS (m_{ex} = 260.165) and HHQ (m_{ex} = 244.170) by SIMS after sputter-coating with 1-2 nm Au. Adapted with permission from American Chemical Society, copyright 2014.

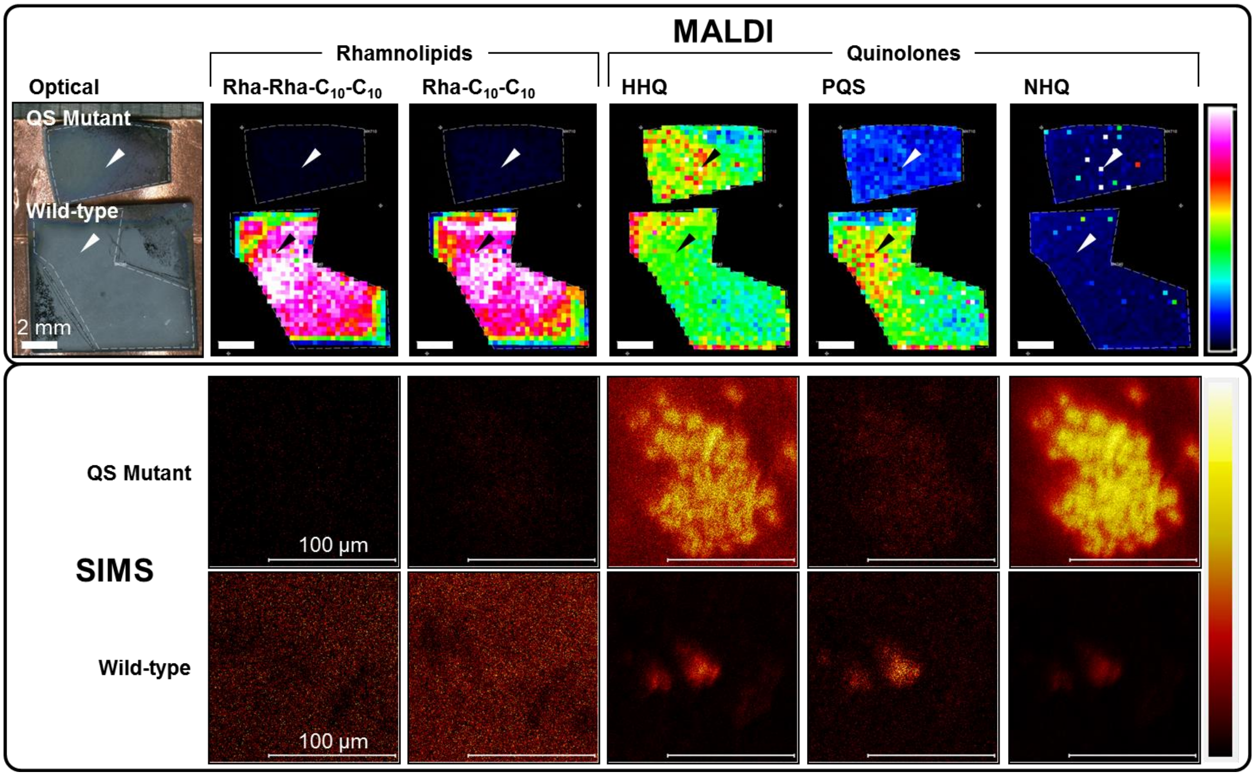

Figure 7.8. MALDI-guided SIMS reveals multi-scale compositional differences between biofilms of wild-type and QS mutant *P. aeruginosa*. Arrows in the optical and MALDI ion images (top row) indicate ROIs where the SIMS images (middle and bottom rows) were acquired. MALDI and SIMS ion image false color scales are shown on right; for each specific ion, SIMS color scale range was set identically: Rha-Rha-C_{10}-C_{10} ($[M+Na]^+$ m/z 673.4), 0-5 cts; Rha-C_{10}-C_{10} ($[M+Na]^+$ m/z 527.3), 0-8 cts; HHQ (MH^+ m/z 244.2), 0-40 cts; PQS (MH^+ m/z 260.2), 0-10 cts; NHQ (MH^+ m/z 272.2), 0-100 cts. Optical/MALDI scale bars = 2 mm, SIMS scale bars = 100 µm. Regions of WT biofilm were excluded where tape was adhered to the surface. Adapted with permission from American Chemical Society, copyright 2014.

Compound ID	Molecular formula	CE-ESI MS			MALDI MS				SIMS			
		$[M+H]^+$ observed	$[M-H]^-$ observed	ΔM (Neg)	$[M+H]^+$ observed	$[M+Na]^+$ observed	$[M-H+2Na]^+$ observed	ΔM	$[M+H]^+$ observed	$[M+Na]^+$ observed	$[M-H+2Na]^+$ observed	ΔM
HHQ (2-heptyl-4-quinolone)	$C_{16}H_{22}NO$	244.170	242.152	-0.003	244.18			0.01	244.17			0.00
PQS (2-heptyl-3-hydroxyquinolone)	$C_{16}H_{21}NO_2$	260.164	258.148	-0.002	260.17			0.01	260.16			-0.01
HQNO (4-hydroxy-2-heptylquinolone-N-oxide)	$C_{16}H_{21}NO_2$	260.165	258.148	-0.002	260.17			0.01	260.16			-0.01
$C_{9:1}$-NHQ (2-nonenyl-4-quinolone)	$C_{18}H_{23}NO$		268.168	-0.002	270.19			0.01				
NHQ (2-nonyl-4-quinolone)	$C_{18}H_{25}NO$	272.202	270.184	-0.002	272.21			0.01	272.20			0.00
$C_{9:1}$-PQS (2-nonenyl-3-hydroxyquinolone) $C_{9:1}$-NQNO (4-hydroxy-2-nonenylquinolone-N-oxide)	$C_{18}H_{23}NO_2$	286.180	284.161	-0.005	286.19			0.01	286.18			0.00
C_9-PQS (2-nonyl-3-hydroxyquinolone) NQNO (4-hydroxy-2-nonylquinolone-N-oxide)	$C_{18}H_{25}NO_2$		286.178	-0.003	288.20			0.01	288.19			0.00
$C_{11:1}$-UHQ (2-undecenyl-4-quinolone)	$C_{20}H_{27}NO$								298.21			-0.01
Rha-C_{10}	$C_{16}H_{30}O_7$	335.208	333.187	-0.005		357.21	379.19	0.02			379.16	-0.01
Rha-C_8-C_{10}	$C_{24}H_{44}O_9$		475.289	-0.002		499.31		0.02		499.28		-0.01
Rha-Rha-C_{10}	$C_{22}H_{40}O_{11}$	481.256	479.247	-0.002		503.27	525.25	0.02				
Rha-C_{10}-C_{10}	$C_{26}H_{48}O_9$		503.321	-0.001		527.34	549.33	0.02		527.30		-0.02
Rha-C_{10}-$C_{12:1}$	$C_{28}H_{50}O_9$		529.337	-0.001		553.38		0.04		553.33		-0.01
Rha-C_{10}-C_{12}	$C_{28}H_{52}O_9$		531.355	0.002		555.38		0.03		555.33		-0.02
Rha-Rha-C_8-C_{10}	$C_{30}H_{54}O_{13}$		621.351	0.002		645.38		0.03		645.34		-0.01
Rha-Rha-C_{10}-C_{10}	$C_{32}H_{58}O_{13}$		649.379	-0.001		673.42	695.41	0.04		673.40		0.02
Rha-Rha-C_{10}-C_{12}	$C_{34}H_{62}O_{13}$		677.411	-0.001		701.46	723.44	0.05		701.40		-0.01

Table 7.1: Combined MALDI MS, SIMS, and CE-ESI MS results for rhamnolipid and quinolone species detected from WT *P. aeruginosa* biofilm. Bold text indicates species confirmed by tandem MS. Rhamnolipid abbreviations are explained elsewhere.[27,31] Adapted with permission from American Chemical Society, copyright 2014.

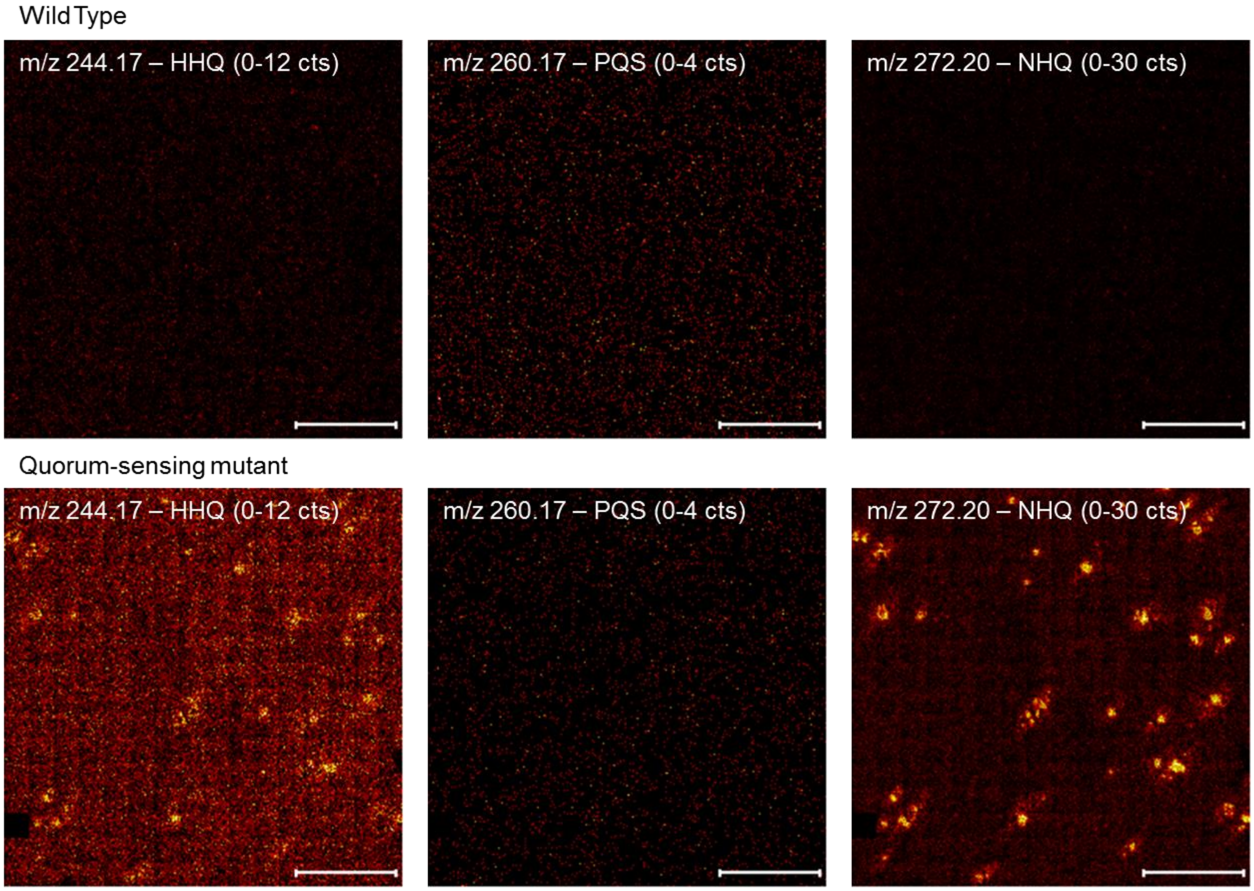

Figure 7.9: Low-resolution SIMS ion images of quinolones on WT (top row) and QS mutant (bottom row) *P. aeruginosa* biofilms. "Hot spots" of HHQ (m/z 244.17) and NHQ (m/z 272.20) are detected in the QS mutant, while virtually no features are observed for any quinolone in the WT biofilm possibly due to low spatial resolution and sensitivity (owing to very low ion dose per pixel). PQS images show relatively little on either film. Color intensity scales for each ion are identical between biofilms to enable comparison. Scale bars = 1 mm. Adapted with permission from American Chemical Society, copyright 2014.

CHAPTER 8

CORRELATED IMAGING WITH C_{60}-SIMS AND CONFOCAL RAMAN MICROSCOPY: VISUALIZATION OF CELL-SCALE MOLECULAR DISTRIBUTIONS IN A BACTERIAL BIOFILM

NOTES AND ACKNOWLEDGMENTS

This chapter is adapted from a manuscript in preparation for publication as of June 11, 2014, coauthored by R. N. Masyuko, C. M. Driscoll, S. J. B. Dunham, J. D. Shrout, P. W. Bohn, and J. V. Sweedler. E. J. Lanni prepared the majority of the manuscript (excluding CRM results and sicussion), developed microspot array printing method, performed SIMS imaging and profiling experiments, and performed manual correlation of SIMS and CRM image data. S. J. B. Dunham assisted with SIMS image acquisition, sample preparation, and acquired all SIMS tandem MS spectra. R. N. Masyuko performed CRM analyses and contributed CRM-related manuscript sections jointly with P. W. Bohn including CRM data analyses and discussion. R. N. Masyuko and C. M. Driscoll prepared biofilm samples. Funding from the Department of Energy Office of Biological and Environmental Research through grant DE SC0006642 is acknowledged. Electron microscopy assistance from Scott Robinson and Cate Wallace in the Beckman Institute Imaging Technology Group, partially supported by the National Science Foundation grant DBI-9871103, is also gratefully acknowledged.

INTRODUCTION

Biological systems are comprised of a vast, diverse assortment of chemical species ranging in size and complexity from monatomic electrolytes up to massive biopolymers such as proteins, complex carbohydrates, and nucleic acids. Since function arises not just from *what* is present but also *how* it is distributed spatially (and temporally), visualizing the distribution of such components within biological systems – chemical imaging – is therefore critical to comprehensively understanding them. While labeling analytes with *e.g.* fluorescent dyes or radioisotopes is one well-established way to accomplish this, label-free imaging approaches present an alternative with several advantages: effective probes need not be developed for each analyte, nor must the system be perturbed by introduction of exogenous compounds, and parallel imaging of multiple analytes is not limited by the number of simultaneously usable and/or detectable probes.

Mass spectrometry imaging (MSI)[1-3] and confocal Raman microscopy (CRM)[4-6] are two such label-free molecular imaging techniques which operate on different fundamental principles. MSI detects and visualizes analyte distribution on the basis of molecular weight; this is commonly accomplished by scanning a microprobe across the sample surface, ionizing constituents in a spatially-registered fashion which can then be analyzed, detected, and used to generate ion images, or maps of relative abundance.[1] Many MSI microprobes are available with unique characteristics and advantages, two of the most common being focused lasers for matrix-assisted laser desorption/ionization (MALDI)[3] which provides high upper mass range, and focused ion beams for secondary ion mass spectrometry (SIMS)[7-8] which provides high spatial resolution to <100 nm in ideal cases.[9] In contrast with mass-based detection by MSI, CRM visualizes chemical distributions based on the characteristic vibrational frequencies of different chemical bonds; in the Raman scattering process, these vibrational frequencies shift scattered light away from the frequency of an incident laser beam by an amount which is characteristic of the chemical bonds present. CRM utilizes a standard confocal microscope, therefore the lateral and axial spatial resolution are defined by $\Delta x = \frac{0.61\,\lambda}{NA}$ and $\Delta z = \frac{2.2n\lambda}{\pi(NA)^2}$ respectively, where λ represents laser wavelength, NA is numerical aperture of the microscope objective, and n is the refractive index of the medium.[10-11] Image acquisition is performed by scanning the focal volume of the laser which allows for nondestructive (and therefore potentially live sample) imaging in three dimensions at submicron spatial resolution.[6, 12]

Given the orthogonality of these techniques, combining MSI and CRM (or other vibrational imaging methods) for molecular imaging can be advantageous. More specifically, *correlating* mass and vibrational images – chemically imaging the exact same location by orthogonal detection modes – imparts numerous benefits for biological studies beyond their combined individual application. Molecules which do not ionize efficiently may produce a strong vibrational signature or *vice versa*, thus total chemical coverage is expanded. One technique may also resolve subtly differing compounds that are indistinguishable by the other, for example structural isomers with different vibrational modes, or functionally-similar molecules with slightly different mass. In cases where an analyte is mutually detectable, observed distributions can be cross-validated;[13] this is especially helpful in conjunction with MSI where artifacts can arise in ion images due to ion suppression[14-15] or image processing.[16] Several reports illustrate the advantage of correlating MSI with CRM or related vibrational imaging techniques for biological analysis, a subject we have also reviewed in depth recently.[17] Li et al. correlated CRM, SIMS, and LDI MS imaging to elucidate the subcellular localization of carbohydrates (cellulose and hemicellulose) in biofuel feedstock grass, allowing more definitive mass and vibrational assignments from mutually-observed chemical features.[13] Petit and colleagues demonstrated that Synchrotron-FT-IR and -UV microspectroscopies and SIMS images could be correlated in liver tissue analysis, with FT-IR visualizing broad molecular classes – lipids, proteins, DNA, and sugars – while SIMS resolved specific lipid species.[18] More recently Fagerer et al. correlated single cell fluorescence and Raman imaging with MALDI MS profiling of algae in order to visualize secondary metabolite production and the associated depletion of cellular ATP,[19] impressively demonstrating how combining these techniques can yield a more comprehensive biological picture.

Here we present a method for correlating molecular images from two label-free techniques – SIMS and CRM – and demonstrate how the complementarity of these techniques can be exploited for enhanced molecular imaging of a biological sample. We apply this correlated method to investigate cultured bacterial biofilms of the opportunistic pathogen *Pseudomonas aeruginosa*, which (unlike tissue sections, a common imaging subject) do not present easily distinguishable anatomical features for image registry. Thus, we also developed a chemical microspot-based system for navigating and locating microscopic regions of interest, a critical step in precise correlation of images acquired on a highly uniform surface by two different techniques, in two separate instruments (and at two separate universities). Correlation of MSI and CRM data enables us to broadly characterize the chemical composition of the biofilm microenvironment as well as specific constituent analytes including quinolones, a class of signaling molecules involved in biofilm growth and maturation.

EXPERIMENTAL METHODS

Figure 8.1 shows a schematic representing the overall workflow of the sequential correlated imaging approach demonstrated here, with procedure details described below.

Materials and chemicals

Silicon substrates were purchased from Silicon, Inc. (Boise, ID, USA) as 4 in.-diameter wafers of Si (100), then scored and broken into 2 × 2 cm^2 tiles before use. Quinolone standards 2-heptyl-3-hydroxy-4(1H)-quinolone (*Pseudomonas* quinolone signal, PQS) and 2-heptyl-4-quinolone (HHQ) were purchased from Sigma-Aldrich (St Louis, MO, USA) and dissolved in HPLC-grade methanol (also purchased from Sigma-Aldrich), then deposited and air-dried on clean Si wafers for SIMS and CRM measurements. Ag nanoparticle solution (PELCO NanoXact, 50 nm, 0.02 mg/mL in 2mM aqueous citrate) was purchased from Ted Pella, Inc. (Redding, CA, USA) and diluted 1:1 with HPLC-grade methanol for inkjet printing.

Biofilm preparation

Pseudomonas aeruginosa ATCC strain 15692 was used for all experiments. Cell suspensions were grown in FAB culture medium with filter-sterilized glucose as a carbon source at 30° C overnight. The FAB medium contained the following components: $(NH_4)_2SO_4$ (2 g L^{-1}), Na_2HPO_4. $2H_2O$ (6 g L^{-1}), KH_2PO_4 (3 g L^{-1}), NaCl (3 g L^{-1}), $MgCl_2$(93 mg L^{-1}), $CaCl_2$(11 mg L^{-1}) and trace metals solution (1 ml L^{-1}). The trace metals solution contained $CaSO_4$. $2H_2O$ (200 mg L^{-1}), $FeSO_4$.7H2O (200 mg L^{-1}), $MnSO_4.H_2O$ (20 mg L^{-1}), $CuSO_4$. $5H_2O$ (20 mg L^{-1}), $ZnSO_4$. $7H_2O$ (20 mg L^{-1}), $CoSO_4.7H_2O$ (10 mg L^{-1}), $NaMoO_4$. H_2O (10 mg L^{-1}), H_3BO_3 (5 mg L^{-1}). The cell culture solution was deposited onto silicon wafer tiles placed at the bottom of Petri dishes and additional growth culture medium added to a 50× dilution. The biofilms were allowed to grow under static conditions at 30° C for 72 h. The culture mixture was then removed by pipette and biofilms were permitted to air-dry fully in sterile conditions prior to microspotting and analysis.

Microdroplet array application

Ag nanoparticle solution was printed onto dried biofilm surfaces with a ChIP-1000 Chemical Inkjet Printer (Shimadzu Corp., Kyoto, Japan). A single 100 pL droplet was dispensed at each position in a 500 µm pitch array across the entire biofilm surface. Visual monitoring during deposition and measurement in ion images confirmed that droplets formed single spots of ~170 µm diameter and did not spread on the biofilm surface. To use the array as a Cartesian coordinate grid, an origin was designated at one corner of the tile by inscribing a small unique feature into the biofilm with sharp tweezers.

Confocal Raman microscopy

Raman microscopy was performed on an Alpha 300R confocal Raman microscope (WITec GmbH, Ulm, Germany) with a 60×, NA = 1.0 coverslip-corrected water immersion objective (Nikon Corp., Tokyo, Japan) employing a frequency-doubled Nd:YAG laser (λ = 532 nm) delivered through a single-mode optical fiber, dichroic beam splitter, and focused onto the surface of the sample using a microscope objective operating in epi-illumination geometry. The backscattered radiation was transmitted through a 50 µm diameter multi-mode fiber to a UHTS 300 spectrometer with 600 groove•mm^{-1} diffraction grating and back-illuminated CCD camera cooled to -65° C (Newton DU970 N-BV, Andor Inc., Belfast, UK). The incident laser power on the sample was adjusted to 10mW. Raman spectra were recorded by accumulating 100 spectra at an integration time of 500 ms. Images were acquired by collecting a full Raman spectrum at each image pixel (100 × 100 spectrum array per image) with 100 ms integration time per pixel. Raman chemical images were generated by using a sum filter, which integrates the signal intensity over a defined wavenumber range that is representative of molecular species of interest and subtracts the background as a linear baseline from the first to second border as defined by the sum filter. Data analysis on Raman images was performed using WITec Project 2.1 software and Raman spectra were processed using Igor Pro 6.32A (Lake Oswego, OR, USA).

Mass spectrometry imaging

All MS experiments were performed on a customized hybrid MALDI/C_{60}-SIMS Q-TOF MS instrument which is described in detail elsewhere,[20] operated in positive ion / C_{60}-SIMS mode. This instrument is modified version of the QSTAR XL (AB SCIEX, Framingham, MA, USA) featuring a 20 kV DC C_{60} primary ion beam for SIMS, a translational sample stage which enables imaging experiments, tandem MS capability *via* CID, and high mass resolution (R > 10,000). C_{60}^+ was selected for the primary beam, operated with 70 pA DC sample current and ~15 µm spot diameter. MS-mode acquisition parameters were optimized for detection of quinolones and other small metabolites, collecting m/z 100-300 with ion guide Q1 transmission biased to the upper half of this range (25% at m/z 120, 75% at m/z 200). Tandem MS was performed with 10 eV CID and Ar in the collision cell. MSI was performed in two modes: "step-mode" in which the probe is centered at each discrete pixel location for a specified accumulation time before stepping to the next position, and "continuous raster mode" in which the probe is continuously moved across the sample in a horizontal line scan to acquire each row of the image, allowing images to be acquired several-fold faster but limiting spatial resolution and accumulation time. Step mode acquisition was performed at 10 × 10 μm^2 pixel/step size and 1 s/pixel, while rastering was performed at 20 × 20 μm^2 pixel size and 0.25 s/pixel. In both cases ion dose was well beyond the traditional static limit (1×10^{12} primary ions /$cm^2 \bullet s$); step mode dose is estimated at ~2.5×10^{14} primary ions /$cm^2 \bullet s$, corresponding to an etch rate of ~200 nm/s based on AFM measurements in similar previous work, [21] assuming similar sputter rates. Data was acquired with Analyst v1.2 and oMALDI Server v5.1 software (AB SCIEX), and images were converted to .img files at 20 bins/AMU for processing in BioMap (Novartis, Switzerland). Ion images shown here represent signal intensity (counts) in each pixel with a "rainbow" false color scale ranging from black/violet (no/low signal) to red (high signal). Coating the biofilms with metal (1-2 nm sputtered Au) was found to suppress rather than enhance biological ions, so biofilms were untreated prior to imaging aside from microspot application. Mass calibration was performed with indium/indium oxide clusters.

Scanning electron microscopy

SEM was performed on a XL30 ESEM-FEG (Philips, Amsterdam, North Holland, Netherlands) operating at 2 kV electron beam energy, 2.4 nm spot size, and 8.7 mm working distance. Biofilm samples were analyzed without surface modification (*i.e.* standard metal coating) in order to avoid generating artifact features on the biofilm surface.

RESULTS AND DISCUSSION

Biofilm profiling with CRM and C_{60}-SIMS

Prior to imaging experiments, a biofilm sample was profiled by both CRM and C_{60}-SIMS individually to determine compositional coverage and overlap of the two techniques. An overall initial Raman profile of the biofilm is shown in **Figure 2(a).** Vibrational bands characteristic of known biofilm components could be assigned based on previous work,[22] including 1601 cm^{-1} and 999 cm^{-1}arising from C=C stretching vibrations in phenylalanine and symmetric ring vibrations in tryptophan and phenylalanine representative of proteins[23],1030 cm^{-1} and 1155 cm^{-1} attributed to C-O stretching vibrations and C-C and C-O asymmetric ring breathing vibrations characteristic of carbohydrate moieties.[24-25] A strong band at 1370 cm^{-1}; a common feature in fluoroquinolone associated spectra,[26-27] was also observed at some locations on the sample, and was tentatively assigned to C=C ring stretching vibrations in quinolones,[27] a known *P. aeruginosa* secondary metabolite class[28] detected in biofilms by MS in our own recent work[29] and from cultured colonies the work of others,[30] but not previously reported by Raman spectroscopy. Raman spectra acquired from regions of interest marked by the quinolone associated peak revealed bands characteristic of ring vibrations at 1155 cm^{-1} arising from C-C and C-O asymmetric ring breathing vibrations,[31] 1370 cm^{-1} attributed to C=C ring vibrations in quinolone rings as well as contributions from CH deformation vibrations,[27, 32-33] 1600 cm^{-1} attributed to C=C stretching in aromatic rings[33] and 562 cm^{-1} indicative of out-of-plane ring deformation vibrations.[32] Other significant vibrations were contributions from C=O stretching, amide I and C=C ring stretching marked by the band at 1650 cm^{-1} ,[25, 33] contributions from CH bending and CH twisting giving rise to the wide band with a peak at 1210 cm^{-1},[34] CH in plane bending at 1256 cm^{-1},[31, 34] and CH_2 deformation represented by the band at 1468 cm^{-1}.[24-26] **Figure 8.2(b)** shows a Raman spectrum acquired from a quinolone-rich biofilm region overlaid with a spectrum acquired from a purified quinolone (PQS) standard. The quinolone standard yielded similar characteristic Raman bands, including identical peaks at ~1155cm^{-1}, 1243 cm^{-1}, 1370 cm^{-1}, 1444 cm^{-1},1463 cm^{-1} and 1601 cm^{-1}. Raman profiling of a second quinolone standard (HHQ) yielded a similar vibrational profile, shown in **Figure 8.3**.

Quinolones are a secondary metabolite class of several dozen unique species which function as cell signals, virulence factors, and redox mediators among other roles in *P. aeruginosa*,[35] and they are thus analytes of particular interest. Most quinolones have not been functionally characterized and we have recently reported observing cell-scale spatial distributions of quinolones on *P. aeruginosa* biofilms[29] which may relate to their unique functions, so we chose to focus on these analytes here.

C_{60}-SIMS was conducted in a semi-targeted manner, i.e. acquisition parameters were optimized for detection of quinolones and other small metabolites in the < 300 AMU range. A detail of the *P. aeruginosa* biofilm MS profile is shown in **Figure 8.4(a)**; quinolones were consistently detected as MH^+ ions, in agreement with previous reports[28, 30] as well as our own recent observations in MSI with other probe types (metal-assisted LDI and Au-SIMS, validated by CE-ESI-MS/MS).[29] Assignments were initially made by mass match with previous reports and *in situ* tandem MS was also performed to confirm identities when signal was adequate, as shown for HHQ in **Figure 8.4(b)** and for other analytes in **Figure 8.5**. A total of nine quinolones were detected and confirmed with tandem MS, including two isobaric quinolone pairs – PQS/HQNO and $C_{9:1}$-PQS/$C_{9:1}$-NQNO – made possible by tandem MS yielding unique characteristic fragments. A mass list summary of these results is presented in **Table 8.1**.

Correlated C_{60}-SIMS / CRM imaging

Following characterization, CRM and C_{60}-SIMS were combined to investigate the biofilm surface via correlated imaging. Owing to the relatively large sample area (~2 × 2 cm^2) and limited imaging fields of view (< 150 × 150 μm^2 for CRM when working at 60× magnification), challenges in this work included ensuring precise sample navigation, reliable re-location of microscopic CRM ROIs for subsequent MSI, and proper alignment of imaged regions for precise correlation of CRM and MSI data. To address these issues, we developed a fiducial array approach wherein 100 pL droplets of Ag nanoparticle solution were dispensed in a Cartesian grid (500 µm pitch) across the sample surface. Once dried, the nanoparticle spots were visible in optical, MS, and electron microscope images and could be used to correlate all imaging modes (the CRM microscope was operated in bright field mode for sample navigation and visualization of microspots). An origin was specified at one sample corner, and then features could be located to within a single "cell" of the grid using an (x,y) coordinate. The array also served as a visual sample alignment indicator while remounting in a holder for MSI after CRM.

Results from a correlated imaging experiment are shown in **Figure 8.6**. CRM was performed first as it is nondestructive and thus a good way to survey the sample. A region with intense micron-scale quinolone features was found and imaged by CRM (**Figure 8.6(a)**), then located within the microspot array. Next the sample was physically transferred to the C_{60}-SIMS instrument where the array position was re-located, and step-mode MSI was performed over the entire grid cell including the CRM-imaged ROI. The CRM quinolone image and the SIMS ion image of quinolone HHQ (MH^+ at m/z 244.17) in this ROI (**Figure 8.6(b)**) are in excellent agreement in both spatial distribution and signal density, cross-validating the data and indicating that the observed ion and Raman scattering distributions are accurate, not artifactual (e.g. arising from ion suppression effects or similar vibrational modes in other biofilm constituents). The microspots around the ROI are visible in the optical image (**Figure 8.6(c)**) and also detected as intense spots in several ion images including m/z 250.81 (**Figure 8.6(d)**). These ions were not identified but are likely adduct or inorganic cluster ions formed or enhanced in the presence of the Ag nanoparticles and/or the citrate buffer. The spots are well-defined against the biofilm background, indicating that the nanoparticle solution dried into discrete ~170 µm diameter spots without diffusing into the adjacent sample.

The submicron spatial resolution provided by CRM here was complemented by the chemical specificity of the correlated SIMS data, which detected at least nine quinolones and additional related metabolites present in and around the ROI (images shown in **Figure 8.7**). This allowed discernment of unique distributions for specific quinolone species as observed with C_9-NQNO (MH^+ at m/z 288.20), shown in **Figure 8.6(e)**. Note that the distribution of this quinolone still falls within the composite quinolone distribution observed by CRM based on the common *v* (quinolone ring) vibration, though the distributions of the two quinolones within that feature differ. We also observed an interesting trend between two quinolone sub-classes in the SIMS data; the two detected 3-hydroxyquinolones (PQS at m/z 260.17 and C_9-PQS at m/z 288.20) are similarly distributed in patches throughout the ROI, in contrast with the other (non-3-hydroxy) 4-quinolones which were mostly concentrated in the ROI itself. Fragment ions characteristic of these classes - m/z 175/188 from 3-hydroxyquinolones and m/z 172/159 from 4-quinolones – reflect similar distributions (shown in **Figure 8.8**), further validating these mass assignments and the associated distributions. The significance of such a distribution is not apparent, but may relate to yet-undetermined differences in biological function of the quinolone classes.

Electron microscopy of correlated imaging ROI

To investigate the physical nature of the quinolone "hotspots" which were observed by CRM and SIMS, scanning electron microscopy (SEM) was performed following another correlated imaging experiment. The resulting optical, CRM, SIMS, and SEM images are shown in **Figure 8.9**. SEM in this area revealed single cells exposed in patches on the biofilm, in contrast with uniformly smooth biofilm surface elsewhere (shown in **Figure 8.10**). The cells were consistent in size with the quinolone features observed in the CRM image and also with typical *P. aeruginosa* cell size (1-2 nm) and shape. In addition to detection of quinolones here, SIMS images showed colocalization of phosphocholine (PC, M^+ m/z 184.08), a cell membrane phospholipid fragment. Detection of PC from the outer membranes of the exposed cells in this area is a likely explanation which would fit with the correlated SEM and CRM data, suggesting that quinolone "hotspots" may be consist of perturbed biofilm regions where cells have been exposed.

CONCLUSIONS

In this report we have presented a method for correlation of two label-free molecular imaging techniques, confocal Raman microscopy (CRM) and mass spectrometry imaging (MSI), and demonstrated the utility of this approach with analysis of metabolites on *P. aeruginosa* bacterial biofilms. A chemical microspot array printed on the sample allowed precise navigation, re-location of analysis regions, and alignment of correlated image data. CRM provided nondestructive imaging capability, detection of multiple biomolecule classes, and allowed spatial resolution of submicron-scale quinolone concentrations, while MSI with C_{60}-SIMS allowed mass-based discernment of multiple specific quinolone species with subtly differing distributions, as well as confirmation of mass assignments with *in situ* tandem MS experiments. Scanning electron microscopy of the imaged regions revealed that quinolone concentrations detected with SIMS and resolved by CRM correlate with single cells exposed on the biofilm surface, thus CRM-MSI correlated imaging approach may serve as an effective platform for *in situ* single cell metabolomics experiments in future work.

Current efforts include incorporating the MALDI mode of the hybrid mass spectrometer used here in order to detect larger molecules such as proteins and polysaccharides in conjunction with high resolution CRM and SIMS images. We are also adapting sample preparation techniques to enable correlated 3D imaging with CRM and SIMS in order to explore the complex native 3D biofilm structure, as well as transitioning from bacterial monoculture to plant-microbe co-cultures in order to study metabolic exchange at the biological interface. Finally, while image alignment was performed manually here, future improvements will include automatic image alignment using microspot array features.

REFERENCES

1. Rubakhin, S.; Sweedler, J., A Mass Spectrometry Primer for Mass Spectrometry Imaging. In *Mass Spectrometry Imaging*, Rubakhin, S. S.; Sweedler, J. V., Eds. Humana Press: 2010; Vol. 656, pp 21-49.
2. Setou, M., *Imaging mass spectrometry : protocols for mass microscopy*. Springer: Tokyo, 2010; p 262.
3. Chughtai, K.; Heeren, R. M. A., Mass Spectrometric Imaging for Biomedical Tissue Analysis. *Chem Rev* **2010,** *110*, 3237-3277.
4. Dieing, T., *Confocal Raman Microscopy*. Springer: Berlin, 2011.
5. Gierlinger, N.; Schwanninger, M., Chemical imaging of poplar wood cell walls by confocal Raman microscopy. *Plant Physiol* **2006,** *140* (4), 1246-54.
6. Puppels, G. J.; Demul, F. F. M.; Otto, C.; Greve, J.; Robertnicoud, M.; Arndtjovin, D. J.; Jovin, T. M., Studying Single Living Cells and Chromosomes by Confocal Raman Microspectroscopy. *Nature* **1990,** *347* (6290), 301-303.
7. Boxer, S. G.; Kraft, M. L.; Weber, P. K., Advances in Imaging Secondary Ion Mass Spectrometry for Biological Samples. *Annu Rev Biophys* **2009,** *38* (1), 53-74.
8. Lanni, E. J.; Rubakhin, S. S.; Sweedler, J. V., Mass spectrometry imaging and profiling of single cells. *J Proteomics* **2012,** *75* (16), 5036-5051.
9. Kollmer, F.; Paul, W.; Krehl, M.; Niehuis, E., Ultra high spatial resolution SIMS with cluster ions — approaching the physical limits. *Surf Interface Anal* **2012,** *45* (1), 312-314.
10. Everall, N. J., Confocal Raman microscopy: common errors and artefacts. *Analyst* **2010,** *135* (10), 2512-2522.
11. Juang, C. B.; Finzi, L.; Bustamante, C. J., Design and Application of a Computer-Controlled Confocal Scanning Differential Polarization Microscope. *Review of Scientific Instruments* **1988,** *59* (11), 2399-2408.
12. Klein, K.; Gigler, A. M.; Aschenbrenne, T.; Monetti, R.; Bunk, W.; Jamitzky, F.; Morfill, G.; Stark, R. W.; Schlegel, J., Label-Free Live-Cell Imaging with Confocal Raman Microscopy. *Biophysical Journal* **2012,** *102* (2), 360-368.
13. Li, Z.; Chu, L.-Q.; Sweedler, J. V.; Bohn, P. W., Spatial Correlation of Confocal Raman Scattering and Secondary Ion Mass Spectrometric Molecular Images of Lignocellulosic Materials. *Anal Chem* **2010,** *82* (7), 2608-2611.
14. Jones, E.; Lockyer, N.; Kordys, J.; Vickerman, J., Suppression and enhancement of secondary ion formation due to the chemical environment in static-secondary ion mass spectrometry. *J Am Soc Mass Spectrom* **2007,** *18* (8), 1559-1567.
15. Lay, J. O.; Gidden, J.; Liyanage, R.; Emerson, B.; Durham, B., Rapid characterization of lipids by MALDI MS. Part 2: Artifacts, ion suppression, and TLC MALDI imaging. *Lipid Technology* **2012,** *24* (2), 36-40.
16. Deininger, S.-O.; Cornett, D.; Paape, R.; Becker, M.; Pineau, C.; Rauser, S.; Walch, A.; Wolski, E., Normalization in MALDI-TOF imaging datasets of proteins: practical considerations. *Anal Bioanal Chem* **2011,** *401* (1), 167-181.
17. Masyuko, R.; Lanni, E. J.; Sweedler, J. V.; Bohn, P. W., Correlated imaging-a grand challenge in chemical analysis. *Analyst* **2013,** *138* (7), 1924-1939.
18. Petit, V. W.; Réfrégiers, M.; Guettier, C.; Jamme, F. d. r.; Sebanayakam, K.; Brunelle, A.; Laprévote, O.; Dumas, P.; Le Naour, F. o., Multimodal Spectroscopy Combining Time-of-Flight-Secondary Ion Mass Spectrometry, Synchrotron-FT-IR, and Synchrotron-UV Microspectroscopies on the Same Tissue Section. *Anal Chem* **2010,** *82* (9), 3963-3968.
19. Fagerer, S. R.; Schmid, T.; Ibanez, A. J.; Pabst, M.; Steinhoff, R.; Jefimovs, K.; Urban, P. L.; Zenobi, R., Analysis of single algal cells by combining mass spectrometry with Raman and fluorescence mapping. *Analyst* **2013,** *138* (22), 6732-6736.
20. Lanni, E. J.; Dunham, S. J. B.; Nemes, P.; Sweedler, J. V., Biomolecular Imaging with C60-SIMS: Instrumentation, Matrix Enhancement, and Single Cell Analysis. **2014,** *Submitted for publication.*
21. Robinson, M. A.; Graham, D. J.; Castner, D. G., ToF-SIMS depth profiling of cells: Z-correction, 3D imaging, and sputter rate of individual NIH/3T3 fibroblasts. *Anal Chem* **2012,** *84* (11), 4880-4885.
22. Masyuko, R. N.; Lanni, E. J.; Driscoll, C. M.; Shrout, J. D.; Sweedler, J. V.; Bohn, P. W., Spatial organization of Pseudomonas aeruginosa biofilms probed by combined matrix-assisted laser desorption ionization mass spectrometry and confocal raman microscopy. *Analyst* **2014,** *Accepted for publication.*

23. Puppels, G. J.; Garritsen, H. S.; Segers-Nolten, G. M.; de Mul, F. F.; Greve, J., Raman microspectroscopic approach to the study of human granulocytes. *Biophys J* **1991,** *60* (5), 1046-56.
24. Harz, M.; Rosch, P.; Peschke, K. D.; Ronneberger, O.; Burkhardt, H.; Popp, J., Micro-Raman spectroscopic identification of bacterial cells of the genus Staphylococcus and dependence on their cultivation conditions. *Analyst* **2005,** *130* (11), 1543-1550.
25. Neugebauer, U.; Schmid, U.; Baumann, K.; Ziebuhr, W.; Kozitskaya, S.; Deckert, V.; Schmitt, M.; Popp, J., Towards a detailed understanding of bacterial metabolism - Spectroscopic characterization of Staphylococcus epidermidis. *Chemphyschem* **2007,** *8* (1), 124-137.
26. Neugebauer, U.; Schmid, U.; Baumann, K.; Holzgrabe, U.; Schmitt, M.; Popp, J., Towards an understanding of the mode of action of fluoroquinolone drugs - art. no. 66331W. *Biophotonics 2007: Optics in Life Science* **2007,** *6633*, W6331-W6331.
27. Neugebauer, U.; Szeghalmi, A.; Schmitt, M.; Kiefer, W.; Popp, J.; Holzgrabe, U., Vibrational spectroscopic characterization of fluoroquinolones. *Spectrochim Acta A Mol Biomol Spectrosc* **2005,** *61* (7), 1505-17.
28. Lépine, F.; Milot, S.; Déziel, E.; He, J.; Rahme, L. G., Electrospray/mass spectrometric identification and analysis of 4-hydroxy-2-alkylquinolines (HAQs) produced by Pseudomonas aeruginosa. *J Am Soc Mass Spectrom* **2004,** *15* (6), 862-869.
29. Lanni, E. J.; Masyuko, R. N.; Driscoll, C. M.; Aerts, J. T.; Shrout, J. D.; Bohn, P. W.; Sweedler, J. V., MALDI-guided SIMS: Multiscale Imaging of Metabolites in Bacterial Biofilms. **2014,** *Submitted for publication.*
30. Phelan, V. V.; Liu, W.-T.; Pogliano, K.; Dorrestein, P. C., Microbial metabolic exchange - the chemotype-to-phenotype link. *Nat Chem Biol* **2012,** *8* (1), 26-35.
31. Rosch, P.; Schneider, H.; Zimmermann, U.; Kiefer, W.; Popp, J., In situ Raman investigation of single lipid droplets in the water-conducting xylem of four woody plant species. *Biopolymers* **2004,** *74* (1-2), 151-6.
32. Bolboaca, M.; Kiefer, W.; Popp, J., Fourier transform Raman and surface-enhanced Raman spectroscopy of some quinoline derivatives. *Journal of Raman Spectroscopy* **2002,** *33* (3), 207-212.
33. Frosch, T.; Schmitt, M.; Popp, J., Raman spectroscopic investigation of the antimalarial agent mefloquine. *Anal Bioanal Chem* **2007,** *387* (5), 1749-57.
34. Wang, Y.; Yu, K.; Wang, S., Vibrational spectra study on quinolones antibiotics. *Spectrochim Acta A Mol Biomol Spectrosc* **2006,** *65* (1), 159-63.
35. Huse, H.; Whiteley, M., 4-Quinolones: Smart Phones of the Microbial World. *Chem Rev* **2010,** *111* (1), 152-159.

FIGURES AND TABLES

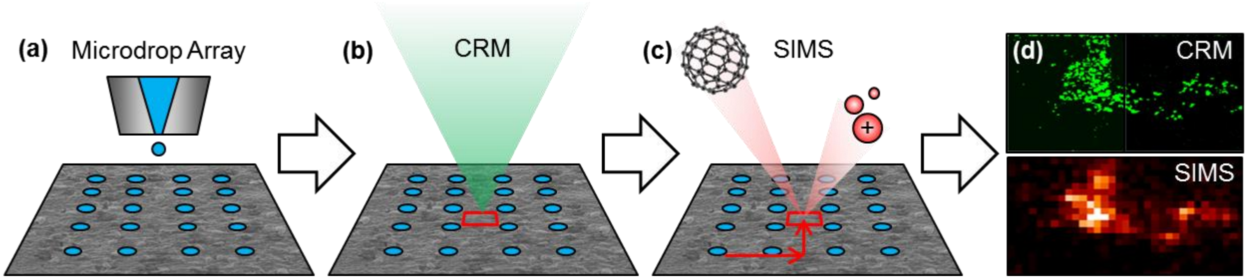

Figure 8.1: CRM/SIMS correlated imaging workflow. (a) Microdroplet array is applied to the dried biofilm, **(b)** CRM is performed to locate ROIs and array coordinates are recorded, **(c)** sample is transferred to the SIMS instrument, the array is used to navigate back to the ROI, and **(d)** CRM and SIMS data are correlated using the array for alignment.

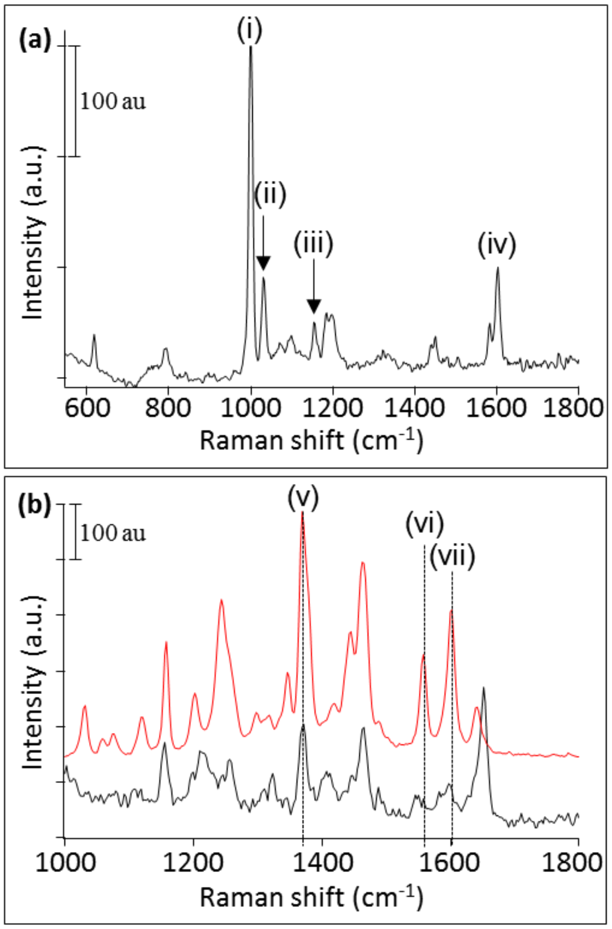

Figure 8.2: CRM spectral profiles of a *P. aeruginosa* biofilm. (a) CRM profiling of a *P. aeruginosa* biofilm detects multiple biomolecular classes by characteristic vibrations, including those labeled here: (i) 999 cm^{-1} from symmetric ring breathing vibrations of phenylalanine and tryptophan (indicating proteins), (ii) 1030 cm^{-1} from C-O stretching of carbohydrate moieties, (iii) 1155 cm^{-1} from C-C and C-O asymmetric ring breathing vibrations of carbohydrates, and (iv) 1601 cm^{-1} C=C stretching in phenylalanine. **(b)** Comparison of a quinolone-rich biofilm ROI (black trace) with a purified commercial PQS standard (red trace) reveals several matching vibrations including: (v) 1371 cm^{-1} from C=C stretching in the quinolone ring, (vi) C-C and C-N-C stretching in the quinolone ring, and (vii) 1603 cm^{-1} symmetric C=C stretching in the quinolone ring. Dotted vertical lines are added to facilitate comparison. All Raman spectra are baseline corrected using a fourth order polynomial function.

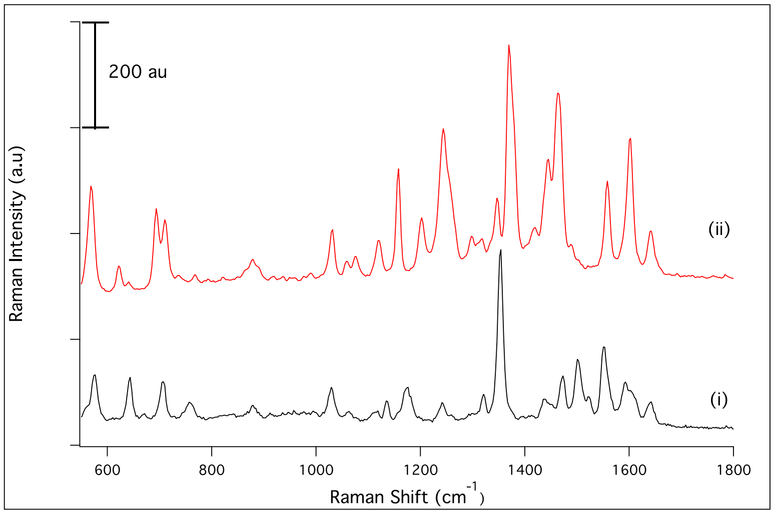

Figure 8.3: Raman spectra of quinolone standards. Raman spectra of quinolones (i) HHQ and (ii) PQS are uniquely characterized by contributions from ring deformation, ring breathing and ring stretching vibrations. Ring deformation vibrations are represented by the bands at 431 cm^{-1}, 490 cm^{-1} and 570 cm^{-1} in PQS and at 489 cm^{-1}, 573 cm^{-1}, 642 cm^{-1} and 753 cm^{-1} in HHQ.[32,33] The band at 1031 cm^{-1} in both PQS and HHQ is indicative of ring breathing vibrations. The bands found in the 1300 -1600 cm^{-1} region of the spectrum are characteristic of ring stretching vibrations which are associated with intense bands. In the PQS spectrum the major bands in this region are at 1371 cm^{-1}, assigned to the C=C stretching vibrations of the quinolone ring with contributions from CH bending vibrations,[27,32,33] 1557 cm^{-1} attributed to (C-C-C) and (C-N-C) ring stretching vibrations,[32,33] and at 1603 cm^{-1} assigned to symmetric C=C stretching vibrations of the quinolone ring.[32,33] In HHQ, the major bands are at 1353 cm^{-1} arising from C=C stretching vibrations of the quinolone ring with contributions from CH bending vibrations,[32, 34] 1553 cm^{-1} attributed to (C-C-C) and (C-N-C) ring stretching vibrations,[32] 1501 cm^{-1} and 1593 cm^{-1} assigned to (C-C-C) and symmetric C=C ring stretching vibrations.[32] Other significant bands characterized by non-ring vibrations in PQS are 1158 cm^{-1} arising from CH bending vibrations[32, 34] and 1245 cm^{-1} attributed to contributions from CH bending and CH twisting vibrations.[34] In HHQ, bands at 1173 cm^{-1} and 1239 cm^{-1} mark similar vibrations.[32, 34] CH_2 deformation vibrations are found at 1464 cm^{-1} and 1471 cm^{-1} in PQS and HHQ respectively.[32, 24, 26]

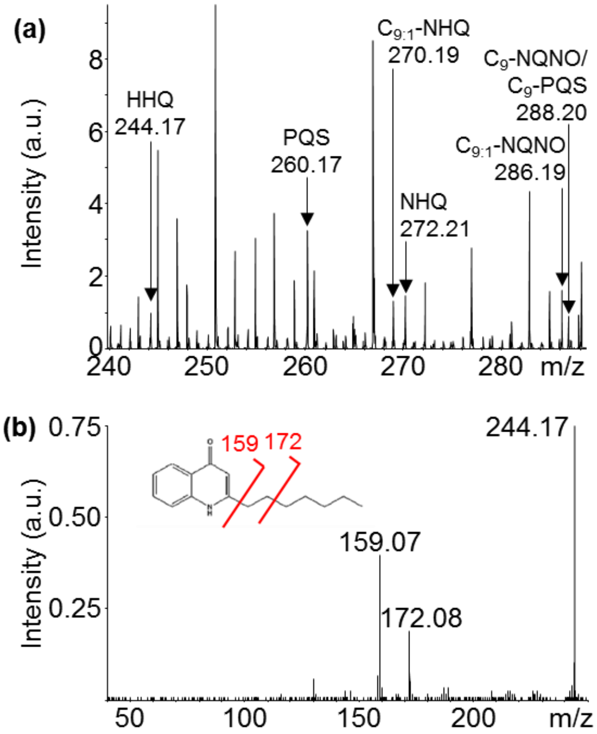

Figure 8.4: C_{60}-SIMS and tandem MS of a *P. aeruginosa* biofilm. (a) C_{60}-SIMS direct analysis of untreated biofilm surface yields a profile including multiple quinolones detected as MH^+ pseudomolecular ions. **(b)** *In situ* tandem MS of putative quinolones supports mass assignments *e.g.* for HHQ at m/z 244.17 shown here, yielding characteristic fragments at m/z 159.07 and 172.08.

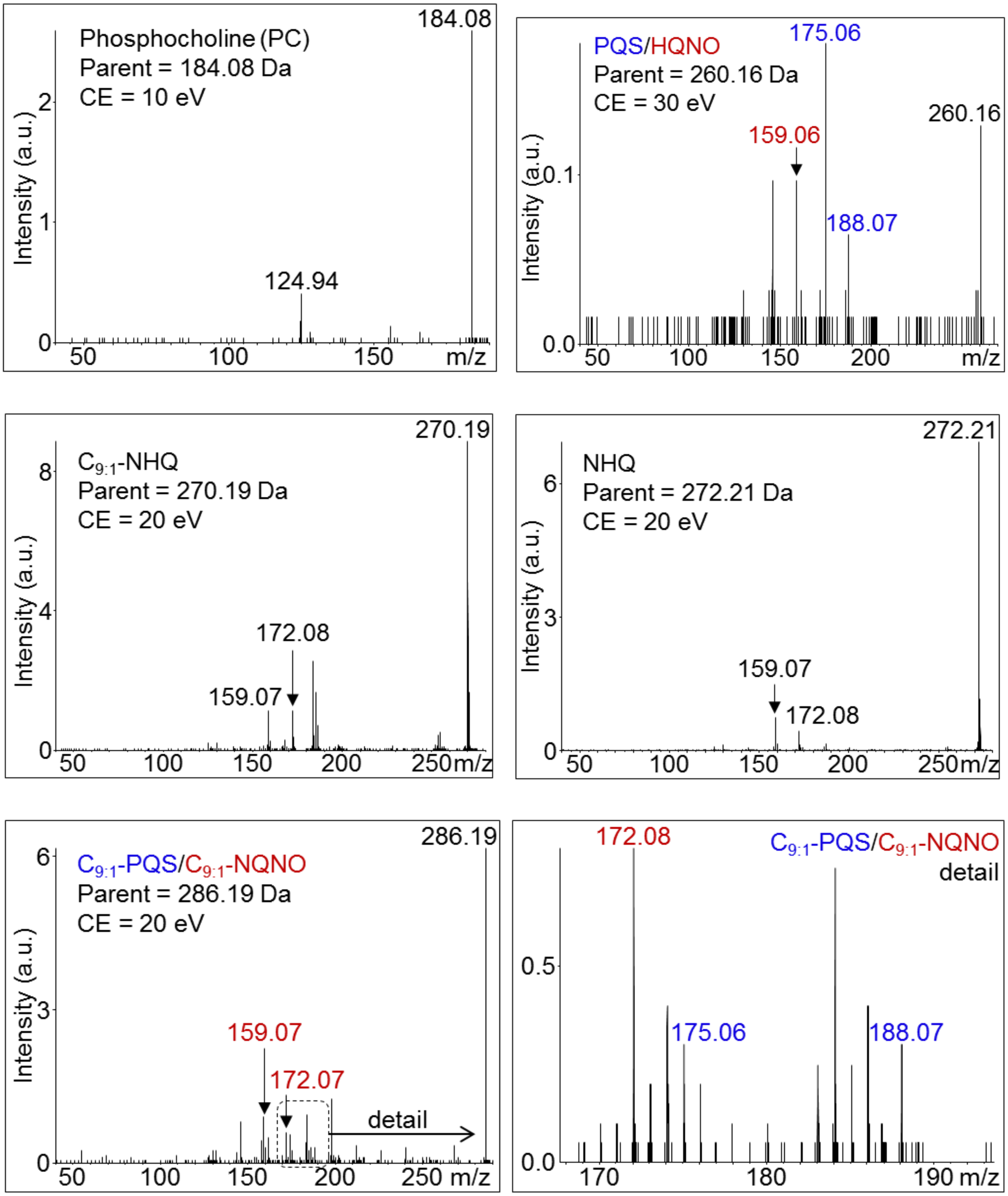

Figure 8.5: C$_{60}$-SIMS tandem MS spectra of biofilm metabolites. Spectra were collected directly from the untreated biofilm surface. Spectra are labeled with metabolite abbreviation (corresponding with mass list in Table 8.1), parent ion mass, and CID collision energy used. Characteristic fragment ions matching those reported in previous work[7] are labeled in the spectra and color-coded in cases of isobaric species.

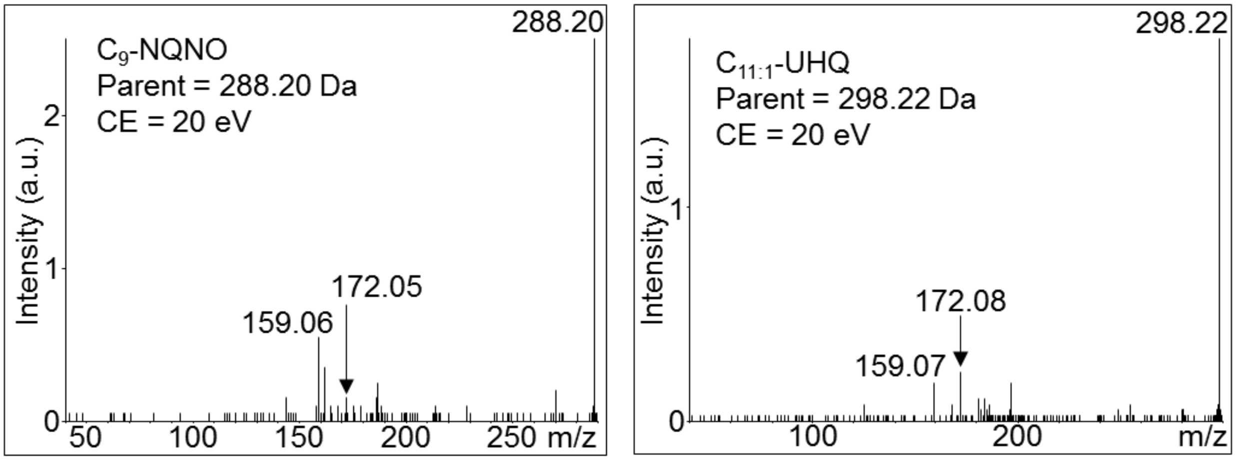

Figure 8.5 (continued)

Compound ID	Molecular formula	M_{ex}	$[M+H]^+$ theoretical	$[M+H]^+$ observed	ΔM
4-quinolone frag.	$C_{10}H_9NO$	159.07	-	159.07*	0.00
3-hydroxyquinolone frag.	$C_{10}H_9NO_2$	175.06	-	175.07*	0.01
4-quinolone frag.	$C_{11}H_{10}NO$	172.08	-	172.08*	0.00
3-hydroxyquinolone frag.	$C_{11}H_{10}NO_2$	188.07	-	188.07*	0.00
PC (phosphocholine)	$C_5H_{15}NO_4P$	184.07	-	184.08*	0.01
1-HP (1-hydroxyphenazine)	$C_{12}H_8N_2O$	196.06	197.07	197.09	0.02
1-MP (1-methoxyphenazine)	$C_{13}H_{10}N_2O$	210.08	211.09	211.10	0.01
HHQ (2-heptyl-4-quinolone)	$C_{16}H_{21}NO$	243.16	244.17	244.17	0.00
PQS (2-heptyl-3-hydroxyquinolone)	$C_{16}H_{21}NO_2$	259.16	260.17	260.17	0.00
HQNO (4-hydroxy-2-heptylquinolone-N-oxide)	$C_{16}H_{21}NO_2$	259.16	260.17	260.17	0.00
$C_{9:1}$-NHQ (2-nonenyl-4-quinolone)	$C_{18}H_{23}NO$	269.18	270.19	270.19	0.00
NHQ (2-nonyl-4-quinolone)	$C_{18}H_{25}NO$	271.19	272.20	272.19	-0.01
$C_{9:1}$-NQNO (4-hydroxy-2-nonenylquinolone-N-oxide)	$C_{18}H_{23}NO_2$	285.17	286.18	286.19	0.01
C_9-PQS (2-nonyl-3-hydroxyquinolone)	$C_{18}H_{25}NO_2$	287.19	288.20	288.20	0.00
C_9-NQNO (4-hydroxy-2-nonylquinolone-N-oxide)	$C_{18}H_{25}NO_2$	287.19	288.20	288.20	0.00
$C_{11:1}$-UHQ (2-undecenyl-4-quinolone)	$C_{20}H_{27}NO$	297.21	298.22	298.22	0.00

Table 8.1: Mass list and tandem MS spectra for metabolites detected by C_{60}-SIMS analysis of *P. aeruginosa* biofilm. Compounds listed in bold typeface were confirmed with *in situ* tandem MS (spectra shown in Figure S2). *Indicates fragment ion detected as M^+ or $M^{\bullet +}$.

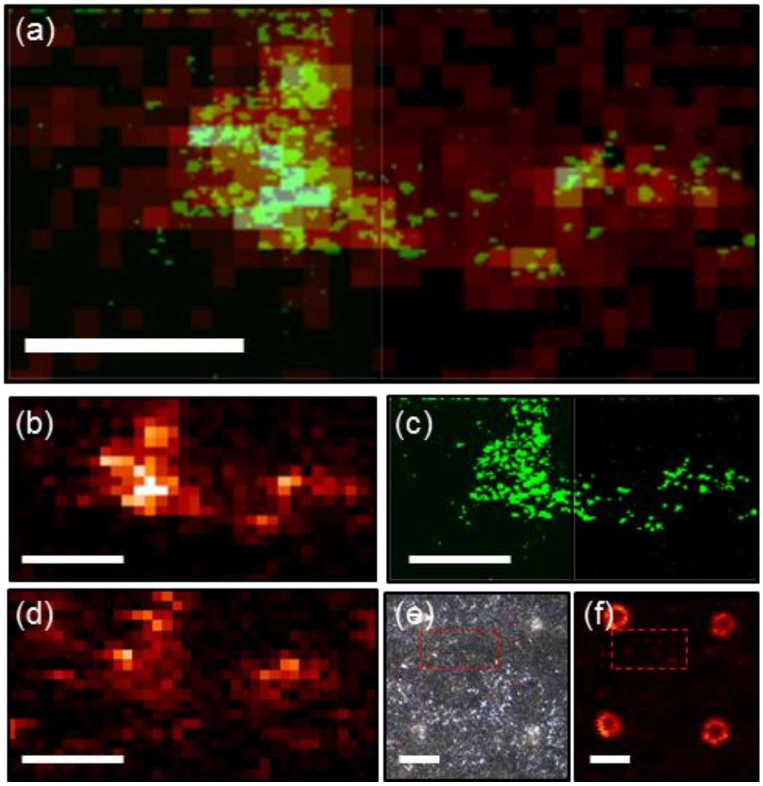

Figure 8.6: Correlated SIMS/CRM imaging provides additional information about signaling molecules in *P. aeruginosa* biofilm. (a) Superimposed CRM "composite quinolone" image (1350-1400 cm^{-1}, C=C quinolone ring stretch) and SIMS 2-heptyl-2-quinolone ion image (HHQ, MH^+ at m/z 244.17) show similar molecular distribution in the selected ROI. The same images are shown individually for **(b)** SIMS and **(c)** CRM, where high spatial resolution enables visualization of micron-scale features within the ROI. **(d)** Another quinolone, 4-hydroxy-2-nonylquinolone-N-oxide (C_9-NQNO, MH^+ at m/z 288.20) is found co-localized, but distribution is unique from that of HHQ within the composite quinolone area. (e) optical and (f) m/z 250.81 SIMS ion images with a larger field of view show how the microspot array is visualized around the ROI, allowing precise navigation and image alignment. Red boxes specify the ROI of CRM / SIMS detail. Scale bars = 100 µm in (a)-(d) and 200 µm in (e)-(f).

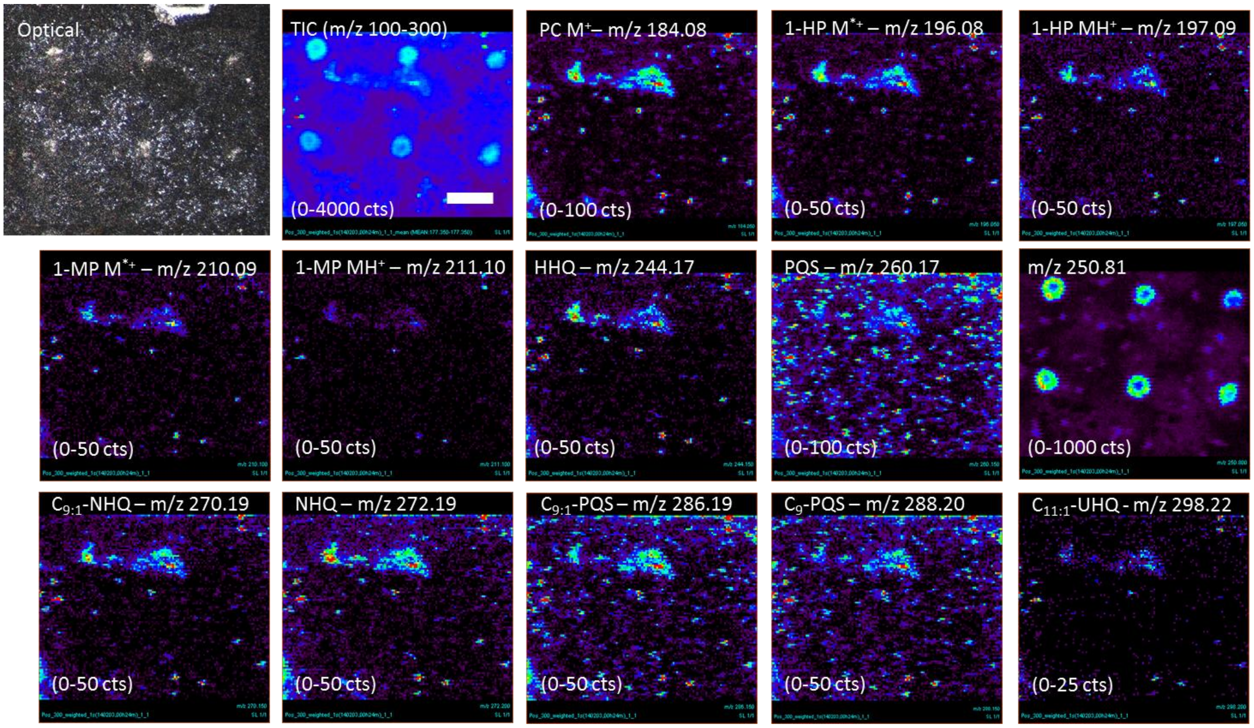

Figure 8.7: Full C$_{60}$-SIMS images of metabolites detected in Fig. 4 ROI. Scale bar = 0.5 mm. Metabolites are labeled with abbreviations used in Table 8.1, m/z value of monoisotopic peak, and peak intensity signal range (in counts, cts) used to generate the shown ion image.

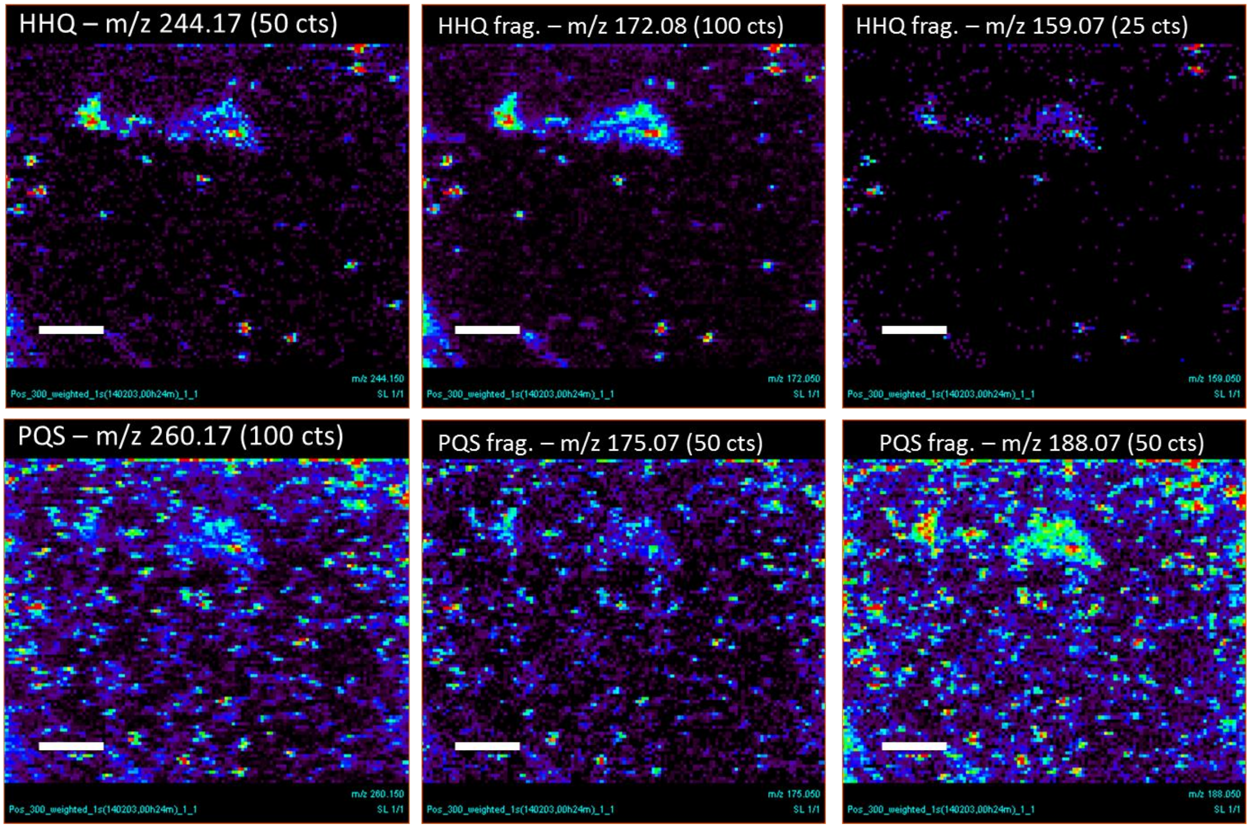

Figure 8.8: Spatial co-location of characteristic fragment ions with parent quinolone classes in Fig. 4 ROI. 4-quinolone HHQ and characteristic fragments m/z 172/159 show good agreement of spatial localization throughout the imaged region, likewise the 3-hydroxy-4-quinolone PQS and characteristic fragments m/z 175/188 are co-localized differently. Scale bar = 200 µm.

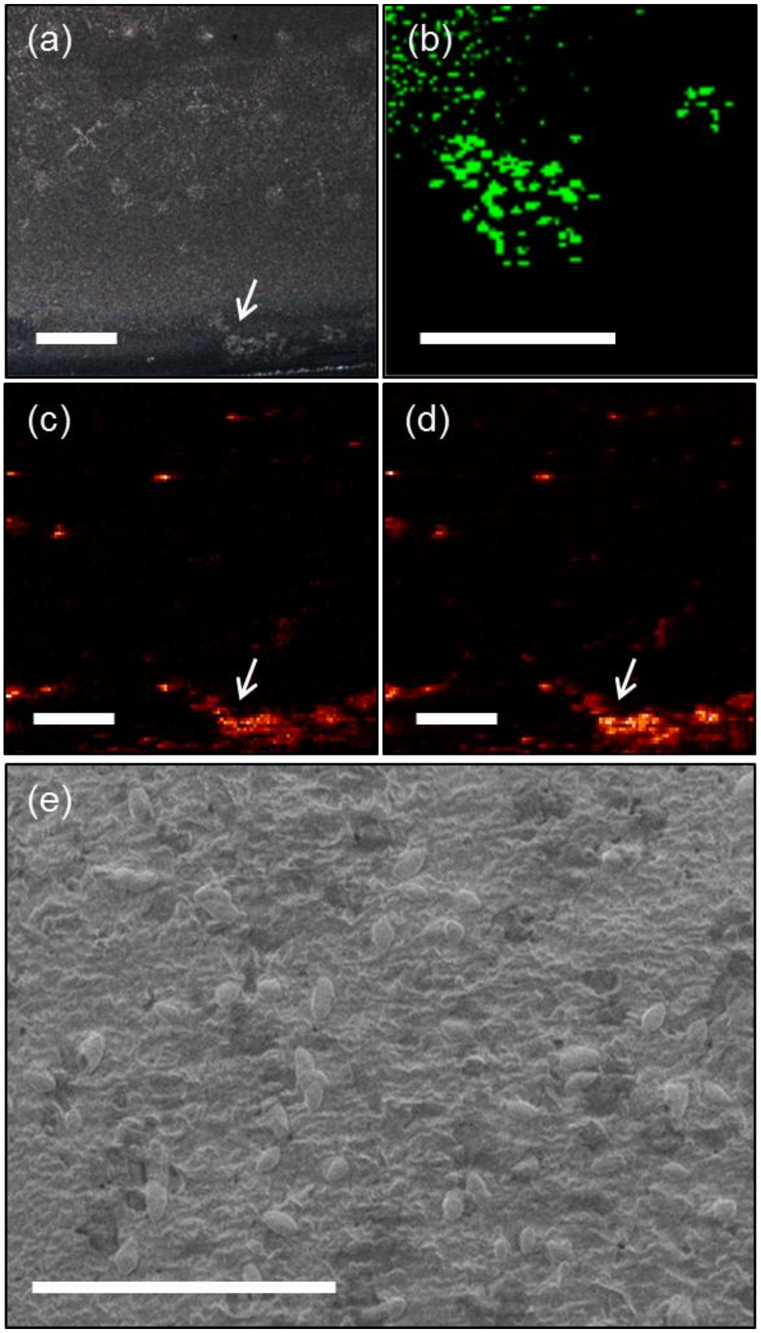

Figure 8.9: SEM of quinolone "hot spot" reveals unique topography and cell features on the biofilm surface. **(a)** Optical, **(b)** CRM image from C=C quinolone ring stretch (1350-1400 cm^{-1}), **(c)** HHQ (m/z 244.17) ion image, and **(d)** PC (m/z 184.08) ion image all indicate a chemical ROI at the edge of the biofilm; CRM location is indicated with red arrows. E) SEM of the same ROI shows a rough patch and micron-sized single cells on the biofilm surface. Scale bars = 500 µm in a/c/d, 100 µm in b, and 20 µm in e.

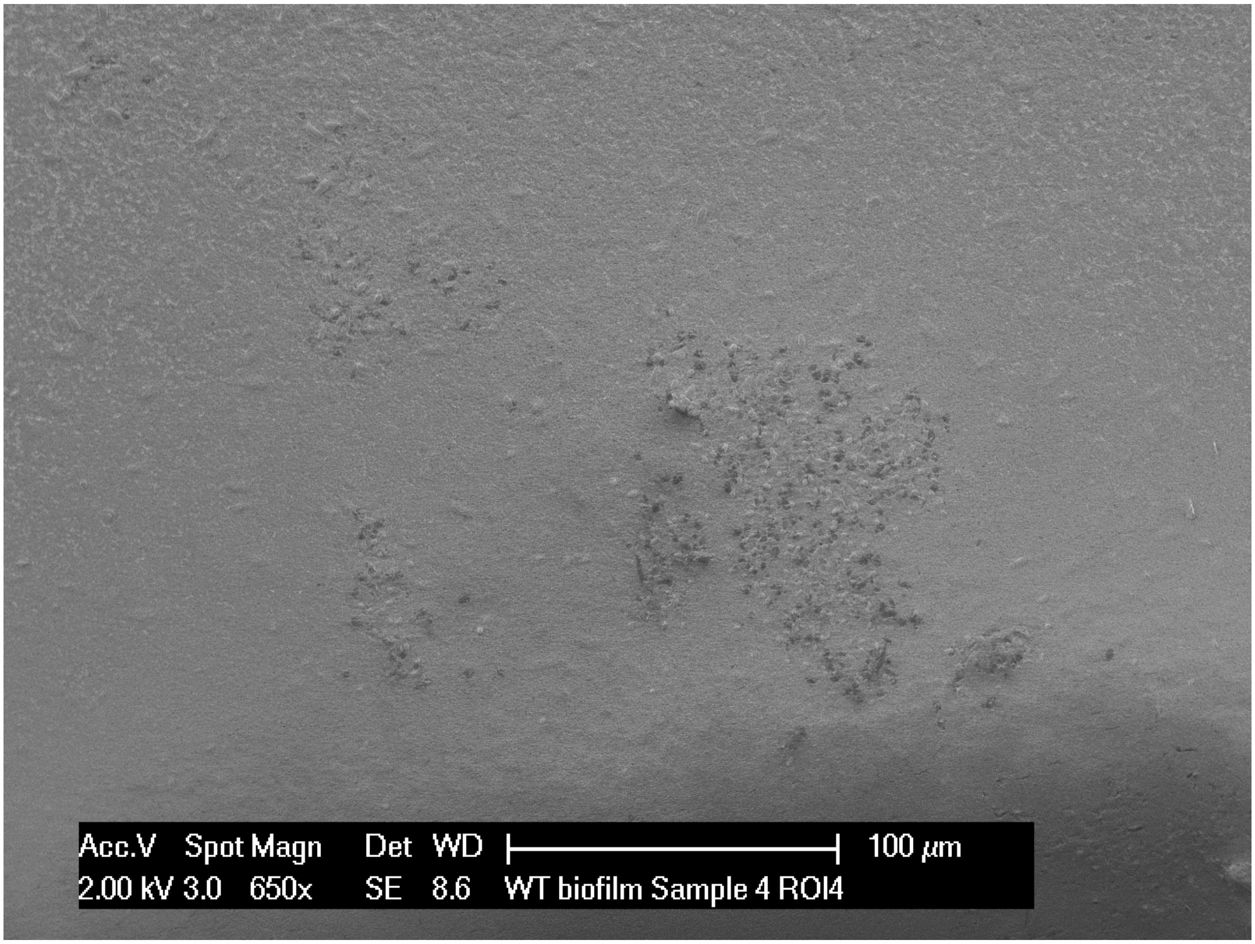

Figure 8.10: Low resolution SEM image of Figure 5 ROI. An electron micrograph of the region around the "quinolone hot spot" shown in Figure 5 shows smooth biofilm surface elsewhere, compared with a coarser texture and visible individual cells in the region of intense quinolone (and phosphocholine) signal.

CHAPTER 9

ASSORTED METHOD DEVELOPMENT FOR MASS SPECTROMETRY IMAGING

NOTES AND ACKNOWLEDGMENTS

This chapter presents three minor MSI-related projects which did not reach publishable conclusions but may do so with additional work or at least offer useful insight for future MSI protocol development and biological application, including:

- Sheath gas-assisted chemical inkjet printing for improved microspot arrays
- MALDI MSI and HPLC for detection of an administered pharmacological agent in rat brain
- Sample preparation for MALDI MSI of lipids and peptides in rat spinal cord

To improve readability, each project is discussed in its entirety, including a brief introduction, experimental details and results. All projects were supported by the Department of Energy Office of Biological and Environmental Research through grant DE SC0006642 and NIH through grants R01DE018866 and P30DA018310. Assistance with rat dissections, biological experimental design and execution by Drs. Stanislav Rubakhin, Paul Gold, and Lori Newman (Gold research group at Syracuse University), spinal cord MALDI MS imaging by undergraduate assistants Alex Ruby and Kevin Joerger, and light microscopy by Scott Robinson in the Beckman Microscopy Suite are gratefully acknowledged. Insightful scientific discussion with Ta Hsuan Ong and Dr. Zhiyong Yang in the Sweedler group is also appreciated.

SECTION 9-1: SHEATH GAS-ASSISTED CHEMICAL INKJET PRINTING FOR IMPROVED MICROSPOT ARRAYS

INTRODUCTION

In a typical MALDI experiment, the analyte(s) must be mixed with the matrix compound so that it becomes included in matrix crystals upon drying. In non-imaging experiments this is easily and robustly accomplished with the “dried droplet” method in which ~1 µL each of sample and matrix are mixed directly on the MALDI target with a pipette. For imaging experiments this is not practical since a dried droplet will coat the surface unevenly and can dry to a spot several mm in diameter, delocalizing analytes and thus limiting lateral spatial resolution to a similar size scale. One common solution to this problem is to apply a drier, uniform matrix coating to the surface with methods such as pneumatic spray[1] and vacuum sublimation;[2] these improve spatial resolution but also reduce detection limits, as less solvent equates to reduced analyte extraction and mixing before analysis. An alternative solution is to print an array of much smaller droplets across the sample surface, and then acquire one pixel of image data from each dried spot.[3-4] This improves analyte extraction as well as enabling special sample treatments such as peptidases, though lateral spatial resolution is limited by microdroplet array pitch. Commercial chemical inkjet printers such as the Shimadzu ChIP-1000 have been used for published work reaching lateral spatial resolutions of 200 µm,[5] below which droplets begin to merge and spatial information is lost. Reducing droplet size and/or improving print consistency could improve this limit and therefore the utility of inkjet printing for MSI applications.

This section explores a method to improve microdroplet array quality by addition of a sheath gas to the Piezo print head on a chemical inkjet printer, which may act to stabilize the droplet, reduce volume and diameter, and/or initiate matrix crystallization prior to deposition. A simple sheath gas apparatus is described, and light microscopy of arrays printed with and without sheath gas allows for an initial evaluation of the modification. Results indicate that more uniform spots are produced with sheath gas, which may translate to improved MALDI MS image quality.

EXPERIMENTAL METHODS

Materials and chemicals

25 × 75 × 1.1 mm indium tin oxide (ITO)-coated microscope slides were purchased from Delta Technologies, Ltd. (Loveland, CO, USA). HPLC-grade isopropanol, water, and 2,5-dihydroxybenzoic acid (DHB) 98% were purchased from Sigma-Aldrich (St. Louis, MO, USA). For sheath gas, nitrogen from the Beckman Institute liquid nitrogen supply tank was delivered to the room *via* copper tubing, regulated at the lab room spigot, and then delivered to the apparatus *via* Tygon tubing.

Biological sample preparation

Intact rat spinal cord tissue was isolated from an adult Long-Evans rat (Harlan, Indianapolis, IN, USA) by rapid decapitation and dissection, frozen promptly in aluminum foil on dry ice, and stored in a sealed bag at -80º C until use. 20 µm-thick spinal cord sections were collected at -18° C on a cryotome (3050S, Leica Biosystems, Germany) and thaw-mounted to clean ITO-coated glass microscope slides, then warmed to room temperature (22-25 ºC) in air prior to inkjet printing. Consecutive sections with similar area and anatomical structure were used to facilitate comparison between printing methods. Animal care protocols and procedures were approved by UIUC Laboratory Animal Care Advisory Committee and fully comply with federal guidelines for humane care and treatment of animals.

Chemical inkjet printing and modification

A ChIP-1000 Chemical Inkjet Printer (Shimadzu Corp., Kyoto, Japan) was used for microdroplet array printing in these experiments. Disposable "one-shot vessels" were also purchased from Shimadzu. Print solution consisted of 25 mg/mL DHB dissolved in 1:1 H_2O:isopropanol. Piezo print head parameters were optimized at 26 V / 35 µsec delay / -0.33 kPa back pressure for printing here, though in general these parameters were found to vary with many parameters such as solvent system, temperature, humidity, print head, and print head condition, thus re-optimization is necessary prior to each run and sometimes mid-run. Printing was performed on spinal cord tissue sections in "area print" mode and "multipass iterative" mode at a 200 µm square array pitch, 100 pL droplet volume, 10 nL total volume per spot, and 3 droplets/spot per round (for 33 print rounds total).

To provide a flow of "sheath" gas around the Piezo print head during printing, a coaxial gas nozzle was constructed and installed on the ChIP-1000; photograph and schematic of the apparatus are shown in **Figure 9.1**. The apparatus was constructed from two 1 mL plastic pipette tips: the first (A) was cut to 18 mm length to fit around the print head (B) with a cutout slot accommodate the Piezo control cable (C) and a hole for the second pipette tip (D), which delivered N_2 sheath gas from a Tygon tube (E). The joint between the two tips was briefly heated to soften the plastic and improve the seal. The apparatus must be installed carefully, as the Piezo control cable is fragile and easily damaged. For sheath-assisted microspotting, N_2 gas was delivered at 2 PSI to the tip. Visual observation of the emitted droplets using the built-in microscope confirmed that this did not disrupt dispensing or significantly change droplet trajectory.

RESULTS AND DISCUSSION

The goal of this work was to improve printing performance of the ChIP-1000 chemical inkjet printer by adding a coaxial flow of sheath gas around the Piezo print head, with the hypothesis that this would improve microspot quality in terms of spot size and uniformity. MALDI matrix (DHB) solution was printed onto spinal cord tissue sections with and without sheath gas flow enabled, and the dried chemical microspot arrays were evaluated with transmission light microscopy as shown in **Figure 9.2**. Four adjacent spinal cord tissue sections were treated - two by each method - and the combined results indicate a clear qualitative change in the array. Sheath gas-assisted printing produced more uniform, regularly shaped spots overall, and matrix crystal size also appears smaller. Improvement in droplet isolation is noted particularly in the peripheral white matter of the cord (appearing darker in the images) where significant mixing is observed in the absence of sheath gas. Magnified detail of sheath gas-assisted microspots on tissue in **Figure 9.3** shows that some mixing does still occur, and also that spots appear to dry differently on the two main tissue types of the spine: crystallization is biased towards the edge of the spot on white matter, while a solid disc of material appears to be produced on gray matter. Spot diameter is approximately 125 µm, suggesting that pitch may be decreased to ~150 µm while still retaining good droplet isolation.

FUTURE DIRECTIONS

While these initial microscopy-based results suggest improved printing performance in a number of aspects with the addition of coaxial sheath gas to the printing process, further work would be useful to demonstrate that this improvement translates into improved MALDI MS image quality in terms of improved lateral spatial resolution and/or reduced signal variation. The cause of improved printing may also be investigated: does sheath gas stabilize the droplet, initiate early crystallization, and/or simply accelerate solvent evaporation resulting in a smaller volume upon deposition? Answering this question could inform on how to further optimize chemical inkjet printing in terms of array pitch and spot uniformity.

SECTION 9-2: MALDI MSI AND HPLC FOR DETECTION OF AN ADMINISTERED PHARMACOLOGICAL AGENT IN RAT BRAIN

INTRODUCTION

In this collaborative project, the Gold research group (then at UIUC, now at Syracuse University) sought to visualize the distribution of a small drug-like molecule – α-cyano-4-hydroxycinnamic acid (CHCA) – in rat brain following systemic injection, and MSI was expected to provide this information easily. CHCA efficiently absorbs the UV laser light ordinarily used in laser microprobe MSI and readily deprotonates in gas phase to protonate other compounds, making it a ubiquitous signal-enhancing matrix treatment for MALDI experiments. These properties were also expected to make it an ideal analyte here, but this turned out to not be the case due largely, it appears, to ion suppression. Thus while unambiguous molecular imaging of CHCA in rat brains was not achieved with MSI, a number of sample treatment approaches were attempted and something useful may nevertheless be gleaned from this work about MSI experimental strategy. Ultimately, a simple liquid chromatographic method was successfully adapted for measurement of CHCA in tissue homogenate extracts, and this yielded promising preliminary data.

The Gold group studies learning and memory, and in previous work they show that memory is enhanced by lactate provided as energy to neurons by astrocytes or artificially by hippocampal injection, [6] thus astrocytes may regulate memory formation through this mechanism. Juvenile animals depend more than adults on lactate and ketones as energy sources and also have higher systemic lactate levels, thus the present study investigated age-related differences in the effect of lactate transport inhibition on working memory in rats. CHCA was used as a neuronal lactate transport blocker, and it (or a vehicle control) was administered systemically to rats before subjecting them to a spatial working memory assessment *via* the spontaneous alternation task. Following this task, the brain of each rat was isolated and delivered to the Sweedler lab in order to visualize CHCA distribution within the brain (particularly the hippocampus, a learning-related structure) by MSI and the HPLC assays.

EXPERIMENTAL METHODS

Materials and chemicals

9-aminoacridine (9-AA), 2,5-dihydroxybenzoic acid (DHB), HPLC-grade acetonitrile, acetone, and acetic acid were purchased from Sigma-Aldrich (St. Louis, MO, USA), and mixtures were prepared in lab. Gold lab utilized its own α-cyano-4-hydroxycinnamic acid (CHCA) which was confirmed (by label and MS analysis) to be an identical compound, and additional CHCA for imaging experiments was purchased from Sigma-Aldrich. Deionized water was prepared by Millipore filtration at Beckman Institute. 25 × 75 × 1.1 mm indium tin oxide (ITO)-coated microscope slides were purchased from Delta Technologies, Ltd. (Loveland, CO, USA).

Behavioral studies and biological sample preparation

Animal handling, spatial working memory assessment, post-test dissection, and organ isolation were performed by collaborators in the Gold research group. 25 day old (junior) and >90 day old (adult) male Sprague Dawley rats were purchased and received four days prior to testing, pair housed and allowed to acclimate for one day. Animals were handled five times for 2-3 min. prior to testing. On the day of the behavioral experiment, rats were given a systemic injection of 0, 0.5, 1.5, or 5.0 mM CHCA in 4% DMSO/0.9% saline × 1 mL/kg body wt. (~400 g for adults), 30 min. prior to the test. Rats were then assessed *via* spontaneous alternation task wherein they were allowed 20 min. to explore a four-arm maze surrounded by spatial cues. Arm entries were recorded and scored as an alternation if the rat visited all four arms within five choices. Following this task, rats were euthanized by injection of Fatal Plus followed by rapid decapitation, dissection on ice, snap-freezing of brain and liver in dry ice-cooled pentane, and collection of whole blood which was promptly centrifuged to isolate blood serum. Samples were stored at -80° C until analysis.

In addition to rats used in the memory assessment tests, several rats were treated with higher CHCA doses for the purpose of MSI method development since the $\leq$5 mM experimental CHCA doses were initially undetectable. Junior and adult rats were either given a 100 mM systemic CHCA dose in the same manner as those tested, or a similar 100 mM intracranial injection was made into the a posterior hippocampus lobe immediately after sacrificing. All MS and HPLC analyses were performed blind to sample identities; these were subsequently provided by collaborators.

For tissue imaging experiments, brain and liver specimens were warmed to -20° C cut coronally at approx. -4-5 mm w.r.t. bregma (see **Figure 9.4**) to expose the lower posterior hippocampal lobes. The caudal brain half was mounted for sectioning on a Leica CM3050S cryotome and several 20 µm-thick coronal sections were collected and thaw-mounted to ITO-coated microscope slides. In some cases the tissue was mounted over a dried droplet of CHCA standard in order to evaluate the detection limit for CHCA in the tissue, or CHCA standard was spotted beside the tissue as a reference. The slide was then warmed to room temperature (22-25 °C) in a vacuum desiccator for ~30 min. Dried and warmed slides were imaged with a Perfection V300 Photo flatbed scanner (Epson, Suwa, Nagano, Japan), chemically treated as described below, and then loaded into the mass spectrometer for analysis.

For HPLC experiments, 200 µL blood serum was diluted 1:1 with acetonitrile + 0.5% AcOH while for brain and liver samples, a 2 mm diam × 5 mm deep tissue punch was extracted from the frozen hippocampal lobe (see **Figure 9.4**), thawed in a 1 mL centrifuge vial, weighed, and acetonitrile + 0.5% AcOH was added in proportion to establish a uniform 10:1 (v/w) solvent:tissue ratio for all samples. Blood and tissue mixtures were each then homogenized with a rotary pestle homogenizer for 1 min., shaken vigorously (vortexed) for 1 min., centrifuged at 20k × g / 20° C for 15 min., sonicated for 15 min., and then shaken and centrifuged again (same conditions). Supernatant was pipetted into new vials and centrifuged again for 5 min. (same conditions), and then this secondary supernatant was manually injected into the HPLC for analysis.

Mass spectrometry imaging and profiling

All MS and MSI experiments were performed on an UltrafleXtreme MALDI-TOF/TOF MS (Bruker Daltonics, Billerca, MA, USA) equipped with a SmartBeam II frequency-tripled Nd:YAG UV laser. Data was analyzed with FlexAnalysis v3.4 and FlexImaging v3.0. Several modes of instrument operation were explored for brain imaging experiments including positive polarity and linear TOF modes (data not shown), but negative polarity / reflectron mode with m/z 20-2,000 was used to produce the results presented here. For imaging and LC fraction analysis, the laser probe was set to “ultra” spot size (D ~150 µm), 1000 Hz firing rate, 200 shots/spot, and intensity adjusted to ~20% above ionization threshold which varied depending on sample preparation. Images were collected in random row mode at 150 µm pixel size. For CHCA detection limit experiments, a dilution series of CHCA standard (in 100× increments) was prepared in acetone and deposited in wells on a clean stainless steel MALDI target. Instrument parameters were similar to those used for imaging, but a medium laser (D ~100 µm) and random walk mode were used, summing signal from 200 shots/position at 10 positions/spot. Tandem MS was performed with CID disabled, i.e. exclusively post-source decay fragmentation mechanism.

MSI was performed with a variety of laser-desorption methods including LDI (no surface treatment), metal-assisted LDI, and MALDI. For metal-assisted LDI, the tissue surface was sputter-coated for 15 s at 40% power and 60 mTorr argon gas using a Desk II TSC sputter coater equipped with a gold target (Denton Vacuum, Moorestown, NJ, USA), yielding a ~5 nm gold layer. For MALDI, 10 mg/mL matrix solution of either 2,5-DHB or 9-AA in 70:30 EtOH:H_2O was applied by manual pneumatic spray onto the sample in ~10 passes, visibly wetting the tissue and then allowing it to dry between each pass.

Liquid chromatography

Liquid chromatography was performed on a Breeze II HPLC system equipped with a 1525µ binary HPLC pump, 2998 photodiode array detector, 5 µL sample loop with manual injector, and a 4.6 × 75 mm, 3.5 µm spherical particle C-18 column (Symmetry, Waters, Milford, MA, U.S.A.). Separation method was adapted from literature[7] and utilized HPLC water (solvent A) and acetonitrile + 0.5% AcOH (solvent B) for mobile phase. Flow rate was a constant 0.5 µL/min and gradient was as follows: 70% A at 0 min., 50% at 5 min., 10% at 7-9 min., and 70% at 10-11 min. 3D (wavelength-resolved) absorbance data was acquired over a 210-400 nm wavelength range. For confirmation of CHCA by MS, fractions were collected in 1 mL centrifuge vials, dried under vacuum, then reconstituted in 5 µL 1:1 acetonitrile + 0.5% AcOH:H_2O and spotted on a stainless steel MALDI target for analysis.

Fluorescence imaging

To detect and visualize CHCA by native fluorescence microscopy, an untreated tissue section was prepared on a plain microscope slide with CHCA standard spotted under and beside the tissue for reference. An image was acquired using an Axiovert 200M (Carl Zeiss, Inc., Jena, Germany) fluorescence microscope equipped with a DAPI fluorescence filter set (~350 nm excitation max, ~460 nm emission max), a xenon arc lamp, and a high resolution color CCD camera.

RESULTS AND DISCUSSION

The initial goal in this project was to apply MSI in order to visualize the distribution of systemically-administered CHCA within the brains of rat subjects following collaborators' memory assessment test. While efforts are typically taken to minimize CHCA signal in mass spectra when it is used as a MALDI matrix, here we sought to maximize signal as it is the analyte of interest. Since CHCA is an organic acid which assists ionization by proton donation, we hypothesized that it would be best detected in negative ion mode as the MH^- pseudomolecular ion, which may be efficiently produced in the MALDI process without much optimization. This was confirmed by analysis of neat CHCA standard in both positive and negative ion modes as shown in **Figure 9.5**; while signal in positive mode is distributed amongst several related species including salt adducts and multimers, the negative mode spectrum shows a single abundant $[M-H]^-$ ion which is also observed when CHCA is spotted on brain tissue. Thus, while positive mode MS and MSI was investigated (data not shown), negative mode was found to yield superior results overall and was used to acquire the data presented.

Many different sample treatments were attempted for MSI of CHCA in rat brain, with several representative results shown in **Figure 9.6**. To avoid chemical interference by adding additional matrix compounds, imaging by LDI and MetA-LDI was evaluated in a single experiment. While ions were detected by both approaches, much higher laser fluence was necessary for LDI which reduced both mass resolution and peak intensity. MetA-LDI generated more signal with lower fluence, and although the ion image of putative CHCA $[M-H]^-$ at m/z 188 suggested some localization of CHCA in the lower cortex and hippocampus of the brain, it was observed in both dosed and control animals, thus the signal was assigned to chemical interference. Furthermore, characteristic CHCA fragment ions such as m/z 144 were not observed to follow the same distribution in the tissue. MALDI was also attempted in negative ion mode using e.g. 9-AA and 2,5-DHB matrices; while these yielded strong signal from spots of CHCA standard placed on or beside the tissue sections, they did not detect CHCA unambiguously within the tissue itself or yield clear contrast between dosed and control tissue. High quality lipid ion (m/z 807.5, tentatively a glycerophosphocholine) images indicated that good analyte extraction and matrix application was achieved in these experiments, thus it was concluded that CHCA was below detection limits, suppressed by the biological matrix, or is chemically modified with a distinct molecular weight we did not monitor. Increasing CHCA concentration with a 20-fold higher systemic dose and even direct intracranial injection of CHCA into the brain tissue did not result in detectable signal, so subsequent effort was directed at identifying the problem as either inadequate detection limit or significant ion suppression.

To determine the detection limit for CHCA, a standard was diluted serially in acetone and spotted neat on a clean MALDI target. Surface density of CHCA was estimated using the known mass of deposited CHCA and the area of the resulting dried drop, which appeared uniform and circular. Densities ranging from 3 nmol/mm^2 to 300 zmol/mm^2 were produced, and the resulting spectra are shown in **Figure 9.7(a)**. Signal at m/z 188 – assumed CHCA MH$^-$ here – was detected from all densities in nonlinear, decreasing intensity, but a background was also detected from a clean well on the same target, possibly arising from lab contamination (CHCA is used abundantly in our lab) or from nonspecific fragmentation of other residual organic contamination. In either case, these results indicated that the effective negative mode LDI MS detection limit for CHCA at 3:1 above background is ~300 fmol/mm^2. For comparison, an estimate of CHCA density in dosed brain tissue section was calculated (assuming a 0.4 kg adult rat, 1 mL/kg injection volume of 5 mM dose, uniform CHCA distribution between 25 mL blood and 26 g brain tissue, 10 µm tissue section thickness, and ablation fully through tissue by laser probe) to be 7.4 pmol/mm^2. While actual concentration in the brain is likely to be lower, these results suggest that detection limit was not the primary issue preventing CHCA detection. On the other hand, when neat CHCA standard was compared with brain extract spiked with an identical amount of CHCA, ~1,000-fold signal suppression was observed as shown in **Figure 9.7(b)**. Thus, while detection limit may be adequate for the concentrations present, signal is clearly suppressed dramatically by the biological matrix.

CHCA is a natively fluorescent molecule with excitation maximum at ~337 nm (which makes it a suitable UV-MALDI matrix), so fluorescence microscopy offers another method of detection which is “orthogonal” in that it circumvents the complication of ion suppression in MS. To confirm that there were not actually high levels of CHCA present in the brain which were simply being suppressed during ionization, a juvenile rat 100 mM systemic-dosed brain section was imaged by fluorescence microscopy with results shown in **Figure 9.8**. Fluorescence was observed from two spots of CHCA standard placed under and beside the tissue section, but not from anywhere in the tissue itself. CHCA density in the under-tissue spot is estimated to be 5.25 ng/mm^2, so this provides an upper limit to the amount of CHCA present in the tissue and indicates that the problem for MSI is likely a combination of low abundance and ion suppression.

While ion suppression may be addressed in non-imaging MS by simplifying the sample *e.g.* with chromatographic separation, options are more limited with MSI. Tissue washes have been used to remove abundant compounds such as phospholipids and inorganic salts which are known to suppress other compounds, though these can also remove analytes of interest especially in the case of small, diffusible molecules. Selective removal of suppressants can be achieved with careful selection of solvents and/or by pH optimization of washes.[8] Several such tissue wash approaches were evaluated here including ethanol, ammonium acetate, and low-pH ammonium acetate, though none allowed detection of CHCA in any of the brain samples (data not shown).

Thus, in order to provide *some* useful results in this collaborative study, actual liquid chromatographic separation of tissue extract was performed by UV-HPLC. A diode array detector provided 3D chromatographic data as shown for a brain extract in **Figure 9.9**, allowing more confident identification of CHCA by absorbance profile as well as retention time (~4 min), both of which matched a pure CHCA standard. LDI MS analysis of the respective HPLC fraction detected putative CHCA $[M-H]^-$ at m/z 188, and LDI MS/MS confirmed this mass assignment.

HPLC analysis was performed with brain extract, liver extract, and blood serum for a total of eight rats in a blind study, including four CHCA doses - control (saline), 5 mM systemic, 100 mM systemic, and 100 mM intercranial within each age group (juvenile and adult). Preliminary results presented in **Figure 9.10** only include 1-2 technical replicate runs for each sample/dose/age and thus statistical significance cannot be determined without additional experiments, nevertheless several features of the data are consistent with sample identities subsequently provided by collaborators. For example, the strongest CHCA signal was detected from juvenile intercranially-injected brain extract, and collaborators confirmed that the tissue punch was taken ipsilateral with the injection. In contrast, relatively little CHCA was detected in the adult intercranially-injected brain, and in this case the injection and punch were contralateral so the locally-dosed tissue would not have been sampled. Low CHCA levels were measured in both blood and liver extract from both of these animals in comparison with the systemic high-dose (100 mM) counterparts, which suggests that the intercranially-injected CHCA remained locally concentrated at the injection sites in the brain and did not diffuse extensively within the brain, cross the blood-brain barrier to enter the blood stream, or accumulate in the liver in the < 1 h before specimen freezing. Relevant to collaborators' hypotheses, relatively high CHCA was detected in the adult systemic 100 mM rat brain but not in the juvenile counterpart; if significant, this would suggest that the blood-brain barrier prevents CHCA transmission in juveniles but not in adults. It is also important to note that a low level CHCA signal was detected in all samples, more so in brain extracts. Although inter-sample rinse runs indicated no cross-contamination and a procedural blank indicated no lab contamination during the tissue processing steps, this background signal could arise from sample contamination at an earlier stage i.e. during tissue punching and collection, and requires further investigation.

FUTURE DIRECTIONS

The initial goal of visualizing CHCA distribution in rat brain by MSI was not achieved in this work despite attempting multiple approaches, and investigation of the problem indicated a combination of low analyte abundance and significant ion suppression as the underlying cause. To acquire useful data liquid chromatography was employed, yielding preliminary data which is consistent with subject treatments and may also provide useful information for the collaborators' behavioral study with ample biological replicates.

SECTION 9-3: SAMPLE PREPARATION FOR MALDI MSI OF LIPIDS AND PEPTIDES IN RAT SPINAL CORD

INTRODUCTION

In this work, MSI was applied to probe the chemical changes occurring in the mammalian (rat) spinal cord in response to acute noxious stimulus *via* the formalin pain test.[9] Immunohistological staining of spinal cord sections after such a test by Zhang et al. revealed a slight increase in several neuropeptides in the ipsilateral to the formalin injection in the dorsal horn where peripheral and central nerves connect, but the results of this work were limited to visualization of known and targeted biomolecules.[10] MSI with MALDI is a technique capable of detecting all of these analytes simultaneously in theory, and current commercial instrumentation allows lateral spatial resolution of <50 µm which is sufficient to resolve relevant anatomical features such as the dorsal and ventral horns. Previous work in the Sweedler research group by Monroe et al. includes MSI and identification (by LC-MS/MS) of several dozen constituents in this tissue and thus provides a basis for identification in the current study as well as established sample preparation methods.[1] Thus, here we sought to use this basis to survey the changes associated with acute pain which occur within the mammalian spine, i.e. at the peripheral-central nervous system interface. Peptide changes were anticipated as peptides such as Substance P are known to be involved in neuromodulation at this location,[10] but lipids are also a molecular class of interest which have been recently implicated in noxious signaling mechanisms,[11] thus methods were developed for imaging both lipids and peptides, and preliminary data presented.

EXPERIMENTAL METHODS

Materials and chemicals

2,5-dihydroxybenzoic acid (DHB), α-cyano-4-hydroxycinnamic acid (CHCA), and HPLC-grade solvents including acetone, chloroform, and acetic acid (AcOH) were purchased from Sigma-Aldrich (St. Louis, MO, USA). Deionized water was prepared by Millipore filtration at Beckman Institute. Solvent mixtures were prepared in lab, including Carnoy's solution which is composed of 60% ethanol, 30% chloroform, and 10% glacial acetic acid. 25 × 75 × 1.1 mm Indium tin oxide (ITO)-coated microscope slides were purchased from Delta Technologies, Ltd. (Loveland, CO, USA). A sublimation chamber was fabricated by the SCS glass shop in the style of the apparatus described by Hankin et al.[2] but with an additional side-port feedthrough allowing for accessories such as a thermocouple or direct heating device to be added to the chamber. A labeled photograph of this apparatus is shown in Appendix B of this thesis.

Biological sample preparation

Adult male Long-Evans rats (Harlan, Indianapolis, IN, USA) were used for the vertebrate animal experiments. Animal care protocols and procedures were approved by the UIUC Laboratory Animal Care Advisory Committee and fully comply with federal guidelines for the humane care and treatment of animals. The formalin pain test is described in detail elsewhere.[9] Briefly, 30 min. after injection of formalin solution into the right hindpaw of the animal it was decapitated, the spinal cord was isolated, rapidly frozen with dry ice to retard decomposition, enzymatic digestion, and chemical diffusion, and stored wrapped in foil and sealed in a plastic bag at -80° C until use. A control animal was treated identically but with a saline injection in place of formalin. ~1 cm segments of the cord were excised from the region immediately anterior to the dorsal root ("proximal" sections) connecting the hindpaw nociceptors, and in some cases also from a region of the cord 1-2 cm rostral of this location ("rostral" sections) for an additional control/comparison. Careful attention was paid to maintaining rostral/caudal cord orientation and identities throughout sample preparation.

To collect tissue sections for imaging, a procedure was precisely defined as follows:

1. Prepare ice mount on cryotome stage (deposit 2-3 mL water in center of clean mount, allow to freeze, then trim to create flat face), label back of stage with identifier.
2. Label and pre-cool one or more ITO-coated microscope slides (keep ITO face up!)
3. Move cord specimens from -80° C freezer to the cryotome rapidly, allow 30 min. to warm.
4. Freeze-mount cord segments rostral face-out side-by-side and level on stage by positioning them at the surface and adding a small amount of extra water. Allow water to refreeze.
5. Mount stage in cryotome, trim until level cutting surfaces are obtained (~1-2 mm)
6. Collect one 12 µm-thick tissue section from each cord, transfer to slide surface with brush (track identities and preserve rostral-up orientation! Be careful not to flip section.)
7. Thaw-mount sections to slide by warming with finger from below, then allow to refreeze.
8. Repeat steps 10-12 as necessary. Mount additional sections horizontally across the slide.
9. Include one spare section in roughly the center of the slide for on-tissue mass calibration.
10. Re-wrap sample in foil and seal in bag, return to -80 C freezer rapidly.

Chemical treatments for MALDI MSI

For peptide imaging, tissue sections were first treated with one or more chemical washes by submerging the entire microscope slide (with tissue sections) into a slowly-gyrating (0.5-1 RPM) Petri dish for a specified duration, then removing and rapidly blowing dry with a gentle stream of dry nitrogen gas before either proceeding to another wash step or to matrix application. Three wash procedures were tested here:

- One 30 sec. wash in ethanol
- Two 30 sec. washes in ethanol
- One 30 sec. wash in ethanol followed by one 2 min. wash in Carnoy's solution

The double ethanol wash was found to be most reliable and effective for peptide imaging. Following chemical wash(es), the dried sections were coated with matrix by either pneumatic spray (manual airbrush) or by matrix sublimation. For pneumatic spray, 20 mL of 10 mg/mL CHCA was prepared in 1:1 H_2O:acetone + 0.1% AcOH and ~3 mL was loaded into a Paasche airbrush. Using 20 PSI N_2 as propellant, tissue sections mounted on ITO-coated microscope slide were clamped vertically and coated to wetness by airbrushing from ~10 cm distance. Once the tissue dried, another coating was applied; coatings were repeated until the ~3 mL loaded matrix solution was consumed. This resulted in a nearly-opaque coating of matrix over the microscope slide and tissue sections. For matrix sublimation, CHCA was applied using the apparatus and procedure provided in Appendix B of this thesis. A subsequent recrystallization step was also applied to improve peptide ion signal, performed precisely as described by Yang et al.[12] for 3.75 min. duration in a condensation chamber with 1 mL H_2O + 5% AcOH at 85° C.

Chemical treatment for lipid imaging

For lipid imaging, tissue sections were first washed in aqueous 50 mM, pH 6.7 ammonium acetate (AmAc) solution by dipping the slide vertically for 3x 5 sec, blowing dry with a gentle N_2 stream, before 2,5-DHB matrix sublimation by the procedure provided in Appendix B of this thesis.

Mass spectrometry imaging

All MS and MSI experiments were performed on an UltrafleXtreme MALDI-TOF/TOF MS (Bruker Daltonics, Billerca, MA, USA) equipped with a SmartBeam II frequency-tripled Nd:YAG UV laser. Data was analyzed with FlexAnalysis v3.4 and FlexImaging v3.0. Images and spectra were typically acquired in positive ion / reflectron mode, *m/z* 20-5000 range, "minimum" laser spot size (*i.e.* maximum focus, ~35 µm spot diameter), power adjusted to 20% above ionization threshold, 200 shots/position at 1000 Hz, and 50-100 µm x/y image step size. Ion images were generated with ±0.25 Da mass filters and typically normalized to total ion count

(TIC) except where indicated otherwise. Quadratic mass calibration was performed using a peptide standard mixture spanning from ~500-2500 Da, spotted on a spare tissue section in order to account for height offset.

RESULTS AND DISCUSSION

Initial effort focused on peptide imaging in order to validate MSI procedure by first reproducing previously reported results, *i.e.* an ipsilateral increase in substance P (SP), neurotensin (NT), calcitonin gene-related peptide, somatostatin, and Met-enkephalin in the dorsal horn.[10] **Figure 9.11** shows the best results from these experiments in terms of signal and image quality. Here three technical replicates each of one formalin-treated and one control spine were imaged in a single experiment, and multiple peptides including SP and NT – two target analytes - were detected and imaged. While these peptides generally showed the expected dorsal horn localization, a high amount of variation was observed across the replicates. It is unlikely that this is biologically significant variation, and more likely that it arose from uneven matrix application by manual airbrush. Results were generally found to be highly irreproducible between experiments with airbrush matrix application as well, with peptide signal (for technical replicates using adjacent tissue sections) ranging from good to undetectable. Therefore, subsequent effort shifted to improving sample preparation and particularly matrix application in order to improve consistency and reduce artifactual signal variation in image results.

In place of airbrush matrix application, vacuum sublimation of matrix was adapted for this work to address reproducibility and coating consistency issues. Sublimation yields highly uniform coatings of fine (micron-sized) matrix crystals which makes it well-suited for high resolution MSI work.[2] With the apparatus and procedure developed here (described in Appendix B), sublimation was found to produce exceptionally consistent matrix coatings in the present study. Peptides were not initially detectable with sublimed matrix (likely due to the fact that they must be efficiently extracted from the tissue, and this does not occur with a “dry” matrix application method such as sublimation), but became detectable with good signal following a subsequent recrystallization step and adequate removal of lipids. Several tissue wash and recrystallization variations were compared for the latter purpose, with results shown in **Figure 9.12**. Best results overall were obtained with two 30-second immersions in an oscillating ethanol bath; although lipids were most completely removed by an aggressive wash including both ethanol and Carnoy's solution, this also reduced peptide signal (likely due to removal of peptides as well) and appeared to damage the tissue section. A second recrystallization cycle was also found to not improve signal beyond the first cycle.

Typical spine imaging results using the matrix sublimation / recrystallization preparation (with double ethanol rinse and single recrystallization) are shown in **Figure 9.13**, where three technical replicates each of Formalin- and control-treated spine were again imaged in a single experiment. Peptide signal intensities were generally lower than those observed with *optimal* airbrush results, though overall peptide image quality, intra-run consistency, and run-to-run consistency all improved markedly. Relative quantitation was attempted from MSI results with the strongest peptide signal, that of SP, which was previously reported to increase in the ipsilateral dorsal horn following acute pain. The pixels from all three replicates were pooled by dorsal horn (control ipsilateral/contralateral and formalin ipsilateral/contralateral), SP signal intensities were averaged for each horn, and two-tailed heteroscedastic t-tests were applied to compare all four horns with each other with results shown in **Figure 9.13(b)**. Pooled SP level was significantly different in *every* dorsal horn relative to all others by this measure, though the ipsilateral dorsal horns show higher SP than the contralateral counterparts in both the Formalin-treated and control spines, with the ipsilateral control dorsal horn showing the highest SP levels of all. These results are ambiguous in meaning; the significance of the measured SP levels could be "real" *i.e.* biologically higher in the ipsilateral dorsal horn even for the water injection, or it could be artifactual. Dorsal horn regions of interest were manually drawn based on light microscope images of the spinal cord sections, and the accuracy of these boundaries would certainly affect the SP intensity averages; a liberally-defined region may include many non-horn pixels with no SP, thus reducing the average. Repeating the experiment especially with biological replicates could clarify this ambiguity.

Lipids were also studied by MALDI MSI in this project, as other recent reports found that certain lipids were involved in similar pain responses.[11] Although identifying specific lipids is a challenging task requiring (for unsaturated species) additional steps *e.g.* analyte derivitization for GC-MS and/or online ozonolysis,[13] partial characterization in terms of head group and combined fatty acid tail lengths (termed "lipid groups" here) can be accomplished with high resolution mass spectrometry, and may be useful as a first screening for analytes of interest. A sample preparation protocol was adapted from various literature reports to consistently yield good lipid signal intensity and image quality, and this was then applied to the Formalin test specimens as a non-targeted lipid survey for pain-induced changes within the spine. Results from one lipid imaging experiment are shown in **Figure 9.14(a)**. While two lipid groups (m/z 806.5, PC(36:0) and 834.5, PC(40:6)) appear relatively uniform between formalin-treated and control spine as well as rostral and proximal positions within the spine, a third lipid group (m/z 734.5) appears lower in both Formalin-treated spine sections relative to both controls. A similar trend was observed in a previous experiment with two different rats (shown in **Figure 9.14(b)**), suggesting that this may be a true biological change; additional biological replicates are required to confirm. There are also many possible lipids at m/z 734.5 including PC(32:0), PE(36:0), and PS(32:1) which could be unsaturated in several dozen positions, thus fully understanding this data would require additional lipid characterization, beginning with tandem MS which could determine head group and fatty acid chain lengths.

FUTURE DIRECTIONS

Robust sample preparation methods were developed and applied for MALDI MSI of peptides and lipids in the mammalian spinal cord. These methods could likely be effective for similar tissue types including brain and non-mammalian nervous tissues *e.g.* with *Aplysia californica*. Initial results obtained with these methods offer promising leads for pain-related chemical changes within the spine, so future work might confirm these findings through additional biological replicates and proper data analysis. Addition of internal standard to the tissue sections may assist quantitation efforts,[14] while microdrop matrix printing (improved by sheath gas as described earlier in the chapter) may improve peptide signal intensity through increased extraction and reduce artifactual signal variability *e.g.* by allowing more laser shots per pixel in a random walk pattern, as others have demonstrated to be effective.[15]

REFERENCES

1. Monroe, E. B.; Annangudi, S. P.; Hatcher, N. G.; Gutstein, H. B.; Rubakhin, S. S.; Sweedler, J. V., SIMS and MALDI MS imaging of the spinal cord. *PROTEOMICS* **2008,** *8* (18), 3746-3754.
2. Hankin, J. A.; Barkley, R. M.; Murphy, R. C., Sublimation as a Method of Matrix Application for Mass Spectrometric Imaging. *Journal of the American Society for Mass Spectrometry* **2007,** *18* (9), 1646-1652.
3. Groseclose, M. R.; Andersson, M.; Hardesty, W. M.; Caprioli, R. M., Identification of proteins directly from tissue: in situ tryptic digestions coupled with imaging mass spectrometry. *Journal of Mass Spectrometry* **2007,** *42* (2), 254-262.
4. Shimma, S.; Furuta, M.; Ichimura, K.; Yoshida, Y.; Setou, M., Direct MS/MS analysis in mammalian tissue sections using MALDI-QIT-TOFMS and chemical inkjet technology. *Surface and Interface Analysis* **2006,** *38* (12-13), 1712-1714.
5. Delvolve, A. M.; Woods, A. S., Optimization of automated matrix deposition for biomolecular mapping using a spotter. *Journal of Mass Spectrometry* **2011,** *46* (10), 1046-1050.
6. Newman, L. A.; Korol, D. L.; Gold, P. E., Lactate Produced by Glycogenolysis in Astrocytes Regulates Memory Processing. *PLoS ONE* **2011,** *6* (12), e28427.
7. Sampedro, M. C.; Unceta, N.; Gómez-Caballero, A.; Callado, L. F.; Morentin, B.; Goicolea, M. A.; Meana, J. J.; Barrio, R. J., Screening and quantification of antipsychotic drugs in human brain tissue by liquid chromatography-tandem mass spectrometry: Application to postmortem diagnostics of forensic interest. *Forensic Science International* **2012,** *219* (1-3), 172-178.
8. Shariatgorji, M.; Källback, P.; Gustavsson, L.; Schintu, N.; Svenningsson, P.; Goodwin, R. J. A.; Andren, P. E., Controlled-pH tissue cleanup protocol for signal enhancement of small molecule drugs analyzed by MALDI-MS imaging. *Analytical Chemistry* **2012,** *84* (10), 4603-4607.
9. Dubuisson, D.; Dennis, S. G., The formalin test: A quantitative study of the analgesic effects of morphine, meperidine, and brain stem stimulation in rats and cats. *Pain* **1977,** *4* (0), 161-174.
10. Zhang, R.-X.; Mi, Z.-P.; Qiao, J.-T., Changes of spinal substance P, calcitonin gene-related peptide, somatostatin, Met-enkephalin and neurotensin in rats in response to formalin-induced pain. *Regulatory Peptides* **1994,** *51* (1), 25-32.
11. Patti, G. J.; Yanes, O.; Shriver, L. P.; Courade, J.-P.; Tautenhahn, R.; Manchester, M.; Siuzdak, G., Metabolomics implicates altered sphingolipids in chronic pain of neuropathic origin. *Nat Chem Biol* **2012,** *8* (3), 232-234.
12. Yang, J.; Caprioli, R. M., Matrix Sublimation/Recrystallization for Imaging Proteins by Mass Spectrometry at High Spatial Resolution. *Analytical Chemistry* **2011,** *83* (14), 5728-5734.
13. Thomas, M.; Mitchell, T.; Blanksby, S., OnLine Ozonolysis Methods for the Determination of Double Bond Position in Unsaturated Lipids. In *Lipidomics*, Armstrong, D., Ed. Humana Press: 2009; Vol. 579, pp 413-441.
14. Pirman, D. A.; Reich, R. F.; Kiss, A.; Heeren, R. M. A.; Yost, R. A., Quantitative MALDI Tandem Mass Spectrometric Imaging of Cocaine from Brain Tissue with a Deuterated Internal Standard. *Analytical Chemistry* **2012,** *85* (2), 1081-1089.
15. Hanrieder, J.; Ekegren, T.; Andersson, M.; Bergquist, J., MALDI imaging of post-mortem human spinal cord in amyotrophic lateral sclerosis. *Journal of Neurochemistry* **2013,** *124* (5), 695-707.

FIGURES

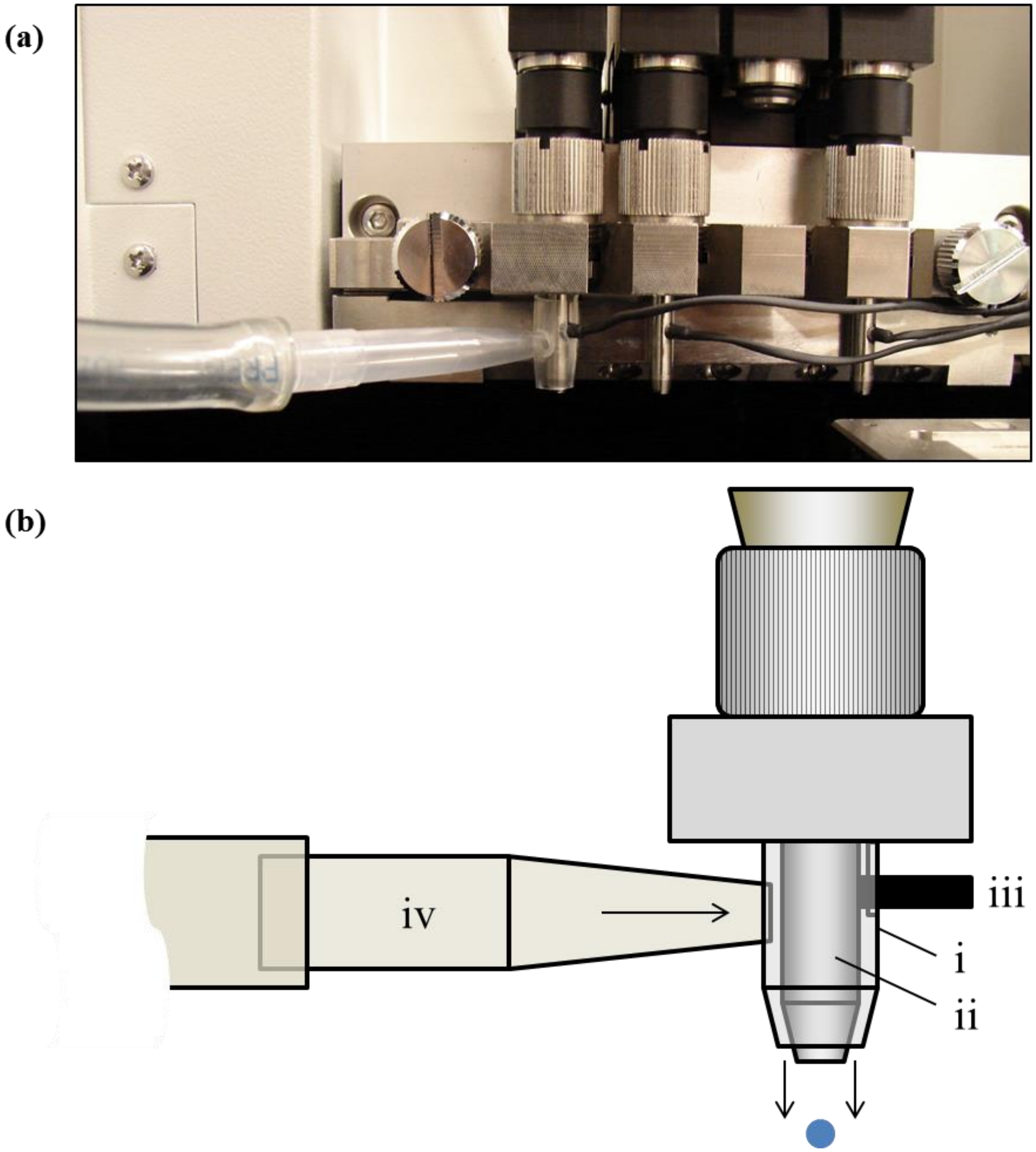

Figure 9.1: Modified chemical inkjet printhead. (a) Photograph and **(b)** schematic of Piezo print head modified with sheath flow adapter. Labeled components include (i) sheath gas nozzle with cutouts for electrical cable and gas inlet, (ii) Piezo print head nozzle, (iii) Piezo electrical control cable, and (iv) sheath gas supply line comprised of tygon tubing connected *via* modified pipette tip.

(a) Untreated Section

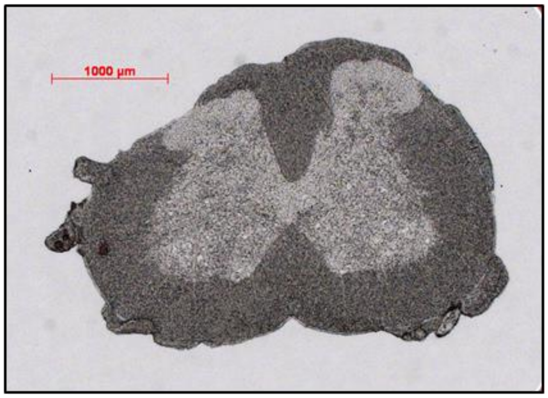

(b) Without Sheath Gas

(c) With Sheath Gas

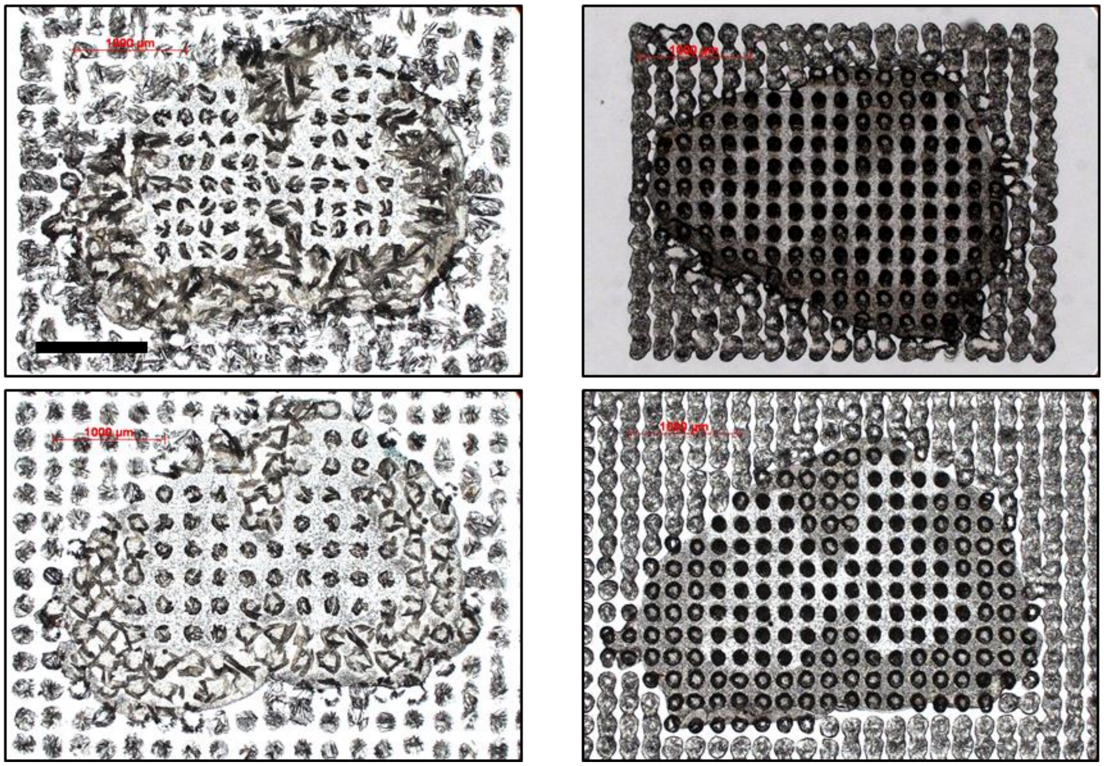

Figure 9.2: Comparison of tissue sections printed with matrix with and without N_2 sheath gas. Bright field optical microscope images of **(a)** Untreated (top) section is compared with four separate sections printed **(b)** without *vs* **(c)** with N_2 sheath gas enabled on the ChIP-1000. Scale bar = 1 mm.

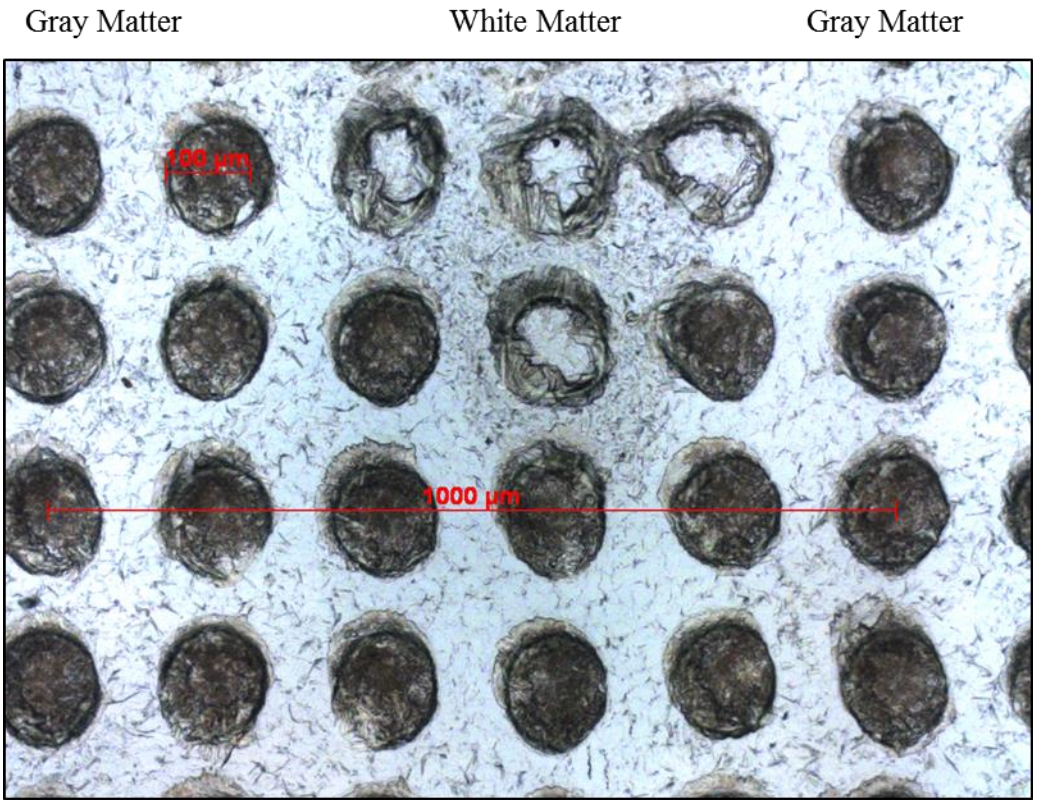

Figure 9.3: Detail of microspot array printed on spinal cord with N_2 sheath gas. Droplets appear to dry into solid disks on gray matter while on white matter hollow rings are formed. Good droplet isolation is observed on both tissue types.

Figure 9.4: Hippocampal brain punch placement. Optical image showing location of brain sections for MSI, as well as tissue punch location for HPLC measurements.

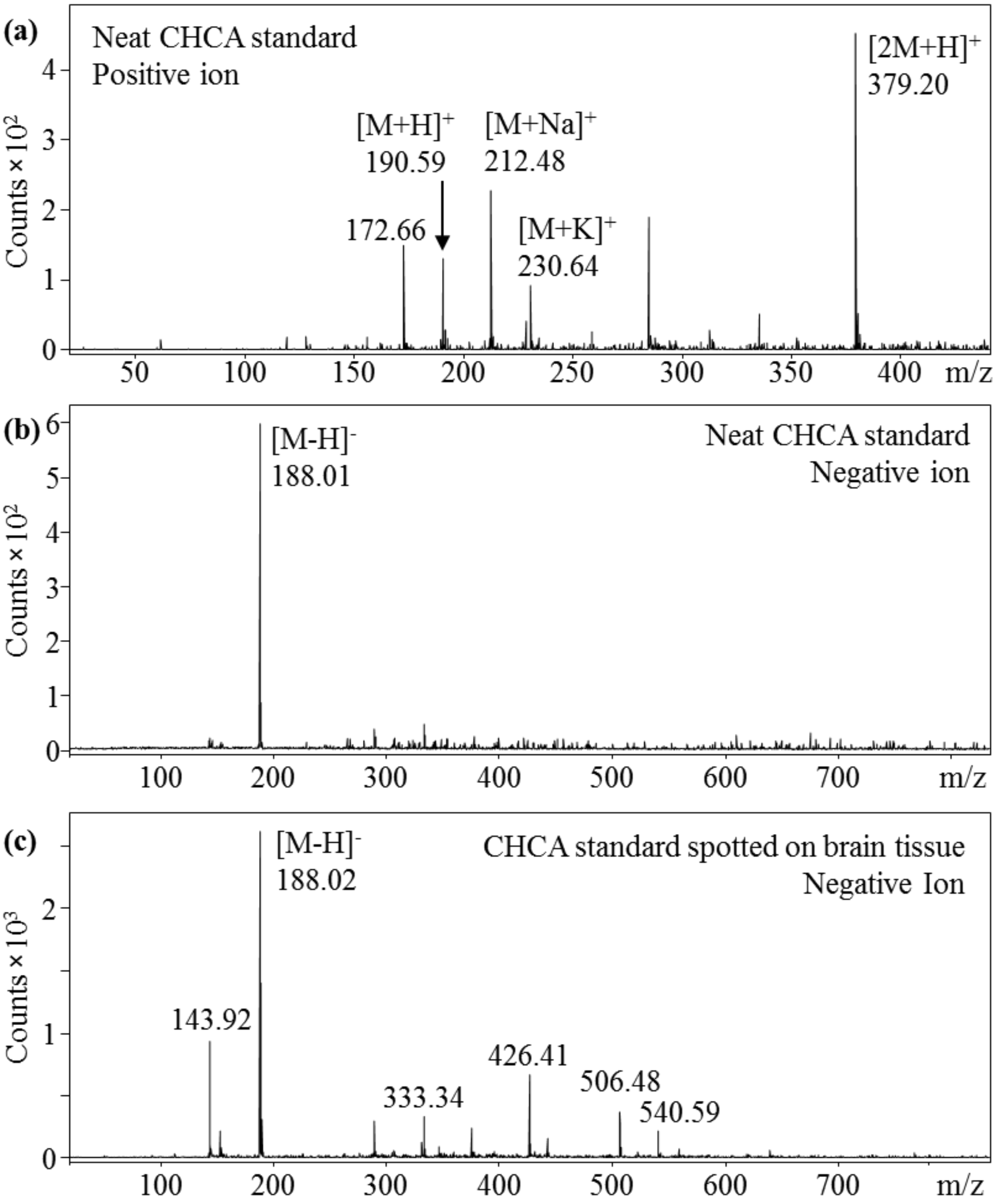

Figure 9.5: LDI MS detection of CHCA in positive and negative ion modes. Neat CHCA standard in acetone was spotted on a stainless steel MALDI target and analyzed by LDI. **(a)** In positive mode signal is distributed amongst several pseudomolecular ions including salt adducts and clusters, whereas **(b)** in negative mode, a single MH^- species yields intense signal. **(c)** The same ion is also observed when CHCA standard is spotted on brain tissue.

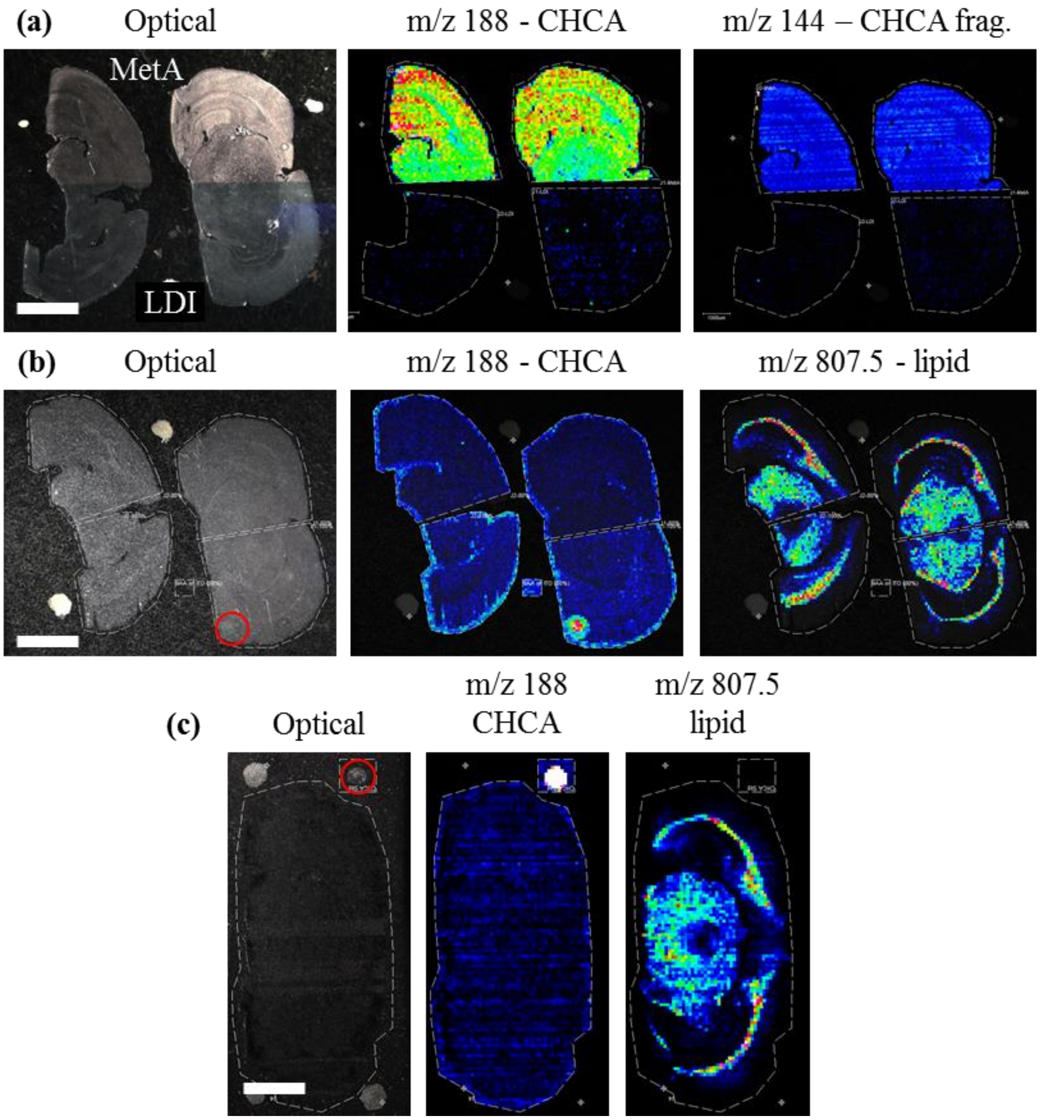

Figure 9.6: MSI of CHCA in rat brain. Two juvenile rat brain sections (control and 5 mM systemic) were **(a)** half-coated with gold and imaged by MetA-LDI and LDI in a single experiment. Ion images for CHCA MH$^-$ (m/z 188) and characteristic fragment (m/z 144) are shown. **(b)** Similar sections were coated with 9-AA and imaged by MALDI; CHCA was clearly detected from a standard spot under the tissue (red circle) and possibly around the tissue periphery, but not inside. A lipid ion (m/z 807.5) image indicates good matrix application. **(c)** MALDI MSI with 2,5-DHB was performed on a 100 mM systemic adult brain section with similar results; CHCA was clearly detected in a standard spot off-tissue, but not on tissue. Scale bars = 2 mm.

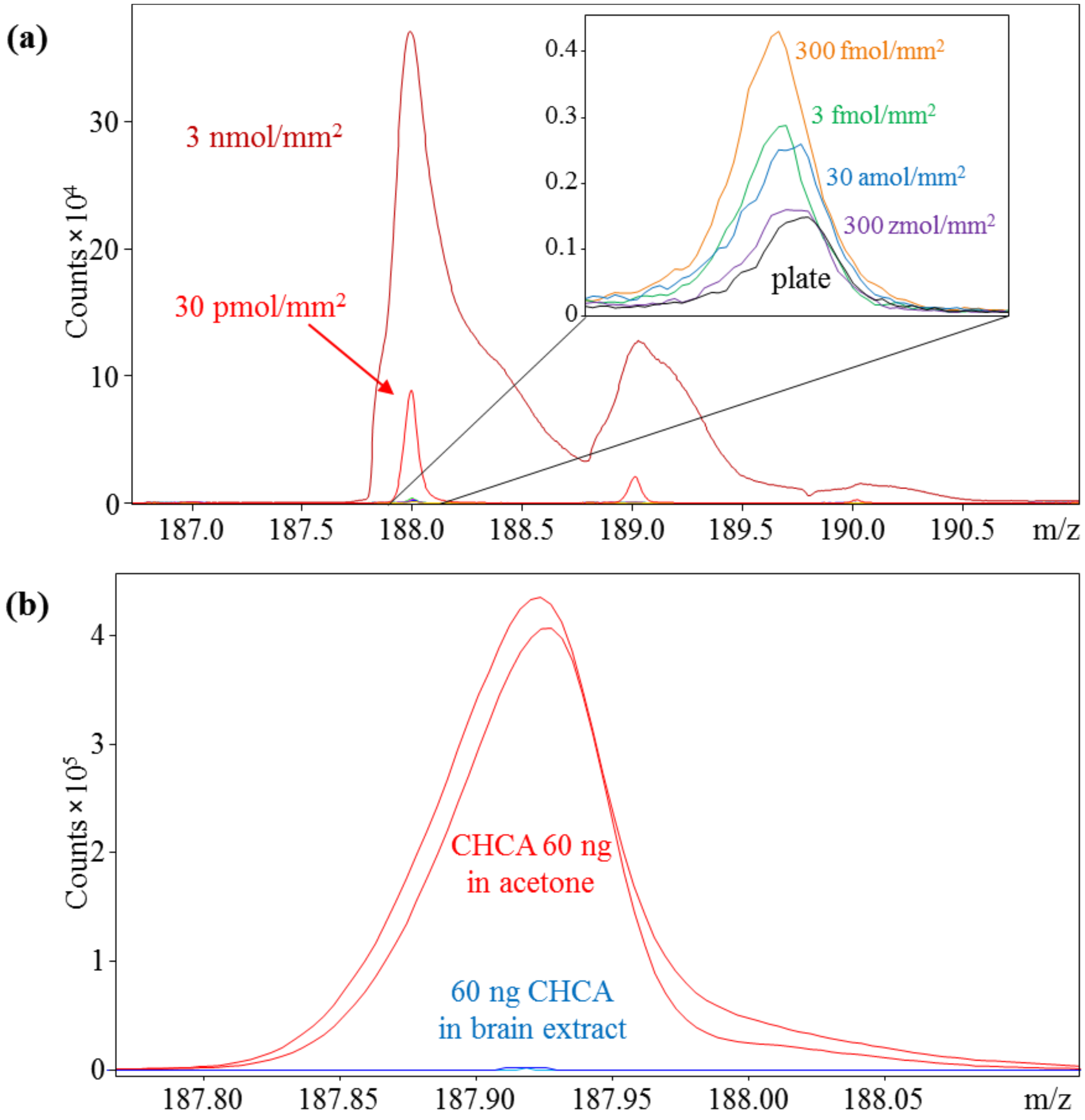

Figure 9.7: LDI profiling of CHCA standard and CHCA-spiked brain extract. (a) LDI MS spectra of CHCA standard dilution series indicate that CHCA is detectable down to amol/mm^2 surface density, below which the MALDI plate background may conceal the signal. **(b)** Comparison of neat CHCA standard (red traces) and rat brain extract spiked with a similar amount (blue traces) indicates signal suppression by ~1,000-fold due to biological matrix.

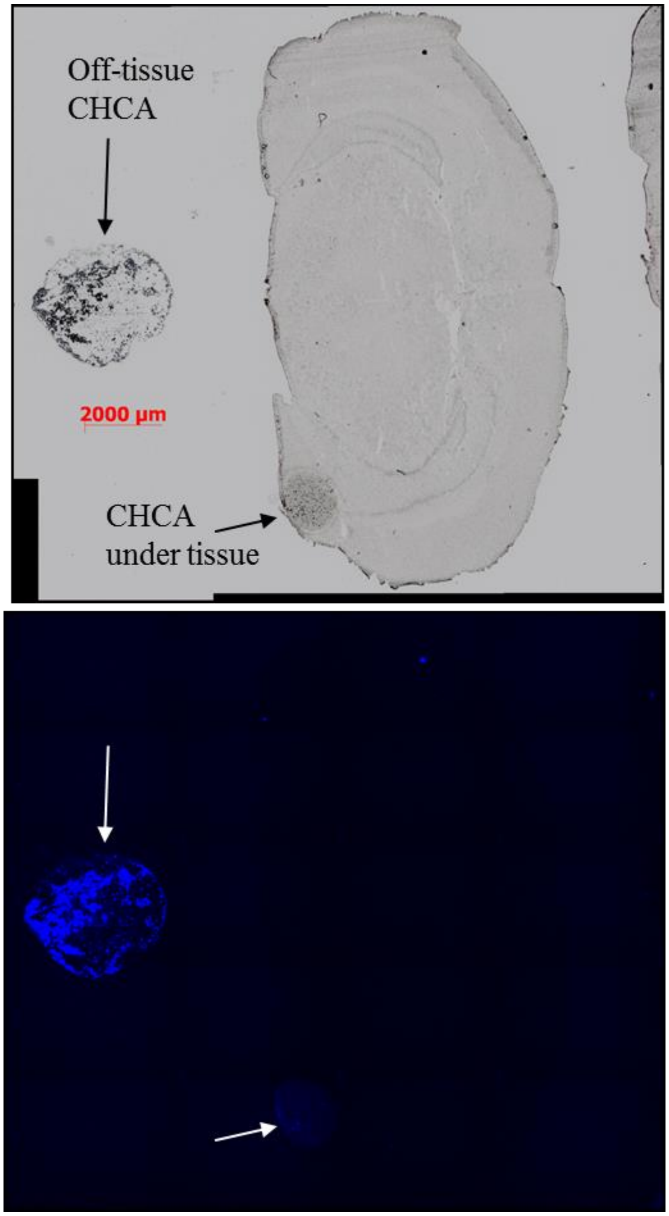

Figure 9.8: Native fluorescence detection of CHCA. A juvenile 100 mM systemic-dosed brain section was inspected along with spots of CHCA standard under and beside the tissue, visible in the bright field optical (top) and fluorescence images (bottom). Fluorescence is observed from both standard spots but not elsewhere in the tissue. Scale bar = 2 mm.

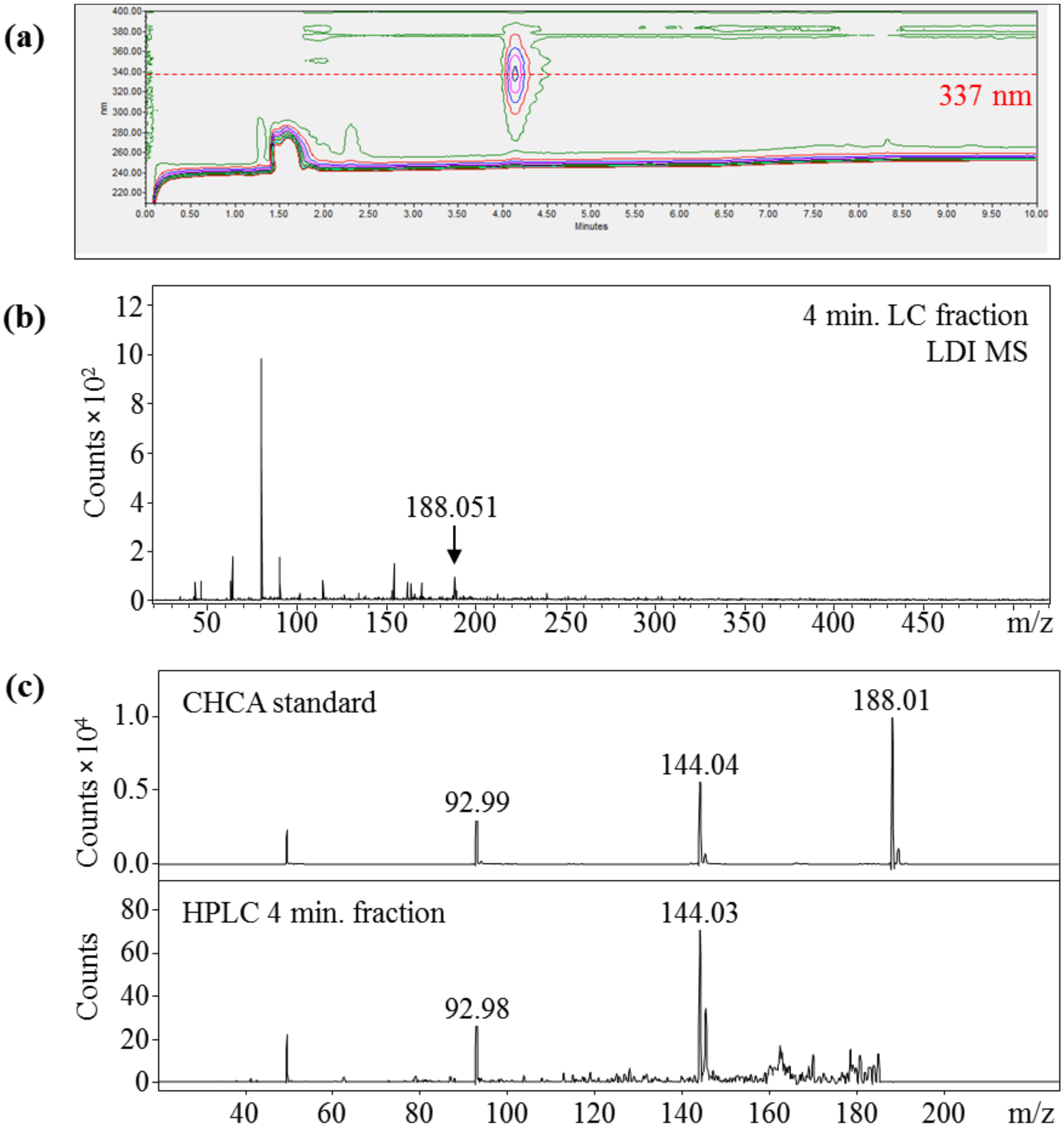

Figure 9.9: Detection and confirmation of CHCA in rat brain by UV-absorbance HPLC and LDI MS/MS. (a) 3D contour chromatogram of extract from intracranially-dosed adult rat brain shows a peak at ~4 min. with A_{max} = 337 nm, consistent with CHCA standard retention time and maximum absorbance wavelength under identical conditions. **(b)** LDI MS of the 4-4.5 min. fraction detects putative CHCA MH^- at m/z 188, and **(c)** LDI-MS/MS confirms this assignment with comparison to CHCA standard.

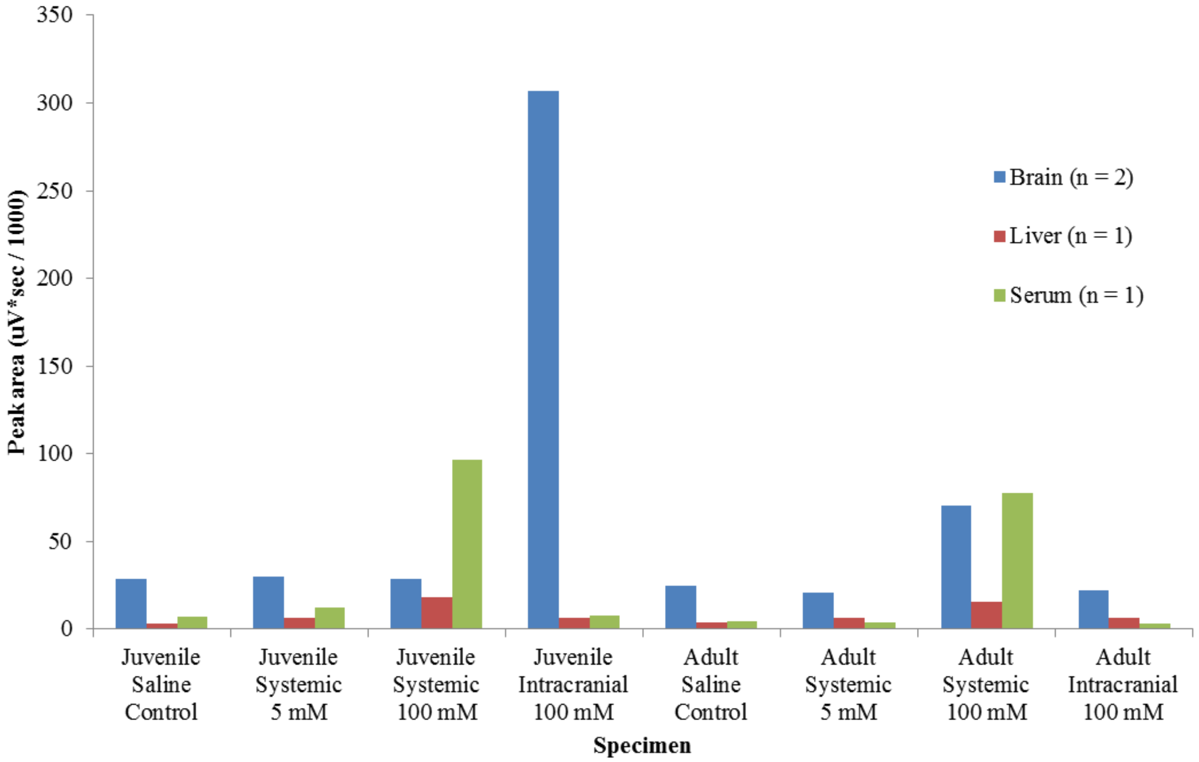

Figure 9.10: Preliminary relative CHCA quantitation in rat brain, liver, and blood serum by UV-HPLC. Relative CHCA amount was estimated by chromatograph peak area integration in the 337 nm wavelength channel. Two technical replicates were run for brain samples, while a single run was performed for liver and blood.

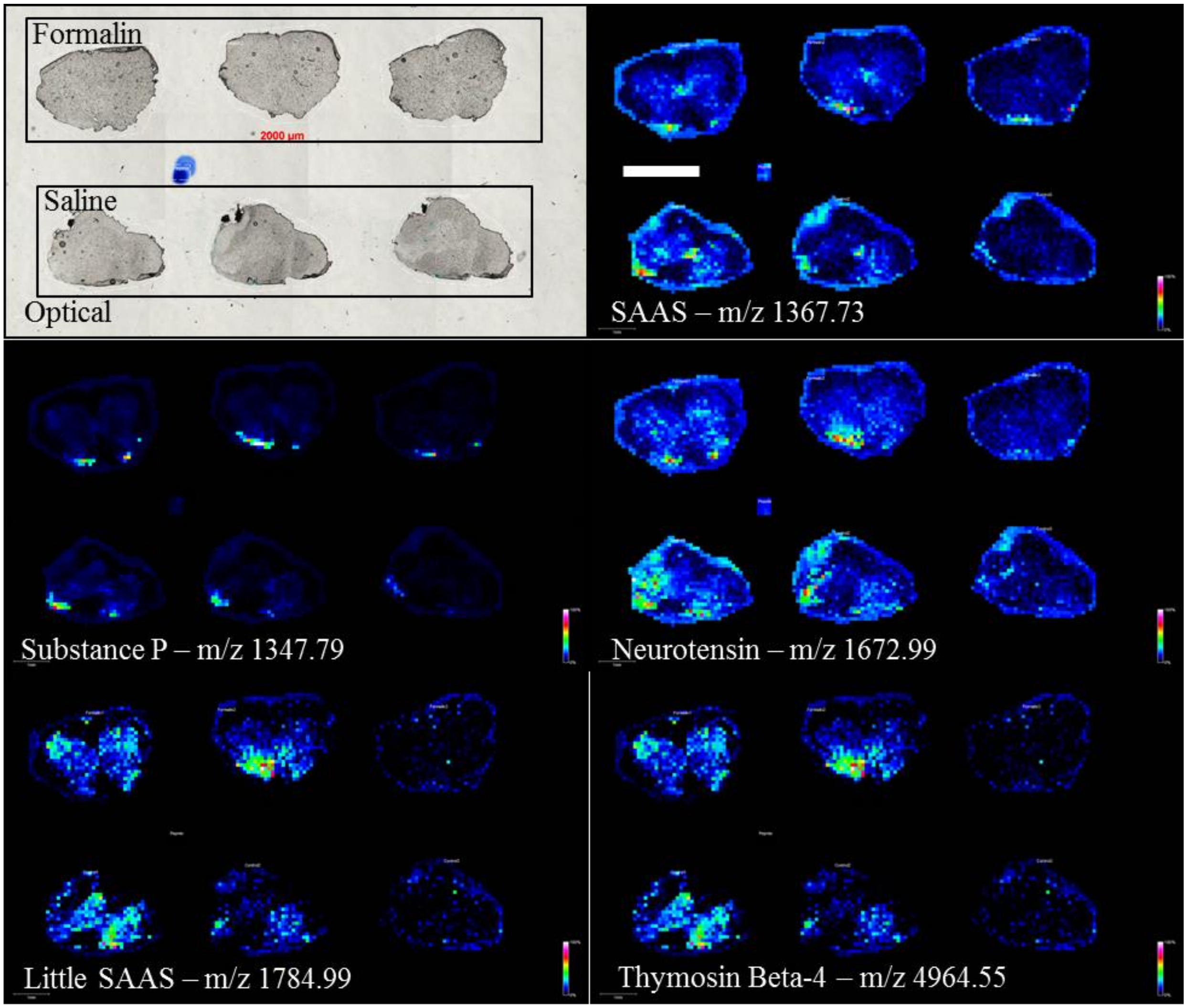

Figure 9.11: MALDI MSI of peptides in spinal cord of formalin-treated *vs* control rats, prepared by manual pneumatic spray (airbrush). Three technical replicates (adjacent tissue sections) were imaged from a single Formalin-treated (top row) and control (bottom row) animal. All images TIC-normalized. Scale bar = 2 mm.

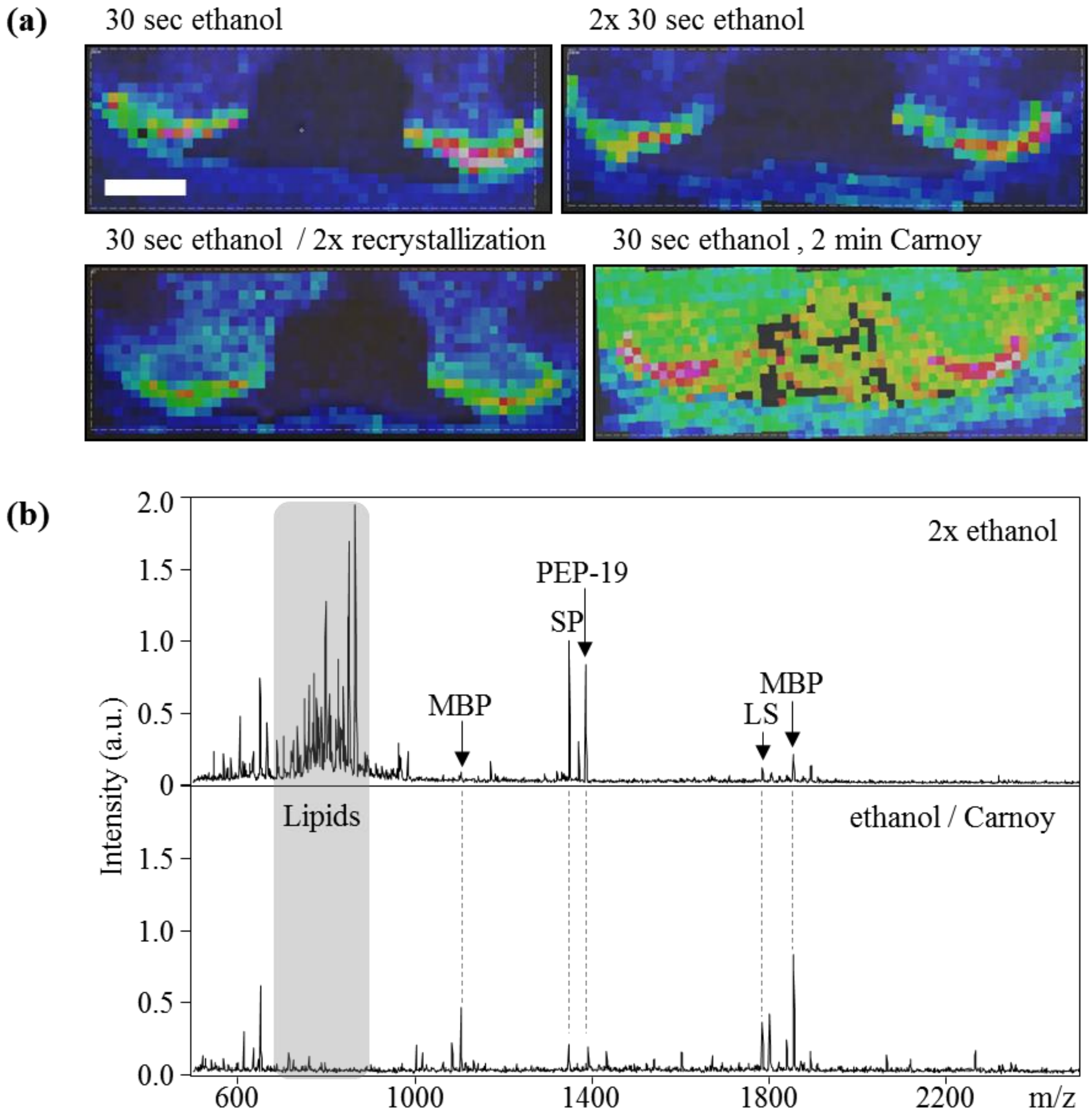

Figure 9.12: Comparison of tissue wash treatments for MALDI MSI of peptides in spinal cord. (a) MALDI MS ion images of substance P in the dorsal horns after various tissue treatments: single ethanol wash, double ethanol wash, single ethanol wash with double recrystallization, and single ethanol wash followed by 2 min Carnoy's solution wash. Wash time was 30 sec and single crystallization step were used except where noted. All ion images RMS-normalized. Scale bar = 0.4 mm. **(b)** Representative single pixel MS spectra from double ethanol and ethanol/Carnoy wash preparations, with general lipid range and several peptides labeled including myelin basic protein (MBP), substance P (SP), PEP-19, and little SAAS (LS).

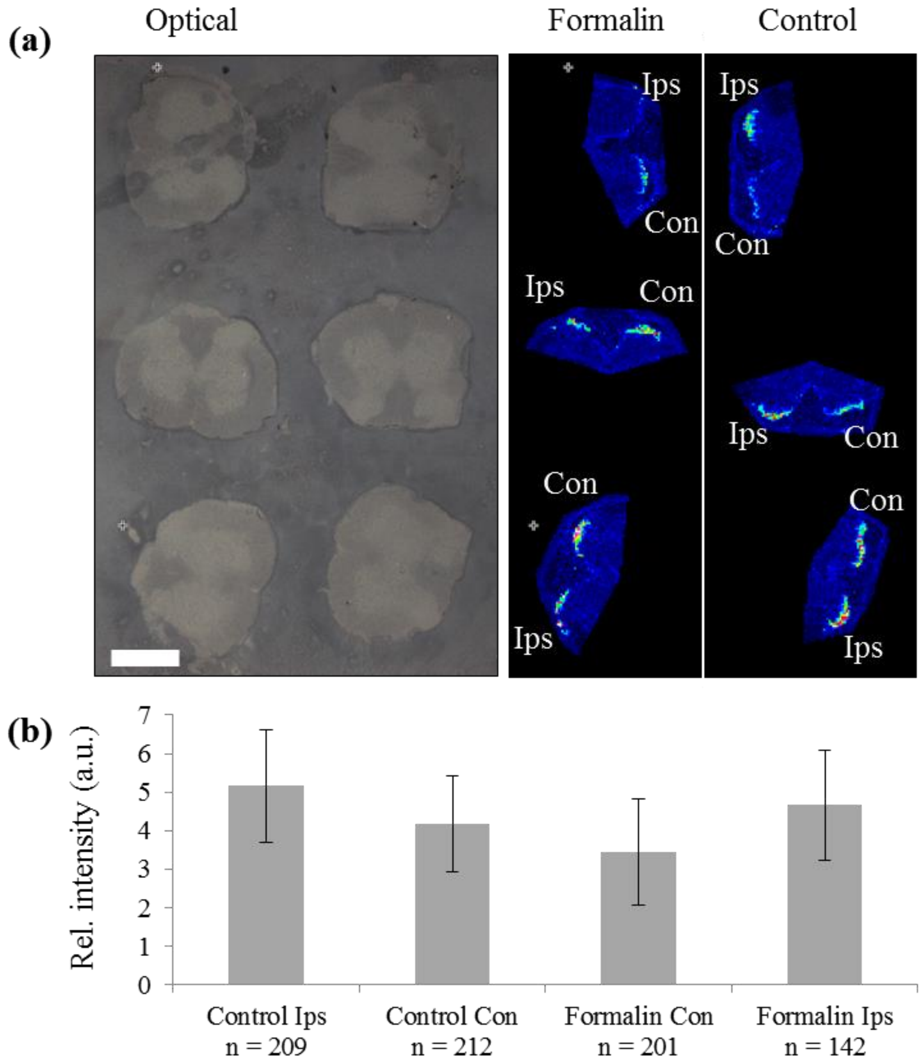

Figure 9.13: MALDI MSI of peptides in spinal cord of formalin-treated *vs* control rats, prepared by sublimation/recrystallization. (a) Optical image of tissue sections after matrix sublimation/recrystallization (left) and ion images of substance P (SP) acquired by MALDI MSI (right), divided into Formalin-treated sections and control sections, with three technical replicates (adjacent tissue sections) of each. Ipsilateral ("Ips") and contralateral ("con") sides are labeled for each section w.r.t. the paw of formalin/saline injection. Only the dorsal horns of each section were imaged in order to reduce time and instrument wear, and tissue sections were oriented at different angles to address the possibility of directional signal bias e.g. due to a slight gradient of sublimed matrix coating thickness. Ion images normalized to TIC. Scale bar = 1 mm. **(b)** Graph of averaged relative SP ion intensity for each dorsal horn region. N for each class represents number of pooled image pixels, and 95% CI bars are shown.

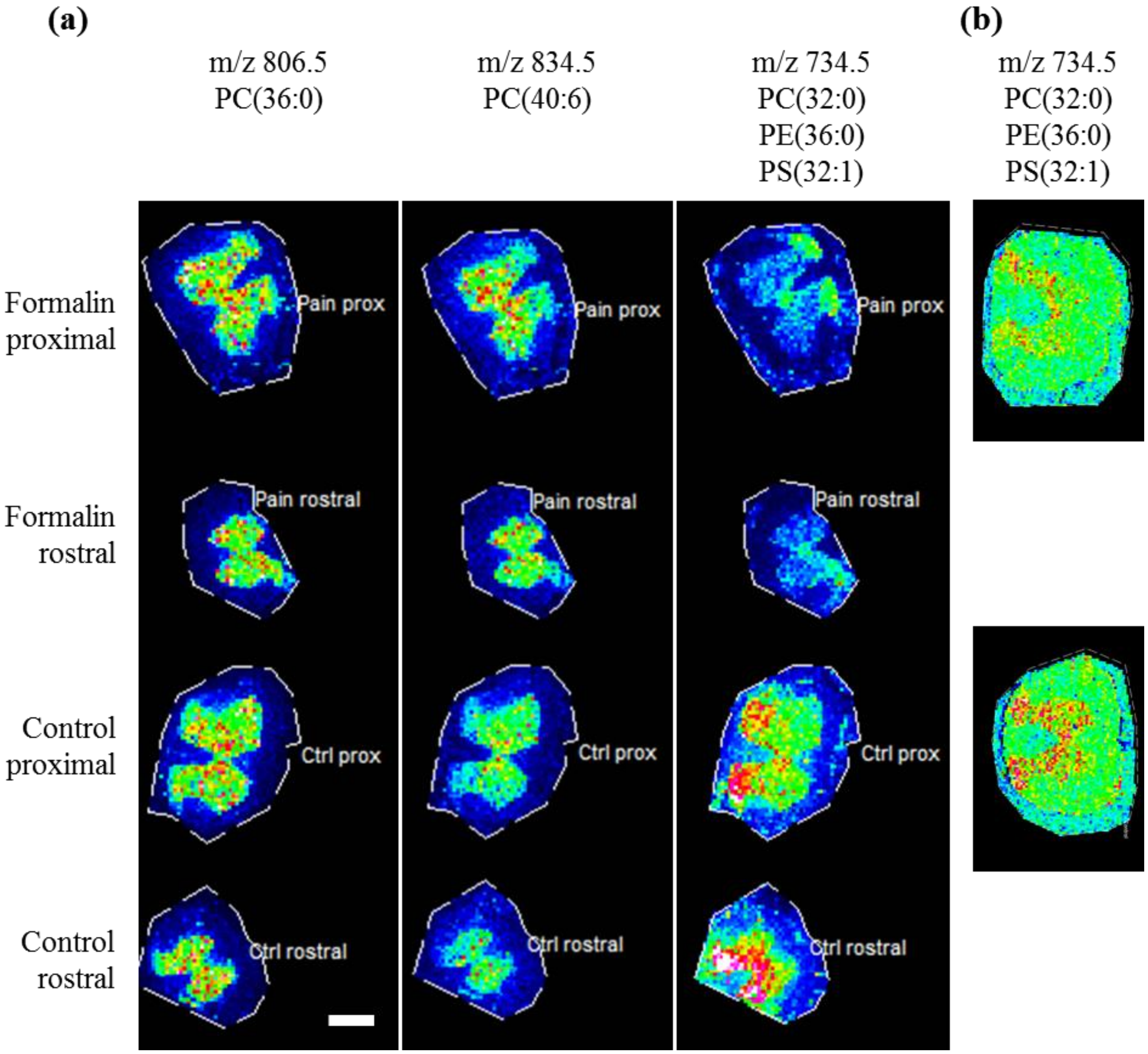

Figure 9.14: MALDI MSI of lipids in rat spinal cord from formalin *vs* control rats. (a) Ion images for three different lipid groups are shown in columns, while rows represent different subjects (Formalin-treated *vs* control) and lateral positions within each spine (proximal *vs* rostral). Two of the lipid groups – m/z 806.5 and 834.5 – appear relatively uniform between spines and positions, while a third group – m/z 734.5 – appears relatively less abundant in the gray matter of both sections from the Formalin-treated spine. **(b)** A similar Formalin/control contrast for m/z 734.5 was observed in another MSI experiment using separate rats. Scale bar = 1 mm.

CHAPTER 10

CONCLUSIONS AND FUTURE OUTLOOK

Mass spectrometry imaging (MSI) is an analytical technique with the unique potential for comprehensive chemical imaging of complex biological systems, providing a tool to more fully understand biological function at the fundamental level of specific chemical composition and its spatial arrangement which gives rise to organismal behavior and function (or dysfunction). That said, MSI still faces numerous major challenges in the path to realizing this ideal goal, especially for analysis of single cells and other microscopic specimens which test the limits of the technique. In particular, the usefulness of MSI would improve greatly with 1) substantial increases in ion yields for intact biomolecules which are currently quite low, especially with ion microprobe sampling in SIMS, and 2) mitigation of the ion suppression problem which complicates data interpretation since lack of signal does not guarantee absence of analyte – a problem discussed in **Chapter 2** and exemplified in **Chapter 9**, where analytes known to be present were not detected due to the presence of other compounds. These are prominent fundamental issues affecting all mass spectrometric work, but they are exacerbated in MSI where pre-ionization chromatographic separation of mixtures is virtually impossible and so ions must be formed directly from the complex biological matrix, *i.e.* under non-ideal conditions. Nevertheless, current MSI development research is focused on addressing these issues at the instrumental and methodological levels, and the work presented in this thesis makes significant progress at both of these levels.

The hybrid MS instrument described in **Chapter 3** represents several instrumentation-side advances in MSI capability. In addition to employing the relatively new C_{60} cluster ion probe to enhance yield of molecular ions, the combination of laser and ion microprobes on a single instrument enables new experiments that would exploit their complementarity. For example, single cells may be imaged at high spatial resolution in SIMS mode, and then subsequently profiled by MALDI to extend covered mass range. Conversely, microspot arrays of MALDI matrix may be printed across a sample surface and used to obtain a coarse MALDI MS map of the sample prior to high-resolution SIMS imaging, similar to the MALDI-guided SIMS and microarray-guided imaging work described in **Chapter 7** and **Chapter 8**, respectively. SIMS with tandem MS is also a powerful and relatively new combination of capabilities, allowing unknown or tentatively-identified SIMS ions (many of which may be "characteristic fragments" of larger molecules) to be characterized and more confidently identified, as demonstrated in **Chapter 3** with animal cell metabolites and in **Chapter 8** with bacterial secondary metabolites. This customized instrument is currently one of only a few in the world with these unique capabilities, and thus offers cutting edge potential for exploring the chemical composition of biological systems.

In addition to the existing advantages of the hybrid MS, further extension of capabilities is possible with additional instrumental improvements: a cryogenically-cooled sample stage would allow cryogenic ("frozen hydrated") sample preparation which has been shown to improve SIMS imaging especially in terms of ion yields and preservation of sample morphology, improved translation stage control (or automated beam deflection, already enabled *via* LabView program) would improve spatial resolution of the system to 1-2 µm with the current ion gun, and a number of chemical or instrumental ionization enhancement methods (as reviewed in **Chapter 2**) could also be incorporated into the existing system without major physical modification. Another major hardware change to consider would be replacement of the C_{60} ion gun with an argon cluster source, which literature suggests would provide reduced sample damage and thus more intact molecular ions and improved capability for sample etching, depth profiling, and 3-D imaging. Additionally, plans have already been made to incorporate a secondary electron detector into the adapted system; this will serve to facilitate ion microprobe focusing and could also allow inspection of sample morphology by scanning electron microscopy, which may be useful in combination with SIMS imaging experiments as proposed and demonstrated in **Chapter 4**.

The second half of this thesis explored another route to more comprehensive molecular imaging, that of combining multiple complementary chemical imaging methods in order to expand chemical or spatial scale coverage. This concept is discussed in detail in **Chapter 5**; the experiments presented in **Chapter 6** explored how MALDI and confocal Raman microscopy (CRM) can be combined to access different subsets of a sample's chemical composition, while the work in **Chapter 7** demonstrates how MSI imaging techniques, SIMS and MALDI, can be combined in order to visualize chemical distributions at multiple size scales on the same specimen. Using this method, intriguing distributions of multiple secondary metabolite classes including many cell-cell signals were visualized in bacterial biofilms, generating numerous new microbiological hypotheses which can be pursued in future work. **Chapter 8** work integrated CRM imaging with SIMS imaging using the custom hybrid MS, taking advantage of the cluster ion microprobe to simplify sample preparation, utilizing SIMS-mode tandem MS capability to confidently identify many metabolites of interest *in situ*, and demonstrating how precise spatial correlation of CRM and SIMS images with new separation methodology can yield additional information as well as cross-validation of the results, which addresses concerns about ion suppression and image artifacts in MSI. In addition to exploration of new microbiological hypotheses (discussed in **Chapters 6**, **7**, and **8**), future directions for this work include applying the imaging methods developed here to investigate metabolic exchange between bacteria and plant roots in the rhizosphere, as well as extending the methods to enable 3-D correlated imaging of biofilms and other samples by SIMS/CRM.

APPENDIX A

C_{60}-QSTAR HYBRID MALDI/SIMS Q-TOF MS
USER'S MANUAL AND TROUBLESHOOTING GUIDE

NOTES AND ACKNOWLEDGMENTS

This user's manual is written as a supplement to existing manuals, including: QSTAR XL System hardware guide, oMALDI 2 ion source installation and testing data instructions, QSTAR XL PM checklist and data log, QSTAR XL installation guide, and C_{60} ion gun user's manual. These manuals are typically kept beside the QSTAR PC and contain useful information about tuning, troubleshooting, performance history, and maintenance. Other important files including tuning procedure, instrument block diagram, ion path schematic, and CAD drawings for custom parts are located on the QSTAR PC and/or backed up on Cerebro. The manual was written primarily by E. J. Lanni with contributions from S. J. B. Dunham.

OVERVIEW

Congratulations on the recent acquisition of your very own "C_{60}-QSTAR" MALDI/C_{60}-SIMS dual ion source hybrid QTOF imaging mass spectrometer! The C_{60}-QSTAR is a customized mass spectrometer featuring both UV laser and C_{60} ion beam microprobes for LDI/MALDI and SIMS modes of operation respectively, as well as tandem MS and MS imaging capability. Performance and hardware specifications are as follow:

- Base commercial instrument: AB SCIEX QSTAR XL
- Mass analyzers: quadrupole filter (MS_1) coupled orthogonally to time-of-flight (TOF) with single-stage reflectron (MS_2)
- Tandem MS: CID with argon gas
- Detector: multichannel plates (MCP), ion counting detection mode
- Mass range: m/z 5-40,000 on original commercial system, up to 2,000 demonstrated on adapted system

- Mass accuracy: < 10 ppm (with internal standard)
- Mass resolution: >8,000 FWHM typical, >13,000 obtained on current system
- 10 µm ultimate lateral imaging spatial resolution (limited by step motors / software)
- C_{60} microprobe: Ionoptika IOG60-20 DC (continuous) C_{60} ion beam, 5-20 kV energy, 2 nA max. sample current, 2 µm ultimate probe focus (at 20 kV / 1 pA sample current), 1.3 × 1.3 mm^2 max. scan field
- Laser microprobe: Spectra-Physics VSL-337 NDS pulsed N_2 , 337 nm wavelength, 6 mW avg. max. power, 40 Hz max. firing rate, ~0.1 × 0.2 mm^2 ultimate probe focus

INSTRUMENT MODIFICATIONS

Several modifications were made to the instrument in order to accommodate the ion gun and to allow SIMS-mode operation. These are discussed along with characterization results in chapter four of this thesis and also highlighted in the schematic shown in **Figure A.1**:

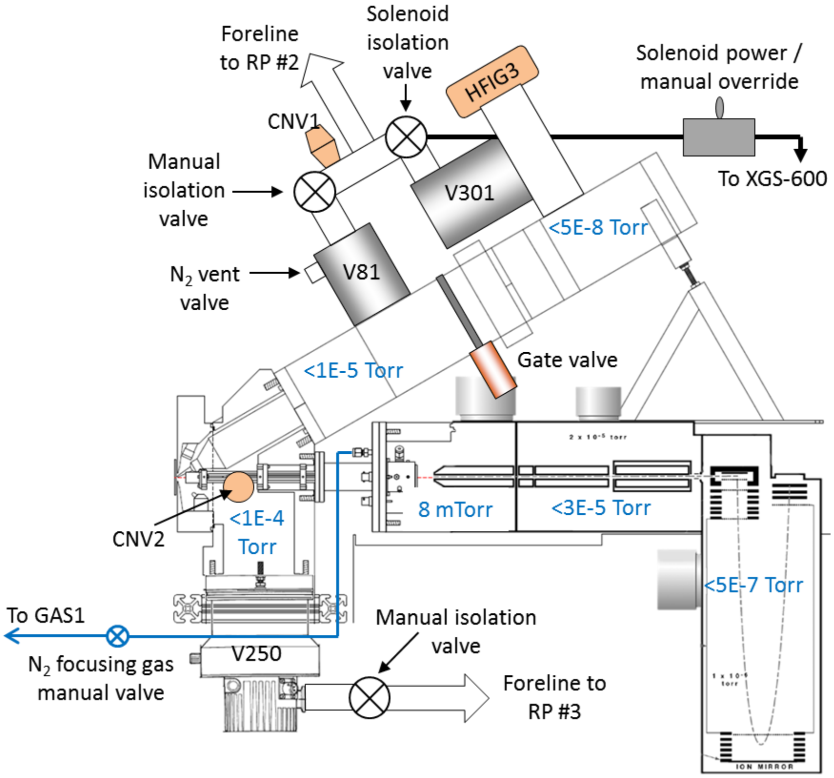

Figure A.1: Modified QSTAR vacuum system schematic. Typical chamber pressures are shown in blue text.

Vacuum system notes

- Original QSTAR pumping system was not modified, and is pumped by rough pump (RP) #1.
- Typical operating pressure for each chamber is shown in blue text.
- All additional TM pumps (V-81, 301, 250) are controlled manually by rack-mounted controllers.
- Added vacuum gauges including convection gauges (CNV1/2) and hot filament ion gauge (HFIG3). CNVs can operate at up to atmospheric pressure while the HFIG should only be activated at sub-mTorr range, and must be manually disabled before venting the C_{60} source.
- The two ion gun TM pumps (V-81 and V-301) are supported by RP #2. Sample chamber TM pump (V-250) has a dedicated RP #3 because it carries a high gas load.
- A solenoid valve will automatically isolate the V-301 and C_{60} source if foreline pressure exceeds 10 mTorr. The C_{60} source can be kept under vacuum during a QSTAR vent by isolating the V-81 with a manual vent valve and closing the internal gate valve.
- A rack-mounted XGS-600 vacuum gauge controller reads all pressure gauges and controls interlocks for C_{60} power supply, Ardara RF power supply, and C_{60} isolation valve.
- The V-301 TM pump (on C_{60} source) is vented manually with a knurled nut. It should be isolated from the QSTAR during pump down/venting to prevent damage.
- The V-81 TM pump (on C_{60} gun lower column) is vented automatically 250 seconds after it has been powered off, and the vent closes after 120 seconds. This is synchronized with the QSTAR's vent timer provided they are powered off together.
- The V-250 TM pump has a knurled nut for manual venting, but can also be stopped by closing the foreline isolation valve once disabled.

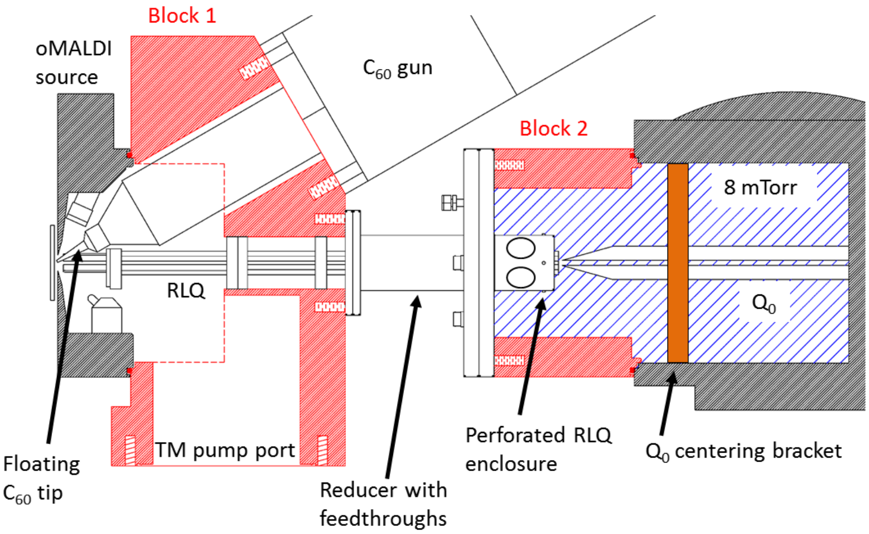

Figure A.2: Modified electronics / ion optics schematic.

Electronics & ion optics notes

Refer to **Figure A.2** for a schematic illustrating the components and modifications described below:

- Ion guide Q_0 was found to have a vertical offset of a few mm, so a centering bracket was added to center it.
- DC voltage for C_{60} floating tip and AC RF voltage for RLQ are supplied through the reducer feedthroughs, along with N2 gas for collisional focusing.
- The Ardara AC RF power supply is installed beneath the sample chamber to minimize cable length to the feedthroughs. Changing cable length will change operation frequency. RLQ DC offset voltage is input to the back panel of the RF power supply. The RF supply is interlocked to shut off if Block 1 pressure exceeds 20 mTorr, to prevent arcing.
- To enable N_2 gas supplies (GAS1 and GAS2 in Analyst), the QSTAR's "source ID" circuit was modified with jumpers to set it to IonSpray (ESI) mode. The circuit board is located to the left of the adapter blocks.
- The C_{60} ion beam is controlled using the ~3V transistor-transistor logic (TTL) signal which fires the laser. This signal is fed to the pulse generator and converted into a 25 msec square pulse which is forwarded to the C_{60} controller. This unblanks the beam for an equal amount of time, and the ion beam will be continuous as long as the laser is being fired at 40 Hz. A

laser interlock switch was installed on the top panel of the instrument in order to disable the laser while operating in SIMS mode.

- The C_{60} power supply is interlocked to shut off if C_{60} source pressure exceeds 5E-6 Torr to prevent arcing.

TYPICAL OPERATING PARAMETERS

- QTOF MS positive ion mode
- C_{60} gun installed with large-diameter floating tip
- V-250 on (block 1 at high vacuum)
- Extended RLQ with detachable tapered tips, 3.2 mm working distance to orifice, 1.5 mm gap to $Q_{0,}$ no conductance limits, no entrance/exit lenses, original structural collars, perforated rear enclosure, collisional focusing N_2 gas delivered into block 2 / Q_0 chamber
- Q_0 centered with Ultem bracket

Sample Plate / Orifice	+34 V (FP = 14 V)
C_{60} tip	+30 V
RLQ DC offset	+24 V
RLQ RF	1100 V p-p @ 2.8 MHz
RLQ/Q_0 gas (N_2)	8 mTorr to Q_0 chamber (3.0E-5 Torr quad chamber with CAD = 3)
Q_0 DC offset	+20 V
IQ1	+18 V
IE1	2.0 eV
ST	+15 V
CAD	3
RO2	+9.5 V
IQ3	+7.5 V
GR	+11.0 V
TFO	+14.1 V
TST	+0.8 V
Mirror	+0.997 kV

Plate	+0.370 kV
Grid	-0.400 kV
Liner	-4.00 kV
Offset	-6.0 V
MCP	+2300 V (installed 2013-11-10)

For **negative ion** experiments, use same potentials with inverted polarity. Switching polarity modes in Analyst will switch most potentials automatically, but some voltages must be retuned manually (as of 2013-11-25).

• IE1	-2.0 eV
• RO2	-9.3 V
• GR	-5 V
• TFO	-10.7 V
• TST	1.5 V
• Plate (negative):	-0.331 kV
• Offset	+16.4 V

For **tandem MS** experiments, collision energy (CE) shifts sample plate, orifice, and Q_0 offsets relative to RO2 in order to increase ion energy at Q_2 for CID, as follows:

- Q_0 = RO2 + CE
- Sample Plate / Orifice = RO2 + CE + FP

Note that with RO2 at ~10 V, CE = 10 eV puts Q_0 at the standard +20 V offset. For CE > 10 eV, C_{60} tip and RLQ DC offset must both be manually shifted up to maintain potential difference w.r.t. Q_0, *e.g.* at 20 eV Q_0 = +30 V, Sample plate / orifice = +44 V, so C_{60} tip = +40 V and RLQ DC = +34 V.

PROCEDURES

MS data acquisition

MS data is best acquired in Manual Tune mode within Analyst, as this allows full control over operating and acquisition parameters. A few notes on use:

- Do not load methods where GAS1 > 5, or QSTAR Q_1/Q_2 pressure will become too high and the instrument will automatically vent.
- Very short accumulation times (<0.25 sec) will crash the system. 1 s is safe and typical.
- TOF mass and display mass should generally be set identically.
- Acquiring data in non-MCA mode is generally recommended as this will retain time-resolved data (allowing generation of mass chromatograms and time-specific mass spectra) rather than summing all signals into a single file.
- Because the QSTAR has an orthogonal TOF geometry, transmission and mass range are inversely related i.e. larger mass range results in lower overall ion transmission especially for smaller ions, due to 1) the necessity of scanning Q_1 between multiple transmission windows, and 2) reducing TOF pusher frequency to accommodate the largest m/z value of the specified range. Q_1 transmission can be manually specified (see below), whereas the TOF transmission T for a given ion of mass m with a specified maximum mass range m_{max} on the QSTAR is as follows:

  $$T(\%) = 0.25\sqrt{\frac{m}{m_{max}}} \tag{1}$$

  Therefore maximum TOF transmission is 25%, and (for example) transmission of a 100 Da ion using a 60-850 Da mass range would be only 9% assuming perfect Q_1 transmission. The only way to improve TOF transmission beyond 25% is to use ion enhancing mode, where a narrow mass range is trapped in Q2 and released synchronously with the TOF pusher.
- TOF pusher should always be run at recommended frequency to maximize transmission.
- Q_1 transmission profile should be adjusted according to ions of interest, which usually means emphasizing the higher mass ions in the spectrum where good transmission is critical. Q_1 typically transmits from 0.8x-2.0x of a given mass set point. For "lipid imaging" with a 60-850 AMU mass range, the following profile is typical:

  10% at 70 AMU

20% at 200 AMU
70% at 400 AMU

- For SIMS-mode operation, disable the laser with the interlock toggle switch on the front of the QSTAR. Laser frequency should usually be set to 40 Hz to generate a continuous C_{60} beam while active.
- For MALDI-mode operation, enable the laser interlock switch and (if the C_{60} beam is active) disconnect the GATE/TRIG IN coaxial cable on the pulse generator in the electronics rack.

MS imaging

MSI experiments are performed from the oMALDI Server program.

- Always confirm that tune mode is disabled in Analyst before beginning an MSI experiment, or the program will crash.
- An MSI experiment calls upon a batch file, which calls upon an instrument method file to specify instrument settings and acquisition parameters. These files must be generated first before setting up the imaging experiment in oMALDI Server.
- Standard imaging mode or “step-mode” imaging moves to discrete stationary positions for each pixel, acquiring data for an arbitrary accumulation time specified in the instrument method. This allows the highest possible spatial resolution (10 µm) and full control over accumulation time per pixel and mass range. Images in this mode are consistently shifted ~100 µm down with respect to the area specified during setup, so the specified area should be shifted upward by an equal amount especially when imaging a small sample e.g. a cell. In the magnified camera view this corresponds to a 0.2” on-screen distance.
- Raster imaging performs a series of continuous horizontal line scans to acquire an image. In this mode imaging is nearly 10x faster, but accumulation time per pixel is determined by specified horizontal spatial resolution which may be no less than approximately 50 µm at 0.25 sec/pixel accumulation. When imaging in raster mode, extra margins should be included to the left and right sides of the desired imaging region as these will be sampled but not recorded in the results.
- oMALDI Server contains a primitive MSI data viewer, but a useful alternative is to convert the data to msi format which can then be viewed in BioMap. Bin size can be specified in the conversion options.

Tuning collisional focusing gas pressure in Q_0

The collisional focusing gas pressure in adapter block 2 / Q_0 chamber can be measured indirectly from the hot cathode gauge on the Q_1/Q_2 chamber of the QSTAR, which outputs measured pressure as a voltage on the “DACS AND VACUUM GAUGE” control board in the QSTAR (see below). These vacuum chambers are separated by a small conductance-limiting aperture (visible at the end of Q_0) which maintains a ~3-order of magnitude pressure difference during operation. Q_1/Q_2 chamber pressure is also increased by gas pressure in the Q_2 collision cell, so this must be considered when interpreting measurements.

1. Set the instrument to “ready” mode (green status icon in Analyst). This opens gas supplies.
2. Load a method in tune mode and confirm GAS1 = “5” and CAD = “3”.
3. Set a digital multimeter to DC voltage measurement mode and plug the black lead (COM) into the GND socket on the LENS PS control board, as shown in **Figure A.3** below:

Figure A.3: Proper configuration of a digital multimeter for QSTAR quad chamber pressure measurement.

4. Pressure will be indicated in units of 100 mV = $1 \cdot 10^{-5}$ Torr. For normal operation (efficient focusing), slowly open the metered manual gas valve on the front of the instrument until the meter reads 300 mV ($3 \cdot 10^{-5}$ Torr).
5. This corresponds to ~8 mTorr N_2 gas in Q_0. To confirm, set CAD = “0” and the measured pressure should drop to ~80 mV ($8 \cdot 10^{-6}$ Torr) in the absence of CAD gas. Don’t forget to reset CAD gas before operation.

Venting QSTAR only (C_{60} source under vacuum)

1. Set C_{60} source to standby and close C_{60} manual gate valve until snug (do not over-tighten)
2. Turn off V-250, close V-250 foreline valve and unplug the V-250 rough pump (black power cord to 230 V transformer on wall)
3. Turn off Ardara power supplies (set RF to 0 V to avoid accidental power-up)
4. Close oMALDI Server, deactivate QSTAR profile in Analyst
5. Confirm that oMALDI source screws are tight on adapter block 1
6. Confirm that adapter block 2 screws are tight on QSTAR interface
7. Stop QSTAR electronics (push in white toggle switch) and V-81 (STOP on controller) simultaneously. V-81 controller should display "stopping" and decreasing speed, and will open vent in 4.2 min (simultaneously with QSTAR internal vent) for 2.0 min
8. Close manual V-81 foreline valve until snug (behind ion gun)
9. When pumps begin to vent, stop QSTAR rough pump (main breaker on rear instrument panel) do not stop C_{60} gun rough pump.
10. Confirm C_{60} gun vacuum is isolated – source (<5E-8 Torr) and foreline (<1E-4 Torr) should not rise. If source pressure rises, tighten C_{60} gate valve slightly and check pressure for recovery.
11. Wait for instrument to reach atmospheric pressure (watch for adapter block 1 pressure to reach 760 Torr) before opening. *Don't rush, if you force the chamber open prematurely you will introduce air/moisture and the next pump down will take much longer!*
12. ALWAYS keep N_2 vent gas supplied to the instrument to keep it purged while vented (reduces subsequent pump down time and protects MCPs from moisture-induced damage).

Pumping down QSTAR (C_{60} source under vacuum)

1. Reattach oMALDI source, push flat against adapter block 1 and secure screws
2. Reconnect oMALDI cables (power cable, control cable, sample/orifice supply, laser fiber, camera, foreline to vent manifold)
3. Recalibrate adapter block 1 pressure gauge (CNV2) if needed
4. Holding sample door closed, start QSTAR rough pump

5. Loosen oMALDI screws on adapter block 1 to allow o-ring compression
6. Close C_{60} source solenoid valve (manual override switch) to isolate C_{60} source temporarily (Source pressure will rise slightly in this time, but do not forget to open it later or V-301 will overheat and shut down!)
7. Open manual V-81 foreline valve
8. Start QSTAR electronics (white toggle switch on frame)
9. When C_{60} foreline reaches mTorr pressure (<1E-2 Torr), start V-81 pump
10. When C_{60} foreline reaches <1E-4 Torr, re-open C_{60} source solenoid valve. Source pressure should drop slightly to previous pressure.
11. Start the V-250 rough pump and the V-250, then open the V250 foreline valve.
12. Monitor system for proper startup:
    a. V-81 should reach full speed (1350 Hz) and settle at 8-9 W power
    b. V-301 should remain at full speed (963 Hz) and 8-9 W power
    c. V-250 should reach full speed (56 kRPM) and <30 W power
    d. Adapter block 1 pressure should reach <1E-4 Torr after several minutes.
    e. Confirm proper QSTAR vacuum startup. *Turbo pumps should begin powering up fully (audibly) after a few minutes, and the "VAC RDY" light on the QSTAR system controller (front panel) should blink constantly. If it stops, the QSTAR has failed pump-down – most likely cause is lack of ample N2 pressure on inlets which the instrument requires for safe venting. In this case, check the N2 pressure at the regulator supplying these lines, as well as valves on the line. Once proper pressure is supplied, "VAC RDY" should begin blinking again and pumpdown will continue.*
    f. Confirm that the TDC starts up correctly. *The TDC (IONWERKS, front panel) "DSP" LED should blink rapidly for several minutes and then settle into a 1 Hz blink indicating healthy idle state. If blinking is 2 Hz or other lights are active on startup, the unit is "unhealthy" and the QSTAR electronics should be power cycled using the white toggle switch. The TDC seems to typically start correctly after one such cycle.*
    g. Confirm that the TOF Penning pressure gauge ignites properly within the first few minutes. *Press "PM" on the QSTAR gauge controller (COMBIVAC, front panel) should display a pressure in the range of 1E-6 – 1E-4 as the system pumps down. If the Penning gauge fails to ignite this value will drop to a very low number (~7E-10*

Torr) and “FAIL” will appear over “DISP.” Sometimes the gauge will ignite after a few more minutes, but if it does not then the instrument should be vented and the gauge must be cleaned / rebuilt after which it will ignite reliably.

   h. TOF HV supplies (Spellman, front panel) should activate at 2E-6 Torr TOF pressure.

13. Re-tighten oMALDI screws on adapter block 1
14. Confirm V-81, V-301, and V-250 cooling fans are on and properly situated.
15. Activate QSTAR profile in Analyst. If it shows “not OK” status this is usually due to 1) system still pumping down or 2) high pressure on GAS2 line which is not used but sometimes connected to a block 1 side port. To relieve pressure, confirm the needle valve on the port is shut tight, then unscrew the gas line to vent it.

Removing and cleaning RLQ tips

1. Vent instrument (see **Venting QSTAR only**).
2. Remove MALDI source chamber and the C_{60} mosquito tip.
3. Unscrew and remove the RLQ tips. *Keep track of orientation and rest with optical faces up.*
4. Clean the RLQ and Q_0: fasten a foam swab into the cleaning rod, confirm it is secure, wet the swab with methanol, and push it down the ion path until it hits IQ1 at the end of Q_0. Avoid scraping the quadrupoles with the cleaning rod. *Make sure to check for fibers after this procedure is complete.*
5. For a quick clean of the RLQ tips:
   - Make slurry of 1:1 Alconox:AlO_2 powder in DI H_2O. *AlO_2 is a lung irritant; do not inhale!*
   - Using a gloved hand, thoroughly scrub the RLQ tips. Pay particular attention to the optical faces.
   - Rinse with DI H_2O and make sure the screw holes are free of slurry. *Water will spread out on clean rods and bead up on dirty rods – reclean dirty rods.*
   - Rinse with MeOH and allow to dry, or dry quickly by blowing with N_2.
6. For a thorough cleaning of the RLQ tips:
   - Perform quick clean procedure from step 5.
   - Sonicate for 30 minutes in Alconox/H_2O solution (about 1 cap of Alconox with a full, ~2L, sonication vat).

- Sonicate for 30 minutes in Citronox.
- Sonicate for 15 min in DI H_2O
- Rinse with water and MeOH and allow for drying. The drying procedure can be expedited by using a drying oven.

7. Gently clean C_{60} tip with methanol/Bemcot wipe, and blow dry with N_2.
8. Re-install tips (in correct orientation) and C60 mosquito tip
9. Check for electrical isolation of C_{60} tip (residual liquid inside tip can short floating segment to ground).
10. Follow the procedures under "Pumping down QSTAR" to prepare the instrument for operation.

Removing the C_{60} gun

1. Cool the C_{60} source to < 80 °C overnight. This should be done as follows
    - Place in standby mode
    - Adjust temperature to 20 °C
    - Once temperature is less than 250 °C turn HV off.
    - Allow to cool overnight
2. Confirm that the C_{60} source has cooled to < 80 °C by turning the HV on briefly.
3. Isolate the C_{60} source with the manual gate valve.
4. Vent the QSTAR as usual (see **Venting QSTAR only**).
5. Close all programs and turn off the C_{60} filament gauge (HFIG3).
6. Isolate the source with the solenoid switch, shutdown V-301, and unplug the C_{60} rough pump (orange 120V power cord to wall).
7. Vent V-301 manually to the air by opening the knurled nut on the pump body.
8. Remove the MALDI source and C_{60} mosquito tip.
9. Power off XGS-600 and disconnect CNV1/CNV2/HFIG3 gauges.
10. Close the valve on the V-81 N_2 vent line and disconnect from the pump. DO NOT close the QSTAR N_2, the instrument should be continuously purged while vented to minimize subsequent pumpdown time.
11. Disconnect the following:
    - C_{60} gun cables (store in a clean bag)

- Turbo pump fans (unplug and remove)
- RF supply (unplug and remove from instrument)
- V-81 and V-301 turbo pump cables
- C60 foreline solenoid valve connectors
- V-81 vent valve control cable
- Foreline tubing from V-301 and V-81. *Cover all vacuum faces with aluminum foil.*

12. Remove V-81 and V-301 from the ion gun. *Cover all vacuum faces with aluminum foil.*
13. Raise the gun support frame to support the gun for removal
14. Cover CF ports on the gun with aluminum foil
15. Prepare a clear & clean work area on the high wooden workbench (by the ChIP-1000) to place the gun. Position some foam pads to stabilize it.
16. Remove the gun. *This is a two person job. A good approach is to remove all but the top two screws from the ion gun bolt ring on block 1, then have an assistant remove these final two screws while you support the front of the gun by grabbing the bolts around the bellows. Carefully retract the gun until clear of the vacuum port, allowing it to slide along the support frame, then lift and move to the workbench.*
17. Rest the gun on foam pads with the CF flange faces face down, taking special care not to damage the BNC IMON connection on the same side. Wrap the lower column in aluminum foil.

Installing the C_{60} gun and pumping down full system (QSTAR + Gun)

1. Mount gun, taking care to avoid collision between tip and RLQ. *This is a two person job.*
2. Plug in main power/control cable to the back of the gun, unplug the cable from the back of the rack-mounted control box, and check heater, filament and PT100 connections as detailed in **Figure A.4** below. If any values are far from typical range, the respective source part is likely broken and should be replaced before proceeding.

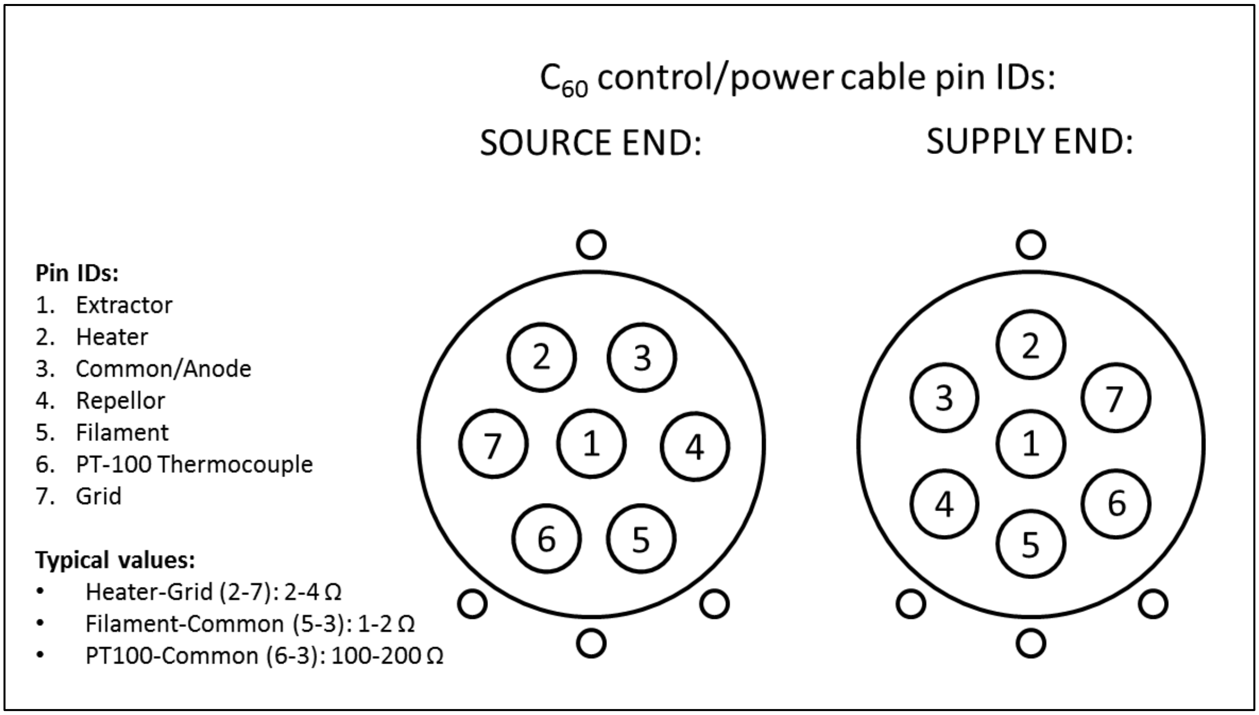

Figure A.4: C60 control/power cable pin IDs and typical measured resistance values.

3. Reconnect control cable to control box and disconnect from gun.
4. Install V-81 and V-301 turbo pumps on the gun. *Use new copper gaskets* each time. Before compressing a gasket, visually confirm it has seated properly within the two faces.
5. Reconnect turbo pump power/control cables and V-81 vent gas line control cable.
6. Connect and open N_2 vent gas line to V-81 vent valve.
7. Turn on XGS-600 gauge controller (if off) and reconnect HFIG3 but do not activate.
8. Power cycle V-81 and V-301 rack-mounted controllers by disconnecting and reconnecting the power cables in the back. They should autotest and then detect pumps in idle state.
9. Open V-81 foreline valve and C_{60} internal gate valve.
10. Recalibrate CNV1 (C_{60} foreline) and CNV2 (block 1) pressure gauges if they are not measuring 760 Torr.
11. Manually set the C_{60} source solenoid valve to open (override pressure interlock) by setting Set Point 3 (CNV1) to ON in the XGS-600.
12. Plug in C_{60} rough pump (orange power cable to 120V wall outlet) and simultaneously turn on main QSTAR breaker.

13. Manually press sample door to ensure it seals. Loosen the screws securing MALDI source to adapter block 1 to allow full o-ring compression, then retighten screws.
14. Start QSTAR electronics (white toggle switch).
15. When C_{60} foreline reaches mTorr pressure (<1E-2 Torr), start V-81 and V-301 turbo pumps. Both pumps typically settle at 8-10 W under normal operating conditions.
16. Once C_{60} foreline reaches <0.1 mTorr, turn on filament gauge (HFIG3).
17. Reenable C_{60} foreline valve interlock by resetting Set Point 3 (CNV1) to AUTO in the XGS-600.
18. Wrap gun in heat tape and bake at or below 150 °C for 2-3 days, or until C_{60} source pressure reaches <1E-8 Torr. (If using the Variac then 120 V at about 80% power – monitor with DMM and thermocouple under heating tape.).
19. Remove heat and allow the gun to cool to < 60 °C.
20. Connect all cables to C_{60} gun, inspecting all connectors (especially main HV power/control cable) for any foreign material (and removing it).
21. Power on the C_{60} control box and start the C_{60} control program on the PC.
22. Override the C_{60} supply interlock by switching XGS-600 Setpoint 1 (HFIG3) to "ON."
23. In the C_{60} control program:
    a. Turn HV on. The status bar at the bottom of the window should read "OK"
    b. Activate temperature and filament degas cycles.
    c. Load the preset "Standby" configuration.
    d. Monitor current and voltage readings for abnormalities.
    e. Source pressure will typically rise briefly to ~1E-5 Torr during degas.
    f. If temperature does not exceed ~80 °C during the degas routine, the heater is likely broken and must be replaced.
24. Once degas routines are complete, re-enable the C_{60} supply interlock (Setpoint 1 to "AUTO") and then load the preset 10 kV configuration. Adjust temperature to 350 °C (standby temp) and confirm that system is stable (voltages stable at set points, acceptable leak currents, no ticking).
25. Load the last good 20 kV configuration. Raise temperature manually to keep heater power below ~75%. If the source module is new or recently recharged, beam current will be high at low temperatures (<400 °C) and unstable initially until the source is re-conditioned.

26. Once the system has stabilized, retune the beam (follow procedure in C_{60} gun manual) perform the "finding the beam" procedure if necessary.

Removing and cleaning the rectilinear quad

1. Remove C_{60} gun. Follow the procedures outlined under "Removing C_{60} gun."
2. Disconnect Block 2 from the QSTAR (two hex head screws on top of mounting adapter and two Philips head screws on bottom flange face – do not disassemble mounting adapter from Block 2 or adapter realignment may be required!)
3. Retract adapter assembly (pull assembly back on support frame and/or pull assembly with support frame back away from instrument, taking care to keep adapter feet on frame and frame supported by instrument frame) and angle away from the instrument.
4. Inside Block 2, remove the screws attaching RLQ enclosure to Block 2 and pull the entire assembly straight back. Internal feedthrough connections should disconnect on their own but may need some assistance using needle-nose pliers.
5. Transfer RLQ to a clean work area and disassemble. *To disassemble, start in back and work forward*. It is recommended to collect small parts in Petri dishes.
6. Clean RLQ rods. Follow procedure under "Removing and cleaning RLQ tips."
7. Clean Q_0 tips in situ by wiping with a lint-free Bemcot wipe wet with MeOH.

Reassembly and installation of rectilinear quad

1. Reassemble RLQ as shown in **Figure A.5** and reinstall in Block 2, check for proper connections, and inspect both RLQ and Q_0 for any foreign material e.g. tissue lint.
2. Slide adapter assembly and support frame back into position on instrument. Block 2 mounting adapter fits very snugly with the instrument and so the assembly may need to be wiggled a bit to get it into position, but do so gently, perturbing the QSTAR minimally, as this may result in physical changes to the instrument that require retuning.
3. Install RLQ into adapter and re-align block with instrument. DO NOT tighten screws.
4. Install V-250 foreline and confirm manual valve is shut
5. Use blank with KF25 cap to seal off C_{60} inlet on the block
6. Install MALDI source

7. Turn on the main breaker for rough pump and lift adapter block slightly to allow block 2 – QSTAR seal to compress fully.
8. Tighten screws to secure block 2 to the QSTAR
9. Turn off main breaker for rough pump, allow instrument to vent, then remove blank from C_{60} port and follow instructions under “Installing the C_{60} gun.”

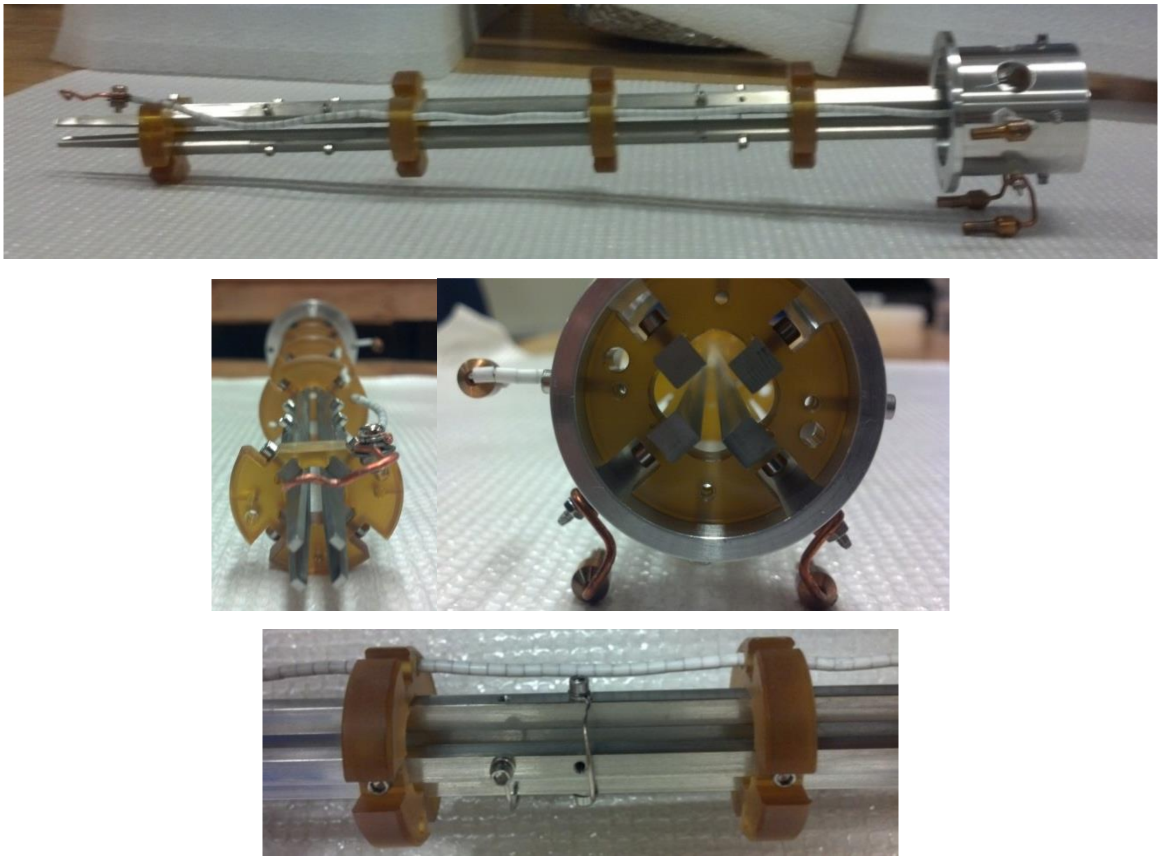

Figure A.5: Photographs of a properly assembled rectilinear quadrupole guide

Complete disassembly of the adapter

For any future modifications to the adapter blocks (e.g. adding new ports), they must be fully disassembled and stripped to bare metal.

1. Follow the “removing the rectilinear quad” procedure. Cleaning the RLQ is not imperative but might as well be done since it’s being removed.
2. Remove other components on the block e.g. CNV gauge, gas valve, and SED.
3. Prepare a clean and clear workspace to rest the full adapter assembly, and prepare foam pads to support block 2.

4. Lift the adapter blocks with V-250 straight up from the support frame.
5. Set the blocks down on their left (featureless) sides, with foam supporting block 2.
6. Remove adjustable foot pads on block 1, noting previous positions as accurately as possible.
7. If block 2 is being modified, remove the adapter block that connects it to the QSTAR.
8. Remove screws on CF flanges connecting block 1 - V-250, block 1 – CF reducer, and block 2 – CF reducer. Take special care not to scratch CF faces as the aluminum is easily damaged.
9. To transport blocks down to the machine shop, cover CF faces with metal protector plates.

Reinstallation of the adapter

1. Clean any parts from the machine shop thoroughly with methanol and Bemcot wipes prior to reinstallation.
2. Reassemble and tighten CF seals using new aluminum gaskets.
3. Reinstall block 1 foot pads to previous positions.
4. Reinstall block 2 adapter if removed.
5. Reinstall adapter assembly on QSTAR, taking care to center support frame underneath with both foot pads securely supported.
6. Slide adapter assembly and support frame into position. Wiggle gently to get block 2 into proper sealing position.
7. Using a bubble level, adjust foot pads to level adapter assembly w.r.t. QSTAR both front-to-back and side-to-side. Note that the QSTAR itself is not perfectly level.
8. Follow “reassembly and installation of rectilinear quad” followed by “installing the C_{60} gun.”

ROUTINE MAINTENANCE

- Relubricate translation stage worm gears with 1-2 drops of Tri-Flow if they become noisy
- Relubricate translation stage vacuum seals with a thin layer of Apiezon L vacuum grease any time the stage is disassembled
- Clean MALDI orifice with methanol/Bemcot wipe to remove excess grease after any vent
- Always check o-ring seals and ion optics for foreign material (e.g. lint) before reassembly
- Wipe Q_0 rods gently with methanol/Bemcot wipe after any adapter block removal
- Check argon tank pressure and replace when necessary (this will not cause an error but performance will decline significantly when the Ar is exhausted)
- Change rough pump oil yearly
- Always monitor turbo pumps for changes in performance (temperature, power, noises especially during startup/shutdown). Preemptive maintenance/exchange is preferable to catastrophic failure!
- Always ensure N_2 vent gas is supplied to the instrument, especially when vented (reduces subsequent pump down time and protects MCPs from moisture-induced damage).

MAJOR REPAIRS / KNOWN ISSUES

General troubleshooting

Instrument status is indicated with a small icon in the lower right corner of Analyst. Green icon = active/ready, yellow icon = idle, and red icon = problem on instrument which will prevent operation. Double-clicking on this icon will provide some information, e.g. vacuum system and ion source status, and sometimes this will indicate the problem (e.g. vacuum system still pumping down to operational pressures, or quad chamber pressure is too high). In other cases it will not, and in this case Analyst Service Diagnostic (ASD) should be run from the QSTAR PC desktop to check instrument status. This interface provides more information including instrument voltage/pressure set points and readbacks, allows control of these directly, and also shows a status message window which gives more useful descriptions of any existing errors. Note that ASD is not a user-friendly program, and allows a user to make permanent changes to the instrument's firmware which could be very difficult to restore. Do not utilize the other features (besides instrument status page) if you don't know what you're doing! ASD will always give an error upon quitting.

When the instrument is not performing as expected e.g. not acquiring data and ASD does not indicate any specific errors, software and/or communication glitches are likely at fault. Typically a standard series of debugging steps can be performed stepwise in order of increasing involvement, until the problems are resolved:

1. Disconnect and reconnect QSTAR within Analyst (instrument profile).
2. Restart Analyst and oMALDI software.
3. Restart PC (along with C_{60} control software – restart promptly to avoid ion gun shutdown).
4. Cycle QSTAR electronics – push white button on frame in to deactivate, allow 5-10 seconds off, then pull button out to restart.
5. Power down instrument completely and vent (leave C_{60} source under vacuum), then restart.

oMALDI errors

The oMALDI source will encounter numerous errors during use which can typically be worked around. Some common errors and solutions:

- Communication error – controller box is off or power/control cables have become disconnected from oMALDI source. Power off the controller, quit the program, and reconnect the cables.
- Movement encoder error – the program moves the stage in motor steps and looks for similar movement on the striped digital encoder strips attached to the stage. A significant mismatch results in an error and can arise from 1) a loose stage e.g. motors were disengaged for maintenance and not properly reattached, 2) an overtightened stage which the motors cannot move, 3) stage is physically obstructed and cannot move properly, 4) encoder strips are damaged or obscured e.g. by an electrical cable which has moved out of place. In the case of physical stage obstruction or overtightened stage, vent the instrument, power off the oMALDI, disengage the worm gears, and free the stage manually before reassembling and powering back on.
- Imaging acquisition errors – these occur for numerous reasons, and the reason is not always clear. It is generally good practice to restart the PC after several image runs, and certainly before a large/important image run, as this seems to reduce the error likelihood. Aborting image runs is also likely to cause an error and require a PC restart, especially for raster-mode image runs. Another common cause of error is an image run which calls on a non-existent method or batch file.
- File conversion (wiff to TissueView) error – the program will often fail to convert image files to msi format. Restart oMALDI Server and, without performing any other actions, reattempt the conversion.

Gas supply pressure errors

The QSTAR dynamically adjusts internal valves to match gas supply pressures (for Curtain gas, GAS1, GAS2) with software set points. If pressure is too far from set point, it will flag an error and prevent instrument operation until resolved. This error will be stated in the Analyst Service Diagnostics window, as well as the set point / measured pressure discrepancy. Typically this problem arises from excessive pressure on a closed line, and a solution is to manually vent the gas supply line to relieve it. A minimum constant flow must always be maintained on the curtain gas line, and this is achieved by connecting it with a “bleed adapter” and allowing it to push N_2 into the room at a low rate.

Ionwerks TDC glitches

The QSTAR time-to-digital converter (Ionwerks x8 TDC) has a blinking “status” light on the front panel which should blink rapidly (>4 Hz?) when initializing during instrument pump-down or electronics cycling, then switch to a 1 Hz blink in idle state. If the light blinks at 2 Hz instead, this indicates “unhealthy” state and data acquisition will not be possible until the device is restarted. Likewise, if the other lights are active upon startup, it will also not perform properly until restarted. To solve this problem, power cycle the QSTAR electronics and verify that the TDC initializes properly i.e. settles into a 1 Hz status blink with no other active lights.

The TDC also frequently errs during the first few TOF MS acquisitions run after a QSTAR startup / power cycle. This will manifest as all four green LEDs lighting (including Overload) during acquisition, and no data appearing in the mass spectrum on screen. To solve this problem, immediately stop the acquisition; the TDC should return to healthy idle status, then try again. Typically this needs to be performed twice to debug the TDC, after which acquisition can be performed as usual.

C60 controller/supply nuances

- COM port conflict - the oMALDI and C_{60} controllers both communicate with the QSTAR PC via COM ports. The C_{60} software must be activated first, otherwise it will not detect/connect to the controller if oMALDI Server is already running.
- Whenever you load a settings file, the gun will automatically unblank and begin bombarding whatever is under the beam at the time. Be sure to point the beam at a non-critical material and re-blank it promptly after startup.
- The C_{60} reservoir heater seems to burn itself out if it is allowed to run at maximum power (99%) during warmup. Therefore, warmup should be performed stepwise, manually limiting heater power to <75% or so.

- Use 350 °C as short-term (daily) standby temp. Cycling to/from 250 °C as the original manual states places unnecessary stress on the system and appears to result in source instability and reduced heater lifetime.
- The anode will typically show 10-15 µA leak current during startup to 20 kV, and then will settle to <0.1 µA during operation. Ionoptika engineers state that this is normal and likely charging in the cables.
- As the source becomes contaminated with C_{60} deposits, ticking (electrical discharging) will become more frequent. This is characterized by a distinct clicking sound, loss of signal over several consecutive pixels in an image run, and temporary spike in C_{60} source pressure (on HFIG3).

RLQ RF arcing

If sample chamber, Block 1, or Block 2 pressures get too high (>100 mTorr) while RF is active on the RLQ, arcing will occur within the chamber, observable as flickering light in the sample chamber camera view. This is most likely to happen if a sample is loaded with RF on, since the translational stage will always introduce a large amount of air to the system as it moves into place. Following an arcing event the RLQ will not perform properly and fails to transmit ions for ~1 day, after which it has historically recovered on its own.

The RF supply was interlocked to the XGS-600 with a 20 mTorr setpoint to avoid this occurrence in the future.

Step motor control board failure

November 2011 – While working on the oMALDI sample stage, the control/power PCB for the stage (located in the oMALDI control box on the side of the instrument) was damaged and one step motor began to fail intermittently. A replacement PCB was purchased from AB SCIEX and swapped in to solve the problem. Note that a small box with four toggle switches on the board MUST be set identically on the new PCB (see **Figure A.5** below), or it will not communicate properly with the QSTAR PC.

Part # 1013125	PCB,CTRL QUIET MOTOR #2 RETRO

Figure A.6: oMALDI control/power board with configuration switch labeled.

The cause of failure was likely disconnection of the stepper power cable during operation, according to an Electrocraft engineer:

> The stepping motor is actually a linear actuator. I agree that it sounds like you blew the drive. The components likely to fail are the power output stage. Probably a module with 8 or more pins on it and a heatsink. Should be mfgs markings on the chip. You could try replacing it. I don't think increasing the load would cause the drive to blow since steppers run at rated current all the time. More than likely you disconnected somehow while playing with it, or you had a bad connector and all the energy from the coil got into the power module on the board. (sort of like an ignition coil). { v= L di/dt… if you interrupted the flow of current you'd get a very high di/dt term and the resulting voltage would fry the power module…find a EE around campus somewhere and ask them J)

Following installation of a new PCB, the onboard flash memory must be accessed and configured properly for our system as follows, and as shown in **Figure A.7**.

1. Open oMALDI Server
2. Operate menu -> Expert control -> Service mode, password "Omicron1"
3. Import proper parameters:

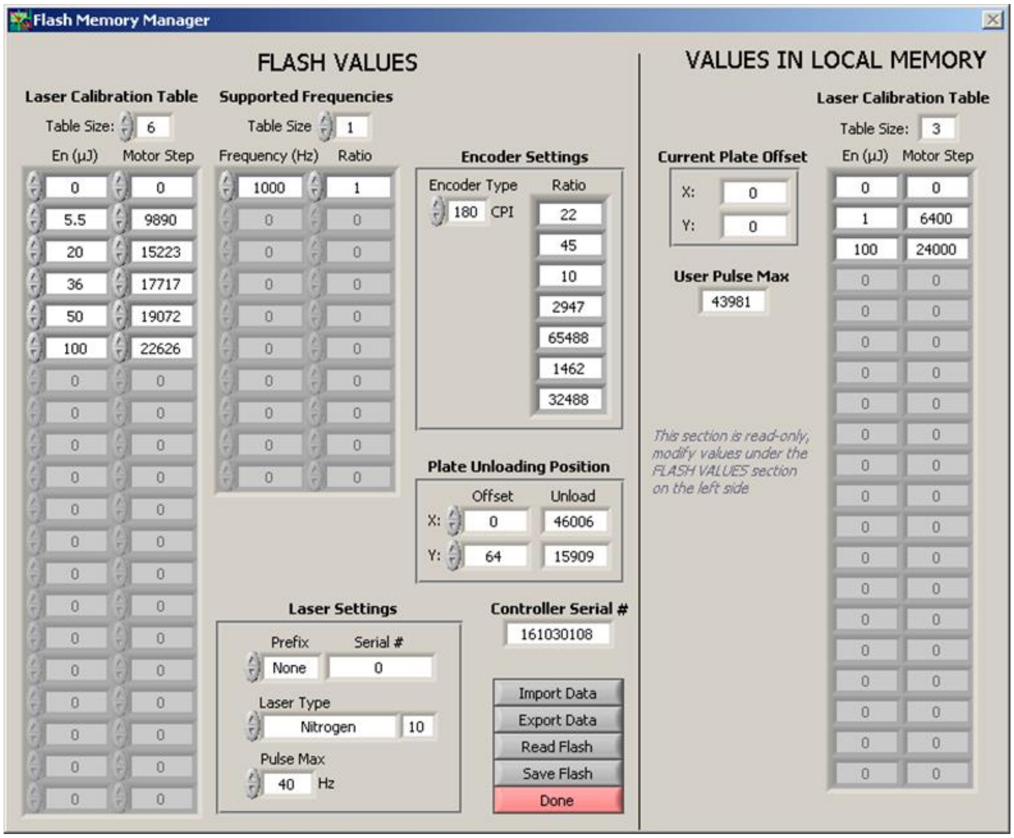

FLASH VALUES

Laser Calibration Table

Table Size: 6

En (µJ)	Motor Step
0	0
5.5	9890
20	15223
36	17717
50	19072
100	22626
0	0
0	0
0	0
0	0
0	0
0	0
0	0
0	0
0	0
0	0
0	0
0	0
0	0
0	0

Supported Frequencies

Table Size: 1

Frequency (Hz)	Ratio
1000	1
0	0
0	0
0	0
0	0
0	0
0	0
0	0
0	0
0	0

Encoder Settings

Encoder Type: 180 CPI

Ratio
22
45
10
2947
65488
1462
32488

Plate Unloading Position

	Offset	Unload
X:	0	46006
Y:	64	15909

Laser Settings

Prefix: None
Serial #: 0
Laser Type: Nitrogen 10
Pulse Max: 40 Hz

Controller Serial #: 161030108

VALUES IN LOCAL MEMORY

Current Plate Offset

X: 0
Y: 0

User Pulse Max: 43981

This section is read-only, modify values under the FLASH VALUES section on the left side

Laser Calibration Table

Table Size: 3

En (µJ)	Motor Step
0	0
1	6400
100	24000
0	0
0	0
0	0
0	0
0	0
0	0
0	0
0	0
0	0
0	0
0	0
0	0
0	0
0	0
0	0
0	0
0	0

Figure A.7: Proper values for oMALDI controller PCB flash memory, accessed through oMALDI Server.

TW-700 replacement/failure

The frontmost TM pump on the QSTAR (Leybold TW-700/701) carries a high gas load as it removes most collisional focusing gas, and therefore runs very warm and requires maintenance more frequently than the others. The pump should be exchanged or overhauled at any sign of performance decline (i.e. new noises during spin up/down).

May 2014 – TW-701 pump controller spontaneously began smoking during operation under idling conditions (under vacuum, minimal gas load). The pump was stopped promptly and removed; rotor assembly appeared undamaged.

V-81 TM pump failure

The V-81 TM pump on the C_{60} gun column failed several times during instrument assembly and characterization, likely due to improper gas loads at the inlet during venting. Failure typically began as increased operating temperature and power consumption of the pump, followed by a rapid increase in temperature to the automatic shutoff point, 60 °C.

A timed N_2 backfill vent valve was added to the pump and timed to vent synchronously with the QSTAR's backfill system, and the pump has not failed since this modification.

TOF penning gauge rebuild

Over time the penning pressure gauge on the QSTAR TOF chamber will become contaminated and begin failing to ignite during instrument pump down. When this is the case, the COMBIVAC pressure gauge controller in the QSTAR will show a very low number ($<10^{-9}$ Torr) for the PM channel. The system should be vented, gauge removed, disassembled, and rebuilt with spare parts located in a box on the shelf of BI 2542 according to the instructions located in the "manuals" box in the bookshelf by the door of BI 2542. The removable metal parts of the gauge may also need to be polished clean with fine-grit sandpaper until ion burn (rainbow discolorations) is no longer visible, then rinsed thoroughly with methanol to prevent instrument contamination before reassembly.

MCP replacement

October 2013 – Low mass resolution (<5,000 FWHM) and/or split peaks were observed in mass spectra and could not be improved with tuning. This was caused by damaged MCPs, likely cracked by prolonged exposure to moisture and/or room air (i.e. not properly vented to dry N_2). New plates were ordered from Photonis Inc. (see below) and replaced in the detector assembly under laminar flow conditions. The new MCPs were tuned to 2300 V initially and yielded improved resolution (>10,000 FWHM) and reduced background noise, but did not appear to affect signal intensity significantly.

Detection Quality Long-Life™ Microchannel Plate Set
MCP 40/12/10/8 D 60:1 27-79UA MS
PS33550
$1,792.12 / set of 2

Mike Benjamin
Telephone: 508-347-4000
E-mail: m.benjamin@usa.photonis.com

QSTAR quad chamber hot cathode gauge replacement

April 2014 - The filament in the QSTAR's hot cathode pressure gauge (located on the quadrupole chamber, beside the TM cone pump and Ar gas inlet) broke, resulting in inability of the instrument to successfully pump down (TM pumps would spin up but time out waiting for pressure setpoint). A new gauge ("Triode Mini Ion Gauge Tube with 90° Elbow") was purchased from SIS (link below) and swapped in to resolve the issue.

http://www.sisweb.com/vacuum/mini-iongauge-90deg.htm

oMALDI x-stepper rail set info

Translation stage bearings are easily damaged, and while ours have remained in good condition, Winograd group had to replace theirs. The dimensions of the cage which the roller bearings sit in is 0.59mm thick, 5.5 mm high, and ~93.4mm long. The actual roller bearings are cylindrical. Part/contact information is:

Rail set part # NB-2135SS, $382.00 for complete set
Roller cages part # 2K23ZSS, $92.00 per strip (2x strips for set)

DelTron Precision Inc.
5 Trowbridge Drive
Bethel, CT 06801
P: (203)778-2727
F: (203)778-2721
Karen Fusaro, Sales
karen@deltron.com
www.deltron.com

OUTSTANDING PERFORMANCE ISSUES

Ion lag, ion path contamination/charging, and “conditioning”

Ion transmission through the adapted system appears to change with use, and despite significant characterization the phenomenon is not fully understood but seems to arise from a combination of electrical charging and contamination of the RLQ tips. Observations are:

- After cleaning the RLQ *ex situ*, poor transmission is initially observed in either source mode (MALDI/SIMS), especially for >500 Da ions e.g. Renin Substrate. Transmission improves with several minutes of constant ionization until finally “good” signal is observed, i.e. Renin Substrate MH+ signal meets/exceeds specification in a 2 min / 500 fmol MCA MALDI test.
- After some time in use, ion transmission appears to decline again especially for >500 Da ions. This can occur over weeks or hours of use depending on many variables: it seems to occur only (or much faster) in SIMS mode, high C_{60} sample currents (>100 pA) accelerate the decline greatly, and a non-centered probe position also accelerates the decline. The effect appears to not be caused by MALDI mode use, though once caused by SIMS mode the effect persists in MALDI mode.
- Also with use after conditioning, a delay between C_{60} beam unblanking and secondary ion detection occurs and appears to grow in length until, at worst, no signal is observed until several seconds of constant bombardment.
- Transmission can be partially and temporarily restored by generating negative ions for several minutes to “uncharge” the system, though fully restoring performance requires *ex situ* RLQ tip cleaning and reconditioning.
- When an HFIG was used with mTorr N_2 focusing gas in adapter Block 1, signal was lost within a few minutes of operation, and was partially reversible by negative ion uncharging. HFIGs produce up to mA-scale ion currents to measure pressure, so it possibly produced an effect similar to whatever occurs in SIMS mode to cause transmission decline.
- The conditioning effect is observed even without a C_{60} tip installed, suggesting that it does not contribute significantly to the problem.

Instrument performance could be significantly improved by characterizing and fully solving this problem, especially since the “ion lag” effect causes loss of the initial ions generated upon sampling, which is also when most intact biomolecules will be generated by SIMS. One hypothesis: RLQ rods are particularly susceptible to contamination and subsequent charging due to having a large active electrode face and a stainless steel surface which (according to Ardara Tech.) may present abundant ion “adsorption sites” due to carbon content. Possible solutions therefore include 1) coating the RLQ rods in a more inert metal e.g. Ni shim stock, Au plasma coating, or electroplating, or 2) replacing the RLQ altogether with a gold-coated round-rod quadrupole similar to the Q0 guide.

Sample chamber vacuum seals

While the oMALDI sample chamber / adapter Block 1 are maintained at high vacuum (<0.1 mTorr) overall for SIMS-mode compatibility, the seals in and around the sample chamber were not designed for this vacuum level and were found to leak significantly, evidenced by oxidation of analytes and confirmed by He leak detection. Steps were taken to remedy this problem – translation stage tightened, softer gaskets used, non-contaminating vacuum grease (Apiezon L) was used on the translation stage seals, and sample door seal was modified to improve contact area – but subsequent He leak detection indicated that leaks persisted, so local pressure may still be too high, compromising SIMS-mode performance. Improving these vacuum seals beyond current performance might be accomplished in two ways: addition of a secondary sealing layer around the sample chamber, or complete redesign of the source assembly. The latter would more likely ensure improved performance but would also involve significant engineering and reverse-engineering to build a new source which is still controllable by existing oMALDI electronics and software.

Spatial resolution upgrade

The current C_{60} ion gun is specified to a 2 micron ultimate probe diameter, delivering a few pA of sample current. Assuming the ion lag issue is resolved (allowing satisfactory ion transmission with single-pA sample current), upgrading imaging spatial resolution from the current 10 micron step motor limitation to match this may become worthwhile. One way to accomplish this may be to modify oMALDI control so that step motors may be disabled and movement signals instead redirected to the ion gun deflector plates in order to move the beam electrically.

APPENDIX B

MATRIX SUBLIMATION PROCEDURE

NOTES AND ACKNOWLEDGMENTS

This procedure was created by E. J. Lanni, modified from work published by J. Yang and R. M. Caprioli in *Anal. Chem.* (**2011**) 83, 5728-5734. **Figure B.1** shows apparatus and labels components referenced throughout the procedure below.

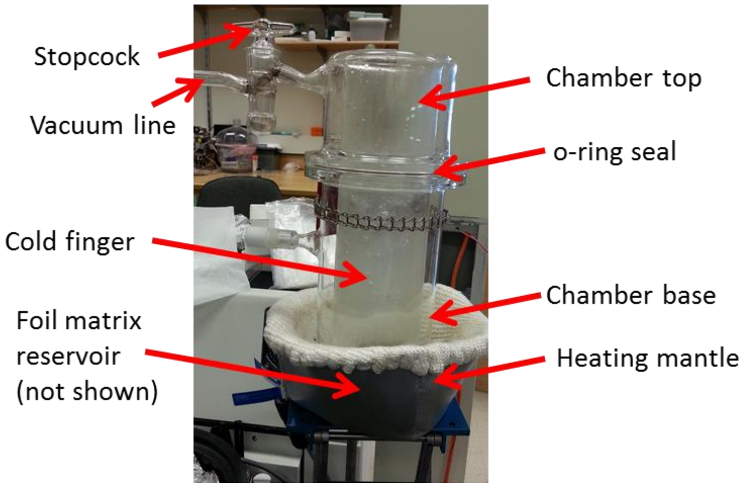

Figure B.1: Photograph of assembled sublimation chamber on heating mantle with major components labeled.

WEAR SAFETY GLASSES!

1. **Clean reservoir** with a Kimwipe, discarding previous matrix. Replace/repair if damaged.
2. **Clean chamber** internal surfaces with methanol and paper towels. *Remove excess matrix from cold finger and chamber bottom, as this affects results.*
3. **Deposit matrix** in the foil reservoir and distribute evenly by shaking chamber base gently.
4. **Seat chamber base in heating mantle** and secure with metal chain.
5. **Position sample on the metal plate** attached to cold finger, then tape down securely with strips of copper tape. *If sample is not secure or old tape is reused, it may fall during sublimation and ruin the coating.*

6. **Verify o-ring is seated properly** in groove on top of chamber base, then seat chamber top over it. *Align sample with matrix reservoir to ensure even matrix coating.*
7. **Connect vacuum line** to glass inlet on chamber. Confirm vent valve (metal valve on vacuum line) is closed.
8. **Activate vacuum pump** below table while holding chamber top down against base. It should begin loud but quickly quiet down. *If pumping remains loud and a gushing sound is heard, typically o-ring is not seated properly between chamber top and base; stop pump, reposition o-ring, and try again. If gushing continues, check vent valve, vacuum line connection to chamber, stopcock position, and Teflon stopper on chamber base for leaks.*
9. **Add water/ice mix to cold finger** and allow sample to cool for ~2 min.
10. **Activate variac** below table to begin heating mantle. Begin timing promptly.
11. After desired sublimation time, shut down:
    a. **Verify sand bath is dry**. *Exposing the glass chamber to ice or cold water while under vacuum can result in glass cracking / implosion.*
    b. **Remove chamber from mantle** and transfer gently to sand bath.
    c. **Stop vacuum pump.**
    d. **Vent chamber** by twisting off the vacuum line or by opening the manual vent valve.
    e. **Open chamber** and dump ice/water into a beaker.
    f. **Remove sample** promptly to avoid wetting from condensation.
    g. **Deactivate variac.**
    h. **Open air vent above chamber base** to remove matrix fumes from room.
    i. **Place beaker with ice water in mantle** to cool quickly.

Note: an easy way to measure coating thickness is to weigh the substrate before and after sublimation, then calculate matrix density based on approximate coated area. Best MALDI results are typically with 0.2-0.4 mg/cm^2 *for DHB and CHCA.*

Typical parameters for MALDI prep (times will vary with changes to apparatus, substrate, matrix etc.)

- For DHB: 350 mg, 12 min from room temp, variac set to 55%/120 V
- For CHCA: 350 mg, 22 min from room temp, variac set to 55%/120 V